Fall 2013

Development Of Quantitative FT- IR Methods For Analyzing The Cure Kinetics Of Epoxy Resins

Sang Ha Son
Purdue University

Follow this and additional works at: https://docs.lib.purdue.edu/open_access_dissertations

Part of the Analytical Chemistry Commons, Chemical Engineering Commons, and the Polymer Chemistry Commons

PURDUE UNIVERSITY
GRADUATE SCHOOL
Thesis/Dissertation Acceptance

This is to certify that the thesis/dissertation prepared

By SANG HA SON

Entitled
DEVELOPMENT OF QUANTITATIVE FT-IR METHODS FOR ANALYZING THE CURE
KINETICS OF EPOXY RESINS

For the degree of   Doctor of Philosophy

Is approved by the final examining committee:

James M. Caruthers   R. Byron Pipes
_____
                Chair
W. Nicholas Delgass

You-Yeon Won

Alejandro H. Strachan

To the best of my knowledge and as understood by the student in the *Research Integrity and
Copyright Disclaimer (Graduate School Form 20)*, this thesis/dissertation adheres to the provisions of
Purdue University's "Policy on Integrity in Research" and the use of copyrighted material.

Approved by Major Professor(s): James M. Caruthers
_____

_____

Approved by: Michael T. Harris   12/02/2013
                    Head of the Graduate Program   Date

DEVELOPMENT OF QUANTITATIVE FT-IR METHODS FOR ANALYZING THE
CURE KINETICS OF EPOXY RESINS

A Dissertation

Submitted to the Faculty

of

Purdue University

by

Sang Ha Son

In Partial Fulfillment of the

Requirements for the Degree

of

Doctor of Philosophy

December 2013

Purdue University

West Lafayette, Indiana

To My Precious Wife Zooyeon and Sunshine Lucas

ACKNOWLEDGEMENTS

First of all, I would like to give a special thanks to Dr. James M. Caruthers who provided me ways to solve scientific problem, how to approach the scientific issues and ways of academic and professional thinking to resolve those issues. He has also given noble advice on life throughout the years at Purdue. With his endless support, I could live a successful life here.

 I also wish to express my great appreciation to Dr. Grigori Medvedev who gave me tons of valuable advice in every moment of my research, from brain storming to modeling. I could not have found my way with my dissertation without his kind and continuous support.

My appreciation goes to my committee members, Dr. W. Nicholas Delgass, Dr. R. Byron Pipes, Dr. You-Yeon Won and Dr. Alejandro Strachan, who provided many valuable comments to make my research more fruitful.

I would like to thank all my friends from Korean Chemical Engineers at Purdue, Purdue Korean Association, and Purdue Korean Tennis Club. They were not just my colleagues or friends. They were truly all my family at Purdue.

I also give my deep appreciation to my parents, Young Koo Son, Heung Bok Kim, my brother Sang Eun Son, and parents-in-law, Kyoo Chul Cho and Young Suk Koo. Their support in Korea really encouraged me to finish Ph. D work.

The best two things that I have ever had not only for my life at Purdue but also for my entire life are that I met my precious wife, Zooyeon Cho, and that my lovely son, Lucas Son was born. They were the strongest driving force for me to complete Ph.D work and, most of all, the reasons to live. I give all my appreciation and love to them.

TABLE OF CONTENTS

LIST OF TABLES

LIST OF FIGURES

ABSTRACT

Son, Sang Ha. Ph.D., Purdue University, December 2013. Development of Quantitative FT-IR Methods for Analyzing the Cure Kinetics of Epoxy Resins. Major Professor: James M. Caruthers.

Epoxy thermosets are important engineering materials with applications in coating, adhesives, packaging and as structural components in a variety of advanced engineering products. The ultimate performance of polymer critically depends upon the details of the cure chemistry used to produce the thermoset. In order to better understand and monitor the cure chemistry, quantitative analysis of the FT-IR response has been developed for describing the epoxy-amine curing reaction as well as monitoring the hydrogen bonding that occurs in these systems The FT-IR analysis includes (i) quantitative deconvolution of complex peaks into individual spectral contributions, (ii) peak identification via DFT analysis and (iii) appropriate baseline correction. These FT-IR analysis methods were utilized to resolve spectral complexity in epoxy-amine thermoset resin systems.

Using the quantitative FT-IR tools described above, the hydrogen bonding of amine and hydroxyl groups was determined for (i) the self association and inter-association of N-methylaniline (NmA) and isopropanol and (ii) the reaction with a series of hydrogen bonding acceptors, including toluene, triethylamine, epoxy butane and dipropylether that represent π-bond, electron pair on amine, epoxide and ether groups. Simple mass-action

equilibrium models of the amine and hydroxyl group hydrogen bonding were developed, where both the extinction coefficient and equilibrium constants were determined from the data. However, this simple analysis was only valid for dilute concentrations, where an unexpected maximum in the free hydrogen as measured by FT-IR vs. total amount of NmA or isopropanol was observed. It was postulated that a phase transition occurs at high NmA or isopropanol concentrations.

The epoxy-amine reaction kinetics was studied using quantitative FT-IR. First, the reaction kinetics of a monoepoxide with a monoamine was studied, where reaction kinetics was followed by (i) HPLC analysis and (ii) then compared with FT-IR analysis. Subsequently, quantitative FT-IR was applied to the thermoset system of a digylcidyl ether of bisphenol-A epoxy cured with aniline, where multiple absorbance profiles for the different vibrational peaks enabled self-consistent determination of the various reacting species. This analysis demonstrates the power of quantitative FT-IR analysis to follow detailed reaction kinetics in thermoset systems. The effect of temperature on the FT-IR spectra was measured for the fully cured Epon825-aniline system, where the hydrogen bonding peaks exhibited significant changes in temperature dependence of the absorbance near the T_g of 95^oC. Finally relaxation of fully cured polymer was examined by observing the absorbance evolution following a temperature jump. In summary, quantitative FT-IR analysis provides valuable information on the chemical kinetics in curing thermoset systems as well as changes in the structure of the resulting glassy thermoset with temperature and sub-T_g thermal annealing.

.

CHAPTER 1. INTRODUCTION

1.1   History of Epoxy Thermoset

General meaning of epoxy is any chemical that contains epoxide functional groups. The

thermoset cured from epoxy resin or prepolymer has superior properties, both in chemical

and mechanical points of view such as good thermal and chemical resistance, good

adhesion property, and exceptional electrical property. The epoxy thermoset have been

utilized in various fields of industry since 1930's. The first applications of epoxy

thermoset were paints and coatings. Then, as a variety of cure methods were developed,

usages of epoxy were extended to the state of the art aircraft industry with a form of

composite material.

1.2   Epoxy Cure Chemistry

Epoxide group can react with amine group to form a network. Epoxide-amine cure

system is one of the most commonly used. Primary amine has two hydrogen branches

and a single lone pair of electrons. These lone pair electrons attack the carbon on the

epoxide group. Epoxide ring opens as a result of being attacked by the electron pair and

the nitrogen atom becomes positively charged and the oxygen atom becomes negatively

charged. At the same time, hydrogen atom transfer occurs to form a hydroxyl group and secondary amine. This secondary amine also has a pair of electrons and it becomes a driving force to form a linkage with an epoxide group. Figure 1.1 shows crosslinking mechanism of epoxide-amine system. In typical amine-epoxide cure system, there are two major reaction categories, which are an epoxide reaction with a primary amine to form a secondary amine, and an epoxide reaction with a secondary amine to form a tertiary amine. At higher temperature, an epoxide can also react with a hydroxyl group to form an ether linkage. However, this etherification is a minor reaction and the rate constant of etherification is relatively small compared with those of primary amine reaction and secondary amine reaction.
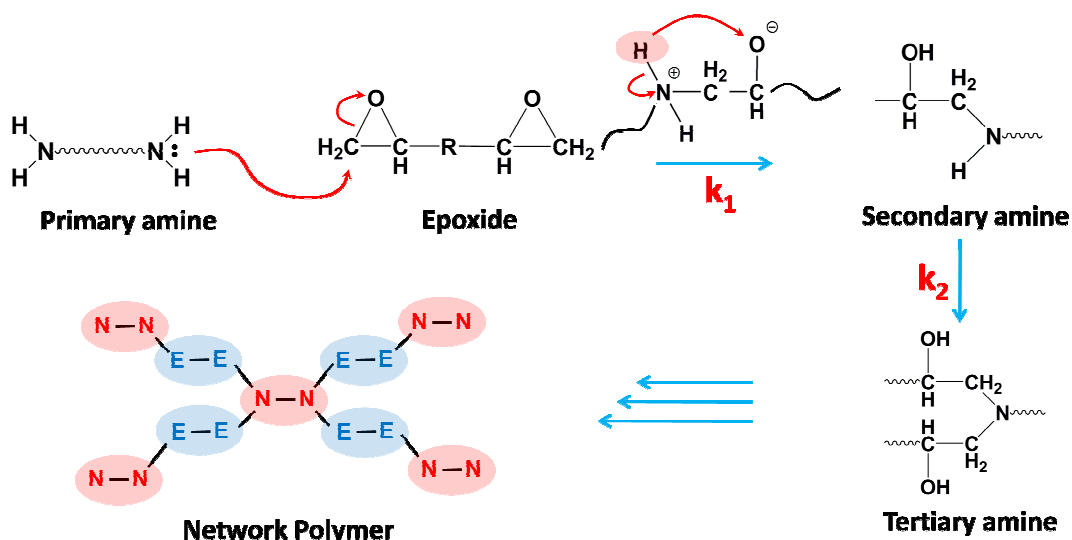
Figure 1.1 Reaction mechanism of diepoxide with diamine curing

Table 1.1 Typical epoxy resins and diamine crosslinkers

Compound	Structure
Phenylglycidylether	
Epon825	
Epon828 (n= 0.14)	
MY720	

Table 1.2 Typical amine crosslinkers

Compound	Structure
3,3'-DDS	
Jeffamine M-600 n from 6 to 12, nave=9	
Jeffamine T-403 (x+y+z=5 to 6)	

1.3   Curing Analysis Techniques

The conventional method for monitoring cure of polymeric material has been conducted

by Differential Scanning Calorimetry (DSC). DSC measures heat flow of both the

reference pan (with air) and the sample pan. By subtracting the heat of the reference pan

from that of sample pan, it provides real time heat flow rate into or out of the sample with

respect to time or temperature. DSC can measure heat flow of the sample either at the

isothermal condition with a constant heating temperature or at a dynamic environment

with a specific ramp rate. Degree of cure is related to the exothermic heat flow rate in that,

as cure reaction goes on, more heat is released. This relationship can be expressed by the

equation,

$$\frac{d\alpha}{dt} = \frac{1}{H_t}\frac{dH}{dt} \tag{1.1}$$

$$\alpha(t) = \frac{H(t)}{H_t} \tag{1.2}$$

Where, H(t) is the heat of reaction at time t. H_t is total amount of heat released during the

whole cure reaction. By determining α with respect to time or temperature, lumped

kinetics could be performed.

FT-IR Spectroscopy is a widely used analytical method to track cure/degradation of

epoxy system [1-6]. Infrared radiation emitted from a light source passes through the

sample. Each chemical species in the sample absorbs the energy of the light causing its

chemical bonds to vibrate.

For a group of three atoms adjacent to each other, there are totally six vibration modes,

Symmetric and asymmetric vibrations (stretching vibration), scissoring and rocking (in-

plane vibration), and wagging and twisting (out-of-plane vibration). Theoretically, a non

linear molecule that contains n atoms has *3n-6* fundamental vibrational modes that can be responsible for the absorption of infrared light [7].
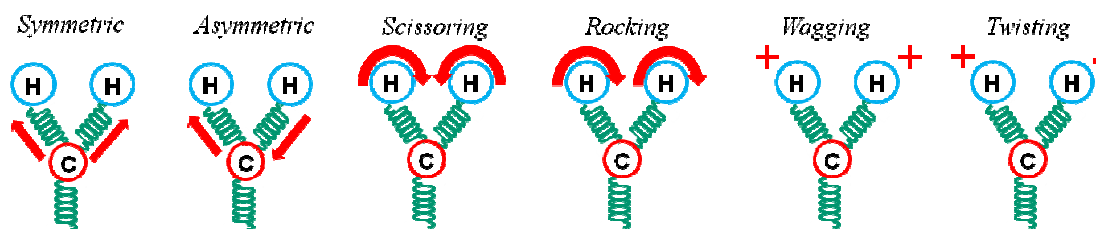
Figure 1.2 Six molelcular vibrational modes shown in FT-IR spectra

FT-IR calculates and shows the amount of absorbed light by all chemical species at a whole spectral region. The spectral analysis region is commonly divided into three major areas of interest such as far-IR (100-400 cm^{-1}), mid-IR (400-4000 cm^{-1}), and near-IR (4000-12000 cm^{-1}). In a mid-IR region, fundamental peaks due to molecular vibration or stretching modes of chemical species are located. This region is characterized by strong peak intensity but the peaks usually overlap with complexity. In near-IR region Combination and overtone bands are found. In this region, the peak intensity is 10 to 100 fold less than that in the mid-IR region but the peaks are more sparsely distributed so it is relatively easy to identify individual peaks without deconvolution process. Near-IR region has been employed to investigate cure kinetics of polymers for decades due to its sparse distribution of the peaks. However, in some near-IR spectral range, it is difficult to distinguish a peak from a convoluted spectral line shape because of the absence of peak assignment for the neighboring peaks. Mid-IR analysis is getting more powerful than near-IR analysis if it is accompanied by peak assignment and deconvolution techniques.
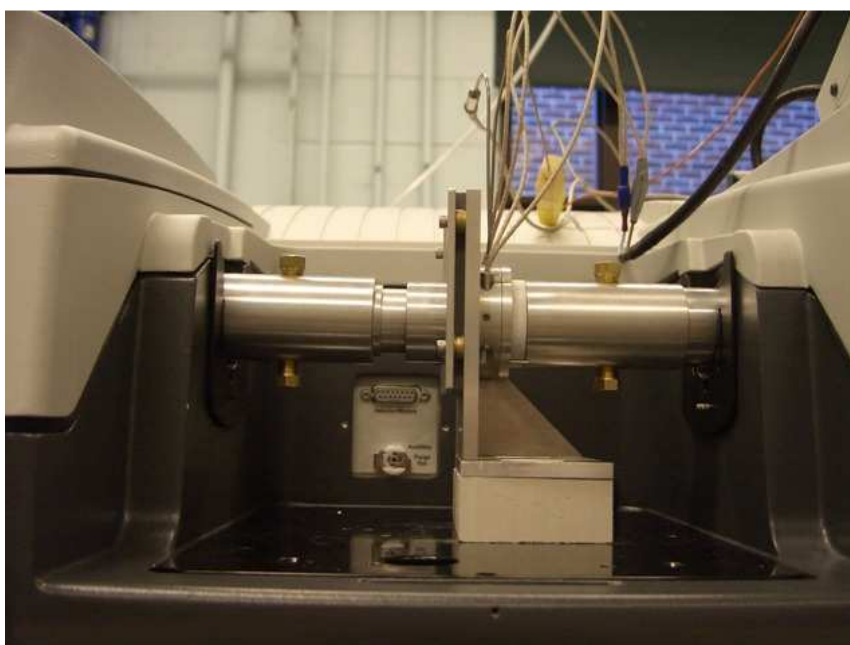
Figure 1.3 In-situ FT-IR spectroscopy with heating assembly installed

1.4   <u>Thesis Organization</u>

The thesis is organized as follows. Quantitative FT-IR method is demonstrated first, since

the technique is utilized for every system of interest. Peak line shape equation and the

application as well as peak assigning method via Density Functional Theory calculation

of frequency are presented in Chapter 2. In Chapter 3, hydrogen bonding associations of

amine and hydroxyl groups with various proton acceptors are investigated. Hydrogen

bonding association is discussed first due to not only the importance in properties but also

the contribution to the spectral complexity in certain wavenumber area of IR spectra. Self

and inter-association of amine and hydroxyl groups were investigated using N-

methylaniline and isopropanol as representative amine and hydroxyl groups respectively.

Proper association theories are adapted to fit the association spectral line shapes.

Finally, experimental approach of epoxy amine reaction is dealt in Chapter 4. Basic

epoxy amine reaction and its reaction participant analysis via HPLC method are

presented here. Reaction byproduct analysis via LC-MS at high temperature is also

presented at the end of this chapter. Then, conventional IR analysis of epoxy cure with

amine monitoring is introduced. The practical applications of FT-IR methodology for

non-polymeric and polymeric systems were introduced in Chapter 5 and 6 respectively.

In Chapter 5, in-situ FT-IR cure monitoring of model systems of monoepoxide and mono

amines is conducted and the validation of quantitative methodology is examined by

reaction component analysis with HPLC analysis. In Chapter 6, polymeric system of

DGEBA type Epon825 and Aniline cure is conducted and various examinations of cured

epoxy material such as glass transition temperature measurement and relaxation

monitoring were performed using quantitative FT-IR methodology.

CHAPTER 2. QUANTITATIVE FT-IR METHODOLOGY

2.1   Peak Deconvolution

A major objective of this paper is the quantitative fitting of FT-IR spectra in order to determine the evolution of the various chemical species in the epoxy-amine cure reaction. Prior to the deconvolution, the obtained spectra should be preprocessed to correct curvilinearly shifted baseline, which can be resulted from scattering. The detrending method was applied for the baseline correction; specifically, (i) several baseline points are selected in regions of the spectra where there are no IR peak and (ii) then these points are fit to a quadratic line (i.e. $a\lambda^{*2} + b\lambda^{*} + c$) via least square regression. The corrected absorbance intensity at wavelength λ^{*}, $x_{i,DTR}$ is then determined from the intensity x_i measured in the FT-IR by $x_{i,DTR} = x_i - (a\lambda^{*2} + b\lambda^{*} + c)$. For the epoxy-amine systems of interest, four regions without clear FT-IR adsorption are 1795-1803 cm^{-1}, 1880-1884 cm^{-1}, 2503-2507 cm^{-1} and 3718-3725 cm^{-1}, where the absence of adsorption bands was confirmed by Density Functional Theory (DFT) calculation of IR adsorption frequencies for the various reaction participants. Figure 2.1 shows an example of detrending for a series of spectra obtained during the reaction of phenylglycidylether with N-methylaniline at 80°C for 24 hours. Green lines are the quadratic line shape which is subtracted from each original FT-IR spectrum.
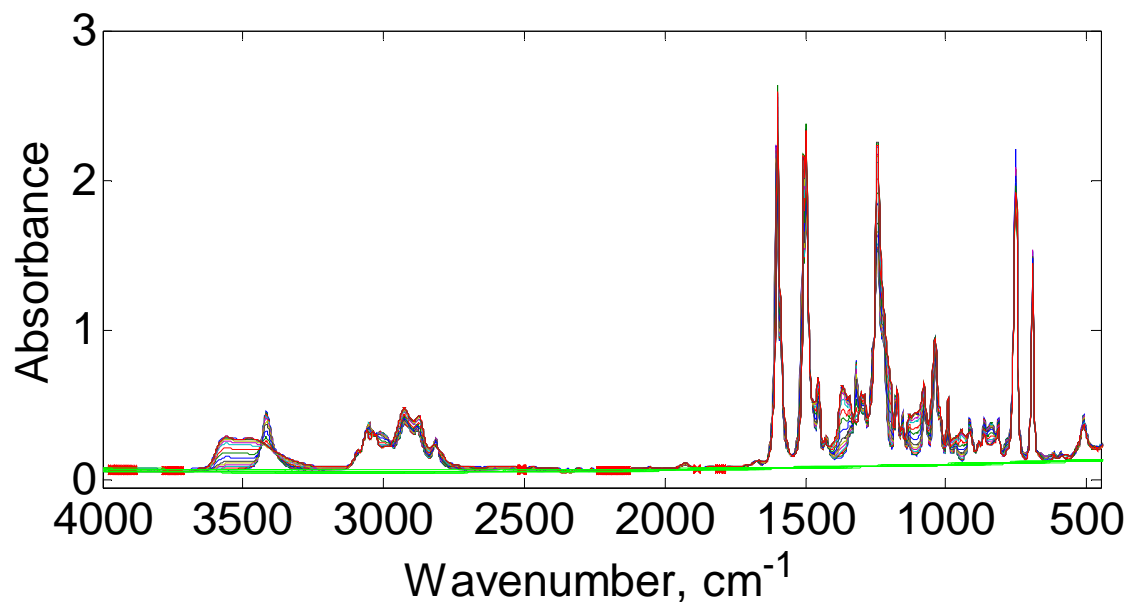
Figure 2.1 Baseline correction procedure for PGE-NmA reaction spectra by detrending method

Quantitative fitting of the FT-IR spectra requires deconvolution of the overlapping peaks

in the spectra and assignment of the peaks to the underlying molecular vibrations. The

initial deconvolution of the FT-IR spectra into individual vibrational modes was done

using CasaXPS Version 2.3.15 (Casa Software Ltd), where in a given spectral range the

program determines the number of lines, their intensity, width and Gaussian-Lorentzian

mixture. CasaXPS is an excellent tool for the initial spectral deconvolution of spectra,

but it does not allow sufficient fidelity for quantitative FT-IR analysis, e.g. in CasaXPS

spectral lines cannot have the optimized value of the Gaussian-Lorentzian mix but only

manual input of the value is possible. Moreover, one cannot constrain the ratio of

intensities for sets of spectral lines as is needed if two or more spectral lines come from

the same chemical group. In order to address these additional requirements, an additional

spectral fitting code was developed, where (i) the intensity and shape of each line could

be optimized or fixed as desired, (ii) arbitrary functional relationships between spectral lines can be specified and (iii) bounds on the various line shape parameters can be set. The code allows easy input in a spreadsheet like format, where the code then generates the appropriate MatLab^{TM} code with model parameters that are determined via optimization with respect to experimental FT-IR spectra. The line shape of an individual spectral line is given by the following product form of Gaussian and Lorentzian function

$$f\left(x;x_{O},m,A,F\right) = \frac{A\ exp\left\{-4\log 2\,(1-m)\left(\dfrac{(x-x_{0})}{2F\,/[1+\exp(a(x-x_{o})^{2})]}\right)^{2}\right\}}{1\ +\ 4m\left(\dfrac{(x-x_{0})}{2F\,/[1+\exp(a(x-x_{o})^{2})]}\right)^{2}} \quad (2.1)$$

Where, x_0 is position (i.e. wavenumber) of the i-th spectrum, F is peak width at half maximum, A is peak height, m is ratio of Gaussian and Lorentzian and the parameter 'a' describes asymmetry, a=0 for a symmetric peak. The error, E, between the experimentally determined spectra, I(x), and the N spectral lines in a given region with individual intensity $f_i(x;x_{oi},m_i,A_i,F_i)$ is given by

$$E\ =\ \sum_{k=1}^{M}w(x_k)\left[I(x_k)-\sum_{i=1}^{N}f_i(x_k;x_{oi},m_i,A_i,F_i)\right]^{2} \quad (2.2)$$

Both $I(x)$ and the individual spectral contributions $f_i(x)$ are discretized to $x=\{x_k:k=1,M\}$ with a discretation interval of 1.9285 cm^{-1}. The weighting function $w(x_k)$ is shown in figure 2.2, where the triangular regions at high/low wavenumbers control the effect of contamination from the tails of large peaks just outside the spectra region of interest. Minimization of E was performed using the constrained nonlinear, multivariate optimization function fmincon in MatLab to determine

$\{x_{oi}, m_i, A_i, F_i : i = 1, N\}$.   The peak area was calculated by numerical integration using

the trust-region-reflective algorithm in MatLab with a wavenumber discretation interval

of 0.1 cm^{-1}.
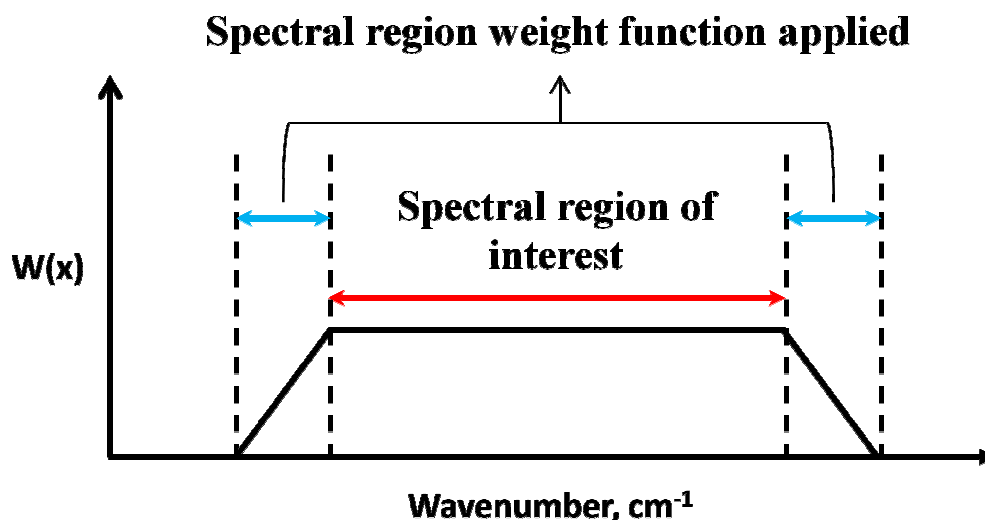
Figure 2.2 Schematics of weighting function

2.2   Peak Assignment via DFT Frequency Calculation

The chemical origins of the various FT-IR peaks were identified using density functional

theory (DFT). The ground state of the molecules of interest were determined with

Gaussian03 (Gaussian, Inc.) using B3LYP functional and lanl2dz basis set. The FT-IR

spectra were determined from the eigenvectors of the force constant matrix as determined

with the second partial derivatives of the potential V with respect to displacement of the

atoms in cartesian coordinates ξ in Gaussian [8].

$$f_{CARTij} = \left(\frac{\partial^2 V}{\partial \xi_i \partial \xi_j} \right)_0 \tag{2.3}$$

The molecular motion associated a particular vibrational line (i.e. eigen value) was determined visually using GaussView (Gaussian, Inc) by observing the identity and type of motion of the atomic centers of the associated eigenvector.   The spectral lines determined by DFT are typically shifted by up to 40 cm^{-1} from those observed experimentally in the lower wavenumber region, 500-1700 cm^{-1} and showed up to 200 cm^{-1} displacement in the higher wavenumber region, 3000-3700 cm^{-1}; however, the relative location and spectral intensity calculated from DFT agree well with that observed experimentally, providing excellent identification of the molecular origin of the various FT-IR lines. The lines and intensities for N-methylaniline and Phenylglycidylether and a reaction product of PGE with NmA (i.e. PN) as determined by DFT area shown in from figures of 2.3 to 2.5. The frequency FT-IR lines as determined via DFT are given in Table 2.1-2.3 along with the experimental FT-IR lines frequencies and molecular motion responsible for that line as determined form the associated eigenvector. Frequency calculation using DFT was also utilized to examine various hydrogen bonding associations of model amine group with model proton acceptor groups. Two molecular structures of associating species were built in a same space and the hydrogen bond lengths were found from geometry optimization. Once the molecular geometry was optimized, frequency was calculated and compared with those shown in the real spectra of hydrogen bonding associations. DFT calculation details and results could be found in Chapter 3.
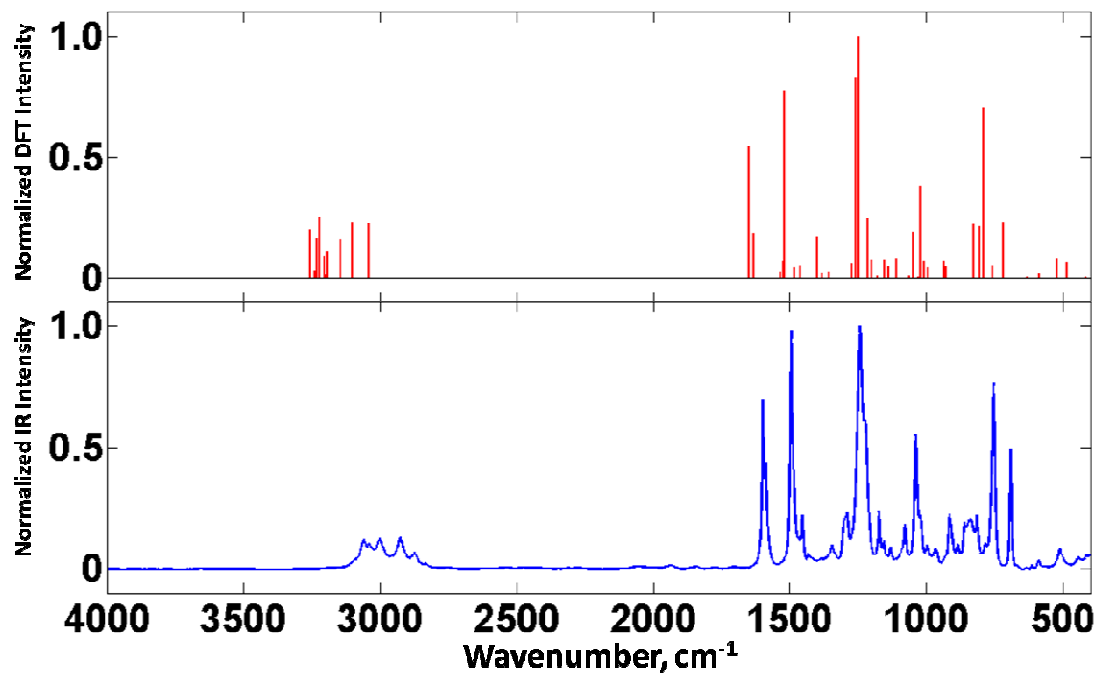
Figure 2.3 Comparison of normalized PGE vibration frequency obtained from DFT with experimental IR spectrum of neat PGE
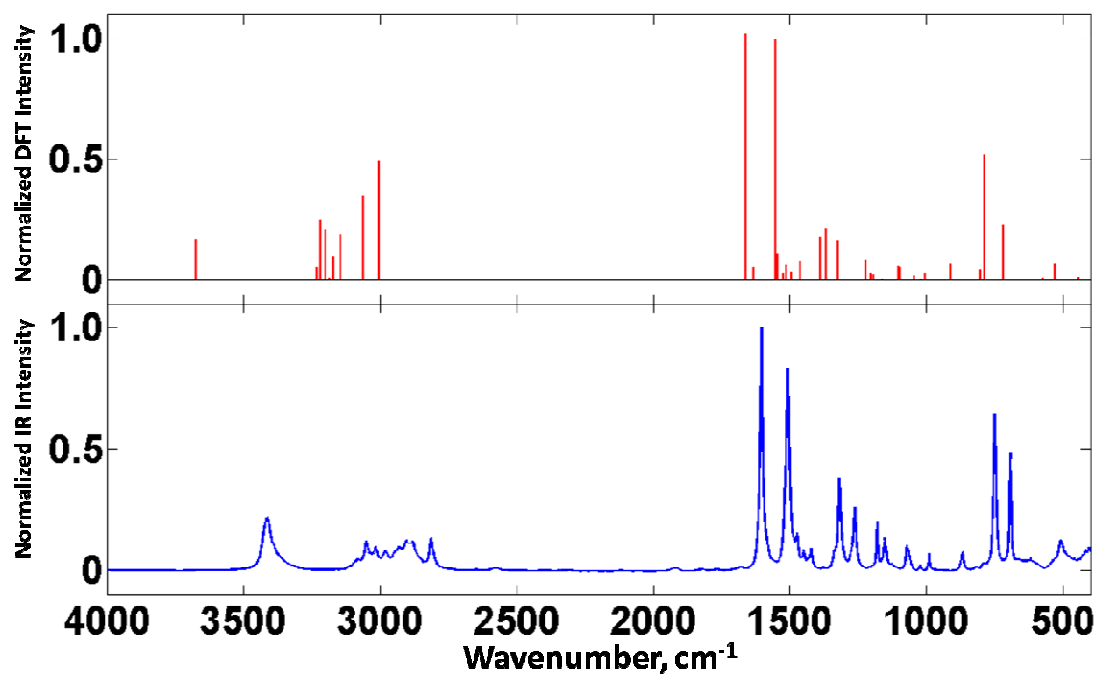
Figure 2.4 Comparison of normalized NMA vibration frequency obtained from DFT with experimental IR spectrum of neat NmA
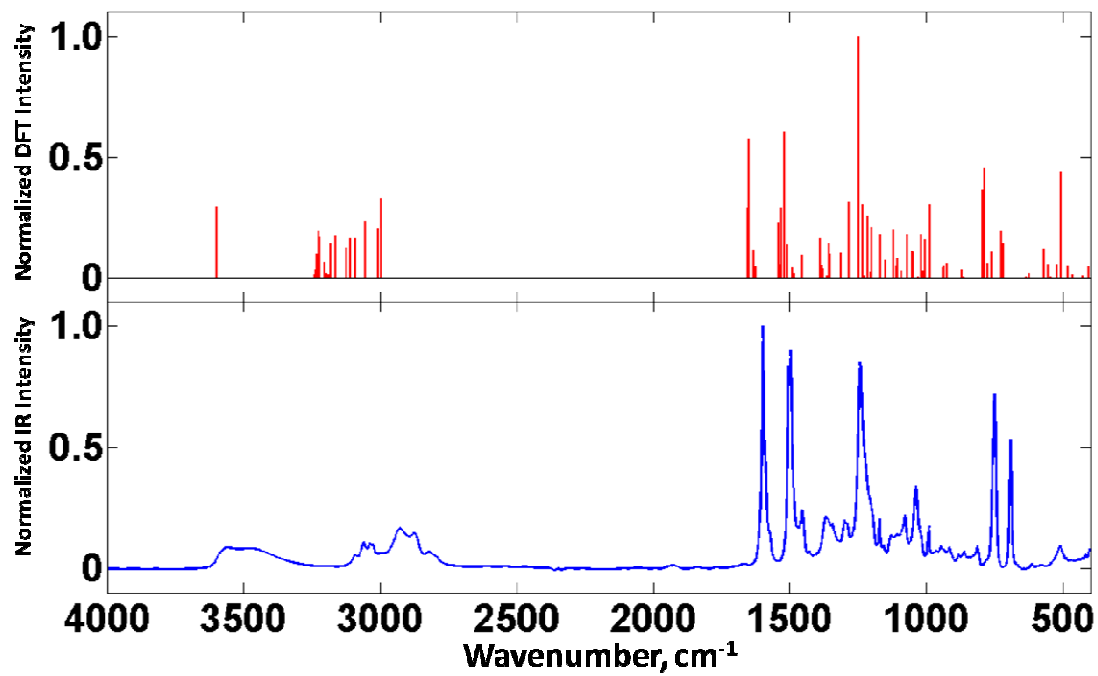
Figure 2.5 Comparison of normalized vibration frequency of PGE cured with NmA (PN) obtained from DFT with experimental IR spectrum of 24 hour cured PN

Table 2.1 DFT and experimentally determined FT-IR lines for PGE

No.	DFT wavenumber (cm⁻¹)	DFT intensity	IR wavenumber (cm⁻¹)	Vibrational modes
1	3256.85	27.5641	3104.42	epoxide C-H2 Asymmetric stretching
2	3239.41	3.9327	3091.61	Benzene C-H (all five C-H bonds) Symmetric stretching
3	3231.32	22.5322	3074.52	Benzene C-H (all five C-H bonds) Asymmetric stretching ([2,6] and [3,5]) Two sets are symmetric
4	3221.9	34.772	3060.42	Benzene C-H (all five C-H bonds) symmetric stretching of [2,6] and asymmetric stretching of [3]
5	3203.59	12.6412	3040.82	Benzene C-H Asymmetric stretching ([2,6] and [3,5]) two sets are asymmetric
6	3194.37	1.8578	3030.17	Benzene C-H (all five C-H bonds) Asymmetric stretching ([3,5] and 4 asymmetric)
7	3191.38	15.1702	3007.29	epoxide C-H Stretching
8	3146.45	22.1263	2925.42	epoxide C-H2 Symmetric stretching
9	3100.04	31.3938	2874.6	C-H2 in the middle Asymmetric stretching
10	3038.93	30.8257	2834.02	C-H2 in the middle Symmetric stretching
11	1651.98	74.4557	1599.74	Benzene C-C Asymmetric stretching (1-2-3) and (4-5-6) two sets are symmetric
12	1632.63	25.0847	1587.07	Benzene C-C Asymmetric stretching (1-2-3) and (4-5-6) two sets are asymmetric
13	1535.14	3.6298	1496.31	CH2 and epoxide CH2 CH2 scissoring
14	1523.38	9.6112	1489.95	epoxide C-H2 CH2 scissoring
15	1519.54	105.981	1471.37	Benzene C-H C(2)-H, C(3)-H rocking and C(5)-H, C(6)-H rocking two sets are symmetric
16	1484.81	5.7047	1454.90	Benzene C-H C(3)-H, C(4)-H, C(5)-H rocking, C(2)-H, C(6)-H rocking
17	1459.72	7.4621	1429.51	CH2 and epoxide CH (main) CH2 wagging and epoxideCH wagging
18	1398.73	23.6107	1345.85	CH2(main) and epoxide C-H CH2 wagging and epoxideCH wagging
19	1379.91	2.5824	1302.14	Benzene C-C Asymmetric stretching (1-2-3) and (4-5-6) two sets are symmetric
20	1355.42	3.4072	1291.545	Benzene C-H C(2)-H, C(3)-H rocking and C(5)-H, C(6)-H rocking, two sets are asymmetric
21	1271.97	8.2404	1264.16	CH2 and epoxide C-H(main) CH2 twisting and epoxideCH wagging
22	1256.49	113.428	1244.00	CH2 and Benzene C-N CH2 twisting and C-N stretching
23	1247.91	137.116	1222.13	CH2 and Benzene C-N CH2 twisting and C-N stretching (opposite direction from 1256.49)
24	1213.35	33.757	1174.57	Benzene C-H C(2)-H, C(3)-H scissoring, C(3)-H, C(4)-H scissoring, C(5)-H, C(6)-H scissoring
25	1200.48	10.3672	1155.56	Benzene C-H C(4)-H, C(5)-H scissoring, C(5)-H, C(6)-H scissoring
26	1176.7	1.251	1132.14	epoxide C-H2 (main), C-H and C-H2 epoxide C-H2 wagging C-H scissoring and C-H2 twisting
27	1152.92	9.9239	1080.22	epoxide C-H2 (main) and C-H2 epoxide C-H2 wagging and C-H2 twisting
28	1137.67	6.123	1039.63	epoxide C-H2, C-H(main) and C-H2 epoxide C-H2 twisting C-H scissoring and C-H2 twisting

Table 2.1 Continued.

29	1109.56	11.5174	1021.45	Benzene C-H C(2)-H, C(3)-H scissoring, C(4)-H, C(5)-H rocking, C(5)-H, C(6)-H scissoring
30	1061.32	1.1241	996.48	epoxide C-H2 (main), C-H epoxide C-H2 twisting C-H scissoring
31	1046.93	25.9914	967.11	Benzene C-H C(2)-H, C(3)-H rocking, C(5)-H, C(6)-H rocking two sets are symmetric
32	1029.54	0.79	933.07	Benzene C-H C(2)-H, C(3)-H twisting, C(3)-H, C(4)-H twisting, C(4)-H, C(5)-H twisting, C(5)-H, C(6)-H twisting
33	1022.32	52.4278	906.71	O-C (main), and benzene C-C O-C stretching, and C(1-2-3), C(4-5-6)scissoring, two sets are asymmetric
34	1009.57	9.8734	885.92	benzene C-C O-C stretching, and C(1-2-3), C(4-5-6)scissoring, two sets are symmetric
35	1006.27	4.6471	863.27	Benzene C-H C(2)-H, C(3)-H twisting, C(5)-H, C(6)-H twisting
36	993.195	5.6035	838.23	epoxide C-H2 and C-H2 (main) epoxide C-H2 twisting and C-H2 twisting
37	934.233	9.7498	849.58	Benzene C-H C(2)-H, C(5)-H wagging, C(3)-H twisting
38	926.27	6.4771	832.36	epoxide C-H2 (main) and C-H2 epoxide C-H2 twisting and C-H2 twisting
39	859.473	0.2851	818.70	Benzene C-H C(2)-H, C(3)-H wagging and C(5)-H, C(6)-H wagging, two sets are asymmetric
40	825.12	30.4506	916.36	(epoxide) C-O-C O-C-C asymmetric stretching
41	803.571	29.5052	844.57	(epoxide) C-O-C C-O-C symmetric stretching
42	789.419	96.5433	754.84	Benzene C-H C(2), C(3), C(4), C(5) wagging
43	757.024	7.5881	785.14	(epoxide) C-O-C C-O-C asymmetric stretching
44	716.001	31.6341	692.50	Benzene C-H C(2), C(4), C(6) wagging
45	630.91	0.6225	633.94	benzene C-C C(1-2-3) scissoring and C(4-5-6) scissoring, two sets are asymmetric
46	585.503	2.3369	614.25	benzene C-C C(6-1-2) scissoring, C(3-4-5) scissoring, two sets are symmetric
47	520.966	11.1409	564.19	Benzene C-H C(2)-H, C(3)-H, C(5)-H, C(6)-H wagging
48	484.692	8.7868	512.52	C(benzene)-O-C C-O-C scissoring
49	428.009	0.1444	N/A	benzene C-C C(2), C(5) wagging and C(3), C(6) wagging, two sets are asymmetric
50	415.011	0.5362	N/A	C-C(epoxide)-C(epoxide) C-C-C scissoring
51	311.32	9.2865	N/A	C-C(epoxide)-O(epoxide) C-C-O scissoring
52	251.107	7.685	N/A	O-C-C(epoxide) O-C-C scissoring
53	238.544	1.7246	N/A	C(benzene)-O-C C-O-C wagging
54	114.143	8.5452	N/A	O-C-C(epoxide) O-C-C wagging
55	103.983	2.6189	N/A	O-C-C(epoxide) O-C-C wagging
56	58.998	3.8215	N/A	C-C(epoxide)-C(epoxide) C-C-C scissoring
57	42.4448	0.5001	N/A	C-C(epoxide)-C(epoxide) C-C-C scissoring

Table 2.2 DFT and experimentally determined FT-IR lines for NmA

No.	DFT wavenumber (cm^{-1})	DFT intensity	IR wavenumber (cm^{-1})	Vibrational modes
1	3673.88	30.6499	3414.27	N-H Asymmetric stretching
2	3231.39	10.1465	3050.53	Benzene C-H (all five C-H bonds) Symmetric stretching
3	3219.59	45.7729	3017.09	Benzene C-H (all five C-H bonds) symmetric stretching of [4,5] and asymmetric stretching of [2]
4	3199.74	38.0717	2982.59	Benzene C-H (all five C-H bonds) symmetric stretching of [3,4] and [5,6], two sets are asymmetric
5	3186.88	1.8892	2946.39	Benzene C-H (all five C-H bonds) symmetric stretching of [2,4] asymmetric stretching of [3]
6	3172.15	17.4164	2929.46	Benzene C-H Asymmetric stretching of [5,6]
7	3144.48	34.1423	2905.15	C-H Stretching (C-H)
8	3063.66	63.6896	2879.81	C-H2 Asymmetric stretching
9	3005.59	89.7721	2812.64	C-H3 (all Hs) Symmetric stretching
10	1662.59	186.39	1604.87	Benzene C-C Asymmetric stretching (1-2-3) and (4-5-6) two sets are symmetric
11	1631.24	9.5509	1586.82	Benzene C-C Asymmetric stretching (1-2-3) and (4-5-6) two sets are asymmetric
12	1553.7	182.594	1509.36	C-H3 and N-H CH3 scissoring and C-N-H scissoring
13	1544.04	20.5029	1493.33	C-H3 H-C-H scissoring
14	1523.96	5.1987	1473.66	N-H and Benzene C-H N-H scissoring and C(3,4)-H rocking, C(5,6)-H rocking
15	1511.97	10.9242	1448.50	CH3 C-H twisting
16	1493.18	5.8023	1433.06	CH3 C-H scissoring (all symmetric)
17	1460.84	14.4181	1421.95	N-H and Benzene C-H N-H scissoring and C(3,4,5)-H rocking
18	1388.9	32.3962	1339.89	Benzene C-C Asymmetric stretching of (6-1-2) and (3-4-5), two sets are symmetric
19	1367.55	38.9089	1319.58	Benzene C-H C(2,3,4,5,6)-H rocking
20	1322.56	30.0258	1263.99	Benzene C-H and N-H C(5,6)-H rocking and N-H scissoring
21	1221.63	14.9361	1179.67	Benzene C-H C(2)-H, C(3)-H scissoring and C(5)-H, C(6)-H scissoring
22	1203.27	5.2198	1152.34	Benzene C-H C(2)-H, C(3)-H scissoring and C(3)-H, C(4)-H scissoring C(4)-H, C(5)-H scissoring and C(5)-H, C(6)-H scissoring
23	1192.72	4.8547	1125.39	H-C-N H-C-N scissoring
24	1159.14	0.9434	1110.19	CH3 C-H2 twisting
25	1103.83	10.7244	1073.33	Benzene C-H C(2)-H, C(3)-H scissoring and C(3)-H, C(4)-H rocking and C(4)-H, C(5)-H rocking and C(5)-H, C(6)-H scissoring
26	1094.97	9.6556	1066.38	N-C N-C stretching
27	1043.08	4.1618	1023.55	Benzene C-C C(2-3-4) symmetric stretching
28	1019.89	1.0907	990.30	Benzene C-H C(3,5)-H wagging and C(2,4,6)-H wagging
29	1003.04	5.6633	979.90	Benzene C-C C(6-1-2) symmetric stretching, C(3-4-5) symmetric stretching
30	999.52	0.0233	947.53	Benzene C-H C(2,5)-H wagging and C(3,6)-H wagging, two sets are asymmetric

Table 2.2 Continued.

31	909.768	12.3641	869.31	Benzene C-H C(2,6)-H wagging and C(6)-H wagging, two sets are asymmetric
32	849.312	0.0773	818.68	Benzene C-H C(2,3)-H wagging and, C(5,6)-H wagging, two sets are asymmetric
33	802.379	8.2361	777.12	Benzene C-C and N-C combination C(6-1-2) symmetric stretching, C(3-4-5) scissoring and C(benzene)-N-C symmetric stretching
34	785.779	95.2161	751.02	Benzene C-H C(3,4,5)-H wagging
35	716.146	41.8212	693.23	Benzene C-H C(2,4,6)-H wagging
36	634.391	0.3395	617.68	Benzene C-C C(1-2-3) scissoring and C(4-5-6) scissoring Two sets are asymmetric
37	572.595	1.3067	N/A	Benzene C-N-C and benzene C-C C(benzene)-N-C scissoring and C(6-1-2), C(3-4-5) scissoring, two sets are symmetric
38	527.551	11.9828	N/A	Benzene C-C C(2,3,5,6)-H wagging
39	442.954	2.4625	N/A	C-N-C C(benzene)-N-C scissoring
40	426.476	0.0705	N/A	Benzene C-C C(2,5) wagging and, C(3,6) wagging
41	334.71	114.581	N/A	N-H N-H scissoring
42	244.489	3.5025	N/A	C-N-C C-N-C wagging
43	231.818	0.3715	N/A	C-N-C C-N-C scissoring
44	174.619	2.5782	N/A	C-H3 C-H3 twisting
45	97.6055	10.0665	N/A	C-N-C C-N-C wagging

Table 2.3 DFT and experimentally determined FT-IR lines for the reaction product of PGE with NmA

No.	DFT wavenumber (cm^{-1})	DFT intensity	IR wavenumber (cm^{-1})	Vibrational modes
1	3599.11	63.5328	3570.43	PGE O-H O-H stretching
2	3239.46	2.7282	3104.46	PGE Benzene C-H (all five C-H bonds) Symmetric stretching
3	3235.19	6.8806	3092.54	NMA Benzene C-H (all five C-H bonds) Symmetric stretching
4	3232.25	21.4672	3070.85	PGE Benzene C-H (all five C-H bonds) [2,3] symmetric stretching and [5,6] symmetric stretching, two sets are asymmetric
5	3223.93	41.15	3061.57	NMA Benzene C-H (all five C-H bonds) symmetric stretching of [4,5,6] and asymmetric stretching of [2]
6	3221.86	36.8459	3053.32	PGE Benzene C-H (all five C-H bonds) [2,6] symmetric stretching and [3,4,5] symmetric stretching, two sets are asymmetric
7	3221.36	33.7557	3039.62	NMA Benzene C-H (all five C-H bonds) [3,4] symmetric stretching and [5,6] symmetric stretching, two sets are asymmetric
8	3202.33	14.2795	3027.18	PGE Benzene C-H (all five C-H bonds) [2,5] symmetric stretching and [3,6] symmetric stretching, two sets are asymmetric
9	3195.86	3.8398	3013.76	NmA Benzene C-H (all five C-H bonds) [2,5] symmetric stretching and [3,6] symmetric stretching, two sets are asymmetric
10	3193.12	1.6407	2999.41	PGE Benzene C-H (all five C-H bonds) [2,4,6] symmetric stretching and [3,5] symmetric stretching, two sets are asymmetric
11	3188.84	3.1139	2980.46	NmA Benzene C-H (all five C-H bonds) [2,4,6] symmetric stretching and [3,5] symmetric stretching, two sets are asymmetric
12	3182.55	29.8025	2955.35	NmA C-H3 H-C-H asymmetric stretching
13	3161.74	37.6403	2937.00	PGE C-H2 H-C-H asymmetric stretching
14	3124.88	26.703	2924.36	PGE epoxide C-H2 H-C-H asymmetric stretching
15	3109.64	34.8811	2904.30	NmA C-H3 H-C-H symmetric stretching, C-H stretching, two sets are asymmetric
16	3090.42	35.2409	2884.15	PGE C-H2 H-C-H symmetric stretching
17	3054.18	49.86	2870.91	PGE epoxide C-H C-H stretching
18	3007.26	44.3058	2822.33	PGE epoxide C-H2 H-C-H symmetric stretching
19	2996.7	70.6647	2797.36	NmA C-H3 C-H3 symmetric stretching
20	1653.13	62.8382	1604.87	NmA Benzene C-C C (6-1-2) symmetric stretching and (3-4-5) symmetric stretching, two sets are symmetric
21	1650.38	124.561	1599.74	PGE Benzene C-C C (6-1-2) symmetric stretching and (3-4-5) symmetric stretching, two sets are symmetric
22	1631.41	24.7829	1587.07	PGE Benzene C-C C (6-1-2) asymmetric stretching and (3-4-5) asymmetric stretching, two sets are asymmetric
23	1624.39	9.658	1586.82	NmA Benzene C-C C (6-1-2) asymmetric stretching and (3-4-5) asymmetric stretching, two sets are asymmetric
24	1542.76	48.8499	1509.36	NmA C-H3 H-C-H scissoring

Table 2.3 Continued.

25	1535.71	11.9678		PGE CH2
				CH2 scissoring
26	1528.9	62.1109	1493.33	NmA C-H3
				H-C-H scissoring
27	1520.9	429		NmA C-H3, PGE-NmA benzene C-H
				NmA H-C-H scissoring and benzene C(2,3)-H rocking, C(5,6)-H rocking
28	1520.59	130.543	1471.37	PGE Benzene C-H
				benzene C(2,3)-H rocking, C(5,6)-H rocking, two sets are symmetric
29	1507.99	28.9012	1489.95	PGE epoxide CH2
				C-H2 scissoring
30	1489.54	9.0192	1433.06	NmA CH3
				C-H scissoring (all symmetric)
31	1483.68	3.864	1454.90	PGE Benzene C-H
				C(3,4,5)-H rocking, C(2,6)-H rocking
32	1481.77	1.5519		NmA Benzene C-H
				C(3,4,5)-H rocking, C(2,6)-H rocking
33	1453.29	19.9098		PGE C-C-C
				C-C-C asymmetric stretching
34	1418.39	0.429		PGE CH2 and epoxide CH2
				[CH2 wagging], [epoxide CH wagging and epoxide CH2 wagging] two are asymmetry
35	1387.65	35.3202		PGE CH2 and epoxide CH2
				[CH2 wagging],[epoxide CH wagging and epoxide CH2 wagging] two are symmetry
36	1383.01	11.5667	1302.14	PGE benzene C-C
				C(6-1-2) asymmetric stretching and C(3-4-5) asymmetric stretching, two sets are symmetric
37	1377.6	8.299	1319.58	NMA benzene C-H
				C(2,3,4,5,6)-H rocking
38	1362.31	2.2365		PGE CH2 and epoxide CH
				CH2 wagging, epoxide C-H scissoring and epoxide CH2 twisting
39	1357.28	4.0871		NMA benzene C-C
				C(6-1-2) asymmetric stretching
40	1354.8	30.2426		PGE benzene C-C
				C(6-1-2) asymmetric stretching
41	1351.82	20.9933		NMA C-N-C
				C-N-C asymmetric stretching and entire vibration
42	1313.83	22.1293		PGE epoxide C-C and O-H
				Epoxide CH2 twisting, epoxide C-H scissoring and O-H scissoring
43	1285.34	67.5613	1264.16	PGE CH2
				CH2 twisting
44	1249.07	214.816	1244.00	PGE epoxide CH2 and O-H
				Epoxide CH2 twisting and O-H scissoring
45	1231.88	65.2122		PGE C-O-C(benzene)
				C-O-C asymmetric stretching
46	1226.36	1.5219		NMA benzene C-H
				C(2,3)-H scissoring and C(5,6)-H scissoring, two sets are symmetric
47	1213.99	55.6338	1155.56	PGE benzene C-H
				C(2,4)-H r scissoring and C(5,6)-H scissoring, two sets are symmetric
48	1205.49	5.2474	1152.34	NMA benzene C-H
				C(3,4)-H scissoring , C(4,5)-H scissoring and C(5,6)-H scissoring
49	1200.78	44.6872		NMA C-N-C(benzene)
				C-N-C symmetric stretching and entire vibration
50	1198.93	4.5594	1174.57	PGE benzene C-H
				C(2,3)-H scissoring, C(3,4)-H scissoring, and (5,6)-H scissoring
51	1167.04	39.1429		PGE Epoxide C-C-C and NMA C-N-C(benzene)
				C-C-C scissoring and C-N-C asymmetric stretching
52	1150.05	15.7729	1110.19	NmA CH3
				CH3 twisting
53	1119.79	42.95		Epoxide C-C-N
				Asymmetric stretching and entire vibration
54	1110.95	10.9617	1073.33	NmA benzene C-H
				C(2,3)-H scissoring, C(3,4)-H scissoring, and (5,6)-H scissoring

Table 2.3 Continued.

55	1107.22	17.8456	1021.45	PGE benzene C-H
				C(2,3)-H scissoring, C(4,5)-H scissoring, and (5,6)-H scissoring
56	1089.65	6.0146		PGE Epoxide C-C-C, NMA epoxide C-N-C
				C-C-C asymmetric stretching and C-N-C asymmetric stretching
57	1069.13	38.5049		PGE Epoxide C-C-C
				C-C-C symmetric stretching
58	1050.87	24.1741	1023.55	NmA benzene C-C
				C(3-4-5) symmetric stretching
59	1046.68	22.6093		PGE benzene C-C
				C(3-4-5) symmetric stretching
60	1029.94	0.447		NmA benzene C-H
				C(3,5)-H wagging and C(2,4,6)-H wagging, two sets are asymmetric
61	1028.82	1.2407		PGE benzene C-H
				C(3,5)-H wagging and C(2,4,6)-H wagging, scissoring, two sets are asymmetric
62	1017.29	38.7944	906.71	PGE O-C and benzene C-C
				C(6-1-2) scissoring and C(3-4-5) scissoring, O-C stretching
63	1012.08	6.4186		NmA benzene C-C
				C(6-1-2) scissoring and C(3-4-5) scissoring
64	1007.62	1.4329		NMA benzene C-H
				C(2,5)-H wagging and C(3,6)-H wagging, two sets are asymmetric
65	1006.95	1.5445		PGE benzene C-H
				C(2,5)-H wagging and C(3,6)-H wagging, two sets are asymmetric
66	1002.77	34.3788	885.92	PGE O-C and benzene C-C
				C(2-3-4) scissoring and C(5-6-1) scissoring, O-C stretching
67	984.286	64.7725		PGE-NmA
				PGE epoxide C-C-C symmetric stretching and epoxide C-C-N asymmetric stretching
68	937.157	8.4659		NmA benzene C-H
				C(2,6)-H wagging and C(4)-H wagging, two sets are asymmetric
69	933.641	10.4402		PGE benzene C-H
				C(2,6)-H wagging and C(4)-H wagging, two sets are asymmetric
70	926.207	13.4605		PGE epoxide CH2 and CH2
				Epoxide CH2 and CH2 rocking
71	868.668	7.0298		PGE epoxide C-C-C
				C-C-C symmetric stretching
72	864.963	0.9678		NmA benzene C-H
				C(2,3)-H wagging and C(5,6)-H wagging, two sets are asymmetric
73	862.648	0.9001		PGE benzene C-H
				C(2,3)-H wagging and C(5,6)-H wagging, two sets are asymmetric
74	794.607	78.1031	751.02	NmA benzene C-H
				C(3,4,5)-H wagging
75	787.765	97.6736	754.84	PGE benzene C-H
				C(3,4,5)-H wagging
76	777.283	13.5616		PGE benzene C-C and Benzene C-O-C
				C(3-4-5) symmetric stretching and C-O-C symmetric stretching
77	761.948	23.1316		NmA benzene C-C and Benzene C-N-C
				C(3-4-5) symmetric stretching and C-N-C symmetric stretching
78	723.144	41.6464	693.23	NmA benzene C-H
				C(2,4,6)-H wagging
79	717.808	29.5739	692.50	PGE benzene C-H
				C(2,4,6)-H wagging
80	635.486	1.1221		NmA benzene C-C
				C(2-3-4) symmetric stretching and C(5-6-1) symmetric stretching, two sets are asymmetric
81	633.079	0.7448	633.94	PGE benzene C-C
				C(2-3-4) symmetric stretching and C(5-6-1) symmetric stretching, two sets are asymmetric
82	621.688	3.8223		NmA benzene C-N-C and PGE epoxide C-C-N
				C-N-C symmetric stretching and C-C-N symmetric stretching
83	569.812	25.4285		PGE benzene C-O-C
				C-O-C symmetric stretching

Table 2.3 Continued.

84	553.079	12.2027		NmA benzene C-H
				C(2,3,5,6)-H wagging
85	542.125	0.5986	512.52	PGE benzene C-O-C and O-H
				C-O-C scissoring and O-H scissoring
86	521.405	12.6707		PGE benzene C-H
				C(2,3,5,6)-H wagging
87	508.603	94.4715	N/A	PGE O-H
				O-H scissoring
88	482.123	10.9246	N/A	PGE O-H and epoxide C-C-C, NMA C-N-C
				O-H scissoring C-C-C scissoring, NMA C-N-C scissoring
89	462.489	2.6071	N/A	PGE epoxide C-C-N and NMA C-N-C
				C-C-N scissoring, NMA C-N-C scissoring
90	427.881	0.0849	N/A	PGE benzene C-C
				C(6-1-2) twisting and C(3-4-5) twisting
91	426.184	2.146	N/A	NmA benzene C-C
				C(6-1-2) twisting and C(3-4-5) twisting
92	404.535	9.454	N/A	PGE-NmA C-C-C-N
				C-C-C-N vibration
93	341.061	3.1252	N/A	PGE-NmA
				Epoxide C-N-C(NMA) scissoring
94	339.011	1.3157	N/A	PGE-NmA C-C-C-N
				C-C-C-N vibration
95	332.607	18.6825	N/A	PGE-NmA C-C-C-N
				C-C-C-N vibration
96	285.597	1.8666	N/A	PGE benzene C-O-C
				C-O-C rocking
97	245.697	2.8177	N/A	PGE benzene C-O-C
				C-O-C wagging
98	234.507	6.3207	N/A	PGE-NmA epoxide C-N-C and epoxide C-N-benzene C
				epoxide C-N-C scissoring and epoxide C-N-benzene C scissoring
99	177.422	4.8792	N/A	NmA CH3
				CH3 twisting (all three C-Hs)
100	166.511	2.1199	N/A	PGE-NmA entire vibration
101	125.262	2.7245	N/A	NmA CH3
				CH3 twisting (all three C-Hs) opposite direction from 177.422
102	96.0871	0.0651	N/A	NmA CH3
				CH3 twisting (all three C-Hs) and entire vibration
103	79.5917	0.3254	N/A	PGE-NmA entire vibration
104	65.6114	5.2424	N/A	PGE epoxide C-C-O
				C-C-O rocking
105	48.9814	0.1002	N/A	PGE benzene C-C
				C(6-1-2) twisting and C(3-4-5) twisting
106	47.681	1.8528	N/A	PGE-NmA entire vibration
107	22.881	0.2448	N/A	PGE-NmA entire vibration
108	13.7032	0.0484	N/A	PGE-NmA entire vibration

CHAPTER 3. HYDROGEN BONDING ANALYSIS VIA FT-IR

3.1   Association theories

Hydrogen bonding has been extensively investigated using IR techniques since 1950s for
its importance in biological applications and supramolecular systems such as amino acids
or peptides [9-11]. Earlier efforts on the verification of hydrogen bonding association
were through various alcohol solutions in non-polar solvents. Since Kempter and Mecke
proposed hydrogen bonding equilibrium in alcohol [12], many researchers have found
self association equilibrium of alcohol species in dilution system. Coggeshall and Saier
further developed Kempter and Mecke's equilibrium theory using different association
constants such as dimer and linear oligomer formation constants for alcohol-CCl_4 binary
systems [13]. Fletcher found acyclic and cyclic tetramer were the main association
species in ethanol-d_1 solution dissolved in n-decane system [14]. Shinomiya et al. applied
dimer-tetramer-octamer equilibrium model to the hydroxyl group association in Pentanol-
Heptane system [15]. However the systems they were focused on was only the
association of hydrogen donor with a single hydrogen bonding acceptor and two pairs of
electron attached on the hydroxyl group have made the analysis obscured.
Secondary amine and amide groups have also been spotlighted for a hydrogen bonding
bearer due to their biological importance. Moreover, these groups form a simpler
association with hydrogen bonding acceptors than hydroxyl group since only one pair of

electron exists. The first approach to investigate hydrogen bonding association has been made with various amides in benzene solution by Davies and Thomas [16]. Then, Klotz and Franzen investigated the hydrogen bonding association of amine group on N-methylacetylamide with ether group using dimer and multimer equilibrium constants [11]. Whetsel and Lady first focused on the multiple hydrogen bonding associations of amine species with intramolecular and intermolecular acceptors. They elucidated the association with intermolecular association of amine group with solvent as well as various hydrogen bonding acceptors of additives. However, their work was also limited to a single association species, even though they suspected existence of multiple associations in the system [17, 18]. Later, Nikolić et al investigated self association of N-ethylacetylamide and N-methylpropylamide in CCl_4 at a low concentration range (0.003-0.1 mol dm^{-3}) and π-bond association of those materials in various benzene derivatives independently [19]. Ellison and Meyer utilized N-methylaniline to confirm N-H···N dimer complex formation in Cylcohexane solution and N-H···π complex formation in Benzene separately [20]. Their works provided the possibility of multiple associations in amide and amine groups but the investigation of multiple associations in the system was not considered due to lack of experimental data analysis technique. Multiple self hydrogen bonding associations in a wide range of dilution concentration (from 0.02-9.24 mol dm^{-3}) of N-methylaniline was elucidated here for the first time, based on the literature findings to my best knowledge. Vibrational spectroscopy techniques such as Infrared and Raman have been major tools for monitoring hydrogen bonding since spectral data contain all vibrational frequency information of covalent bond as well as inter- and intra molecular interaction of the vibrational species [21-24]. Hydroxyl and Amine group could associate with various

proton acceptors to form hydrogen bonds by inter or intra molecular interaction. These H bond resulted in broad band formations at a lower frequency area than the frequency of original (free) OH or NH vibration occurred and thus, made spectroscopic interpretation obscured. Therefore, quantitative interpretation of hydrogen bonding peak by resolving spectral complexity was essential to understand the molecular interaction of the system of interest.

Extensive thermodynamic data of monomer fraction vs. composition have been collected to investigate hydrogen bonding association [15, 19, 25-30]. However, most of monomer fraction data were only limited to the diluted concentration range, where the association (equilibrium) models could be applied well. A few monomer data were collected at the entire range of composition (mole fraction), but the collection of data was difficult due to interference of neighboring peaks, especially at the concentrated range. Moreover, obtained data were mostly monomer fraction, not the actual concentration, and the monomer fraction could not provide an accurate data at a concentrated system because monomer fraction at a concentrated range could be underestimated when comparing with that in the lower concentration range. Nevertheless, monomer fraction vs. composition data has been utilized to apply various association theories mainly because of no need to obtain the individual extinction coefficient of the peak.

Various theories were proposed and applied to investigate hydrogen bonding association of alcohol and amine groups. Many researchers have proposed chemical equilibrium of proton donor and acceptor since Kempter and Mecke proposed a simple equilibrium of hydrogen bonding association in alcohol system [13, 24]. However, free monomer fraction data obtained from Near IR spectrum could not be accurate with the absence of

peak resolution techniques such as spectral deconvolution even in the near-IR region,

where less spectral complexity existed comparing with mid IR region [15]. Kristiansson

observed no free monomer existed in the neat CD_3OH spectrum and concluded that the

equilibrium model for free monomer and various oligomers could not entirely

satisfactory [31]. Thermodynamic association theories such as SAFT (Statistical

Associating Fluid Theory), CPA (Cubic-Plus-Association), and NRHB (Non-Random

Hydrogen Bonding) were also proposed to explain hydrogen bonding association in

alcohol-solvent binary systems [27]. However, the applications of various

thermodynamic theories were only limited to the diluted phase where the solvent

molecules were abundant and the associating species sparsely existed. Various models

regarding hydrogen bonding equilibrium in the data obtained from spectroscopic methods

could be found on table 3.1.

Table 3.1 Literature findings on hydrogen bonding equilibrium

material	Detection range	Method	Modeling/ findings
Ethanol in CCl$_4$ [26]	0.227-0.76 mol/L	FT-IR	Equilibrium model, Coggeshall and Saier, J. Am. Chem. Soc.,73, 5414, 1951
1-Hexanol and 1-pentanol in n-Hexane [32]	M.F. 0.0094-0.0504	FT-IR	Extended lattice fluid hydrogen bonding theory with cooperativity theory
1-Pentanol and 3-Pentanol in Heptane [15]	0.62-9.21 mol/L (up to neat)	Near IR	Kirkwood and Frohlich equation, monomer-dimer-tetramer-octamer model
Methanol in Hexane [25]	M.F 0-1 (whole range)	IR-ATR	Factor Analysis, found no spectral evidence of free OH in the mixture
CD$_3$OH in CCl$_4$ [31]	M.F. 0-1 (whole range)	FT-IR	Current equilibrium model cannot explain monomer depletion
Propanol in heptanes Ethanol in Hexane [33]	M.F 0-0.08 Propanol M.F 0-0.13 Ethanol	Data from literatures	Association models, sPC-SAFT, CPA and NRHB to find monomer fractions
N-ethylacetmamide and N-methylprorionamide in CCl$_4$ [19]	0.003-0.1 mol/L	FT-IR	Klotz and Franzen model with two association constants, J. M. Klotz and J. S. Franzen, J. Am. Chem. Soc., 84,3461-3466, 1962
N-methylacetmamide in CCl$_4$ [28]	0.01-0.17 mol/L	FT-IR and Dielectric Polarization	Klotz and Franzen model with two association constants, J. M. Klotz and J. S. Franzen, J. Am. Chem. Soc., 84,3461-3466, 1962
4-ethylphenol in Cyclohexane [24]	0.0019-0.603 mol/L	FT-IR	Modified Coggeshall and Saier model, J. Am. Chem. Soc.,73, 5414, 1951
Hexafluoro-2-phenyl-2-propanol in cyclohexane [34]	0.0801-1.002 mol/L	FT-IR	Modified Coggeshall and Saier model, J. Am. Chem. Soc.,73, 5414, 1951
Methanol, ethanol, and tert-butanol in CCl$_4$ [29]	0.005-1.0 mol/L	FT-IR	monomer-dimer-trimer and high-mer equilibrium model
1-octanol, 1-propanol, 2,4-dimethyl-3-pentanol, 2-methyl-2-propanol, 3-ethyl-3-pentanol, and 3-methyl-2-pentanol in CCl$_4$ [35]	0.001-0.54 mol/L	FT-IR	Self aggregation model was used. Concentrations were obtained from multivariate curve resolution method
2,2-dimethyl-3-ethyl-3-pentanol in tetrachloroethylene [36]	0.1621-0.3243 mol/L	FT-IR	Monomer-dimer self association model
Ethanol in Hexane [30]	M.F. 0.101-16.03 %	FT-IR	UNIQUAC association model using monomer-dimer-oligomers equilibrium

3.2   Hydrogen Bonding Association of Amines

In a practical point of view, multiple hydrogen bonding associations occur at the same time not only in the intramolecular form but also intermolecular form in the actual field of hydrogen bonding formation such as polymer synthesis as well as various biological applications. Therefore, it is important to assign and understand the multiple hydrogen bonding formations and their behaviors in the complex system. Here, in this chapter, multiple self associations with different hydrogen bonding acceptors were investigated using N-methylaniline (NmA), which has a single hydrogen bonding donor and two potential hydrogen bonding acceptors, a pair of electron on the amine group and a π-bond on the phenyl group. Monomer (NmA whose NH group is free from hydrogen bonding association) concentration was obtained from spectral deconvolution technique. To collect spectral evidence of association with different proton acceptors, Toluene and Triethylamine were employed as model proton acceptors additives respectively to investigate π-bond and Amine group associated hydrogen bonding with NH group in low concentration of NmA solution in CCl_4. Collected IR spectra from KBr transmission windows were pre-processed by baseline correction via subtraction of CCl_4 and H-bond acceptor spectra. Then, peak deconvolution was performed with suggested product form of Gaussian and Lorentzian peak line shape function. Density Functional Theory calculation was also performed for the geometry optimization and production of frequency data for the hydrogen bonding peaks and the results were compared with experimental data. Finally IR spectra for NmA-CCl_4 system were deconvoluted according to the spectral line shape information obtained from ternary system and a

postulation of phase transfer was proposed to describe decreasing trend of free monomer concentration as the phase got condensed.

3.2.1 N-methylaniline Associations

N-methylaniline (NmA, Sigma-Aldrich Corp.) was used as a proton donor in the binary system and both proton donor and acceptor in the ternary systems. Model hydrogen acceptors such as Toluene and Triethylamine were used to acquire single equilibrium of π-bond and amine group respectively and Dimethylamine was utilized to obtain double hydrogen bonding formations from two acceptors in the ternary system. All agents were purchased from Sigma-Aldrich with purity of over 99%. These agents were used without further purification. For ternary system, the input amount of NmA was set to under 1 weight percent throughout the entire experimental set to prevent self association and the input amount of other agent varied from 0.5 to 40 weight percent, dissolved in carbontetrachloride (CCl_4, Sigma-Aldrich). For monitoring NmA self association in CCl_4, 0.1-90 weight percent of NmA was dissolved in CCl_4. Three Teflon spacers with different path length were utilized to measure the peak intensity of hydrogen bond in a valid detection limit of IR absorbance. Figure 3.1 showed the NmA spectra dissolved in CCl_4 obtained with different path length. To eliminate path length effect on the intensity, the absorbance values were divided by path lengths. Nicolet 6700 FT-IR (Thermo Scientific Corp.) with KBr beam splitter and deuterated triglycine sulfate (DTGS) detector was used to obtain spectra. Liquid sample holder with 32mm diameter round KBr crystal windows (purchased from New Era Enterprises) was utilized to obtain IR

spectra in a transmission mode. 32 scans were averaged to offset the error. All the spectra were obtained 15 minutes after installing the liquid holder in the transmission sample chamber to eliminate carbondioxide and water impurities in the chamber. IR analysis was performed in a room temperature.
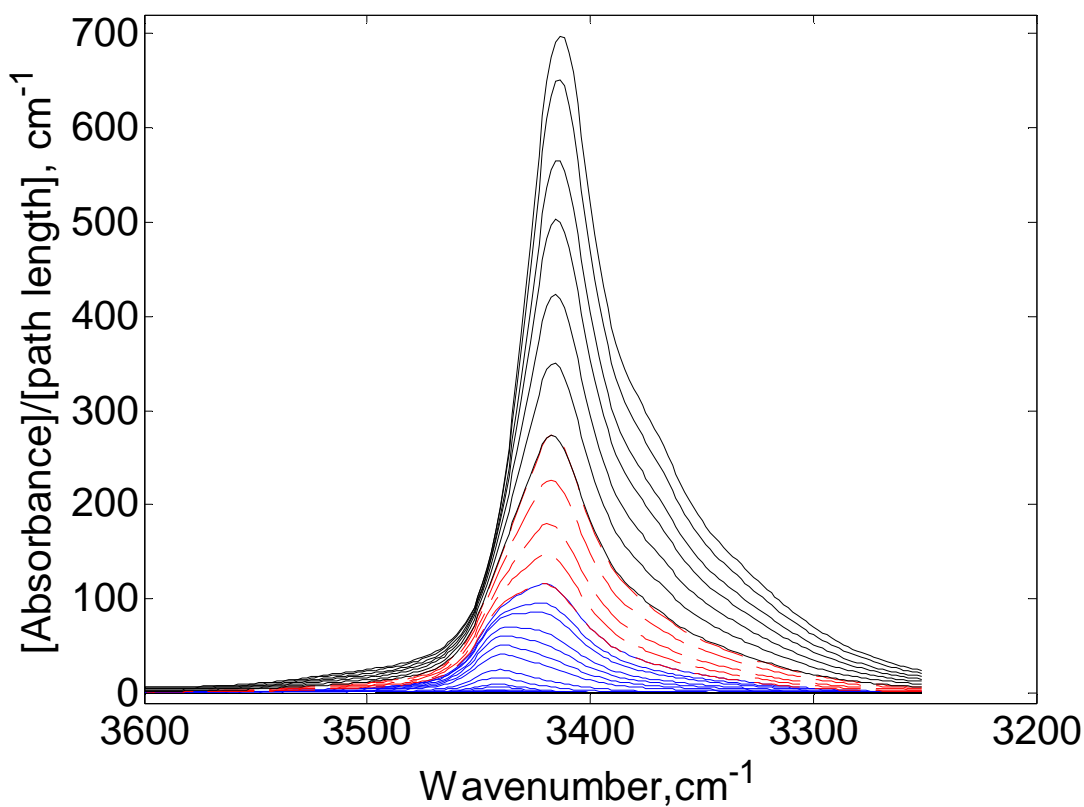
Figure 3.1 Series of NmA spectra dissolved in CCl_4 with various dilution concentrations from 0.002 to 0.92 g cm^{-3}

IR spectral data was pre-processed by baseline correction. For ternary system, IR spectra of hydrogen bond acceptor species were subtracted from those of ternary mixture to eliminate overtone peaks in the spectral range of 3200-3600 cm^{-1}. 5 different spectra of hydrogen bond acceptor agents whose dilution concentration values ranging from 0.048

to 1.004 g cm^{-3} were taken and their concentration-peak intensity (height) relationships were obtained at the wavenumber range of 3200-3600 cm^{-1}. Then, H-bond acceptor spectrum was subtracted from each spectrum of ternary system, after considering H-bond acceptor agent concentration inside the ternary solution.

3.2.1.1. Hydrogen bond equilibrium for ternary system

DFT calculation was first applied to verify theoretical influence of the hydrogen bonding on the chemical conformation as well as IR frequency. NmA-Toluene and NmA-Triethylamine (TEA) systems were chosen to examine hydrogen bonding associations with π bond and amine electron pair respectively. Geometry optimization was conducted first with B3LYP/Lanl2DZ level calculation and then frequency data were obtained using same level of calculation. Figure 3.2 showed optimized geometry of two association systems, NmA-toluene and NmA-TEA. NH vibration affected by hydrogen bonding with π bond and amine group were both present at lower frequency area and the wavenumber differences from the free NH peak of single NmA (red shift) were 25.2 and 251.3 cm^{-1} respectively. The comparison of NH peak shifting obtained from DFT calculation with that from experimental IR frequency was summarized in Table 3.2. The frequency values from DFT were found at higher frequency because the calculations were done under the assumption of gas phase. However, the relative frequency shift indicated that the association of hydrogen bond lowered the vibrational frequency. Iogansen verified that the red shift resulted from hydrogen bonding formation$(\Delta \nu)$ is proportional to the square of hydrogen bonding enthalpy $(-\Delta H)^2$, which indicated that hydrogen bonding

accepting power of amine group is stronger than that of π group [37]. Rozenberg et al.

empirically obtained correlation between vibrational red shift and distance in between

associating atoms and elucidated hydrogen bond enthalpy of alcohol was proportional to

the inverse third power of hydrogen bond donor-acceptor distance [38]. The calculated

association length of H with π-bond and amine group were 2.79 and 2.21 Å respectively,

which supported that amine hydrogen bonding was stronger than π-bond hydrogen

bonding.
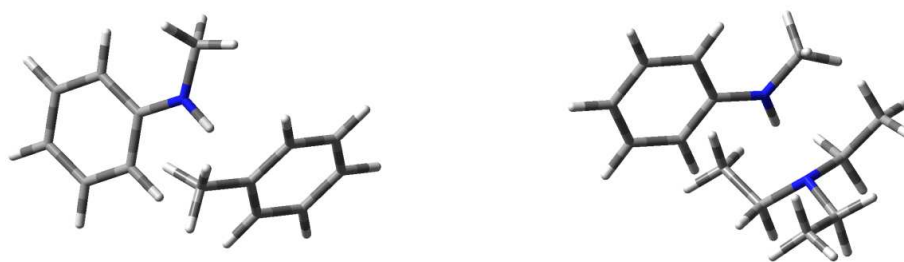
Figure 3.2 Optimized geometry of NmA-toluene (left) and NmA-TEA (right) system
from Density Functional Theory calculation

Table 3.2 Comparison of NH peak shift

	NmA	NmA-Toluene	NmA-Triethylamine
Frequency from DFT (Δv)	3673 (0)	3648 (25)	3422 (251)
Frequency from FT-IR (Δv)	3441 (0)	3425 (16)	3292 (149)

To find free monomer peak line shape information as well as the extinction coefficient,

spectra of 0.1 wt. % to 0.9 wt. % of NmA dissolved in CCl_4 were obtained. Figure 3.3

showed IR spectrum of 0.1 wt. % NmA in CCl_4 from 3300 to 3600 cm^{-1}. It was found

that the peak line was composed of 99.9% Lorentzian line shape which indicated that the

peak was from a single stretching vibration, not associated with the environment. The

spectral lines for Amine group up to 0.9 wt. % samples could be fitted with single

Lorentzian line shape function and the extinction coefficient could be obtained from

slope of absorbance vs. concentration plot as shown in figure 3.4. Experimentally defined

extinction coefficient value of free monomer was 16478 cm^2 g^{-1}, which was taken from

the slope of [Absorbance]/[path length] vs. Dilution concentration plot in figure 3.4.
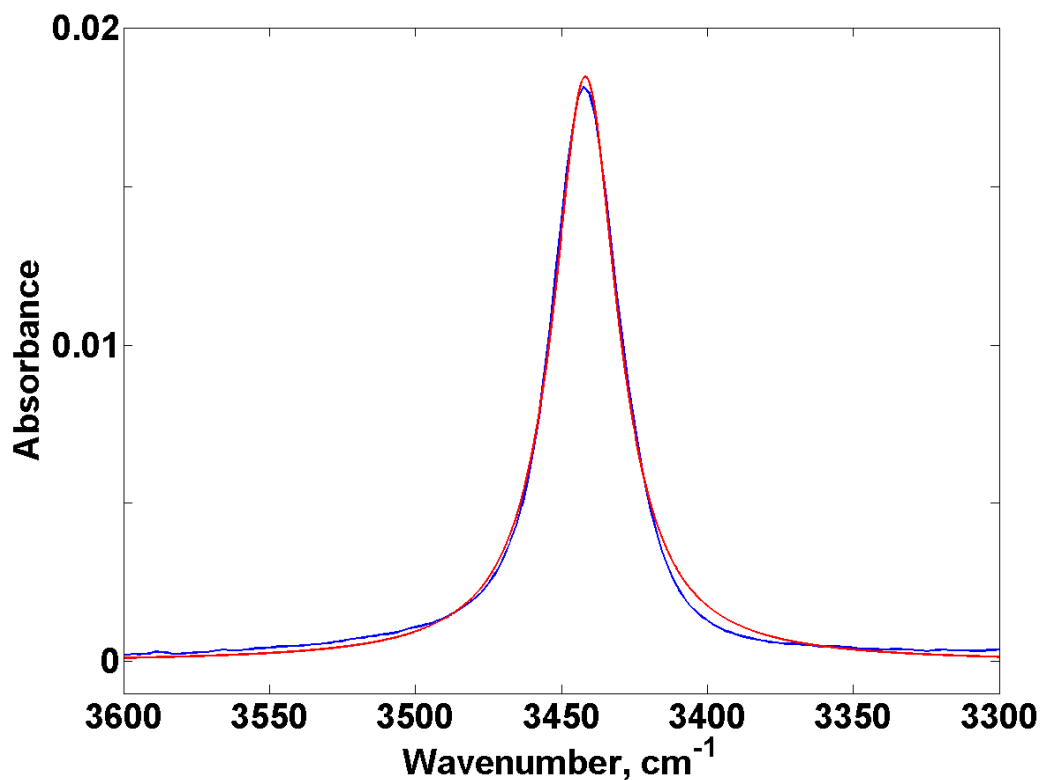
Figure 3.3 Peak fitting of 0.1% NmA diluted in CCl_4 (blue: experimental spectrum, red: 99.9% Lorentzian peak)
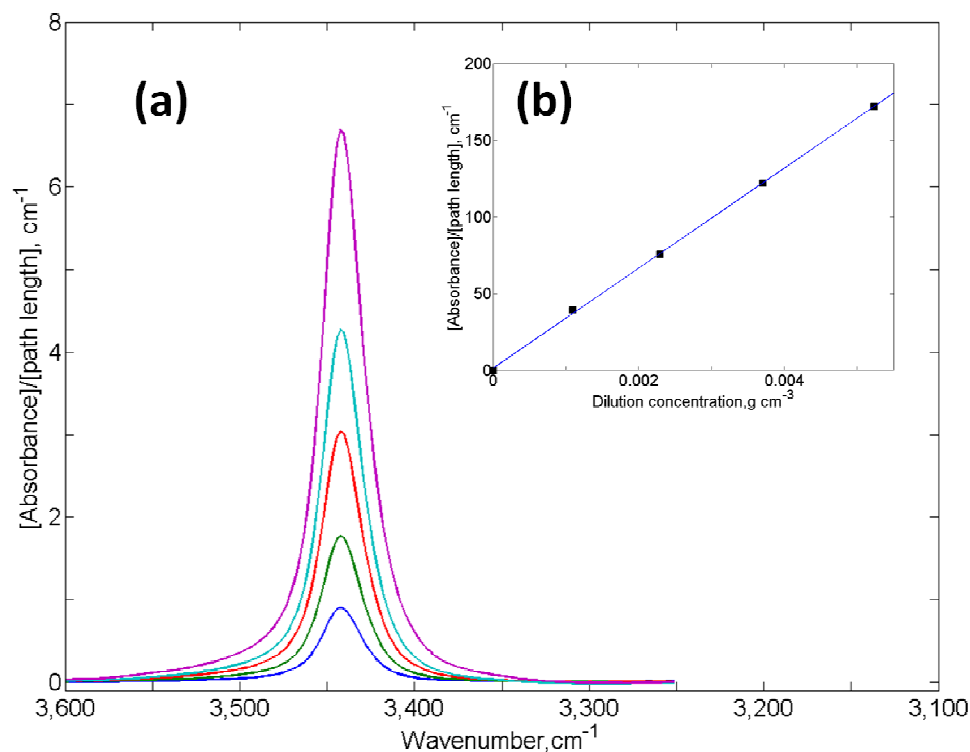
Figure 3.4 Extinction coefficient determination of free monomer of NmA in CCl_4 solution, (a): spectra of NmA with low dilution concentrations (0.002, 0.005, 0.007, 0.010 g cm^{-3}), (b): plotting for extinction coefficient evaluation

Figure 3.5 showed spectral evolution in two different ternary systems. IR spectra of NmA-Toluene-CCl$_4$ and NmA-Triethylamine-CCl$_4$ were obtained to investigate single hydrogen bonding with π-bond and Amine group respectively. NmA concentration was limited to be below 1 wt. % of the solution to prevent self association of NH in NmA with the hydrogen bonding acceptors of phenyl and amine electron pairs in NmA molecules. Therefore, only two peaks were expected from ternary system, which were free monomer peak and the hydrogen bonding peak from each proton acceptors. For monomer peak, the same peak line shape information with 99.9% of Lorentzian line shape was applied, which was obtained from low concentration NmA spectra (ranging

from 0.0022 to 0.010 g cm^{-3}). Peak line shape constraints applied for the hydrogen

bonding peaks were listed in Table 3.3.

Table 3.3 Constraints applied to NH and hydrogen bonding peak parameters for binary systems

	Free NH Value(LB-UB)[†]	NH-Toluene Value(LB-UB)[†]	NH-TEA Value(LB-UB)[†]
H	0.4(0-2)	0.5(0-2)	0.5(0-1)
m	0.999(0.99-1)	0.9(0.8-1)	0.95(0.85-1)
X0	3441(3440-3442)	3425(3424-3427.2)	3292(3290-3294)
W	28(26-30)	33(32-35)	132(130-140)

†LB:lower bounds, UB:upper bounds
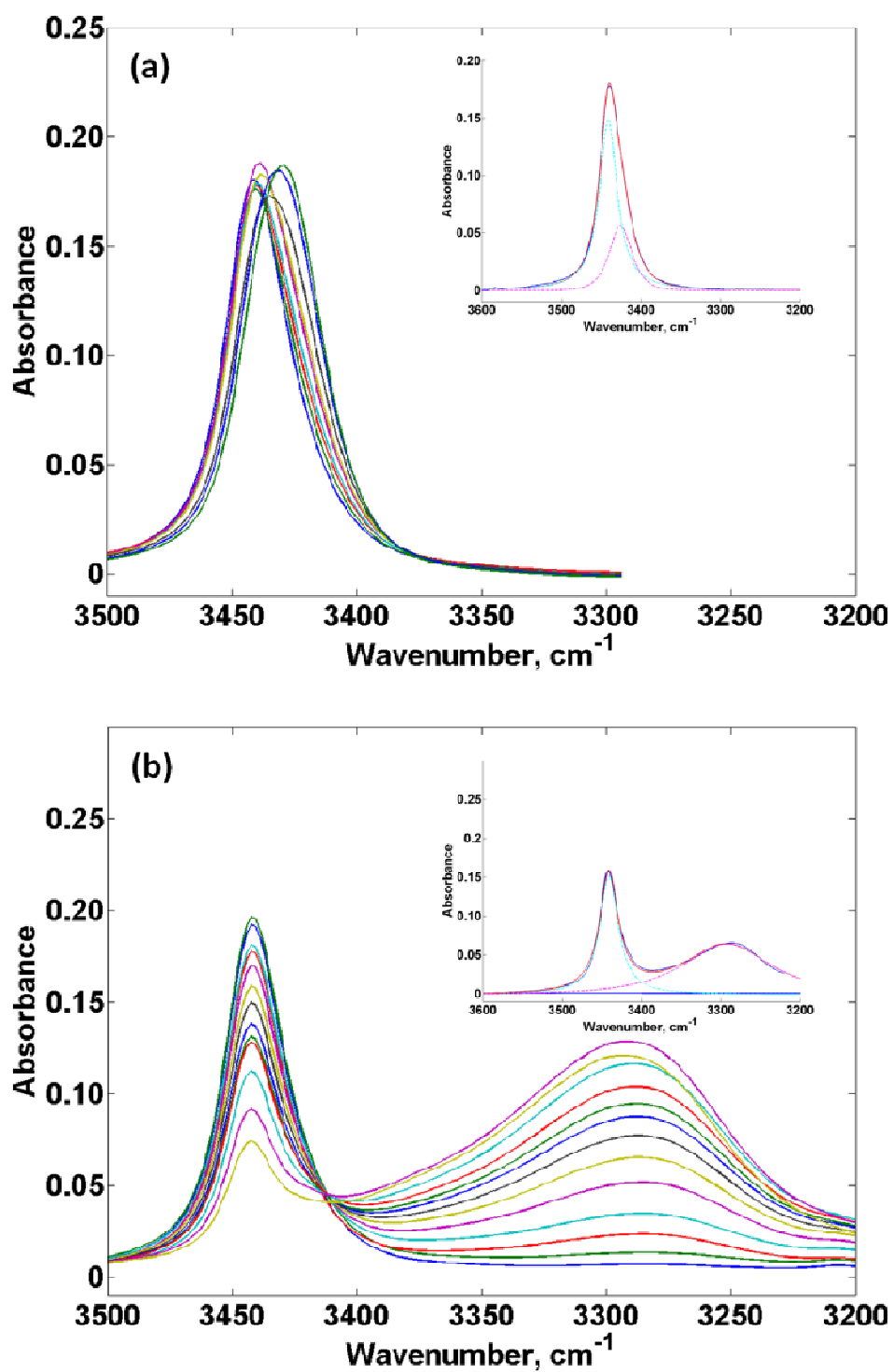
Figure 3.5 Baseline corrected spectra of ternary system and their deconvolution examples of 7 wt. % samples ((a):NmA-Toluene, (b):NmA-TEA)

Since Toluene and Triethylamine have one hydrogen bond acceptor, simple equilibrium model of dimerization could be applied for hydrogen bonding of NH group with single proton acceptor in the ternary systems of NmA-Toluene-CCl$_4$ and NmA-TEA-CCl$_4$.

$$AH + B \overset{K}{\Leftrightarrow} AHB \tag{3.1}$$

Where, AH=free Amine species, B=hydrogen acceptor, AHB=hydrogen bonding species.

Mass balance and equilibrium constant equations are as follows

$$[AH]_0 = [AH] + [AHB] \tag{3.2}$$

$$[B]_0 = [B] + [AHB] \tag{3.3}$$

$$K = \frac{[AHB]}{[AH] \cdot [B]} \tag{3.4}$$

Elimination of [B] and [AHB] by mass balance gives the quadratic solution and with experimentally obtained extinction coefficient of AH, χ_{AH}, peak area could be calculated

$$A_{AH} = \frac{-\{1 + K[B]_0 - K[AH]_0\} \pm \sqrt{\{1 + K[B]_0 - K[AH]_0\}^2 + 4K[AH]_0}}{2K \cdot \chi_{AH}} \tag{3.5}$$

K value that finds minimum error could be obtained by optimization method for multiple data points,

$$Error = \sum_{data}[A_{AH}^{exp} - A_{AH}^{mod}(K)]^2 \tag{3.6}$$

The extinction coefficient calculation of hydrogen bonding peak was important to obtain the concentration profile of the hydrogen bonding species. From equilibrium equation

(3.4), eliminating [B] by applying the mass balance $[B]_0 = [B] + [AHB]$ gives the equation,

$$[AHB] = \frac{K[AH][B]_0}{1+K[AH]} = \frac{K(A_{AH}/\chi_{AH})[B]_0}{1+K(A_{AH}/\chi_{AH})} \tag{3.7}$$

Experimentally determined A_{AHB} vs. calculated concentration of AHB, [AHB] plot gave the extinction coefficient of AHB, χ_{AHB}.

Figure 3.6 showed the peak area estimation of free NH peak with optimized equilibrium constant of the ternary system. Lsqnonlin routine from MatLab was applied to obtain the equilibrium constant with least square method. The extinction coefficient of free NH peak obtained from the lower concentration of NmA solutions was applied to find calculated peak area value from equation (3.5). It was found that the single equilibrium model could successfully estimated monomer peak area of NH group in the ternary systems for the dilution concentration of Toluene and TEA up to 0.45 g cm^{-3}. The optimized equilibrium constants for the ternary systems with toluene and TEA were 1.43 and 1.13 cm$^{3\cdot}$ g^{-1} respectively. Therefore, it was concluded that ternary system with single hydrogen bonding species could be governed by simple equilibrium kinetics of 1:1 H-bond donor and acceptor.
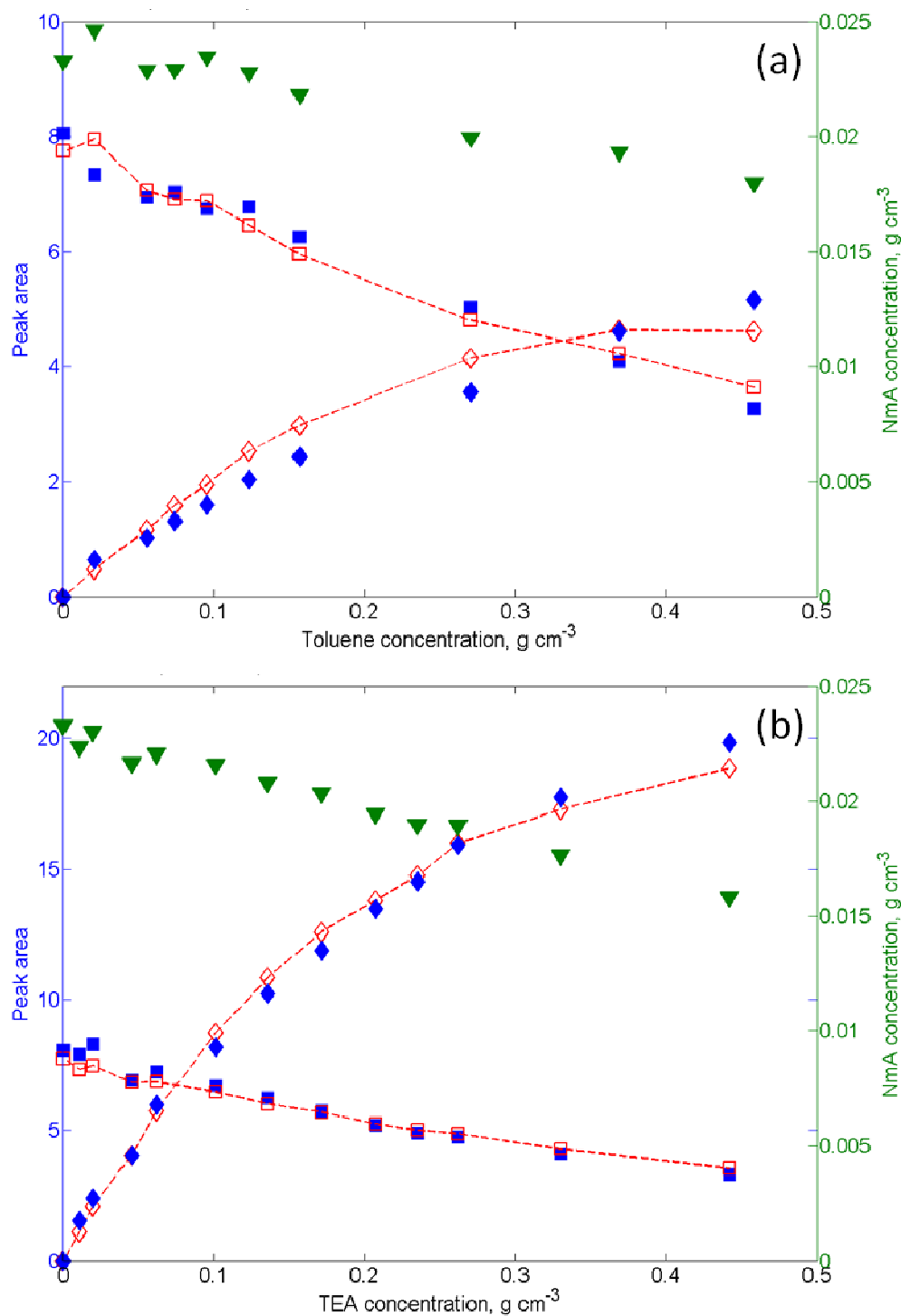
Figure 3.6 Single equilibrium constant optimization for ternary systems (NmA-Toluene-CCl₄ (a) and NmA-TEA-CCl₄ (b), reverse triangle: experimental dilution concentration, solid square: experimental peak area of free monomer, empty square dot: calculated peak area of free monomer, solid diamond: experimental peak area of H-bonding peak, empty diamond dot: calculated peak are of H-bonding peak)

3.2.1.2. Multiple H-bond acceptors in ternary system, NmA-DMA-CCl$_4$

NmA-Dimethylaniline (DMA) system was investigated to examine multiple equilibrium states in a binary system since DMA contained multiple H-bond acceptors, π bond and Amine group inside of the structure. Input amount of NmA was limited to 1 wt. % in the total solution to prevent self association effect of NmA. Figure 3.7 (a) and (b) showed series of NmA-DMA spectra and a deconvolution example of 7wt. % of DMA sample respectively. The first approximation of the peak parameters were obtained from each ternary system, NmA-Toluene-CCl$_4$ and NmA-TEA-CCl$_4$ system. Free monomer peak parameters were the kept the same throughout the systems investigated here. However, for the peak line shape parameters of hydrogen bond associated NH peaks were not exactly same as those from NmA-Toluene and NmA-TEA binary system due to the structural differences and difference in electron density of hydrogen bonding acceptors. Therefore, rough guess on the peak line shape information and peak positions were possible from each ternary system. The constraints for the peak parameters in NmA-DMA system were summarized and compared with those from each binary system in table 3.4. For NH-phenyl group, the peak position was shifted by only 10 cm^{-1} to the lower wavenumber area when it is compared with NH-Toluene because of its resemblance in chemical structure. However, peak position of NH-Amine hydrogen bond was shifted by 90 cm^{-1} when it was compared with that of NH-TEA in binary system. Steric hindrance effect as well as electron density change resulted from the difference in chemical structure might contribute to the large peak position shift.
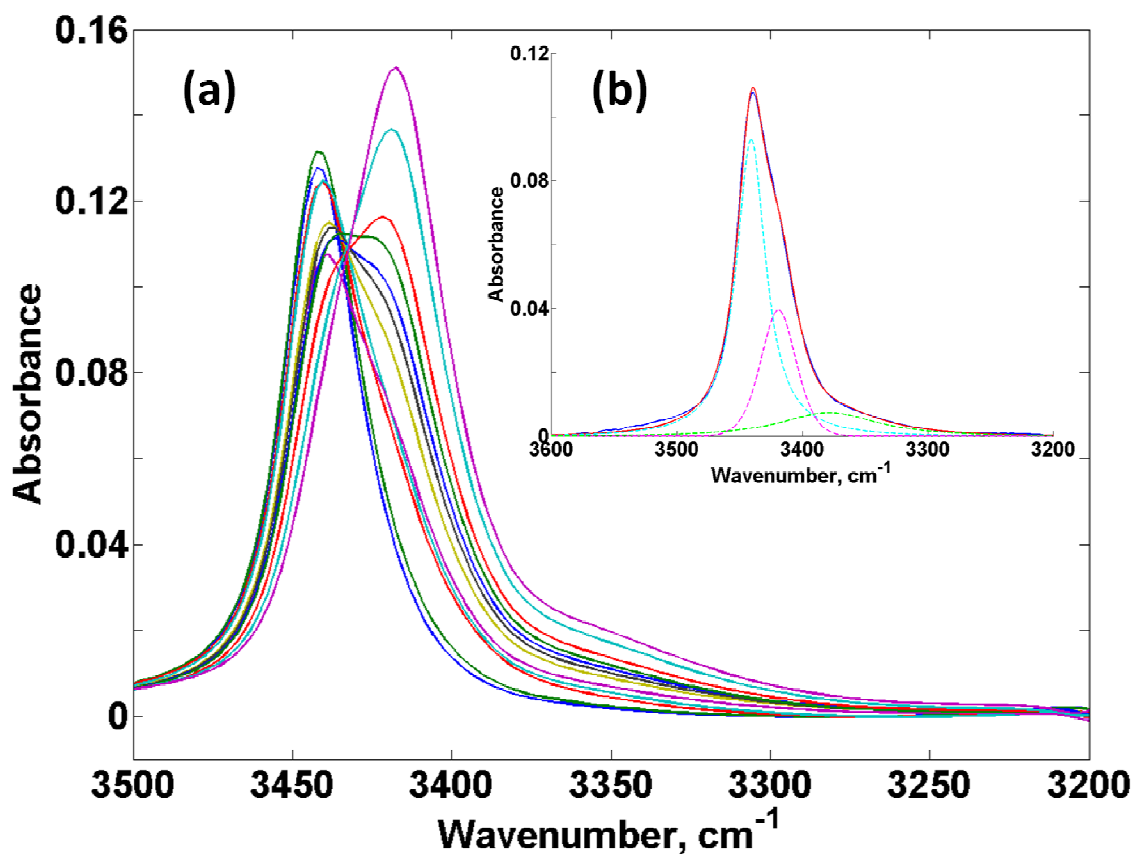
Figure 3.7 Series of NmA-DMA spectra (a) and spectral deconvolution of 7 wt. % sample (b)

Table 3.4 Constraints applied to the hydrogen bonding peak parameters for NmA-DMA system and comparison with other binary system parameters

	NH-π bond in NmA-DMA system (LB-UB)†	NH-Amine group in NmA-DMA system (LB-UB)	NH- π bond in NmA-Toluene system (LB-UB)	NH-Amine group in NmA-TEA system (LB-UB)
H	0.5(0-2)	0.5(0-2)	0.5(0-2)	0.5(0-1)
m	0.45(0.4-0.5)	0.92(0.9-0.95)	0.9(0.8-1)	0.95(0.85-1)
X0	3418.5(3417-3419)	3378.5(3378-3379)	3425(3424-3427.2)	3292(3290-3294)
W	34.5(34-35)	92(90-94)	33(32-35)	132(130-140)

Two equilibrium equations of dimer formation were applied at the same time since DMA

had multiple hydrogen bonding acceptors.

$$AH \ + \ B_1 \ \overset{K_1}{\Leftrightarrow} \ AHB_1 \qquad\qquad\qquad (3.8)$$

$$AH \ + \ B_2 \ \overset{K_2}{\Leftrightarrow} \ AHB_2 \qquad\qquad\qquad (3.9)$$

Two quadratic equations obtained from (3.8) and (3.9), and mass balance equations were

solved at the same time with lsqnonlin routine in MatLab. Figure 3.8 showed the

comparison of measured peak area with the calculated ones using optimized equilibrium

constants. Optimized equilibrium constants and extinction coefficients of the hydrogen

bonding peaks were listed in table 3.5. It was shown from the comparison of optimized

equilibrium constants with each other, NH-π bond formation was preferred in NmA-

DMA-CCl$_4$ system, which was shown to be consistent in the ternary system. However, π

bond associated equilibrium constant increased by 43%, where as amine group associated

equilibrium constant decreased by 42%. This seemed to be resulted from the steric

hindrance effect of DMA species. In DMA abundant environment, π bond could be

associated with NH group more easily than the pair of electron on the amine group

because that bond had relatively larger size and easier access than the amine group had.
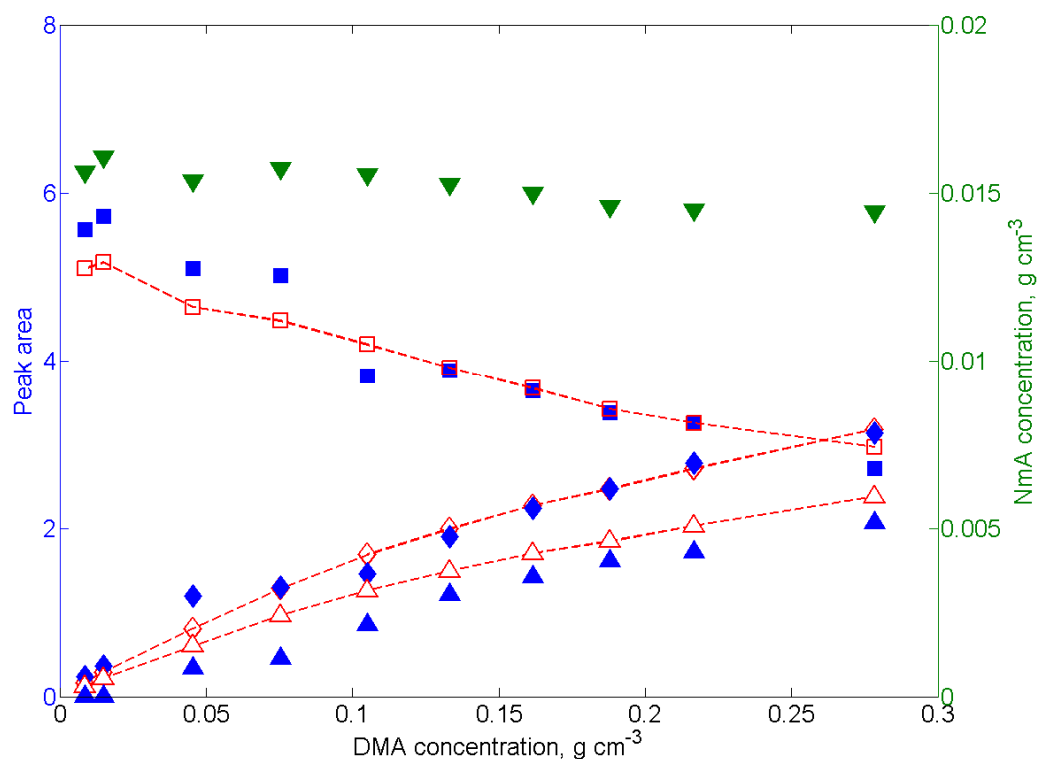
Figure 3.8 Double equilibrium constants optimization for ternary system of NmA-DMA-CCl$_4$, reverse triangle: experimental dilution concentration, solid square: experimental peak area of free monomer, empty square dot: calculated peak area of free monomer, solid diamond: experimental peak area of H-bonding with π-bond peak, empty diamond dot: calculated peak are of H-bonding with π-bond peak, solid triangle: experimental peak area of H-bonding with amine peak, empty triangle dot: calculated peak are of H-bonding with amine peak)

Table 3.5 Optimized parameters for NmA-DMA system

parameter	K_{B1} (cm^{-3} g)	K_{B2} (cm^{-3} g)	χ_{B1} (cm^{-3} g)	χ_{B2} (cm^{-3} g)
Value	2.001	0.269	6524.08	3627.68

3.2.1.3. Self association of NmA

Multiple hydrogen bonding association with different hydrogen bonding acceptors have been investigated with ternary system as well as DFT calculation of frequency data so far. It was found from the hydrogen bond association study that the spectral red shift and peak line shapes due to hydrogen bonding were dependent on the characteristics of hydrogen bonding acceptor, such as electron density and molecular structure. Equilibrium analysis of ternary system provided the idea of multiple self association of NH with π bond and amine group inside of NmA structure. Based on the relative peak information of hydrogen bonded species in the ternary systems, peak deconvolution was performed for the spectra of NmA dissolved in CCl_4, as shown in figure 1, with various dilution concentrations, which varied from 0.1 to 90 wt. %. Three peaks were used for the deconvolution, free monomer of NH group, π bond associated NH, and amine group associated NH group. Among them, free monomer concentration could be directly obtained using verified extinction coefficient value from figure 3.4. Figure 3.9 showed the concentration evolution of free monomer with respect to NmA dilution concentration. It was noteworthy that the free monomer concentration was decreasing after the total dilution concentration reached to 0.4 g cm^{-3}. This trend indicated that the equilibrium could not govern the system at high dilution concentration. There were some literatures that were raising the possibility of monomer concentration decreasing at high dilution concentration or in a neat system of Pyrrole or Ethanol in CCl_4 [39, 40]. However, quantification of free hydrogen was not possible due to lack of spectral deconvolution technique. There were also various attempts to find equilibrium of alcohol and amine

hydrogen bonding in the diluted solutions in 2000's [35, 36, 41] using monomer

concentration. However, their works were limited to the very low dilution concentrations,

where only chemical equilibrium dominated. Coggeshall and Saier model has been

chosen for describing hydrogen bonding equilibrium in a wide selection of dilution

systems including amine and hydroxyl groups [19, 24, 26, 28, 34]. This model contained

two equilibrium constants, dimer and multimer formations, for the species having

multiple hydrogen bonding acceptors. Their assumption was reasonable in a view point

of electron density change in hydrogen bonding acceptors, because, once the hydrogen

bonding was formed for one side of hydrogen bond acceptor, the electron density of the

other bonding acceptor could be rearranged by already formed bonding and this could

make the second hydrogen bonding easier or more difficult [32]. Here, modified

Coggeshall and Saier equations were applied to fit the obtained free monomer

concentration as shown in Equations (3.10) and (3.11), where f_m is monomer fraction and

C is total dilution concentration [34]. Equation (3.10) and (3.11) were solved to minimize

error in equation (3.6) with fminsearch routine in MatLab.

$$K_2 = \frac{2\left(\frac{1}{K_1} - \gamma\right)}{f_m C\left[\frac{2}{K_1} - \frac{\gamma}{2} + \left(\frac{2\gamma}{K_1} + \frac{\gamma^2}{4}\right)^{0.5}\right]} \tag{3.10}$$

$$\gamma = \frac{2(f_m)^2 C}{(1 - f_m)} \tag{3.11}$$

First, two equilibrium constants optimized for the first 6 data points at low concentration

range provided red dot line in figure 3.9 and their optimized values for dimer (K_1) and

multimer (K_2) equilibrium constants were 1.346 and 0.907 cm^3 g^{-1} respectively. Then,

various K_1-K_2 relationships were tested with the model. It was found from the model

fitting that, as the relative magnitude of K_2 increased, the monomer concentration reached to the saturating point, but it did not decrease. This showed the limitation of equilibrium model and at the same time, suggested that additional explanations beyond the equilibrium theory should be put on at higher dilution concentration and neat system.
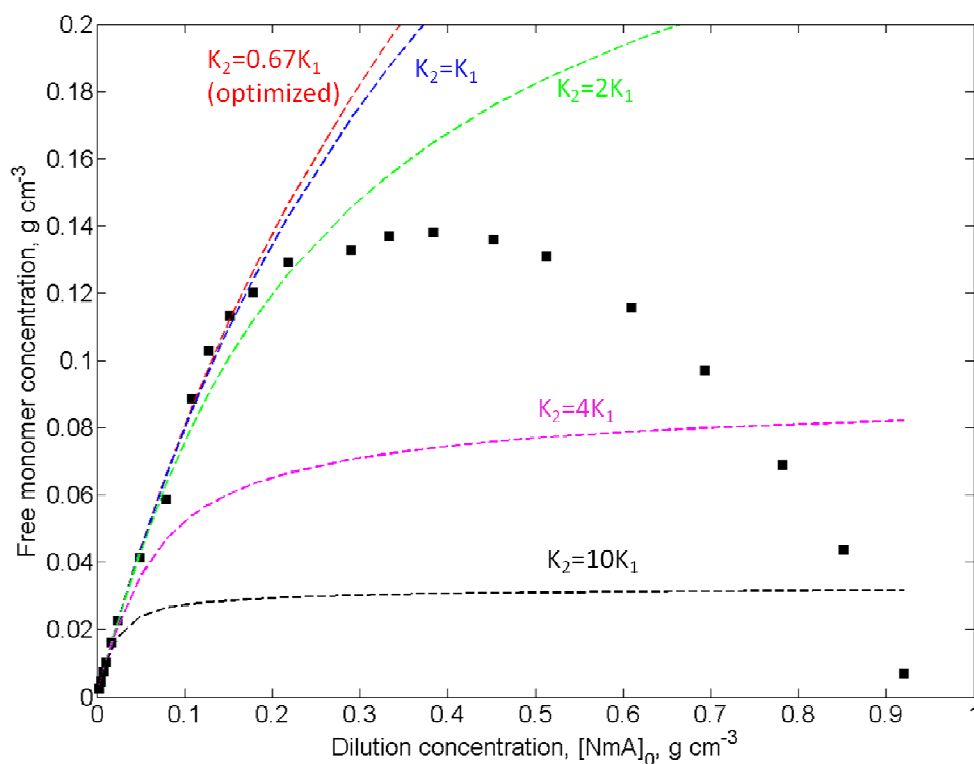
Figure 3.9 Free monomer concentration profile and dimer and multimer formation equilibrium model fitting results

However, it was notified that this free monomer concentration behavior of NmA in a concentrated solution was not from a specific choice of the material. In other words, various materials showed similar trends even though the degree of monomer existence in a neat system is different from each other. Table 3.6 showed various examples of free

monomer concentration evolutions of methanol and ethanol as a function of total dilution

concentration in various solvents. Total concentration and monomer concentrations were

calculated from the literature values of mole fractions and monomer fractions by simple

mixing rule, $C_i = \frac{x_i}{\Sigma x_i/\rho_i}$, where C_i was concentration of the species i, x_i was mole fraction

of i species and ρ_i is density of i species at room temperature. Monomer concentration in

neat alcohols was obtained by the authors using 5 micron thick copper spacer with two

3mm thick KBr transmission windows. The extinction coefficient of monomer peak and

peak information for the deconvolution of the spectra could be obtained elsewhere [29].

Tight constraint was applied to the spectral line shape equation for the monomer peak

with over 99% Lorentzian function and it was found from the deconvolution result that

the monomer peak area was almost disappeared in neat alcohol. Therefore, it could be

concluded that monomer concentration decreased as the mixture solution got more

concentrated is the ubiquitous phenomenon found in hydrogen bonding associating

system such as alcohol and amine solutions.

Table 3.6 Comparisons of monomer concentration in solution and neat material

material	solvent	Maximum monomer concentration available in the literature (g cm^{-3}), ($\times 10^{-4}$)	Alcohol mole fraction at maximum monomer concentration (g cm^{-3}), ($\times 10^{-4}$)	Monomer concentration in neat alcohol (g cm^{-3}), ($\times 10^{-4}$)	Neat alcohol concentration (g cm^{-3}), ($\times 10^{-4}$)
MeOH [31]	CCl$_4$	44.65	137.61	0.0008	7918
Ethanol[30]	hexane	50.62	482.41	0.0007	7890
Ethanol[60]	heptane	12.09	345.28	0.0007	7890
2-propanol[61]	CCl$_4$	92.31	120.20	22.81	7860

Decreasing monomer concentration could be explained in a thermodynamic view point. Figure 3.10 showed a schematic diagram of correlation of liquid-liquid coexistence curve and monomer concentration. In the binary liquid system whose components are miscible with each other, NmA-CCl$_4$ in this work could have liquid-liquid equilibrium and phase transition might occur when the new phase of hydrogen bonded clusters were growing. Free monomer concentration had a monotonic increase at a constant temperature of T$_{operation}$ up to the concentration point of C$_{low}$, where the monomer concentration curve hit the coexistence curve. From this point, new phase have been created as the clusters were formed as a result of hydrogen bonding association. Theoretically, Monomer concentration then should show a linear decrease (dotted line inside of the coexistence curve) by lever rule when the system went through the tie line (solid horizontal line

inside of the coexistence curve) inside of coexistence curve in isothermal and isobaric conditions from C_{low} to C_{high}. However, actual monomer concentration showed a curvature line shape instead of a linear line. There has been no discussion on this deviation of monomer concentration behavior, as far as we searched literatures. One plausible explanation of this deviation is the unassociated N-H end group at the surface of the clusters. The very first forms of hydrogen bonding associated clusters could be dimers or trimers and each cluster had one unassociated N-H end group in the cluster. The formation of small sized cluster at low concentration range would increase the number of unassociated hydrogen bonds. However, as the solution got more concentrated, up to C_{high} point, aggregation of small clusters to higher molecular weight clusters also occurred at the same time. The aggregation of small sized hydrogen bonding clusters form a phase itself different from CCl_4 abundant phase. However, N-H groups at the surface of the clusters which are also contacting the original phase could be counted as free N-H in the original phase and this might affect on the curvilinear decrease in the number of total hydrogen bond. The concept of phase transition in the N-H association system could be found on figure 3.11.
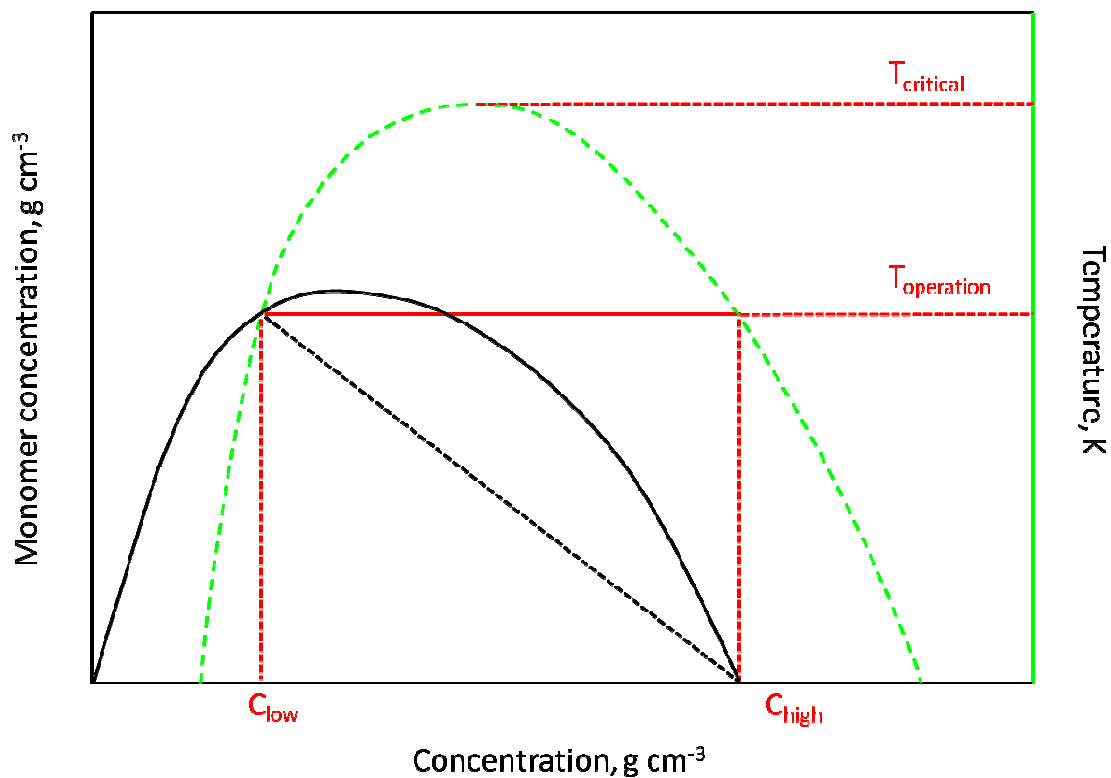
Figure 3.10 Schematic diagram of liquid-liquid equilibrium coexistence curve (dotted green) and monomer concentration evolution (solid black)
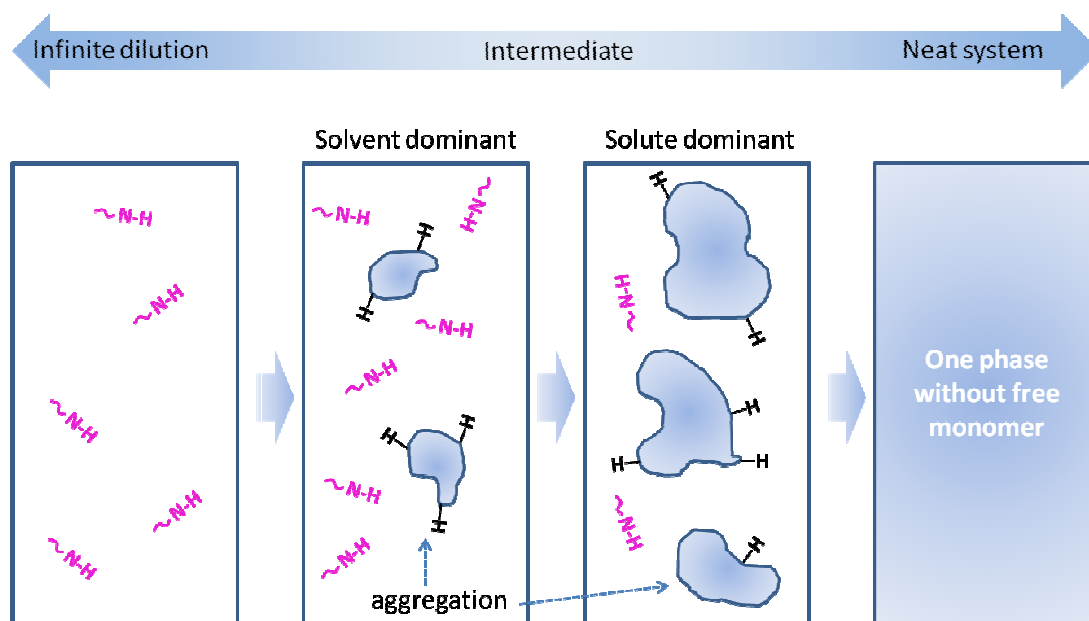
Figure 3.11 A concept of phase transition in hydrogen bonding association system

3.2.2 Aniline Associations

Aniline (purchased from Sigma-Aldrich Corp.) association was investigated with dilution in CCl_4. IR spectra were taken with 0.002-1.02 (neat Aniline) g cm^{-3} samples dissolved in CCl_4. Four Teflon spacers (0.500, 0.095, 0.044 and 0.014 mm) were utilized to measure the peak intensity of hydrogen bond in a valid detection limit of IR absorbance. Figure 3.12 showed the aniline spectra dissolved in CCl_4 obtained with different path length. The absorbance values were divided by applied path length for clear comparison of spectral line shape evolution. The spectra of the same concentration samples with different thicknesses showed perfect overlap with each other. Spectral line shapes of aniline with the lowest concentrations (0.02, 0.04, and 0.08 g cm^{-3}) were on the right top of figure 3.12, and from the spectral line shapes of the most diluted aniline-CCl_4 system, two prominent peaks were found at 3479 and 3394 cm^{-1}, which were assigned to asymmetric and symmetric stretching vibrations of NH_2 by DFT calculation. [Absorbance/path length] vs. concentration line of three diluted aniline spectra provided the extinction coefficients of asymmetric monomer peak (3479 cm^{-1}) and symmetric monomer peak (3394 cm^{-1}), 14315 and 14649 cm^2 g^{-1} respectively.
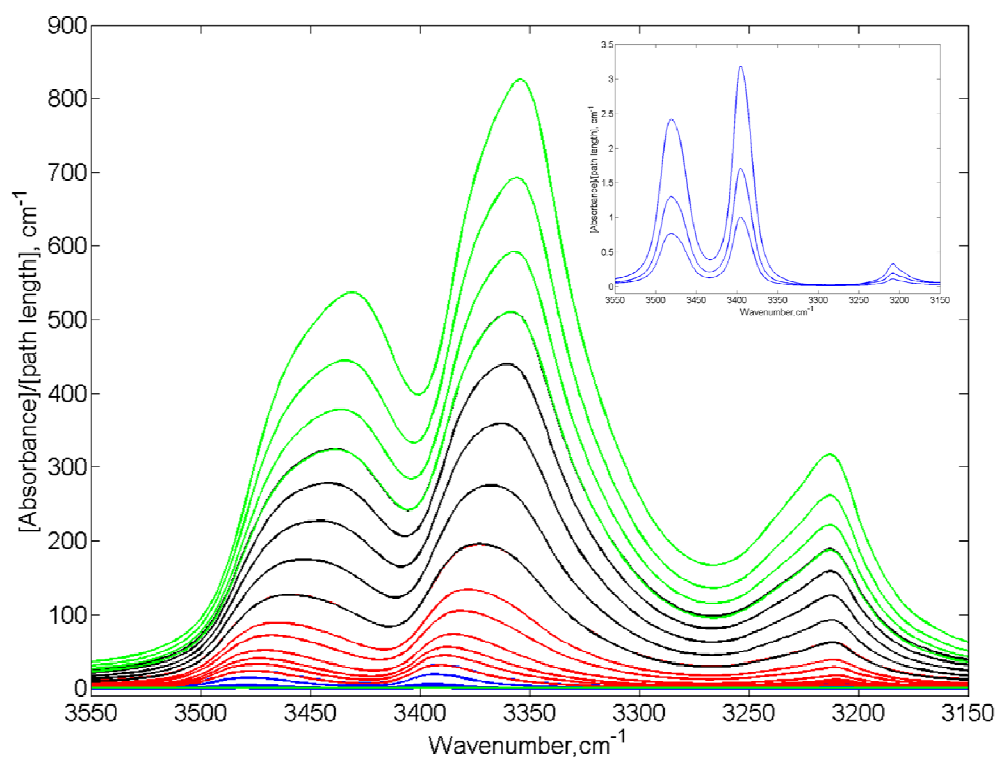
Figure 3.12 Series of Aniline spectra dissolved in CCl$_4$ with various dilution concentrations from 0.002 to 1.02 g cm^{-3}

From the dilution experiment for aniline-CCl$_4$ binary system, another prominent peak was developed at around 3210 cm^{-1}. This peak was verified as an overtone band of N-H bending vibration that was originally found at around 1620 cm^{-1}.

It was noted from the spectral line shape evolution of aniline-CCl$_4$ binary system that multiple hydrogen bonding associated peaks have been developed on the lower wavenumber regions of free monomer peak at 3479 and 3394 cm^{-1} as more isopropanol was added on the system. Self associations of aniline provided more complex spectral line shape than those of NmA system did due to the existence of double vibrational modes of aniline N-H stretching, asymmetric and symmetric stretching as mentioned

earlier. To find the peak positions of hydrogen bonding associations in aniline-CCl_4

binary system, hydrogen bonding associations occurring in various ternary systems that

contain hydrogen bonding acceptor species have been investigated as shown in figure

3.13. Toluene, Epoxybutane (EB), Triethylamine (TEA), and Dipropylether (DPA) were

used as representative hydrogen bonding acceptors of π-bond, epoxide group, amine

group and ether group respectively. 1 weight % of aniline was mixed with hydrogen

bonding acceptors with various concentrations (0.5 to 40 wt. %) in CCl_4. 200 micron

thick Teflon spacer was used with KBr transmission window sample holder purchased by

New Era enterprise, Inc. Obtained spectra for the ternary system was subtracted by

spectrum of hydrogen bonding acceptor-CCl_4 binary system to eliminate the influences of

solvent and acceptor solute on the spectral line shape in the ternary system. From the

spectral images of aniline-Toluene-CCl_4 and aniline-TEA-CCl_4 systems, rough

estimation of π-bond association and amine association peak position and peak parameter

could be made. π-bond association peaks were positioned at 3470 and 3385 cm^{-1}, which

showed Δv from the free monomer NH_2 peak to be about 10 cm^{-1} each. Hydrogen

bonding associations with amine group produced the association peaks centered at 3324

and 3197 cm^{-1}, which showed Δv of 155 and 197 cm^{-1} respectively. Peak position of

amine association peak in aniline-TEA-CCl_4 ternary system provided the possible reason

of the absorbance development at around 3200 to 3350 cm^{-1}, NH-amine group

association. Spectral line fitting with 7 estimated peaks (2 free NH, 2 amine associations,

and 2 π-bond associations and 1 overtone) could not provide a good fitting result. The

reason of spectral complexity in aniline might be the double hydrogen atoms. Unlike a

single NH association in NmA, aniline has two NH bonds linked together. If one NH

bond has been associated with any hydrogen bonding acceptor species, the electron density distribution of the associated NH as well as neighboring NH could be changed and might produce different peak in the aniline spectrum. Therefore, more peaks should be required to investigate aniline self association. Peak deconvolution and hydrogen bonding analysis were not performed here, but it would be investigated in the future, after the exact origins of spectral complexity are unveiled.
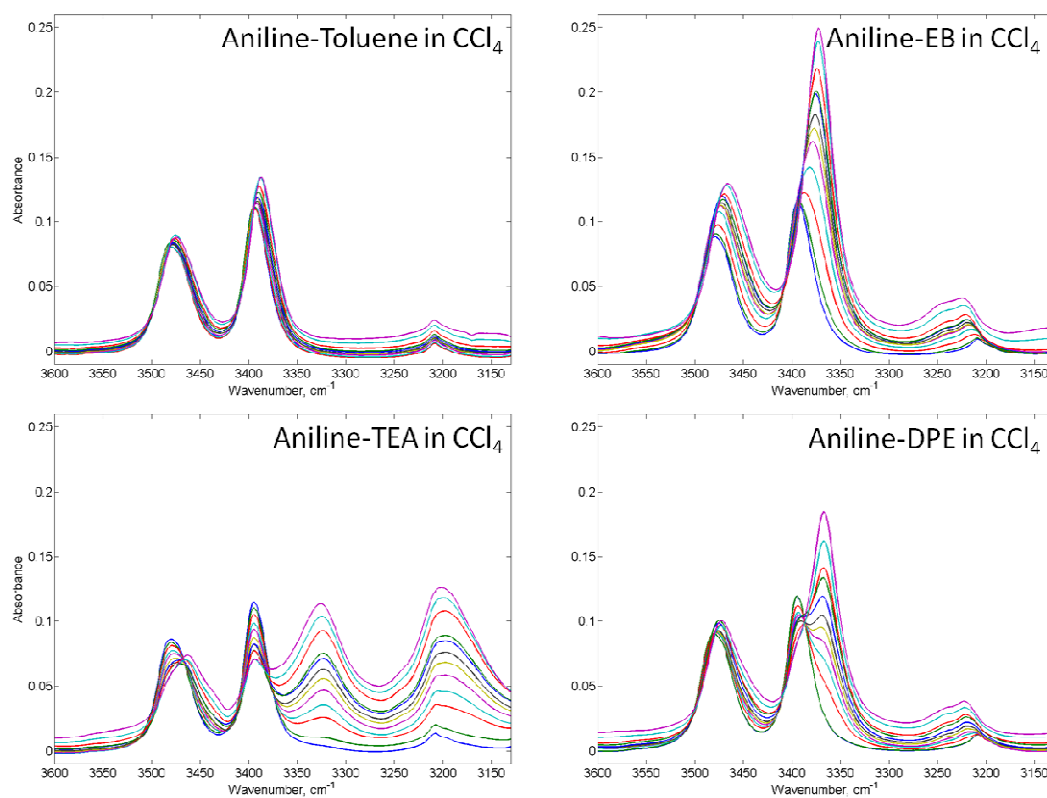
Figure 3.13 Aniline associations with various hydrogen bonding acceptors

3.3   Hydrogen Bonding Association of Hydroxyl Groups

 Isopropanol was chosen as a model alcohol species to investigate inter and intra

hydrogen bonding associations. This study will elucidate the hydrogen bonding

associations equilibrium of hydroxyl groups with various hydrogen bonding acceptor

species such as π bond, amine, ether, epoxide, or other hydroxyl groups (self association),

and finally it will be utilized to estimate hydrogen bonding associations in a amine-epoxy

reaction system.

3.3.1   Self Association of isopropanol

Self associations of OH groups in various alcohol species have been in a great attention

due to its importance in chemical and biological applications [24, 25-27, 30-31, 32-36].

However, even though several postulations were proposed for the type of hydrogen

bonding associations of hydroxyl groups, the explicit explanation of association is still in

controversial. There have been two main postulations for interpretation of hydrogen

bonding spectrum of hydroxyl group self-association, aggregation type and OH type.

Aggregation type theory categorizes the types of association into specific aggregation

species, i.e. monomer-dimer-multimer. This postulation has a good estimation of number

of peak formations found at highly diluted concentration (low concentration) ranges but

gives poor estimation of associations at the entire concentration range. OH type theory

was first proposed by Graener et al [42]. The authors found hydrogen bonding dynamics

of OH group in ethanol dissolved in CCl_4 by time-resolved infrared spectroscopy and

introduced various OH types that were recognized by IR spectrum. The OH type theory

categorizes the types of association by binding conditions of hydroxyl group moieties, acceptor O and donor H. In this theory 4 types of species are present, free unbound donor and acceptor in monomer (α), bound acceptor and unbound donor in multimer (β), unbound acceptor and bound donor (γ), and bound acceptor and donor (δ). Figure 3.14 showed schematic concepts of OH type classification. It was found from the schematics that only monomer contains α OH group and the number of β and γ OH groups are same throughout the any multimer species including dimer. The number of δ OH group was (N-2) in a chain of N-mer. This quantification of OH types will be utilized for setting up the equilibrium kinetics of multimer formation in isopronanol-CCl_4 binary system.
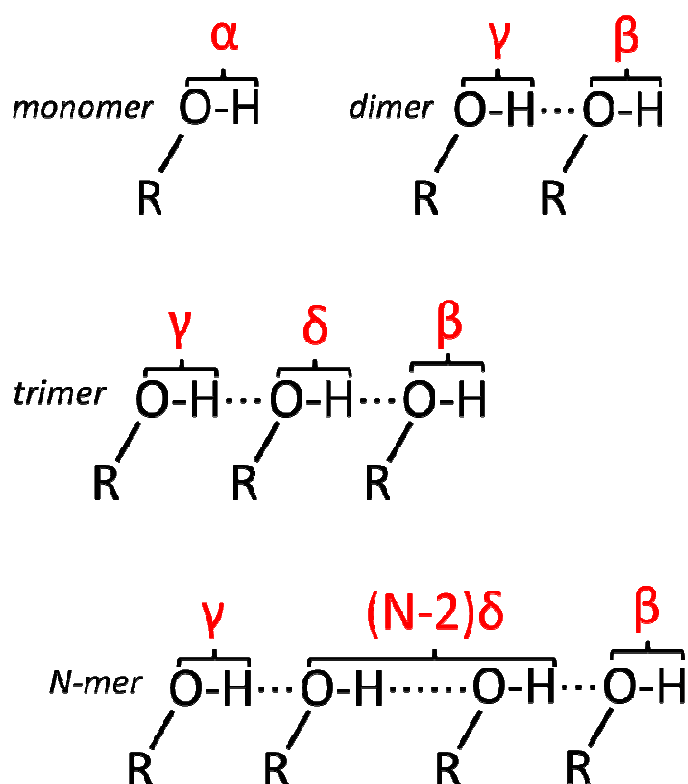
Figure 3.14 Schematics of OH type classification

This type of categorizing is especially effective at high concentration. The peak deconvolution was performed based on OH type classification since the concentration range of isopropanol varies from 0.09 mol l^{-1} to neat alcohol (13.07 mol l^{-1}). Figure 3.15 showed a series of spectra obtained at various dilution concentrations. Three different thickness (200, 34 and 20 micron) spacers were used to minimize signal to noise ratio. Obtained spectral data was baseline corrected and then the spectral intensity was divided by spacer thickness.
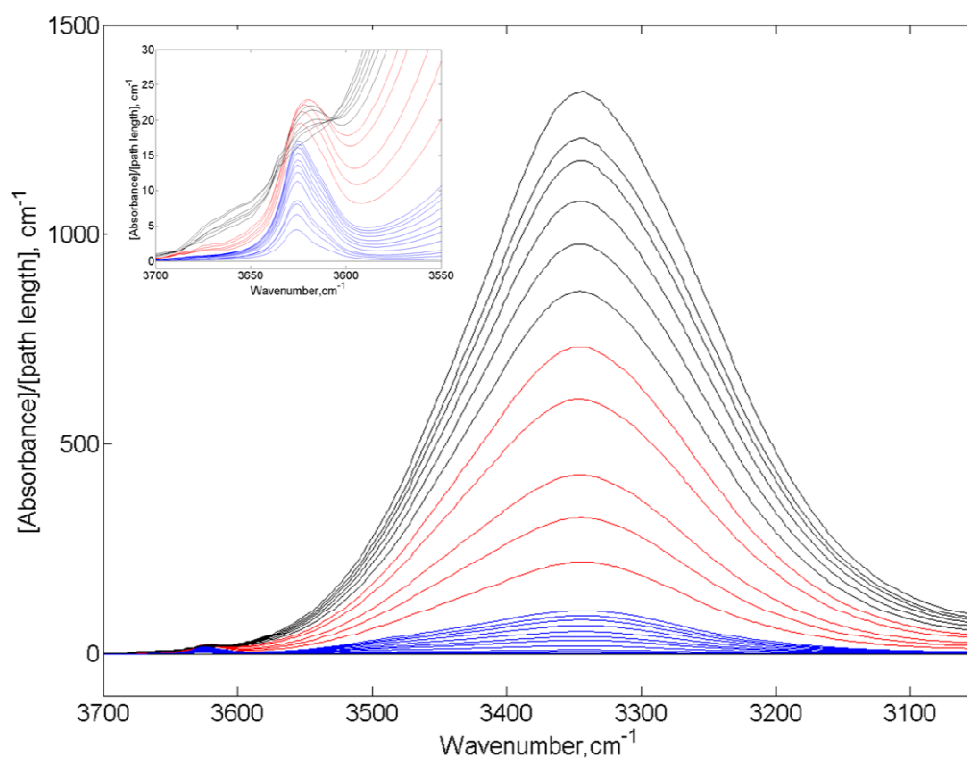
Figure 3.15 Series of isopropylalcohol spectra dissolved in CCl_4 with various dilution concentrations from 0.002 to 1.02 g cm^{-3}

It was observed that, at lower concentration range, free monomer peak (α) was shown at around 3625 cm^{-1} and a peak was shown at a shoulder of free monomer peak, which was β peak, at 3611 cm^{-1}.

At around 3345 cm^{-1}, a big peak was developed as the dilution concentration got higher and a peak was found on the shoulder of the peak at around 3480 cm^{-1}. These peaks were assigned to δ and γ peaks respectively. The development of δ peak at 3345 cm^{-1} was consistent with the fact that δ OH got dominant at higher concentration range where multimers were formed as a result of H bond association.

Therefore, totally four peaks were used to deconvolute the given wavenumber area (3000-3650 cm^{-1}) and the selected deconvolutuion results and peak absorbance profiles of α, β, γ, and δ peaks were shown in figure 3.16 and 3.17 respectively.
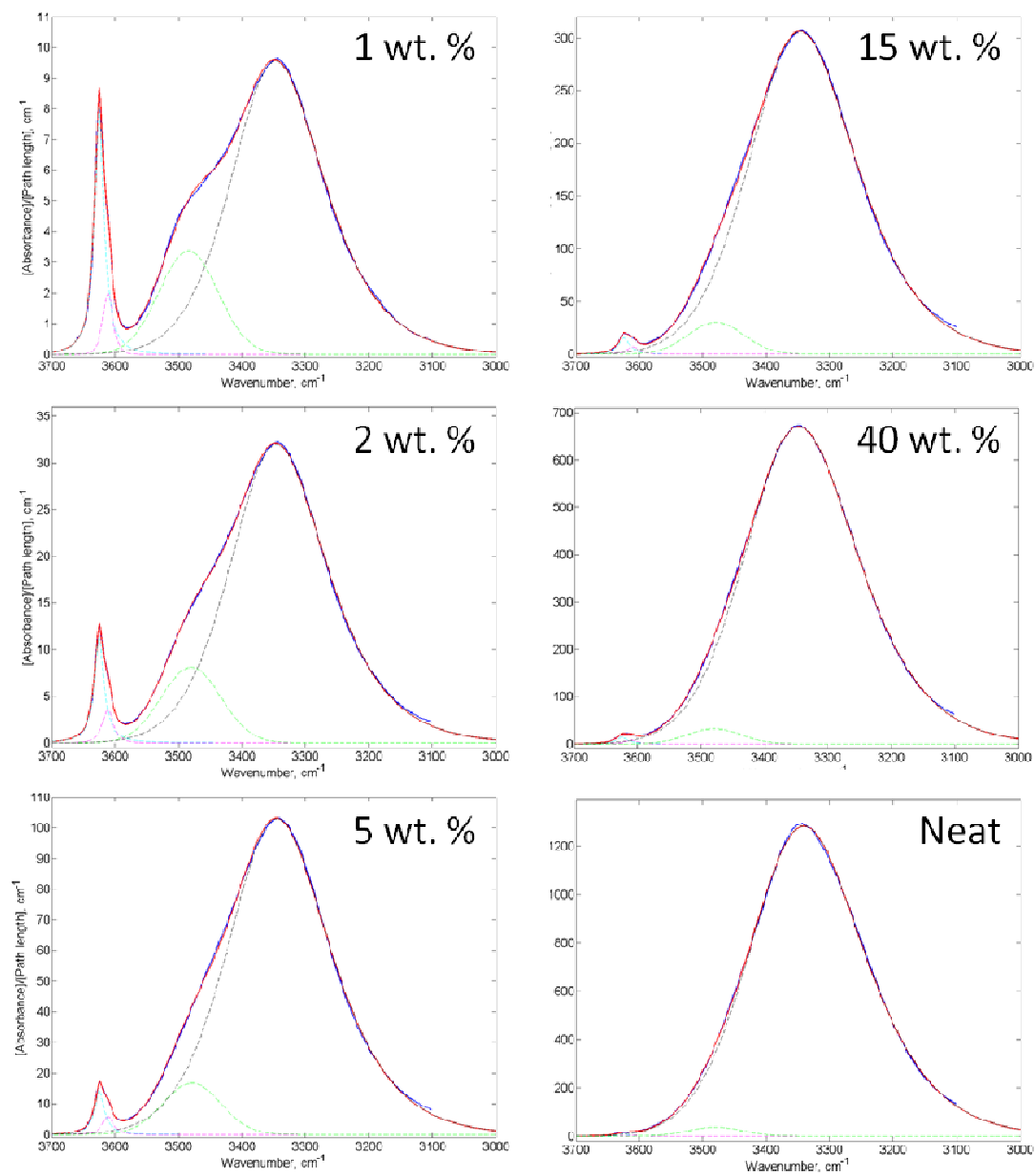
Figure 3.16 Selected deconvolution results for isopropanol-CCl$_4$ binary system
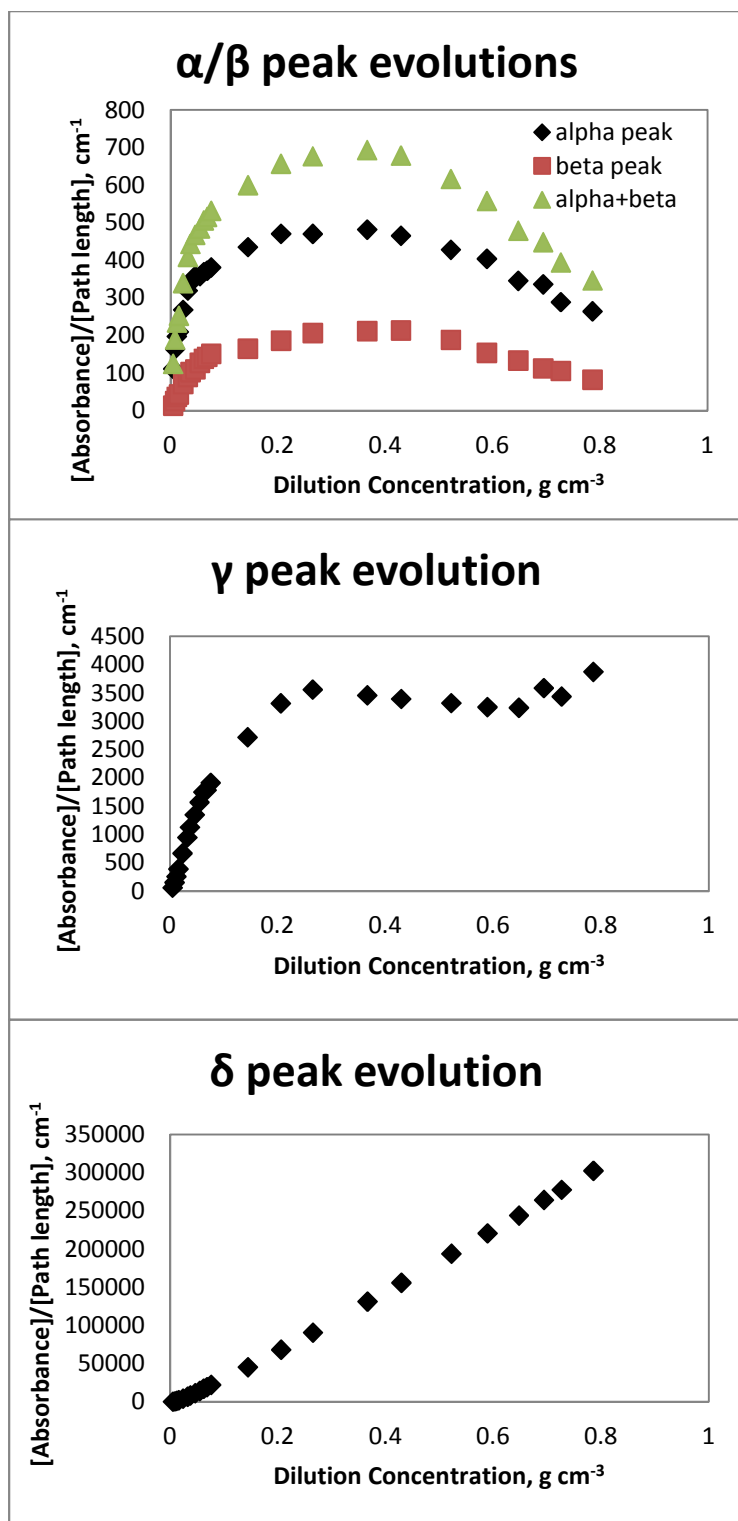
Figure 3.17 Obtained peak absorbance data as a function of dilution concentration for non hydrogen bonded and hydrogen bonded peaks

It was noteworthy that the intensity of α and β peaks hit a plateau and started to decrease as the concentration got higher. This trend was the same phenomenon found in the dilution experiment of NmA for self association study, which indicated that this phenomenon is ubiquitous in the self association of the hydrogen bonding and is strongly related with the phase behavior.

Coggeshall and Saier model was also applied to model free monomer behavior. Equations of (3.10) and (3.11) was used to fit the data as it was used for elucidating NmA self associations. First, concentration profile of free monomer could be obtained via Beer-Lambert's law shown in equation (3.12), where ε, c, and l were extinction coefficient, concentration, and path length respectively.

$$Absrobance = \varepsilon \cdot c \cdot l \tag{3.12}$$

Extinction coefficient of free monomer could be determined by extrapolating the fitting curve in [Absorbance]/[path length] versus [concentration] plot at a high dilution range by using the relationship of equation (3.13)

$$\varepsilon = \lim_{c \to o} \left| \frac{Absorbance}{c \cdot l} \right| \tag{3.13}$$

Then, K_1, which was dimerization equilibrium constant value, was also evaluated at a high dilution range by extrapolating the fitting equation in the plot of γ versus total dilution concentration with the relationship shown in (3.14).

$$\frac{1}{K_1} = \lim_{c \to o} |\gamma| \tag{3.14}$$

With the fixed value of K_1, multimerization equilibrium constant K_2 was optimized using the equations (3.10), and (3.11) of Coggeshall and Saier model for the 16 low concentration data points by fminsearch routine in MatLab software. Figure 3.18 showed

the fitting result of free monomer of isopropanol in CCl$_4$. It seemed that the model could fit the monomer data to the maximum concentration value, which also indicated that the equilibrium equation was only valid in a single phase where monomers were dominant. Optimized K$_1$ and K$_2$ values were 1.33 and 2.75 l mol^{-1}, which were reasonably agreed with the reported equilibrium constant values for ethanol in CCl$_4$,(0.76 and 2.57 at 40°C) [26] and phenol in CCl$_4$ (1.09 and 2.74 at room temperature) [43].

$$K_2 = \frac{2\left(\frac{1}{K_1}-\gamma\right)}{f_m C\left[\frac{2}{K_1}-\frac{\gamma}{2}+\left(\frac{2\gamma}{K_1}+\frac{\gamma^2}{4}\right)^{0.5}\right]} \qquad (3.10)$$

$$\gamma = \frac{2(f_m)^2 C}{(1-f_m)} \qquad (3.11)$$
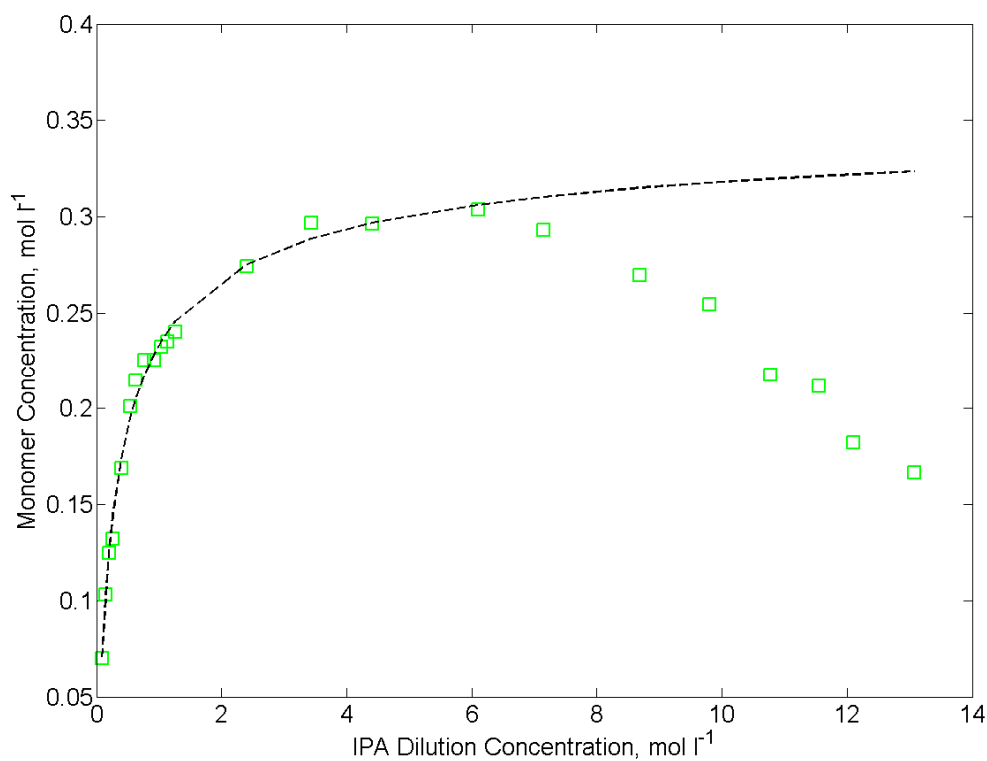
Figure 3.18 Free monomer concentration profile and dimer and multimer formation equilibrium model fitting results for isopropanol with Coggeshall-Saier model

Based on Coggeshall and Saier, number and weight fractions could be described by

equation (3.15) and (3.16), where f_m, K_1, K_2 and C were monomer fraction, dimerization

equilibrium constant and multimerization equilibrium constant and total concentration

respectively.

$$number\ fraction\ N_i = f_m \frac{K_1}{K_2} (K_2 f_m C)^{i-1} \tag{3.15}$$

$$weight\ fraction\ W_i = i f_m \frac{K_1}{K_2} (K_2 f_m C)^{i-1} \tag{3.16}$$

Dividing by total number and total weight shown in equations of (3.17) and (3.18) from

equations (3.15) and (3.16), normalized number and weight fraction distribution could be

derived.

To obtain total number and weight fraction, series expansion equation, $\sum_{i=1}^{\infty} p^i = \frac{1}{1-p}$ was

utilized.

$$\sum_{i=1}^{\infty} N_i = f_m \frac{K_1}{K_2} \frac{1}{1-K_2 f_1 C} \tag{3.17}$$

$$\sum_{i=1}^{\infty} W_i = f_m \frac{K_1}{K_2} \frac{1}{(1-K_2 f_1 C)^2} \tag{3.18}$$

The normalized chain length (number) distribution and molecular weight distribution

from Coggeshall and Saier model was shown in figure 3.19. It was noted from the

distribution that long chain associated multimers over 10 chain length were rarely formed

in the self association system.
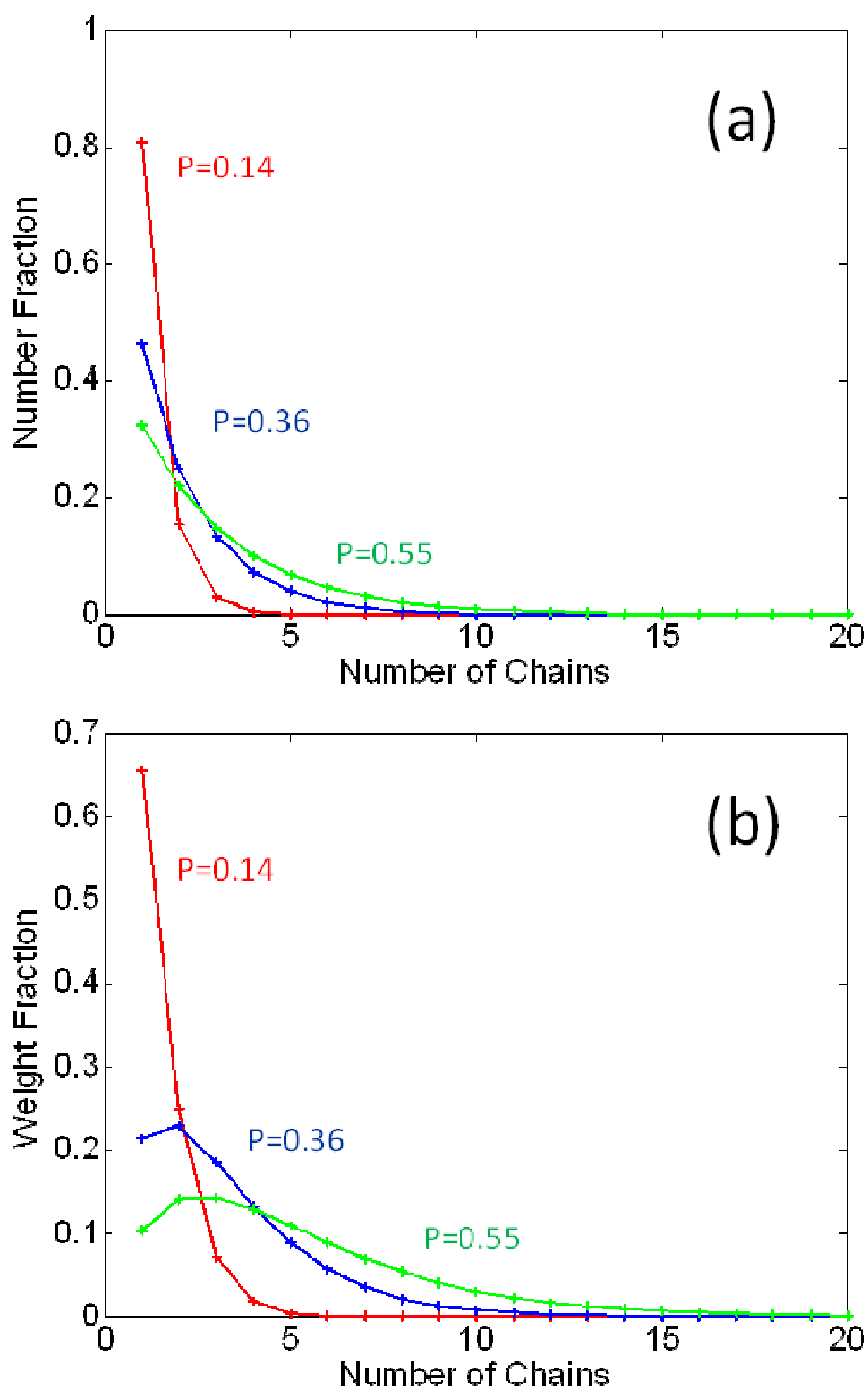
Figure 3.19 Normalized chain length (a) and molecular weight distribution (b) of isopropanol-CCl$_4$ system up to 20-mer existence by Coggeshall-Saier model

Painter et al further modified Coggeshall and Saier model and utilized dimensionless

equilibrium constants by introducing molar volume, since Coggeshall and Saier model

showed poor estimation of γ in the equation (3.14) at highly diluted concentration range

since the denominator, $(1 - f_m)$ in the equation (3.11) approached to zero value at highly

diluted solution and this made a large error on estimation of K_2 value.

Modified equilibrium constant used in Painter's model is shown in equation (3.19).

$$K_B = \frac{1000 \cdot K_C}{V_B} \tag{3.19}$$

where, V_B and K_C equal to the molar volume of self associating species and equilibrium

constant obtained from Coggeshall and Saier model respectively[44, 45].

Simple association model was used here. As Coggeshall and Saier demonstrated,

dimerization (K_1) and multimerization ($K_2=K_3=K_4=\cdots$) could provide a good association

equilibrium for alcohol self association system.

$$B_1 + B_1 \overset{K_1}{\Leftrightarrow} B_2 \tag{3.20}$$

$$B_1 + B_{h-1} \overset{K_2}{\Leftrightarrow} B_h \tag{3.21}$$

Coleman et al set up an equation (3.22) for free monomer as a function of equilibrium

constant and volume fraction of associating species, where f_m^{OH}, Φ_B, Φ_{B1} are free

monomer fraction, volume fraction of B and volume fraction of free monomer

respectively [44].

$$f_m^{OH} = \frac{\Phi_{B1}}{\Phi_B} = \left[\left(1 - \frac{K_1}{K_2}\right) + \frac{K_1}{K_2}\left(\frac{1}{(1-K_2\Phi_{B1})^2}\right)\right]^{-1} \tag{3.22}$$

With fixed K_1 value obtained from equation (3.11), Optimization of K_B was performed

using least square routine in MatLab. Fitting result was shown in Figure 3.20 and

obtained dimensionless K_2 and K_B was 17.42 (1.33 in L mol^{-1}) and 36.48 (2.19 in L mol^{-1}).
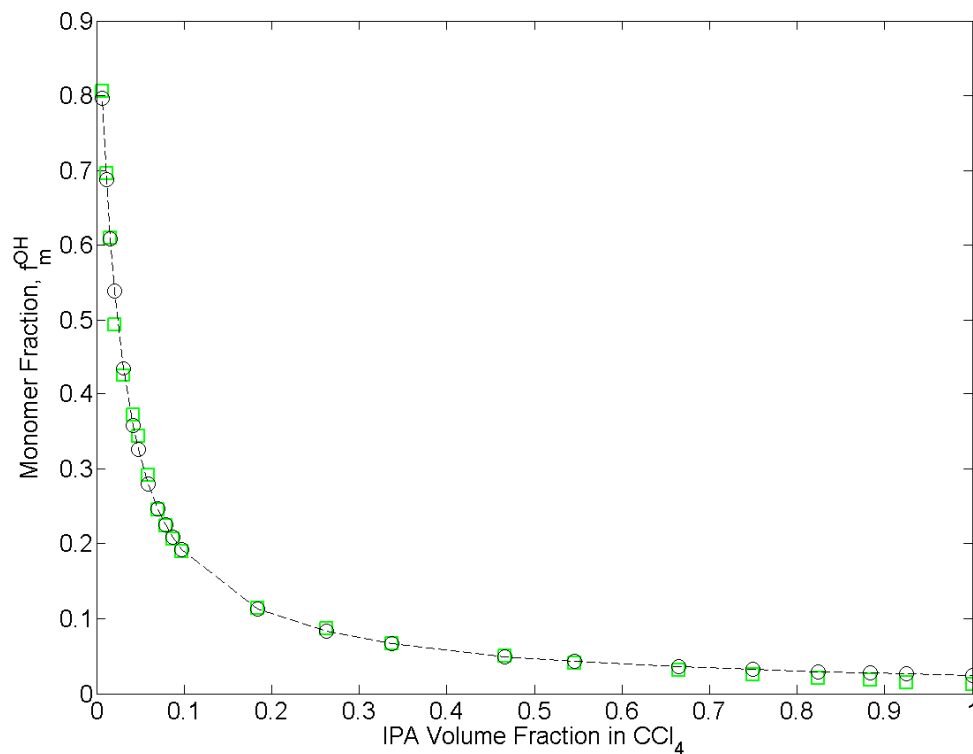
Figure 3.20 Free monomer fraction profile and Painter's model fitting result for isopropanol self association

The main concept of both Coggeshall and Saier's model and Painter's model were the formation of dimers and chain-like multimers from free monomers. Their model could not satisfactorily describe the actual association peaks of α, β, γ, and δ shown in the association system but could give a general idea that chain-like multimer formation would be dominant at higher concentration and δ type OH could also be abundant in the spectra at the high concentration as a result of multimer domination in the system.

To directly quantify OH types found in the spectra, all kinds of multimers with n-chains as well as monomers and dimers should be kept tracking using series of equilibrium kinetic equations shown in from (3.23) to (3.27)

$$B_1 + B_1 \overset{K_1}{\Leftrightarrow} B_2 \qquad K_1 = \frac{k_1^+}{k_1^-} \tag{3.23}$$

$$B_1 + B_2 \overset{K_2}{\Leftrightarrow} B_3 \qquad K_2 = \frac{k_2^+}{k_2^-} \tag{3.24}$$

$$B_1 + B_j \overset{K_2}{\Leftrightarrow} B_{j+1} \qquad K_2 = \frac{k_2^+}{k_2^-} \quad j \geq 3 \tag{3.25}$$

$$B_2 + B_j \overset{K_3}{\Leftrightarrow} B_{j+2} \qquad K_3 = \frac{k_3^+}{k_3^-} \quad j \geq 2 \tag{3.26}$$

$$B_i + B_j \overset{K_3}{\Leftrightarrow} B_{i+j} \qquad K_3 = \frac{k_3^+}{k_3^-} \quad i,j \geq 3 \tag{3.27}$$
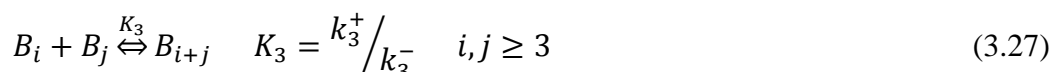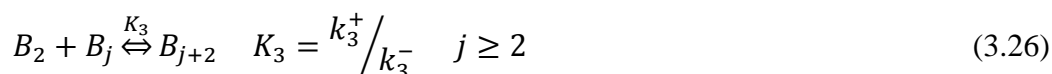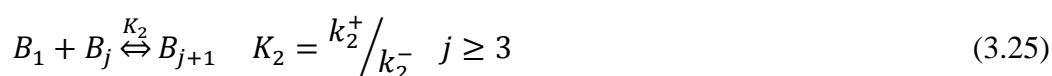
By tracing all the association species, one could find the actual number of α, β, γ, and δ OH groups in the system and these numbers could be directly compared with the absorbance of each OH groups in the experimental spectra.

As shown in figure 3.14 of OH type classification schematics, only free monomer contains single α bond. A dimer has one β and one γ bond and a trimer contains single β, γ, and δ peak.. In general expression, i-mer (i≥3) has single β, γ bond and (i-2) δ bond. Using this relationship, each OH type concentration could be obtained by calculation of n-mer with single polymerization equilibrium constant [46].

Reversible polymerization kinetic equation with single equilibrium constant shown in the equation (3.28), could be modified as W=1 to apply the equation to the system of interest.

$$B_i + B_j \overset{K}{\Leftrightarrow} B_{i+j} + W \qquad K = {k}/{k'} \tag{3.28}$$
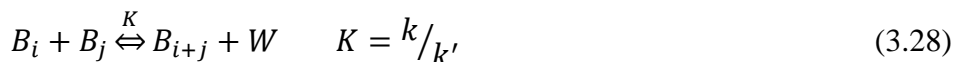
The momentum equation for the kinetic expression of the equation (3.28) was as follows.

$$\frac{d\mu_0}{dt} = -k\mu_0^2 + k'(\mu_1 - \mu_0) \tag{3.29}$$

Where μ_1 and μ_0 are defined by momentum distribution

$$\mu_1 = \Sigma_{i=1}^{\infty}[B_i] = [B]_0(1 - p), \text{ p=conversion} \tag{3.30}$$

$$\mu_0 = \Sigma_{i=1}^{\infty} i[B_i] = [B]_0 \tag{3.31}$$

By putting $\frac{d\mu_0}{dt}=0$ at equilibrium condition with the equilibrium constant, $K = {k}/{k'}$,

solving the equation (3.29) gives a quadratic equation (3.32),

$$K[B]_0(1 - p)^2 - p = 0 \tag{3.32}$$

By equilibrium distribution of Flory and Schultz's argument (3.33), individual n-mer

concentration could be calculated as a function of K and total concentration $[B]_0$ as

shown below.

$$[B_i] = [B]_0(1 - p)^2 p^{i-1} \tag{3.33}$$

Monomer: $[B_1] = [B]_0(1 - p)^2 = \frac{p}{K}$ $\tag{3.34}$

Dimer: $\quad [B_2] = [B]_0(1 - p)^2 p = \frac{p^2}{K}$ $\tag{3.35}$

Trimer: $\quad [B_3] = [B]_0(1 - p)^2 p^2 = \frac{p^3}{K}$ $\tag{3.36}$

n-mer: $\quad [B_n] = [B]_0(1 - p)^2 p^{n-1} = \frac{p^n}{K}$ $\tag{3.37}$

Once single equilibrium constant K was determined, absorbance of α, β, γ, and δ peak

could be fitted by using n-mer concentration–OH peak type relationship described above.

Optimized K value through the first seven data points of iPA-CCl$_4$ system was 2.18 L

mol^{-1}, which was similar to the K_B value obtained from Painter's model (2.19 L mol^{-1}).

The absorbance of 4 OH types could be rewritten as a function of extinction coefficient and n-mer concentration which were shown below, where ε in an extinction coefficient.

$$\alpha = \varepsilon_1 [B_1] \tag{3.38}$$

$$\beta = \varepsilon_2 \sum_{i=2}^{\infty} [B_i] \tag{3.39}$$

$$\gamma = \varepsilon_3 \sum_{i=2}^{\infty} [B_i] \tag{3.40}$$

$$\delta = \varepsilon_4 \sum_{i=4}^{\infty} (i-2)[B_i] \tag{3.41}$$

Using series expansions, the analytical solution of absorbance profile in terms of the extinction coefficient, K and conversion p_B could be obtained.

$$\alpha = \frac{\epsilon_1}{K} p_B \tag{3.42}$$

$$\beta = \frac{\epsilon_2}{K} \left(\frac{1}{1-p_B} - 1 - p_B \right) \tag{3.43}$$

$$\gamma = \frac{\epsilon_3}{K} \left(\frac{1}{1-p_B} - 1 - p_B \right) \tag{3.44}$$

$$\delta = \frac{\epsilon_4}{K} \left(\frac{p_B}{(1-p_B)^2} - \frac{2}{1-p_B} + p_B - p_B^3 + 2 \right) \tag{3.45}$$

Figure 3.21 showed the fitting results of the absorbance profiles of 4 OH types. The equilibrium constant measured with 7 data points at low concentration range could provide good estimation of each type of hydrogen bonding absorbance of OH up to 12 data points (1.26 mol l^{-1}). However, similar to NmA self association analysis, the analysis provided overestimation of the absorbance profiles of all OH types at high isopropanol concentration range (1.27-13.08 mol l^{-1}). Especially for the free monomer species, the model could not describe decreasing trends in the absorbance of α and β peaks but only provided a saturated trend, which was also figured out in NmA self association analysis. Therefore it would be concluded that phase transition and aggregation of small sized clusters to large sized cluster might reduce the actual number of proton donor for

hydrogen bond formation including free monomer species (α and β) as well as hydrogen bond acceptor species (γ). The reduction of number of reactive donor and acceptor species further results in a decrease of associated species (δ) so that the actual δ peak could be underestimated at higher concentration. The optimized extinction coefficient of β, γ and δ were 533, 6460 and 72541 l mol^{-1} mm^{-1} respectively. When they were compared with the fixed extinction coefficient of α peak obtained from the equation (3.13), the extinction coefficient of γ and δ showed factors of 4 and 30 greater than that of α peak. It was reported that the extinction coefficients of γ and δ peaks were larger than those of α and β peaks [47] and the extinction coefficient values optimized here are agreed with the reported fact.
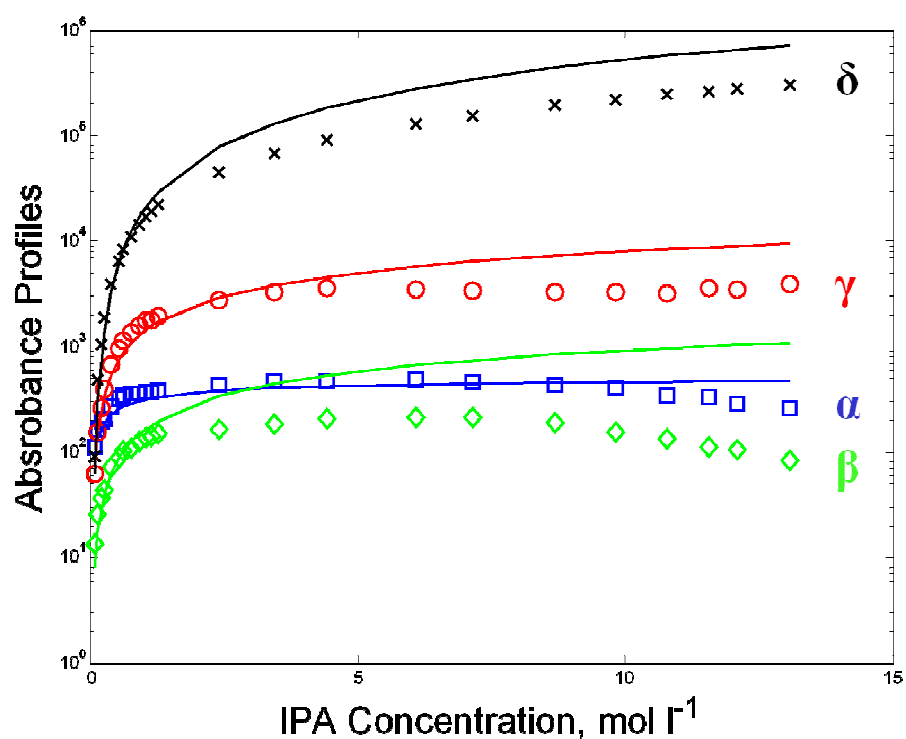
Figure 3.21 Absorbance data fitting with single equilibrium constant: α (square), β (diamond), γ (circle), and δ (x)

Number averaged molecular weight (MW_N) and weight averaged molecular weight

(MW_W) were compared as a function of isopropanol concentration in figure 3.22. Based

on the molecular weight distributions, polydispersity index (PDI) could be obtained by

equation (3.46).

$$PDI = \frac{MW_N}{MW_W} \tag{3.46}$$

Under the assumption of up to 10-mer existence, the polydispersity index (PDI) varied

from 1.1 to 1.5, which meant that at a very diluted solution, it behaved like a mono

dispersed solution because only monomer existed in the solution and as the system got

more concentrated, the PDI reached to 1.5. This index also indicated that even at

concentrated system, association provided relatively narrower distribution of molecular

weight of the associated species than polymeric materials provided, whose PDI varied

from 2 to 10.
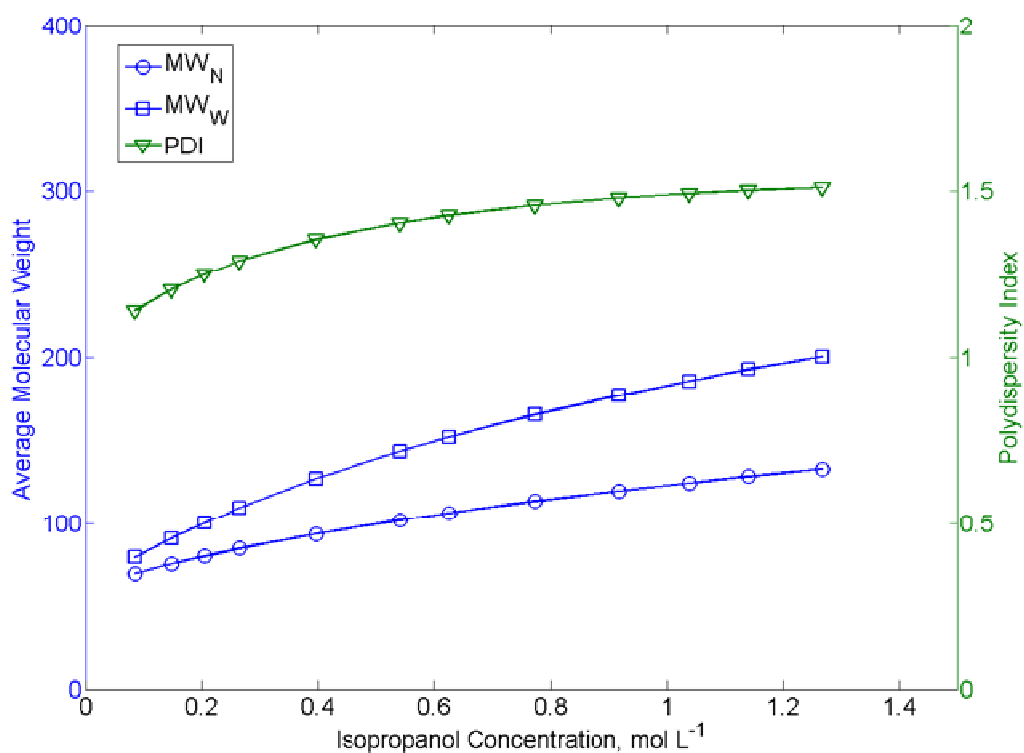
Figure 3.22 Molecular weight distributions and its polydispersity index as a function of isopropanol concentration

The chain length distribution and molecular weight distribution as a function of chain length, i, could also be obtained by modifying Flory-Schultz's distribution in equation (3.33).

Geometric chain length distribution could be obtained with the simple equation (3.47)

$$N_i = [B]_0 (1-p)^2 p^{i-1} \tag{3.47}$$

By taking summation of N_i,

$$N = \sum_{i=1}^{\infty} N = [B]_0 (1-p)^2 \sum_{i=1}^{\infty} p^{i-1} = [B]_0 (1-p) \tag{3.48}$$

Therefore, normalized chain length (number) distribution could be obtained by taking N_i/N,

$$N_i/N = (1-p) p^{i-1} \tag{3.49}$$

Geometric molecular weight distribution had a simple relationship with Flory-Schultz's

distribution as shown in equation (3.50).

$$W_i = i[B]_0(1-p)^2 p^{i-1} \qquad (3.50)$$

By taking a summation of W_i,

$$W = \sum_{i=1}^{\infty} W_i = [B]_0(1-p)^2 \sum_{i=1}^{\infty} ip^{i-1} \qquad (3.51)$$

$$\sum_{i=1}^{\infty} ip^{i-1} = \frac{d}{dp}\left(\sum_{i=1}^{\infty} p^i\right) = \frac{d}{dp}\left(\frac{1}{1-p} - 1\right) = \frac{1}{(1-p)^2} \qquad (3.52)$$

The normalized molecular weight distribution could be derived as shown in equation

(3.53).

$$\frac{W_i}{W} = i(1-p)^2 p^{i-1} \qquad (3.53)$$

Normalized chain length and molecular weight distribution of isopropanol-CCl$_4$ system

was shown in figure 3.23. Three data points were chosen, whose isopropanol

concentrations were 0.087, 0.397, and 1.258 mol l^{-1} respectively. The conversions of

monomer, p, were 0.14, 0.36 and 0.55. It was noted from the comparison of normalized

distribution with those obtained from Coggeshall-Saier model that, in both models that

association of high number of hydrogen bonding chain greater than 10 was seldom

occurring at a given concentration range. Coggeshall-Saier model predicted smaller

existence of dimer than Flory-Schultz model since Coggeshall-Saier model has smaller

dimerization equilibrium constant. Noting that model prediction of monomer

concentration had a deviation from 1.258 mol L^{-1} dilution concentration data point, as

shown in figure 3.18, it could be concluded that the deviation from the model prediction

of monomer behavior might be due to high number chain formation and this high chain

association could coincide with phase transition, which was suspected as a reason of monomer concentration decrease at higher concentration range.
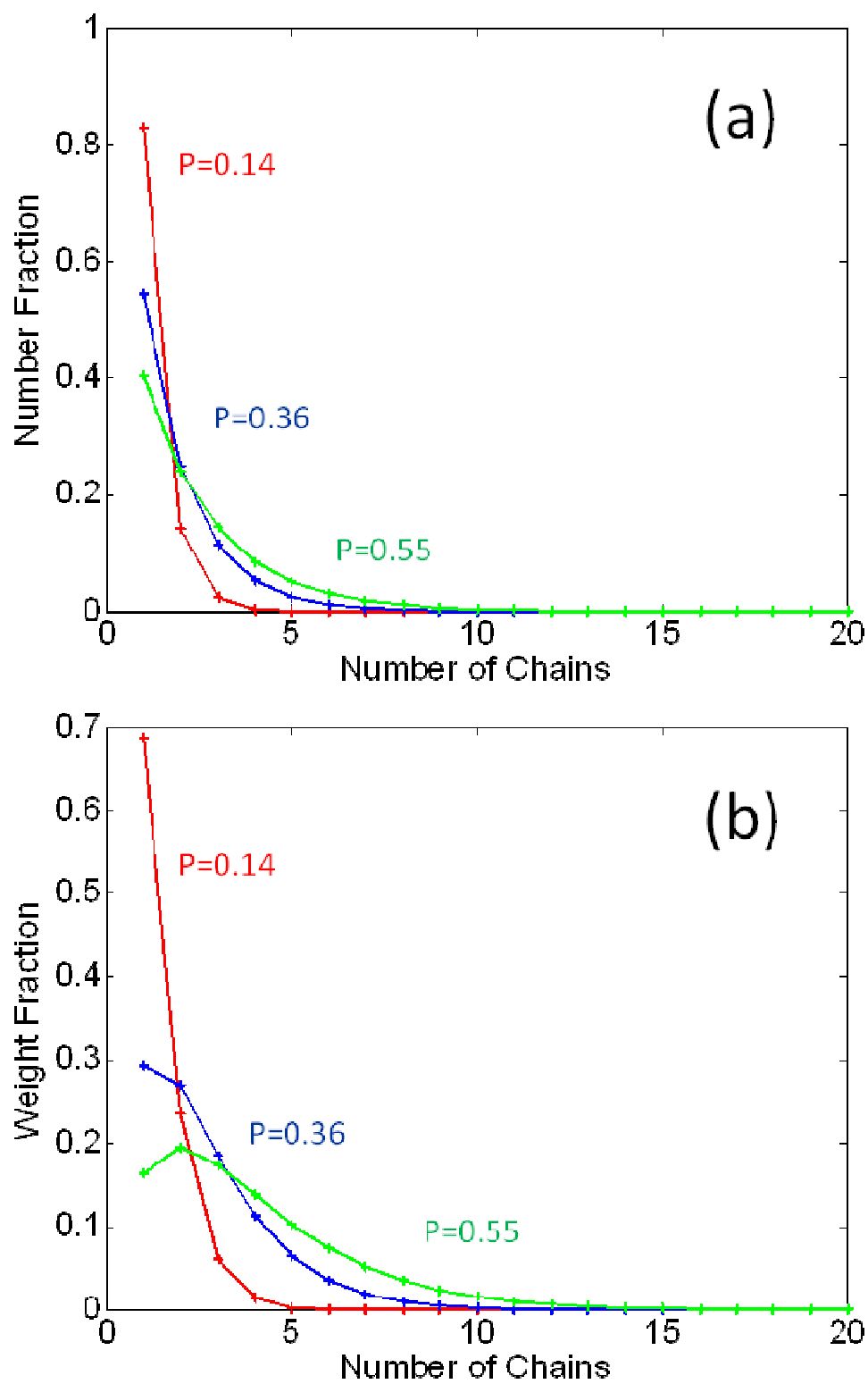
Figure 3.23 Chain length and molecular weight distribution of isopropanol-CCl$_4$ system up to 20-mer existence by Flory-Schultz model

3.3.2   Intermolecular (hetero) Association of isopropanol

Intermolecular associations (or hetero association) of hydroxyl group in isopropanol with various hydrogen bonding acceptors were also examined. Toluene, Epoxybutane, Triethylamine and Dipropylether were used as hydrogen bonding acceptors of π bond, epoxide, tertiary amine, and ether groups respectively. 1 wt. % of isopropanol was mixed with these hydrogen bonding acceptor species, whose concentration range varied from 0.5 wt.% to 40wt.% dissolved in CCl_4. Figure 3.24 showed a intermolecular association of OH groups. It was noted that even 1 wt. % of isopropanol (about 0.2 mol L^{-1}) had self associations in the system and the self association equilibrium competed with intermolecular (hetero) associations. This competition was observed in all systems, the self association peak intensities decreased while the peak intensity of hetero association peak increased as hydrogen bonding acceptor species were added to the system. Painter's model was first used to evaluate intermolecular association with hydrogen bonding acceptors first and then it was compared with modified Flory-Schultz's model.
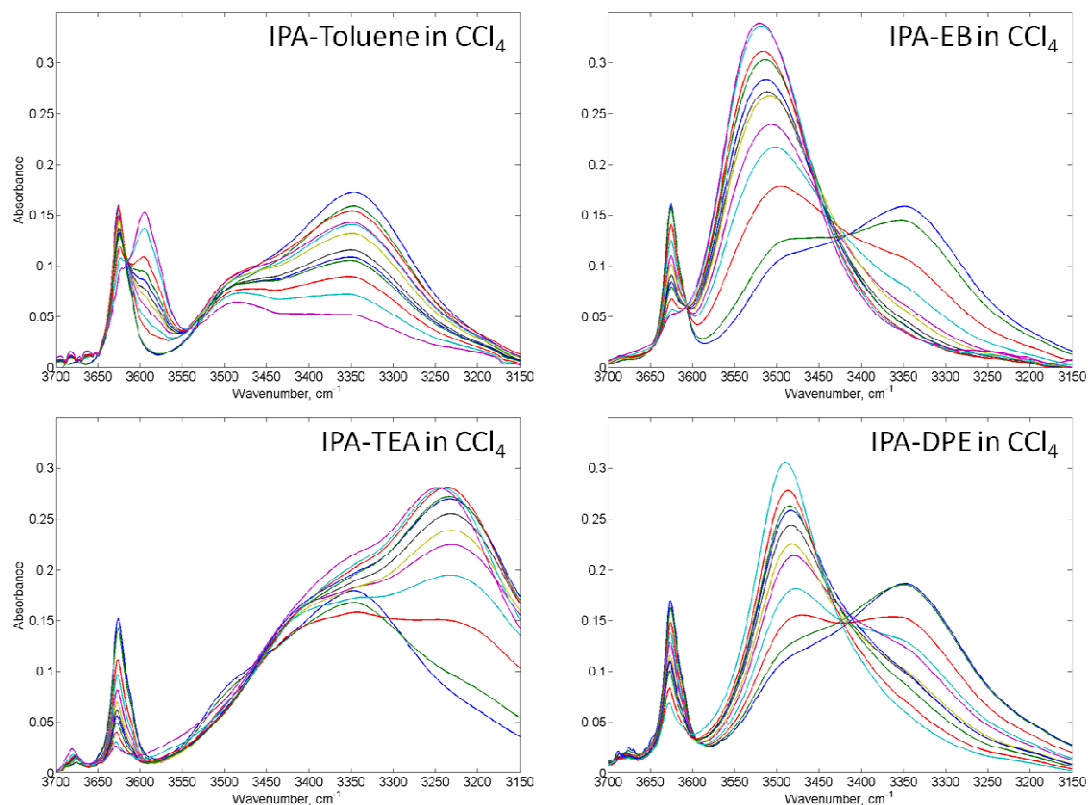
Figure 3.24 Isopropanol associations with various hydrogen bonding acceptors

Five peaks were chosen for spectral deconvolution, α, β, γ, δ OH peaks and one intermolecular association peak. Figure 3.25 showed selected deconvolution result of each system and the peak positions of deconvoluted peaks were summarized in table 3.7. It was reported that the hydrogen bonding energy was proportional to Δν, $(\nu_{free} - \nu_{associated})$. In this perspective, the hydrogen bonding energies of given systems showed in an order of Amine > OH > Epoxide > ether > π bond.
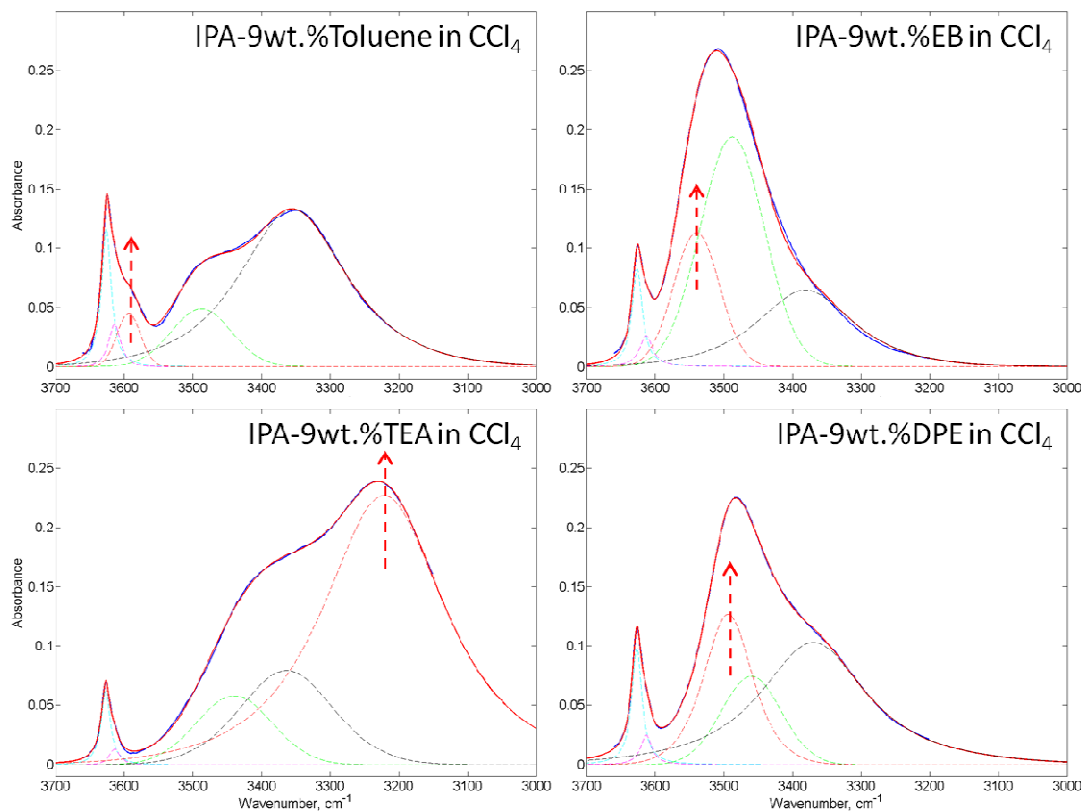
Figure 3.25 Selected deconvolution results of isopropanol-H bond acceptor-CCl$_4$ ternary systems

Table 3.7 Comparison of Associated peak positions of isopropanol ternary system with self-associated peak position

	Free monomer	IPA-Toluene-CCl$_4$,cm^{-1}	IPA-EB-CCl$_4$,cm^{-1}	IPA-DPE-CCl$_4$,cm^{-1}	IPA-CCl$_4$,cm^{-1} (δ)	IPA-TEA-CCl$_4$,cm^{-1}
Peak position (Δv)	3627	3576 (51)	3536 (91)	3546 (81)	3478 (149)	3378 (249)

Coleman and Painter added a simple intermolecular association equilibrium kinetic equation (3.41) to the self association equilibrium equations of (3.20) and (3.21) [48, 49.].

$$B_1 + B_1 \overset{K_2}{\Leftrightarrow} B_2 \tag{3.20}$$

$$B_1 + B_{h-1} \overset{K_B}{\Leftrightarrow} B_h \tag{3.21}$$

$$B_n + A \overset{K_A}{\Leftrightarrow} B_n A \tag{3.54}$$

Where A and B are hydrogen bonding acceptor and donor species

The volume fractions of hydrogen bond donor and acceptor could be given as follows

$$\Phi_A = \Phi_{A1} + K_A \Phi_{A1} \Phi_{B1} \Gamma_1 \tag{3.55}$$

$$\Phi_B = \Phi_{B1} \Gamma_2 \left[1 + \frac{K_A \Phi_{A1}}{r} \right] \tag{3.56}$$

Where, Φ_{A1}, Φ_{B1} and r are volume fractions of free A and B groups in the system and

molar volume ratio, V_A/V_B respectively.

Γ_1 and Γ_2 are given by

$$\Gamma_1 = \left[1 - \frac{K_2}{K_B} \right] + \frac{K_2}{K_B} \left[\frac{1}{(1 - K_B \Phi_{B1})} \right] \tag{3.57}$$

$$\Gamma_2 = \left[1 - \frac{K_2}{K_B} \right] + \frac{K_2}{K_B} \left[\frac{1}{(1 - K_B \Phi_{B1})^2} \right] \tag{3.58}$$

K_2 and K_B could be obtained from previous analysis for isopropanol self association with

dimensionless equilibrium constants of 17.42 and 36.48 respectively.

With given K_2 and K_B values, free monomer fraction in the ternary system could be

obtained using the equations through (3.55) – (3.58)

$$f_m^{OH} = \frac{\Phi_{B1}}{\Phi_B} = \left[\Gamma_2 \left(1 + \frac{K_A \Phi_A}{r(1 + K_A \Phi_{B1} \Gamma_1)} \right) \right]^{-1} \tag{3.59}$$

Figure 3.26 showed the fitting result of f_m^{OH} throughout hydrogen bonding acceptor

concentrations. The equilibrium constants were also in order of Amine > OH > Epoxide >

ether > π bond.
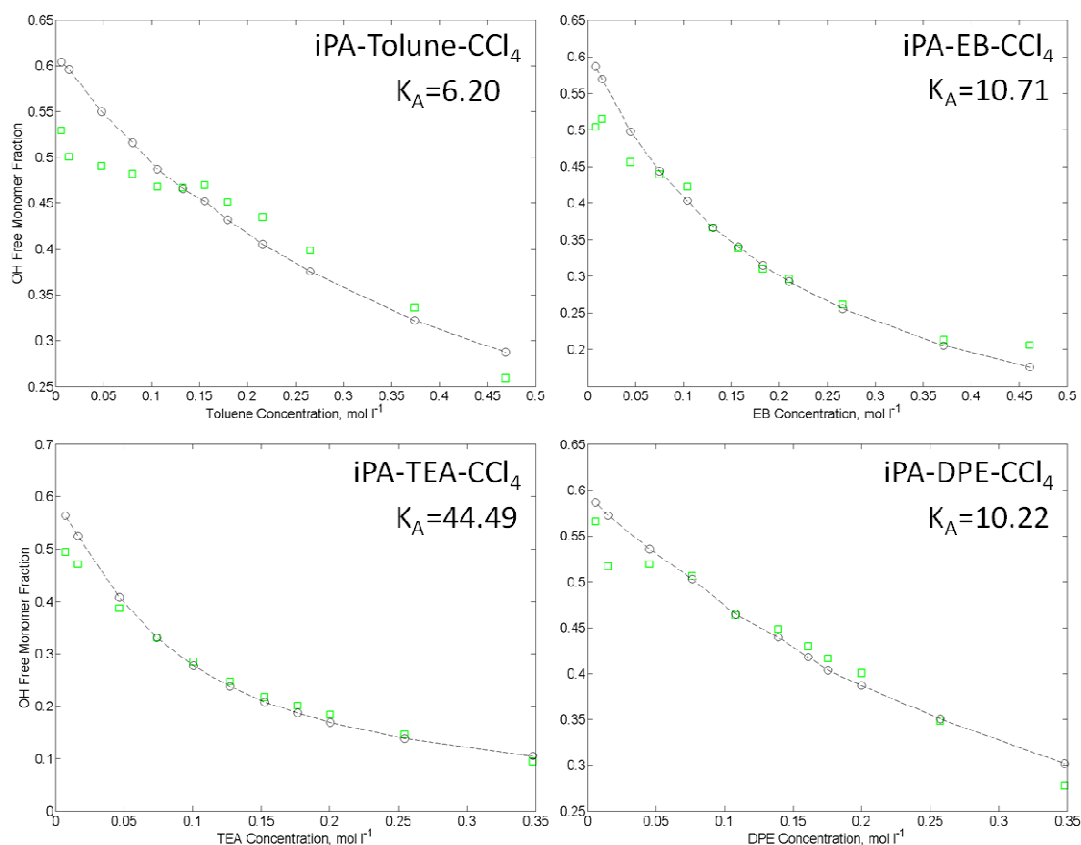
Figure 3.26 Free monomer fractions in iPA-H bond acceptor-CCl₄ ternary systems and data fitting result using Painter's model

Association with external hydrogen bonding acceptor species was also modeled with reversible polymerization kinetics with a single equilibrium constant proposed by Flory - Schultz model [46]. The simplest assumption could be that both self and inter associations followed Flory-Schultz distribution. Under this assumption, the absorbance data obtained from IR spectra could be fitted as functions of p_B and p_A which were conversion by self association and intermolecular association respectively.

$$[B_n] = \frac{p_B^i}{K_A} \tag{3.60}$$

$$[B_n A] = \frac{p_A^i}{K_A} \tag{3.61}$$

Figure 3.26 showed intermolecular association of n-mer with an association species, A. It was noted from the schematic that the associated species also had some of the spectral origins which were same as shown in the self association, γ and δ peaks. α and β peaks did not exist in the form of association species since there is no unbound proton donor in the structure.
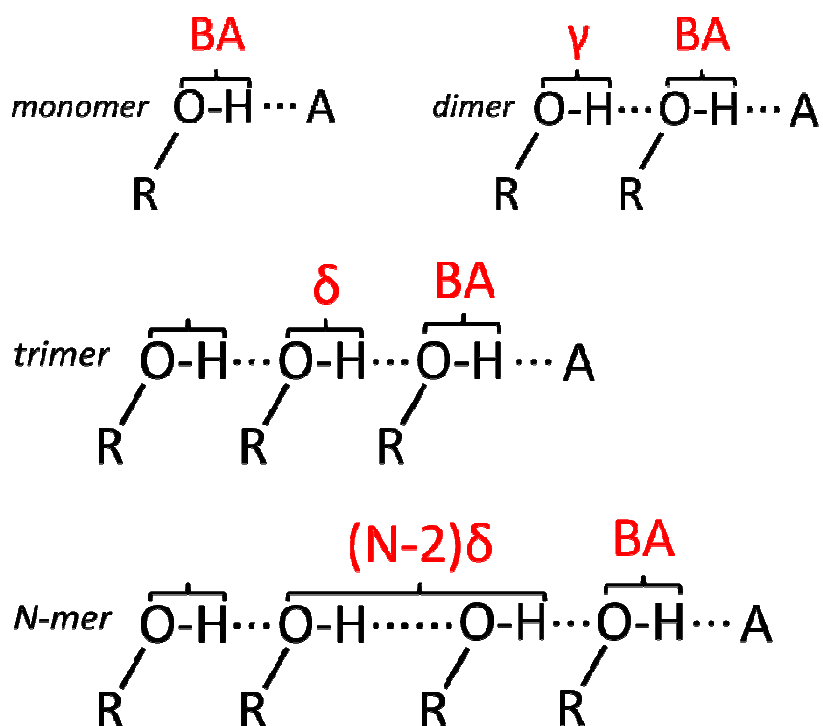
Figure 3.27 Schematics of intermolecular association

From the assumptions of the equation (3.60) and (3.61), the absorbance of α, β, γ and δ peaks could be written as a function of p_B, p_A and the extinction coefficients of the peaks as shown in the equation from (3.62) to (3.63).

$$\alpha = \frac{\epsilon_1}{K} p_B \tag{3.62}$$

$$\beta = \frac{\epsilon_2}{K}\left(\frac{1}{1-p_B} - 1 - p_B\right) \tag{3.63}$$

$$\gamma = \frac{\epsilon_3}{K}\left(\frac{1}{1-p_B} - 1 - p_B + \frac{1}{1-p_A} - 1\right) \tag{3.64}$$

$$\delta = \frac{\epsilon_4}{K}\left(\frac{p_B}{(1-p_B)^2} - \frac{2}{1-p_B} + p_B - p_B{}^3 + 2\frac{p_A}{(1-p_A)^2} - \frac{2}{1-p_A} + p_A - p_A{}^3 + 2\right) \tag{3.65}$$

$$BA = \frac{\epsilon_5}{K}\left(\frac{1}{1-p_B} - 1\right) \tag{3.66}$$

It was also noteworthy that the associated species with monomer had a hydrogen bond whose donor was bound by species A and acceptor was unbound. With a strict classification, this kind of bond was not BA bond, since, unlike other BA bonds found in dimer and multimers, only this BA bond has an unbound donor. However, the spectral uniqueness of this type of BA bond was not found in an actual spectrum. Therefore, this special bond type was included in a general class of BA bond.

Concentrations of i-mer of self associated species and j-mer of inter-asociated species could be calculated by the equation (3.60) and (3.61) and the calculated peak absorbance could be obtained by the relationship in between conversions for self and inter-association and absorbance shown in the equations of (3.62) through (3.66). Equilibrium constant for the self association was obtained in a previous section of isopropanol self association and the value was 2.864 L mol^{-1}.

$$B + A \overset{K_{BA}}{\Longleftrightarrow} BA \tag{3.66}$$

where, $[B] = \sum_{i=1}^{\infty}[B_i]$ and $[BA] = \sum_{i=1}^{\infty}[B_iA]$, respectively.

Applying equations of (3.60) and (3.61) provided a relationship in between conversions and self association equilibrium constant K_B and concentration of hydrogen bonding donor species, $[B]_0$, as shown in equation (3.67) .

$$K_B[B]_0 = \frac{p_B}{1-p_B} + \frac{p_A}{1-p_A} \qquad (3.67)$$

Conversion parameter optimization was conducted using 4 unknown variables (extinction coefficients of β, γ, δ and BA peaks) first and figure 3.28 showed peak fitting result of four ternary system.
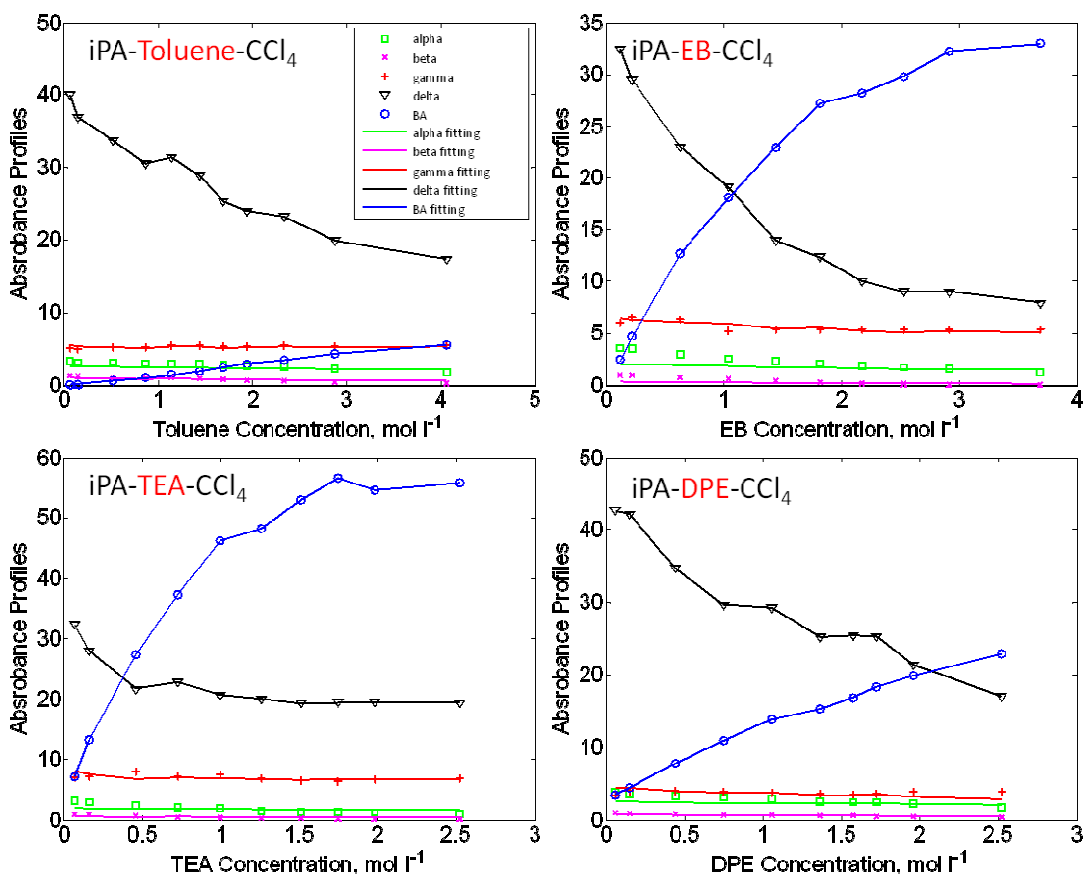
Figure 3.28 Absorbance fitting result of α, β, γ, δ and BA peaks in iPA-H-bond acceptor-CCl_4 ternary system with varying extinction coefficients of β, γ, δ and BA

The optimized extinction coefficients of β, γ, δ and BA peaks were listed and compared with those obtained from the self association in table 3.8.

Comparing with the extinction coefficients obtained from the self association experiment of isopropanol, those obtained from iPA-Tolunene-CCl$_4$ ternary system showed the least deviation. For the other systems, the extinction coefficient of γ and δ showed two orders magnitude deviation from the self association extinction coefficients.

Table 3.8 Optimized extinction coefficients of hydrogen bond associating peaks

species\system	iPA self - Association	iPA-Toluene	iPA-TEA	iPA-EB	iPA-DPE
BA		25737.4	1045691.4	113783.2	395439.6
β	743.9	890.2	866.1	872.3	568.4
γ	6567.8	6347.3	10993.4	14013.3	3248.2
δ	93977.9	108521.9	131014.8	210881.2	52710.9

Then the extinction coefficeints of β, γ and δ peaks were fixed with the values obtained from the self association experiment and conversions were obtained to see how the extinction coefficients effect on the peak fitting. The fitting result was shown in figure 3.29. Fixed value of the extinction coefficients of β, γ and δ still provided good fit of absorbance profiles but showed poor estimation of γ peak. However, it was concluded that the extinction coefficient was insensitive to the peak fitting.
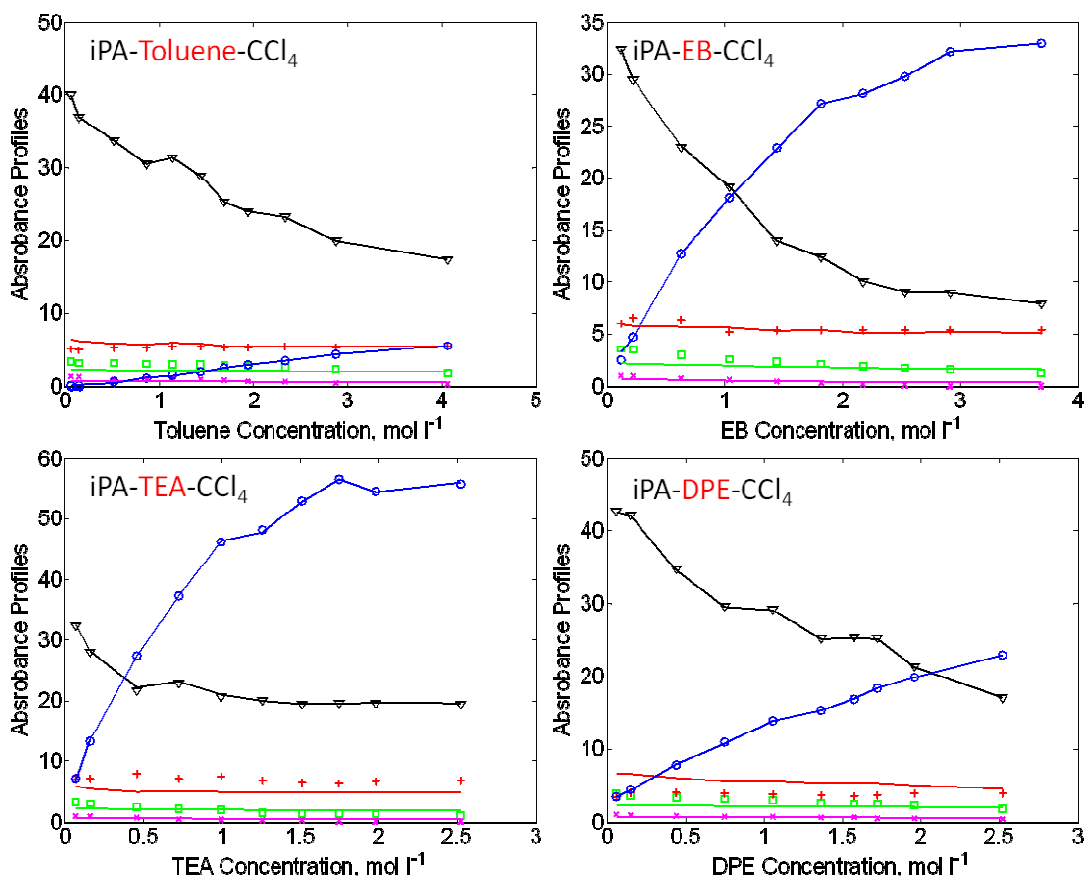
Figure 3.29 Absorbance fitting result of α, β, γ, δ and BA peaks in iPA-H-bond acceptor-CCl$_4$ ternary system with fixed extinction coefficients of β, γ, δ and BA

Validation of the model was conducted by comparison of $K_B[B]_0$ and optimized value of

$\frac{p_B}{1-p_B} + \frac{p_A}{1-p_A}$ as shown in the equation (3.67) for each ternary system was summarized in

table 3.9 and it indicated the model provided an estimation of conversion within 15%

variation from the experimental values.

Table 3.9 Optimized conversion comparison with experimental value using equation (3.61)

System	iPA-Toluene		iPA-TEA		iPA-EB		iPA-DPE	
Acceptor wt.%	pb/(1-pb)+ pa/(1-pa)	Kb*[iPA0]	pb/(1-pb)+ pa/(1-pa)	Kb*[iPA0]	pb/(1-pb)+ pa/(1-pa)	Kb*[iPA0]	pb/(1-pb)+ pa/(1-pa)	Kb*[iPA0]
0.5	0.683	0.731	0.639	0.762	0.668	0.741	0.699	0.782
1	0.6663	0.721	0.613	0.738	0.661	0.732	0.697	0.7792
3	0.6483	0.726	0.574	0.710	0.664	0.739	0.657	0.753
5	0.636	0.711	0.5844	0.711	0.662	0.725	0.627	0.716
7	0.643	0.721	0.5714	0.6961	0.6332	0.693	0.626	0.721
9	0.632	0.702	0.5634	0.668	0.6532	0.704	0.598	0.679
11	0.612	0.666	0.561	0.670	0.6252	0.671	0.601	0.680
13	0.606	0.670	0.562	0.658	0.6092	0.674	0.601	0.693
15	0.606	0.667	0.563	0.635	0.6132	0.662	0.572	0.669
20	0.587	0.646	0.563	0.606	0.5832	0.626	0.537	0.618
30	0.577	0.614			0.625	0.606		
40					0.623	0.564		

Equation for equilibrium constant of inter-association could also be obtained as shown in equation (3.70) under the assumption of Flory-Schultz distribution of equations (3.60) and (3.61) with mass balance shown in the equations of (3.68) and (3.69).

$$[B]_0 = [B] + [AB] \tag{3.68}$$

$$[A]_0 = [A] + [AB] \tag{3.69}$$

$$K_{AB} = \left(\frac{1-p_B}{p_B}\right)\left(\frac{p_A}{1-p_A}\right)\frac{1}{\left([A]_0 - \frac{1}{K_A}\left(\frac{1-p_A}{p_A}\right)\right)} \tag{3.70}$$

The equilibrium constant values at every data point for each ternary system were shown in figure 3.30. The equilibrium constants seem to vary systematically. The final equilibrium constant of K_{BA} could be obtained by taking average of the values from

figure 3.29 excluding two largest values and two smallest values and they were listed in table 3.10.
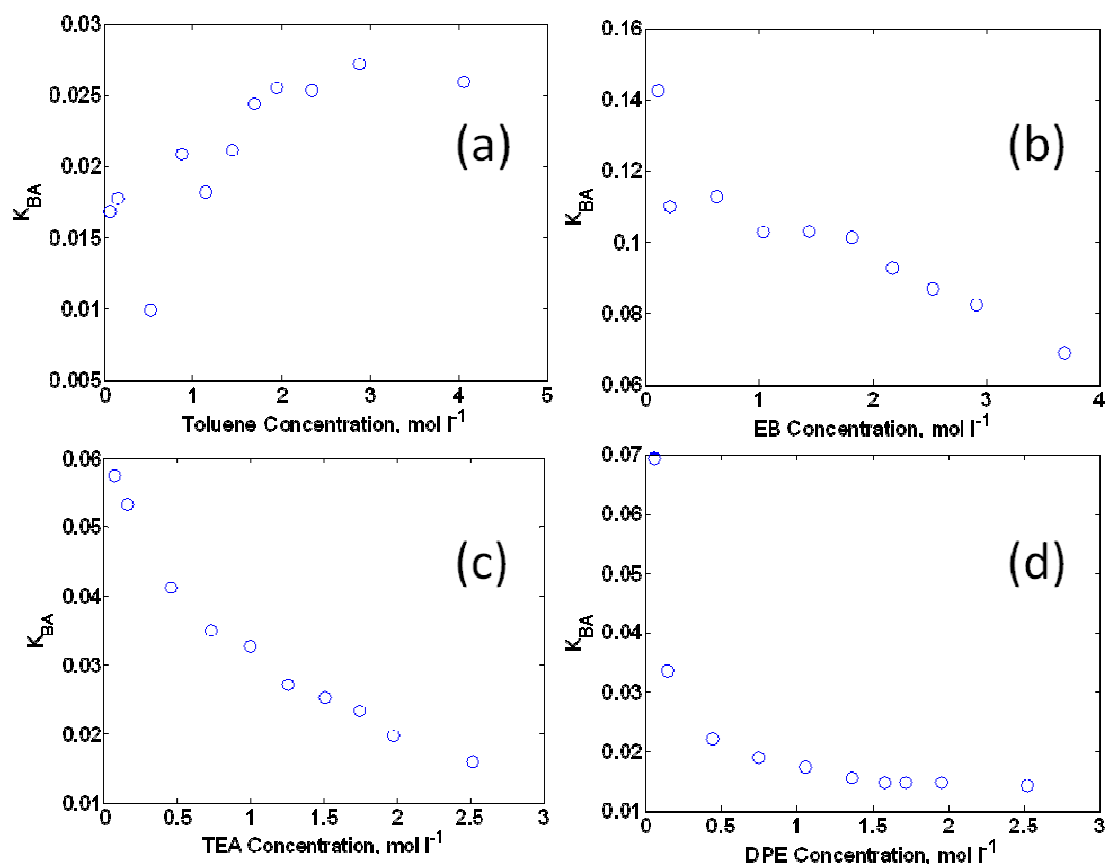
Figure 3.30 Inter-association equilibrium constant K_{BA} determination in ((a): iPA-Toluene-CCl$_4$, (b): iPA-EB-CCl$_4$, (c): iPA-TEA-CCl$_4$, (d): iPA-DPE-CCl$_4$)

Table 3.10 Averaged inter-association equilibrium constants

System	iPA-Toluene	iPA-TEA	iPA-EB	iPA-DPE
K_{BA}	0.022	0.031	0. 099	0.017

Finally,conversion could be obatined with fixed average value of inter-association equilibium constant for each system. Given values of $[B]_0$, $[A]_0$, K_B and K_{BA}, the inter-association conversion, p_A could be calculated first by solving a quadratic equation from

equations of (3.67) and (3.70) followed by the calculation of p_B with equation (3.67). The

results were compared with those obtained from absorbance profiles with varying K_{BA} as

shown in figure 3.31. Blue and red dots indicated conversion values obtained from

optimization process of K_{BA} by minizing error of $\sum([Absorbance_i]_{measured} -$

$[Absorbance_i]_{calculated})^2$. conversion values directly calculated from the initial

concentrations and fixed equilibrium constants were in solid lines. It was noted that inter-

association conversion had relatively little discrepancy when it is compared with self

association conversion, which indicated that the assumption of Flory-Schultz provided

good reproducibility on inter-association but it paid for inaccuracy of self association

conversion. Calculated conversion values from Absorbance data with varying K_{BA} and

concentration data with fixed K_{BA} were listed in table 3.11.

Table 3.11 Conversions and input concentrations for isopropanol-Toluene-CCl_4 system

$[iPA]_0$	$[Toluene]_0$	p_B with varying K_{BA}	p_A with varying K_{BA}	p_B with fixed K_{BA}	p_A with fixed K_{BA}
0.2553	0.0684	0.4054	0.0008	0.4220	0.001
0.2516	0.1571	0.3992	0.0018	0.4180	0.0025
0.2535	0.5238	0.3921	0.0033	0.4179	0.0081
0.2485	0.8737	0.3844	0.0112	0.4112	0.0131
0.2519	1.1509	0.3865	0.0129	0.4130	0.0173
0.2450	1.4428	0.3802	0.0183	0.4049	0.0209
0.2324	1.6895	0.3701	0.0235	0.3909	0.0231
0.2339	1.9434	0.3662	0.0278	0.3913	0.0265
0.2329	2.3426	0.3638	0.0327	0.3882	0.0314
0.2256	2.8817	0.3525	0.0407	0.3780	0.0368
0.2145	4.0594	0.3429	0.0519	0.3608	0.0476

Table 3.12 Conversions and input concentrations for isopropanol-TEA-CCl$_4$ system

[iPA]$_0$	[TEA]$_0$	p$_B$ with varying K$_{BA}$	p$_A$ with varying K$_{BA}$	p$_B$ with fixed K$_{BA}$	p$_A$ with fixed K$_{BA}$
0.2663	0.0723	0.3892	0.0026	0.4321	0.0017
0.2579	0.1636	0.3782	0.0052	0.4236	0.0037
0.2483	0.4609	0.3602	0.0105	0.4122	0.0098
0.2484	0.7296	0.3629	0.0143	0.4104	0.0153
0.2434	0.9972	0.3562	0.0176	0.4035	0.0202
0.2335	1.2579	0.3526	0.0181	0.3918	0.0242
0.2344	1.5083	0.3507	0.0201	0.3909	0.0287
0.2300	1.7456	0.3505	0.0214	0.3848	0.0323
0.2219	1.9777	0.3514	0.0207	0.3747	0.0350
0.2117	2.5170	0.3511	0.0212	0.3602	0.0415

Table 3.13 Conversions and input concentrations for isopropanol-EB-CCl$_4$ system

[iPA]$_0$	[EB]$_0$	p$_B$ with varying K$_{BA}$	p$_A$ with varying K$_{BA}$	p$_B$ with fixed K$_{BA}$	p$_A$ with fixed K$_{BA}$
0.2588	0.1143	0.4107	0.0027	0.4385	0.000
0.2557	0.2157	0.4095	0.0034	0.4375	0.0019
0.2581	0.6279	0.3941	0.0063	0.4276	0.0056
0.2532	1.0394	0.3819	0.0086	0.4141	0.0089
0.2419	1.4443	0.3808	0.0111	0.4146	0.0127
0.2458	1.8154	0.3694	0.0122	0.3987	0.0153
0.2343	2.1769	0.3699	0.0135	0.3984	0.0176
0.2352	2.5340	0.3696	0.0146	0.4025	0.0195
0.2311	2.9126	0.3573	0.0158	0.3929	0.0213
0.2187	3.6901	0.3412	0.0182	0.3719	0.0249

Table 3.14 Conversions and input concentrations for isopropanol-DPE-CCl$_4$ system

[iPA]$_0$	[DPE]$_0$	p$_B$ with varying K$_{BA}$	p$_A$ with varying K$_{BA}$	p$_B$ with fixed K$_{BA}$	p$_A$ with fixed K$_{BA}$
0.2729	0.0580	0.4104	0.0027	0.4385	0.0008
0.2723	0.1482	0.4095	0.0034	0.4375	0.0019
0.2628	0.4433	0.3941	0.0063	0.4276	0.0056
0.2499	0.7465	0.3819	0.0086	0.4141	0.0090
0.2517	1.0569	0.3808	0.0111	0.4146	0.0127
0.2369	1.3622	0.3694	0.0122	0.3987	0.0153
0.2375	1.5781	0.3699	0.0135	0.3984	0.0176
0.2421	1.7196	0.3696	0.0146	0.4025	0.0195
0.2335	1.9569	0.3573	0.0158	0.3929	0.0213
0.2158	2.5202	0.341	0.0182	0.3719	0.0250
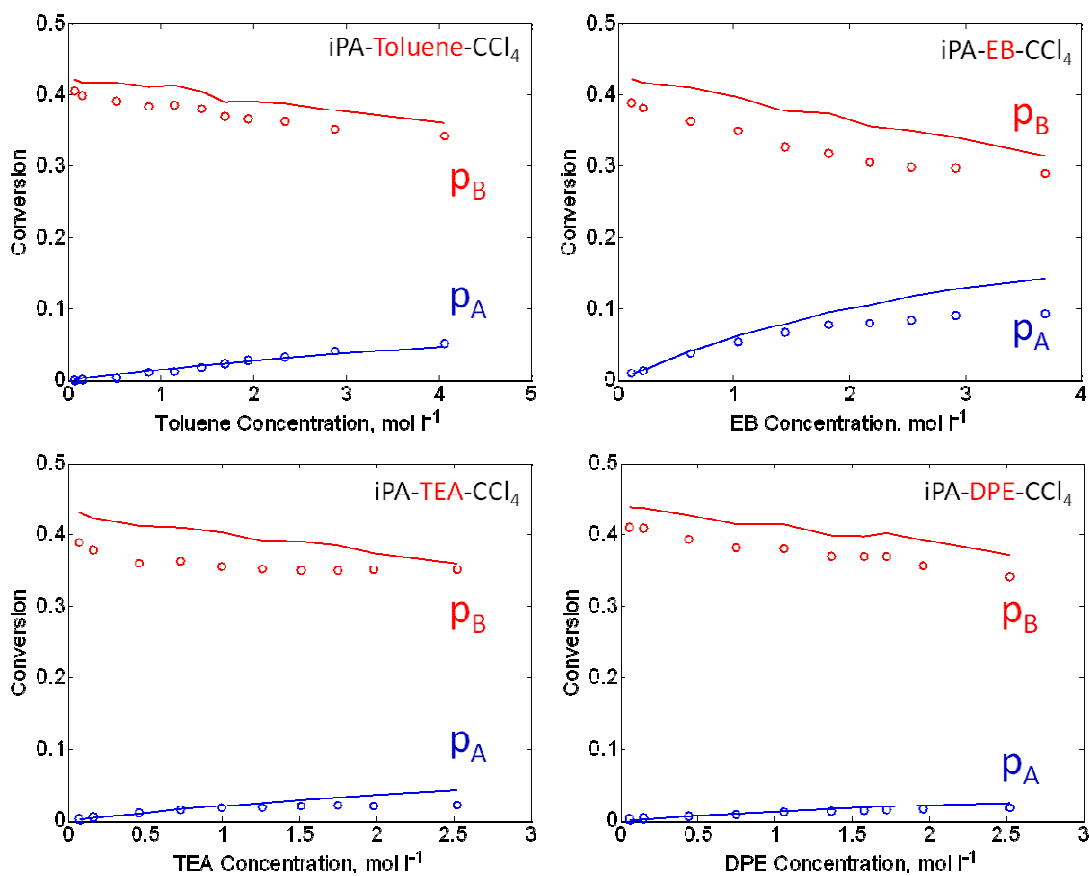
Figure 3.31 Comparison of self association conversion (p_B) with inter-association (p_A) conversion (dotted: conversion obtained by varying K_{BA}, solid line: conversion with fixed average K_{BA})

In this chapter, self- and inter-association of amine and hydroxyl groups were investigated. In the self association analysis of both amine and hydroxyl group, monomer concentration hit the maximum concentration point and showed concentration drop in the less diluted (high concentration region). It seemed that phase transition occurred as more amine or hydroxyl group tool part in the association reaction and it was found that current equilibrium model could not cover the whole range of dilution concentration.

For N-methylaniline (NmA), multiple hydrogen bonding associations were suspected for self association due to the existence of amine electron pair and π bond. Therefore, inter-

associations with amine electron pair and π bond as well as ether and epoxide, which were the existing component in the actual amine-epoxy cure system, were investigated first using simple equilibrium kinetics. The optimized equilibrium constant values for each ternary (NmA-hydrogen bonding acceptor-CCl_4) system could be used to estimate the hydrogen bonding peak in 4-component system (NmA-2 hydrogen bonding acceptors-CCl_4). Finally, self association equilibrium of NmA was investigated and its free monomer behavior could be modeled by Coggeshall and Saier model.

Hydroxyl group had more complex hydrogen bonding equilibrium than amine group had. Spectroscopic evidence indicated that there were three kinds of self-associated peak in isopropanol, β, γ and δ peaks as well as free monomer peak, α. Coggeshall and Saier model could be used to fit the monomer concentration data from the self association of isopropanol-CCl_4 system and their equilibrium constants were well agreed with literature values. In addition to fitting the monomer concentration, in this study, estimation of self associated peaks of β, γ and δ were performed using single equilibrium constant from Flory-Schultz's distribution model. The optimized equilibrium constant was only valid at the diluted concentration range, which was shown in self association of NmA. Inter-associations of hydroxyl group with various hydrogen bonding acceptors were investigated. From the infrared spectra, it was found that isopropanol formed both self association and inter-association in the ternary system with less than 1 wt. % of isopropanol. Therefore, it was assumed that both self- and inter-association species followed Flory-Schultz distribution and the conversion of both associations were obtained by fitting hydrogen bonding peaks in the spectra of ternary systems and finally the inter-association equilibrium constant could be obtained.

CHAPTER 4. EPOXY AMINE CURE

Epoxy resin cure with amine was monitored via conventional FT-IR method, Near IR.

Near IR analysis has been employed for the epoxy amine cure reaction since 1960's

mainly because the overtone and the combinational bands were well separated [1-5, 52-

54, 56-59]. Another reason why near IR method has been utilized was that the essential

vibrational modes of chemical species such as hydroxyl, primary amine and epoxide

groups could be found in near-IR region. However, exact assignment of the peaks around

the target epoxide peak is not possible and the overlapping of the primary amine and the

secondary amine peaks made the analysis inaccurate.

Here in this chapter, near-IR analysis method was performed for Phenylglycidylether and

N-methylaniline to understand the basic epoxy-amine cure chemistry and application of

peak deconvolution method.

Additionally, various side products formed during the cure reaction were verified using

LC/MS analyzer with UV detector.

4.1   In-situ Monitoring of Epoxy Cure with Amine - Near IR Analysis

Stoichiometric amount of phenylglycidylether (PGE) and N-methylaniline (NmA) were mixed at room temperature. Then the sample mixture was contained in between quartz window assembly with 0.1mm thick lead o-ring. Transmission mode was utilized to obtain a series of near-IR spectra. The spectral resolution was 4 cm^{-1} and number of scan for a single spectrum was 32. Figure 4.1 shows a series of spectra during the reaction at 80°C for 15 hours. Peak assignment has been performed from the reported values [1, 52, 55].
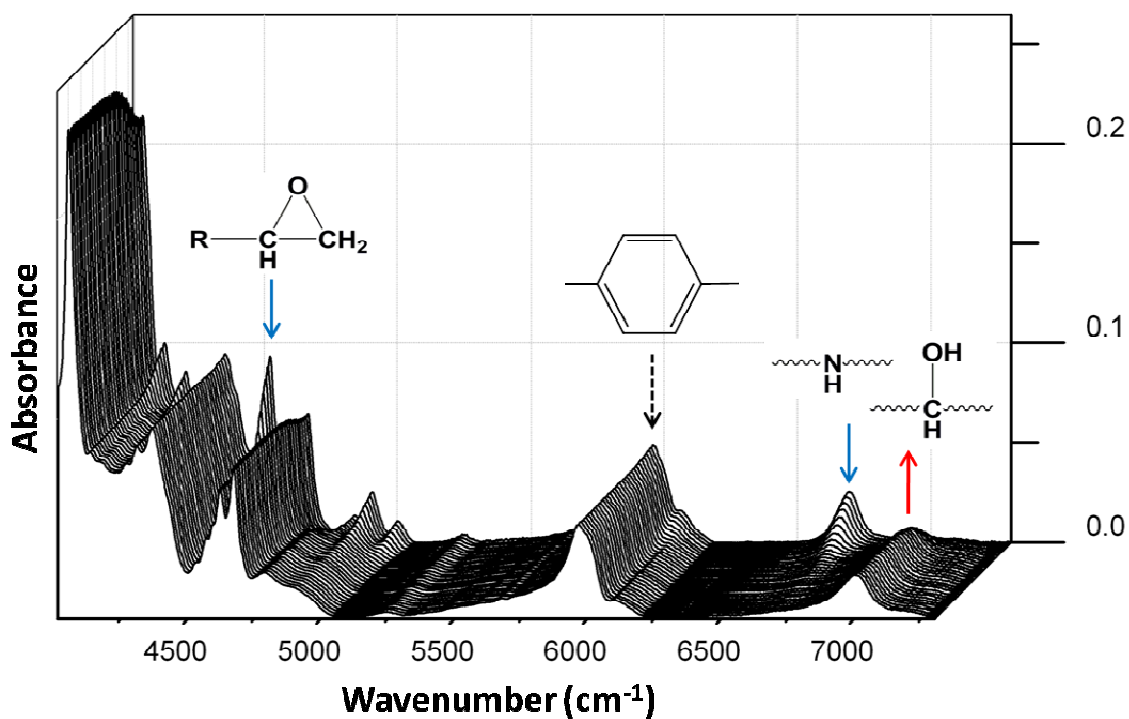
Figure 4.1 Series of Near-IR spectra obtained during the reaction of PGE and NmA at 80°C for 24 hours

Extinction coefficients of epoxide, amine and hydroxyl groups were obtained to convert the absorbance information to concentration profiles. Near-IR spectra of the samples with three different thicknesses (0.1, 0.2, and 0.3mm) were taken and the extinction coefficients were calculated by Beer-Lambert's law shown in equation (4.1) where A=absorbance, ε=extinction coefficient, b=path length, and c= concentration.

$$A = \varepsilon \cdot b \cdot c \qquad (4.1)$$

Figure 4.2 showed the extinction coefficient calculation procedure. Peaks at 4527 cm^{-1}, 6695 cm^{-1} and 7000 cm^{-1} were chosen for epoxide, amine and hydroxyl group peaks respectively. The calculated extinction coefficient values were summarized in table 4.1. Based on the absorbance evolutions from the deconvolution process and the calculated extinction coefficients, concentration profiles of epoxy, amine and hydroxyl group could be obtained from a series of near-IR spectra as shown in figure 4.3. It was found that the epoxide and amine groups were consumed during the reaction and, at the same time, hydroxyl group was developed. However, the collected concentration profile showed unstable development and moreover, mass balance of amine-hydroxyl groups or epoxide-hydroxyl groups were not reasonable. The unstable concentration profile and unreasonable mass balance reflected the fact that the deconvolution process became inaccurate without an aid of exact peak assignment. It was also note that the baseline correction method applied to the near-IR spectra was not good enough to provide accurate spectral information because it was difficult to select the proper wavenumber area where no vibrational band was assigned.
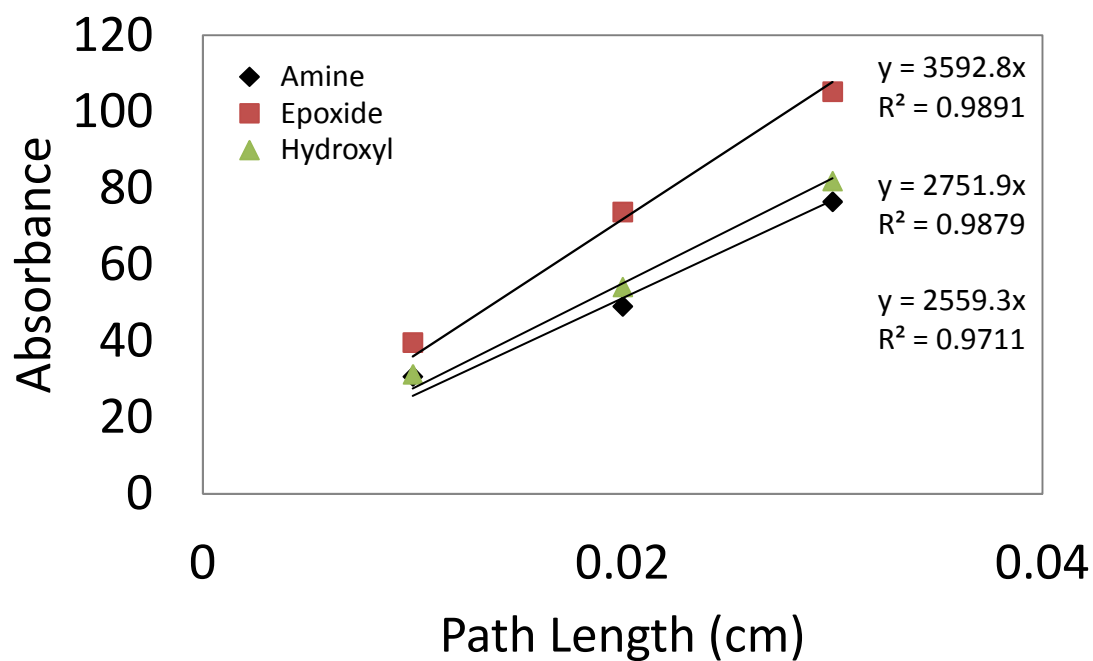
Figure 4.2 Extinction coefficient determination of epoxide, amine and hydroxyl groups in near-IR region
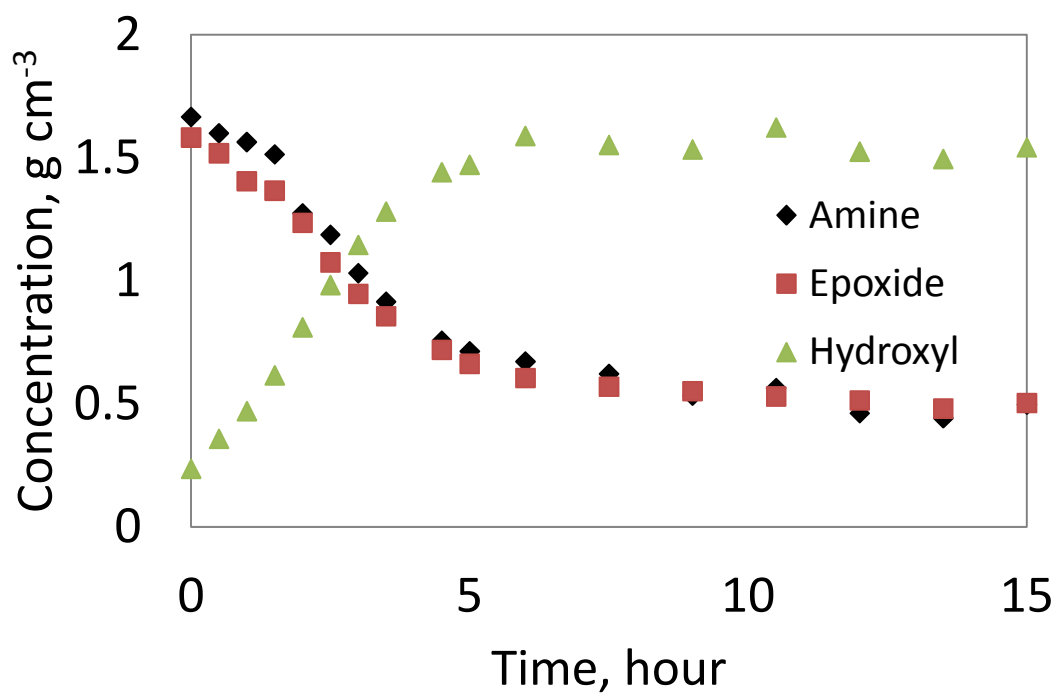
Figure 4.3 Concentration profiles of amine, epoxy and hydroxyl groups obtained from near-IR analysis

Table 4.1 Calculated extinction coefficient values

Species	Extinction coefficient, $cm^2 g^{-1}$
Epoxide	3229.41
Amine	2300.44
Hydroxyl	2473.56

4.2   Byproduct Analysis via LC-MS

It was reported that side reaction of etherification occurs in the amine epoxy cure system with high temeperature and excess epoxide condition. The ether bond is produced with the reaction of epoxide with hydroxyl group and this might affect on the cure mechanism and alter the physical properties of cured material [56-58]. Therefore, it is important to examine the side reaction product in amine-epoxy cure system. LC/MS was used to estimate the chemical structures of reaction intermediates. The same mobile phases with the same gradient schedule was used and the detection wavelength was 292 nm. LC/MS analyses utilized electrospray ionizatiob (ESI) on an Agilent 6320 Ion Trap (Agilent Labs, Santa Clara, CA) mass spectrometer. The capability voltage was set a 2.5kV with a capillary current of approximately 4nA. The nebulizer pressure was set at 5psi and the drying gas flow at 5 liters/min. The drying gas temperature was set as $250^{o}C$ and the vaporizing temeperature at $150^{o}C$.

Input amount of PGE was doubled and the reaction temperature was elevated to $130^{o}C$ and the total cure time was set to 60 hours to expedite the side reactions. Figure 4.4 showed comparison of HPLC results of the sample cured at severe condition with that at mild cure condition. It was found that more than 20 side product peaks were identified as

a result of elavated cure temperature and more input of epoxide species. Major peaks of side products were assigned with the evidence obtained from the LC/MS analysis as well as UV spectrum of the peak obtained from UV detector connected to HPLC. From the sample obtained from PGE+NmA at 70°C for 6 hours, peaks at elution time of 1.2, 5.1 and 8.1 min were assigned to NmA, PGE and a product form of PGE and NmA respectively. 4 peaks were formed after 6 hour cure and this peaks were also found in the sample with extreme condition of cure.
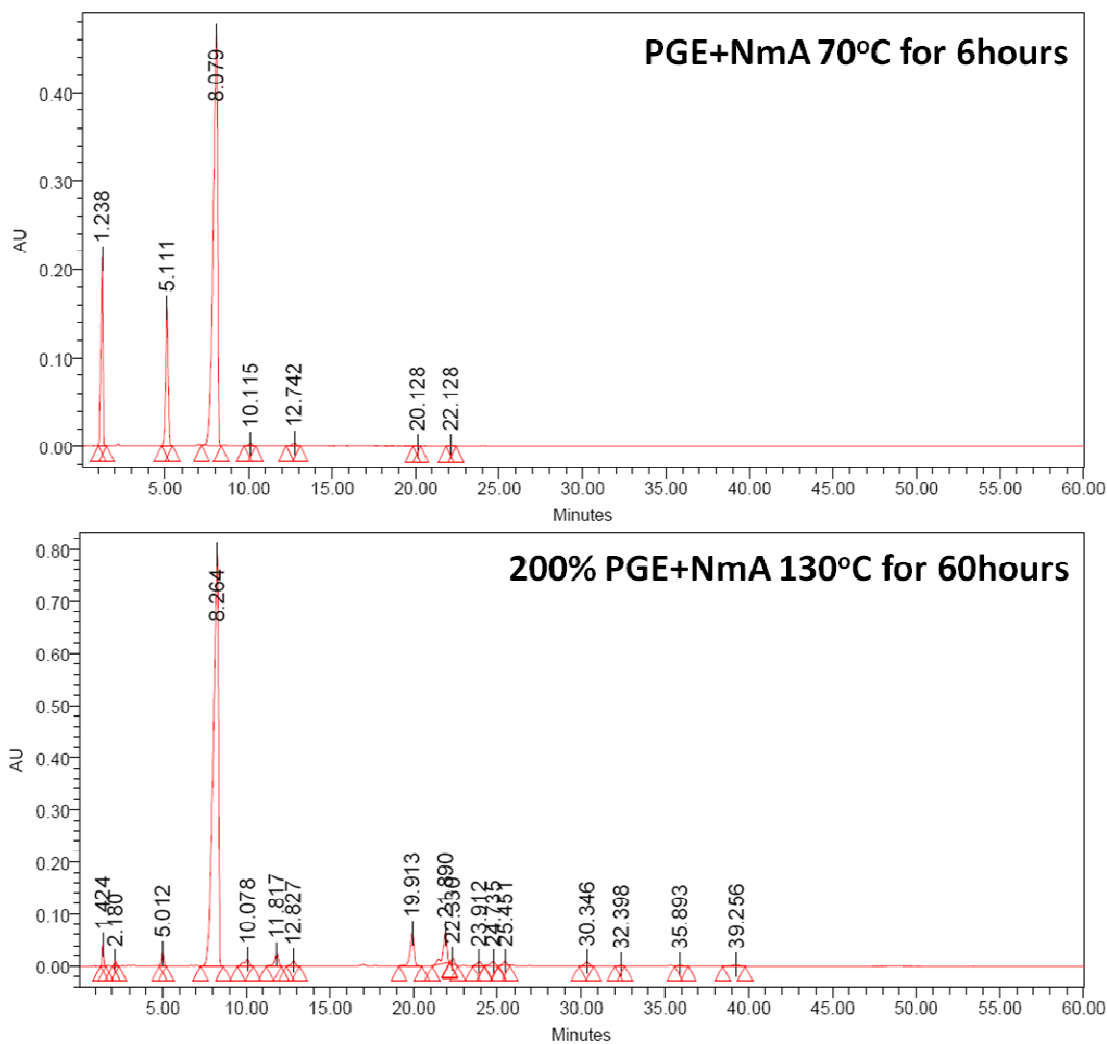
Figure 4.4 Comparison of HPLC results

First of all, concentration profiles of PGE, NmA and a reaction product, named PN, were obtained by applying the extinction coefficient of each material. Figure 4.5 showed that NmA species were completely depeleted in 1.5 hour of cure and concentrations of both PGE and PN were decreased even after the depletion of NmA species, which indicated that side reactions were proceeded after the completion of regular cure reaction. PGE concentration showed more decrease than that of PN, and this revealed that PGE participated in the various side reactions as well as typical etherification reaction. By comparing with PGE concentration, the total amount of side reaction took about 30% as a result of cure at 130°C for 60 hours.
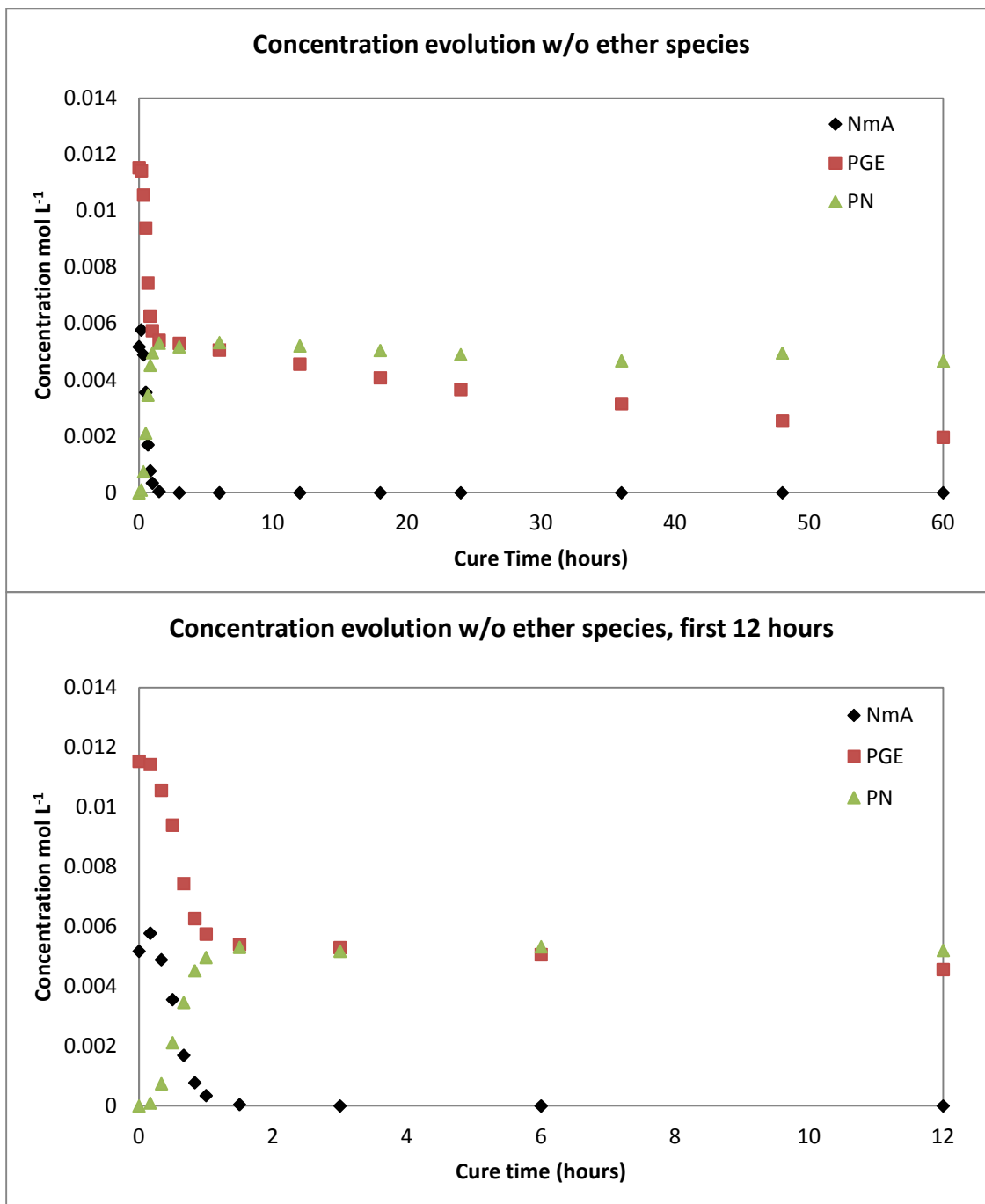
Figure 4.5 Concentration profiles of PGE, NmA and PN for 200% PGE+NmA cured at 130°C for 60 hours set

Figure 4.6 showed peak evoltions of major peaks of side products in order of peak intensity (absorbance). Totally 11 peaks including two ether peaks were investigated here

because the sum of the peak areas of these 11 peaks were 83% of the entire area of side reaction peaks. Among them, peaks at the elution time of 24.7 and 25.5 mins were identified as etherified species. LC/MS analysis indicated that the mass of the peaks were both 408 (407+1), which is the combination of a product, PN (257) and PGE (150). UV spectrum of the peaks also supported that the chemical structure of the peaks were similar to the product form , PN. Moreover, peak evolution behavior revealed that the chemical speices invoved with these peaks were not a result of one step reaction in that the reaction started after 2 hours. These two peaks were indentified as diastereoisomers due to their same mass and clearly showed equal probability of formation from their evolution behavior.

There was another possibility of etherification at 10 minutes of elution time with the mass of 408, but peak evolution behavior showed that the chemical species of the peak was a result of one step reaction. This peak showed the same evolution pattern with PN and from this, it was estimated that this reaction was related with regular NmA-epoxide reaction, not with PGE but with an impurity epoxide species, such as epoxy dimer.

Peak with mass of 272 (elution time of 13.4 minute) also showed one step reaction behavior and UV analysis of the peak showed the same as a product form of PGE-NmA. Therefore, it was postulated that this peak was the product form of NmA with Cresylglycidylether, which was methylated form of PGE whose mass is 164. The chemical structures of postulated epoxy dimer and Cresylglycidylether were shown in figure 4.7.
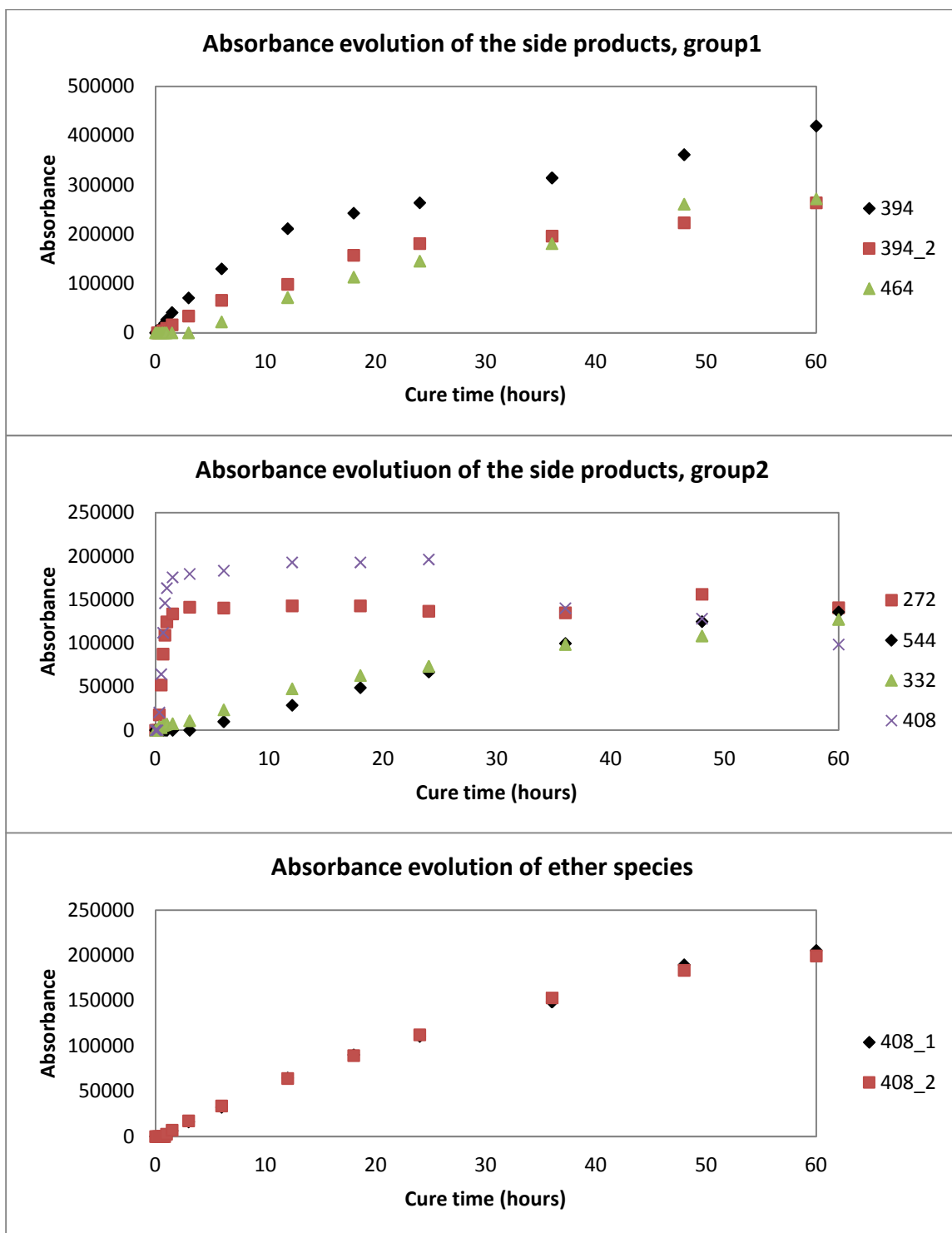
Figure 4.6 Peak evolution of the side products in 200% PGE+NmA cured at 130°C for 60 hours set
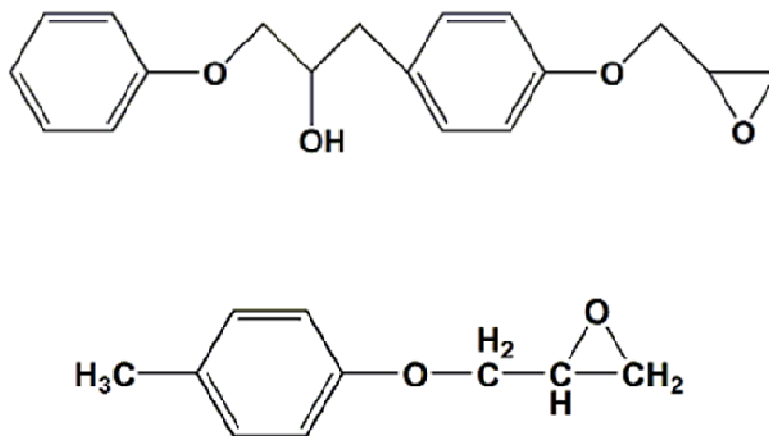
Figure 4.7 Postulated epoxy dimer species (upper) and a chemical structure of Cresylglycidylether (lower)

Peaks at the elution time of 1.5 minutes (mass of 332) and the elution time of 12.5 minutes (mass of 464) showed interesting UV absorption characteristics comparing with that of other peaks. The UV spectra were similar to that of PGE or phenol rather than the amine cured epoxide structure, which had maximum absorption at 217 or 218 nm and 269.2nm. Therefore, mixture of PGE and phenol was cured at 90°C for up to 120 hours to compare the peaks of interest with the cure products from PGE-phenol reaction. More than 10 peaks were formed as a result of 120 hour cure of PGE with phenol at 90°C and most of the peaks showed UV spectrum having maximum at 218.3 and 269.2 nm [supporting information]. Moreover, from HPLC analysis of PGE-phenol reaction, peaks at the elution time of 1.5 min and 12.5 min were found, which strongly supported that the mass of 332 and 464 were from the reaction of epoxide with hydroxyl group, not amine related. The peak evolution trends confirmed that the assigned chemical species were formed via more than two step reactions in that the peak was recognized after 6 hour of cure.
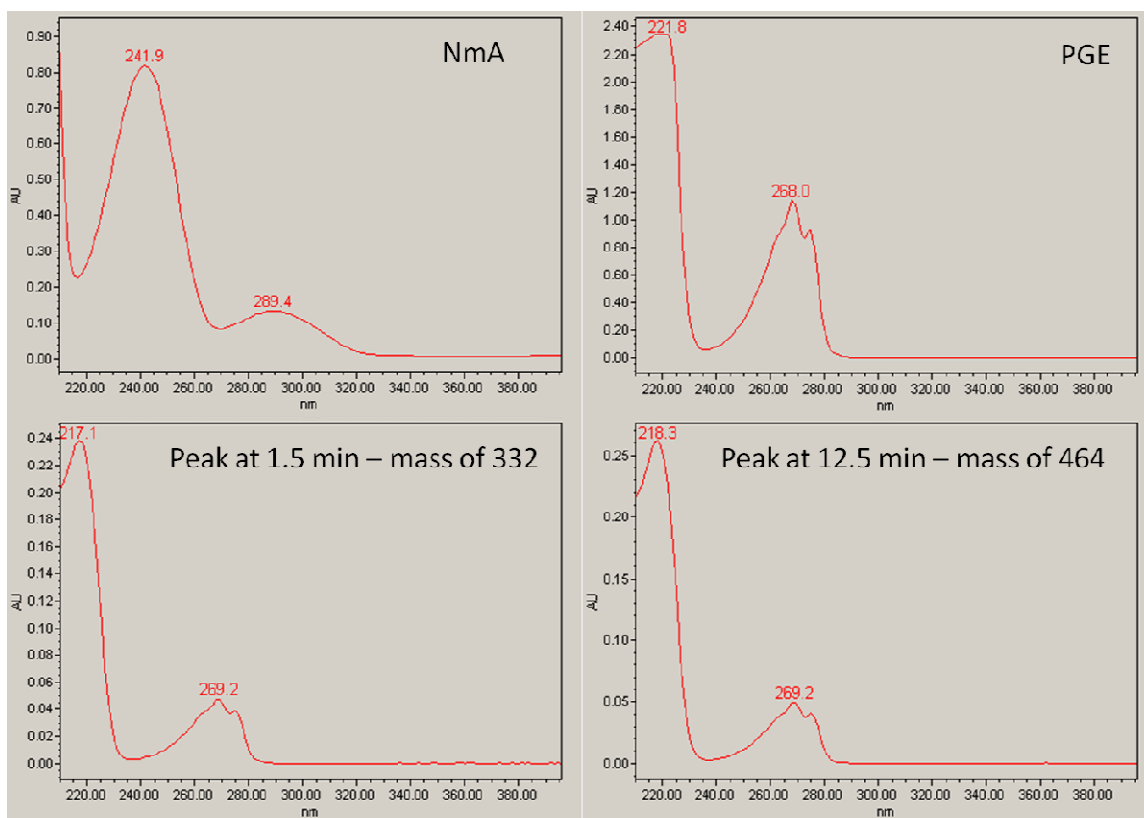
Figure 4.8 UV traces of NmA, PGE, and peaks of interest

It was also noteworthy that two peaks with mass of 394 were evolved during the reaction and it was found that they were tertiary amine forms from the reaction with PGEs with Aniline. PGE-Aniline system has been cured and the same HPLC analysis was done to compare the peaks with the mass of 394 with tertiary amine peaks, which were found at the same elution time in PGE-Aniline system. Figure 4.9 showed the comparison of the UV spectra of the peaks at the elution time of 20 and 22 minutes obtained from both 200PN130C60hr and PA70Ch6hr experimental sets. From the comparison, it was found that the chemical structure of the peaks were same.

The peak with a mass of 544 was verified as an etherified species of tertiary amine species (mass of 394+150) from both mass analysis and UV analysis.

It was concluded that side reactions were much more complex than a simple expected etherification reaction of epoxide and hydroxyl group if little amount of impurities were included in the system.
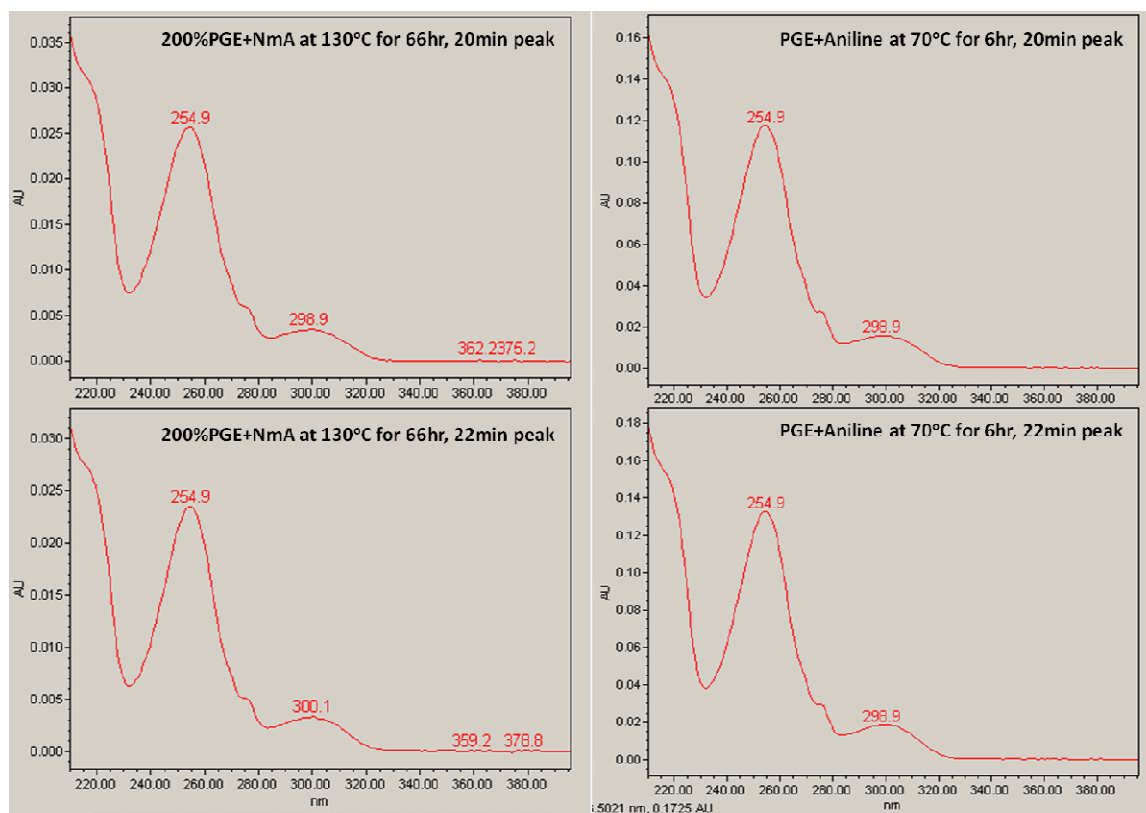
Figure 4.9 Comparison of UV spectra of 20min and 22mion peaks

In this section, various side products were intentionally produced in a condition of higher epoxide concentration and elevated temperature with longer reaction time. Combination of LC-MS and HPLC results revealed that there were more side reactions rather than etherification if there was small amount of impurities in the reaction system. It was also revealed that the hydroxyl group of produced material could be a reaction participant for a further side reaction and this might alter the physical property of the material. Therefore,

it was conclude that setting up the optimal reaction condition is critical to achieve desired

physical properties of cured material in real industrial applications

CHAPTER 5. NON-POLYMERIC SYSTEM ANALYSIS

5.1   HPLC analysis of Non-polymeric Systems

High Performance Liquid Chromatography (HPLC) is the easiest way to obtain the

concentration profile of the reactants and the product by column separation, even though

it is only applicable to the model system that can be dissolved into proper HPLC solvent.

However, this analysis technique can validate the model proposed for describing cure

mechanism excluding any other effect, such as network formation. This will be the

theoretical starting point to model the cure behavior of the desired epoxy cure system.

In this section, Concentration profiles of model epoxy cure system were provided by

HPLC method and proper kinetic modeling for the conventional epoxy-amine cure was

used to fit the concentration profile. Phenylglycidylether (PGE, 1,2-epoxy-3-

phenoxypropane, $C_9H_{10}O_2$, 99%, sigma-Aldrich corp. M.W. 150.18 g/mol) was chosen

for the model epoxy species and N-methylaniline ($C_6H_5NH(CH_3)$, 99%, Sigma Aldrich

corp. M.W. 107.15 g/mol) and Aniline ($C_6H_5NH_2$, 99%, Sigma Aldrich corp. M.W. 93.13

g/mol) were chosen for monoamine and diamine system respectively. PGE was mixed

with NmA or Aniline in the round neck flask with given stoichiometry. The mixture was

cured at various temperature (50, 70, 90, and $110^{o}C$) sets in a heated silicone oil bath

with magnetic stirring. Samples were taken out of the flask reactor at a desired time and

contained in a refrigerator for a quick quenching to prevent additional cure reaction. the

schematic of experimental apparatus is shown in figure 5.1.
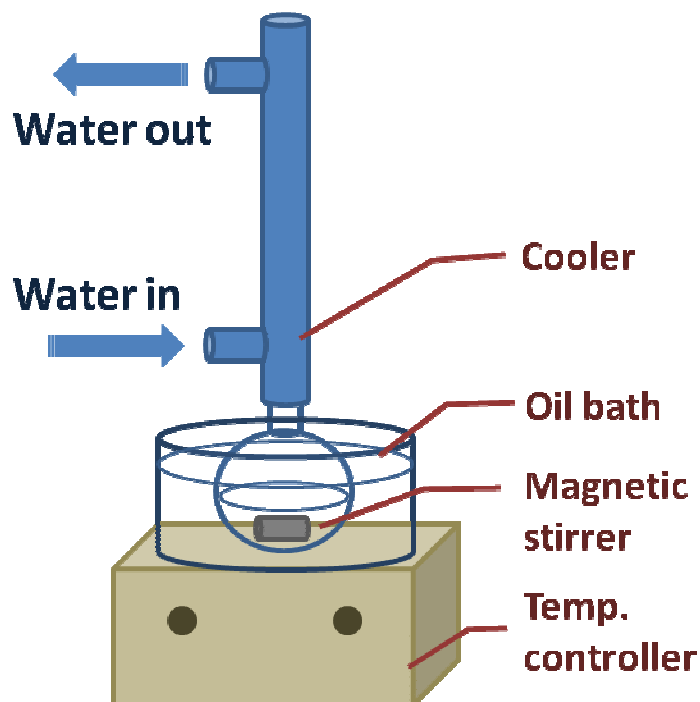
Figure 5.1 Schematic of experimental apparatus for amine-epoxy reaction

For HPLC analysis, samples were diluted with Acetonitrile and the concentration of the

diluted solution was set to 2 mg ml^{-1}.

Concentration profile was also produced via High Performance Liquid Chromatography

(HPLC) analysis of the same system. HPLC (Waters Corp.) with 600 pump, a 717

autosampler, a 996 photodiode array detector, and a 410 differential refractometer was

used to track the intermediates during the curing reaction of PGE with NmA. Sunfire C-

18 reverse phase column (Waters Corp.) was employed. Samples taken out of the reactor

flask were diluted with Acetonitrile (HPLC grade, Sigma Aldrich Corp.) and analyzed via

HPLC. Acetonitrile and water containing 0.1 volumetric % of Formic acid was used as

mobile phases and solvent gradient schedule was applied as shown in table 5.1. Injection

volume was 10 µl and flow rate was 1ml/min. All the spectra was obtained at 254nm of

the wave length and for UV analysis, wave length range of 200-400nm was utilized for

996 detector.

Kientic parameter optimization and solving differential equiations were conducted at the

same time using MatLab subroutines of fminsearch and ode23s solver respectively.

Table 5.1 Gradient schedule for moving phase of HPLC

Time (min)	Volumetric % of Acetonitrile	Volumetric % of water
0	40	60
30	70	30
60	100	0

5.1.1   Phenylglycidylether and Nmehtylaniline System Analysis

The extinction coefficients of the reactant materials were first measured using different

dilution concentrations of the starting materials of PGE and NmA.

For the reactants, extinction coefficients were predetermined from absorbance vs.

concentration plot. Determine the extinction coefficient of the reacted PGE-NmA species,

PN was performed under the assumption of no side reaction, which meant that all the

reactants went to the product. NmA concentration was chosen for the mass balance

because epoxide might participate in the side reaction and the side reaction could

overestimate the actual product concentration of PN. Absorbance vs. $[NmA]_0$-$[NmA]$

plots for various temperature with various stoichiometry were obtained and the extinction

coefficients values were averaged. The averaged value was 3.618×10^9 [Absorbance ·

l/mol].
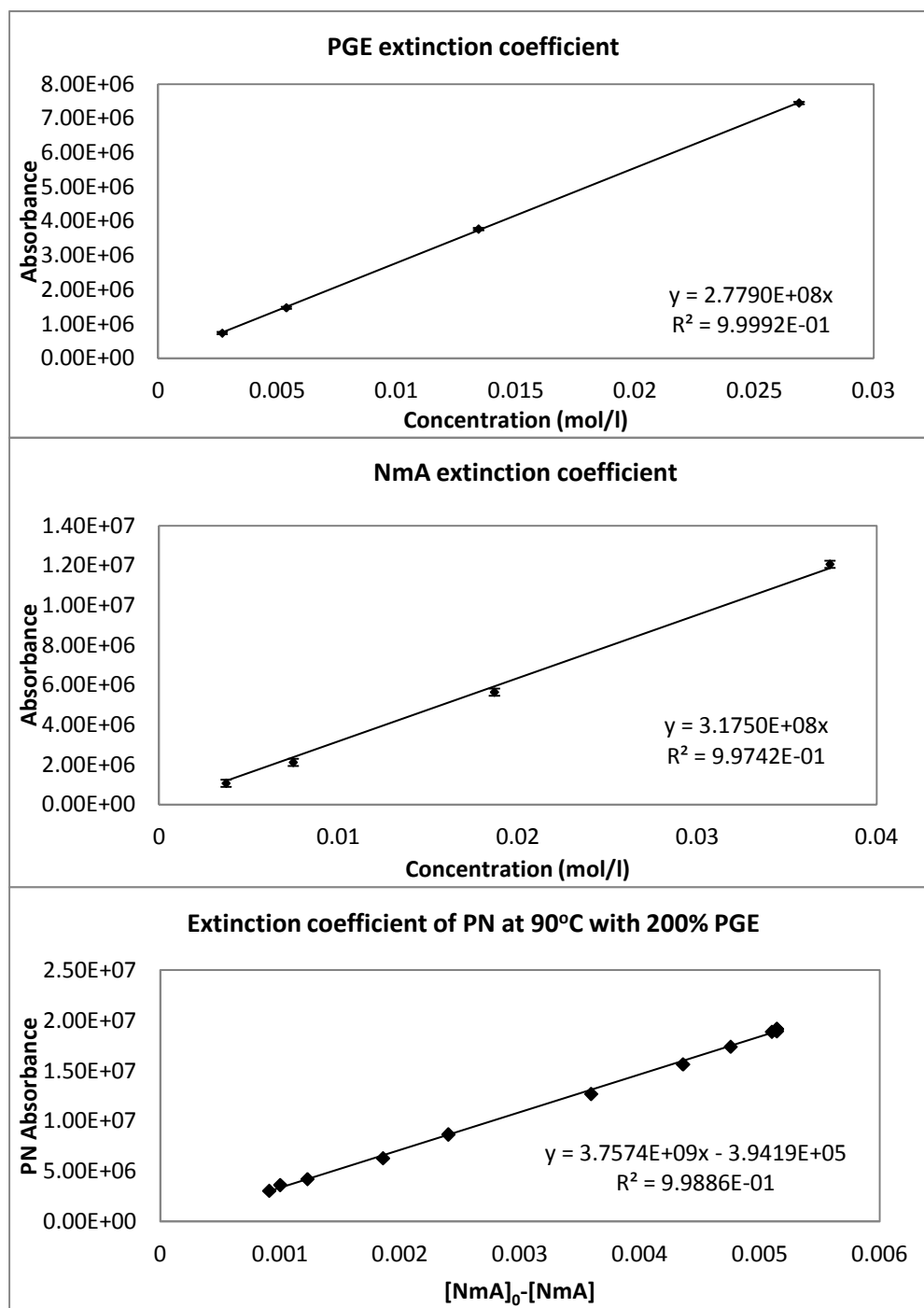
Figure 5.2 Extinction coefficient determination plots of PGE, NmA and PN

Xu et al. proposed termolecular formation mechanism for PGE-NmA system [4]. The proposed model explains well about tertiary amine formation from the complex formation of PGE and NmA. According to Xu's model, termolecular complexes were made by two pathways, one is from an epoxide and a secondary amine, and the other one is from the epoxide and the hydroxyl group. The authors tried to make the rate equation simple by using the overall conversion. In this section, various cure data of PGE with NmA were fitted with Xu's model and the kinetic constants were obtained by solving series of elemental differential equations. Tertiary Amine formation proceeded via two types of complex formations, named C_{PN} and C_{PPN}. C_{PN} was formed by the association of epoxide with secondary amine species and C_{PPN} was formed by the association of epoxide with the hydroxyl group. termolecular complex was finally produced by approaching of secondary amine species to C_{PN} and C_{PPN}. It was found from the kinetic theory that the formation of PN by the complex C_{PN} dominated at the initial stage of cure simply because there was only small amount of hydroxyl group at the initial stage of the reaction. As the reaction proceeded, more amount of hydroxyl group was formed and this made a shift to the second termolecular reaction with C_{PPN}.

Other possible termolecular complex formations were also investigated, i.e. C_{NN} or C_{PNN}, which were the complexes formed by two amine groups or by epoxide-amine-amine respectively. However, they could not successfully describe the concentration evolution of amine, epoxide and PN species.
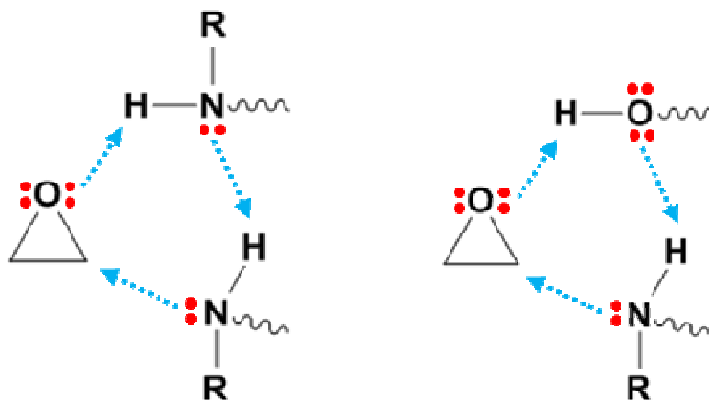
Figure 5.3 Formation scheme of termolecular complexes of C_{PN} (left) and C_{PPN} (right)

$$N + P \overset{K_{PN}}{\Longleftrightarrow} C_{PN} , K_{PN} = {k_{PN}}/{k_{\_PN}} \tag{5.1}$$

$$C_{PN} + N \overset{k_1}{\to} PN + N \tag{5.2}$$

$$PN + P \overset{K_{PPN}}{\Longleftrightarrow} C_{PPN} , K_{PPN} = {k_{PPN}}/{k_{\_PPN}} \tag{5.3}$$

$$C_{PPN} + N \overset{k_2}{\to} PN + PN \tag{5.4}$$
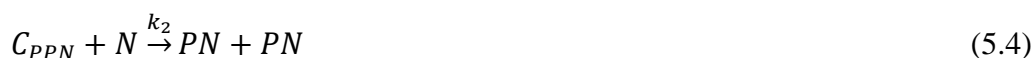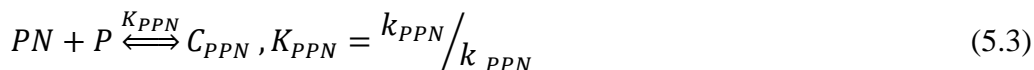
The series of differential equations were listed through equation (5.5) to (5.9)

$$\frac{d[N]}{dt} = -2k_{NN}[N]^2 + 2k_{\_NN}[C_{NN}] + k_1[C_{NN}][N] - k_2[C_{PPN}][N] \tag{5.5}$$

$$\frac{d[P]}{dt} = -k_{PN}[N][P] + k_{\_PN}[C_{PN}] - k_{PPN}[PN][P] + k_{\_PPN}[C_{PPN}] \tag{5.6}$$

$$\frac{d[PN]}{dt} = k_1[C_{PN}][N] - k_{PPN}[PN][P] + k_{\_PPN}[C_{PPN}] + 2k_2[C_{PPN}][N] \tag{5.7}$$

$$\frac{d[C_{PN}]}{dt} = k_{PN}[N][P] - k_{\_PN}[C_{PN}] - k_1[C_{PN}][N] \tag{5.8}$$

$$\frac{d[C_{PPN}]}{dt} = k_{PPN}[PN][P] - k_{\_PPN}[C_{PPN}] - k_2[C_{PPN}][N] \tag{5.9}$$

Kinetic parameters could be obtained for each set of PGE-NmA cure system with various cure temperature and it was possible to calculate the activation energy of tertiary amine formation from those different temperature cure data. 50, 70, 90, and 110°C were chosen as cure temperatures and figure 5.4 showed kinetic analysis of stoichiometric PGE-NmA system with different temperatures. The model showed good optimized fitting for all stoichiometry system and the optimized kinetic constants obtained from different temperature set of experiments were summarized in table 5.2.
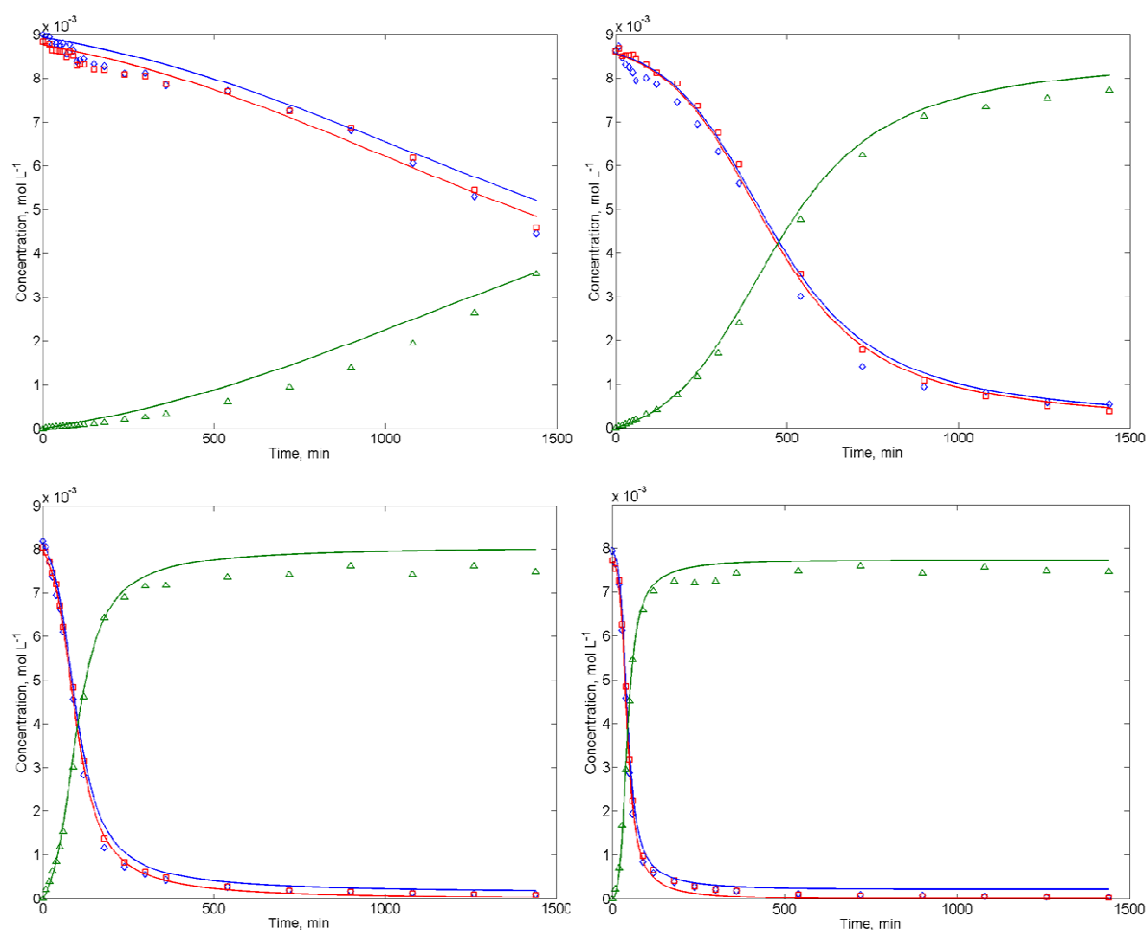
Figure 5.4 Kinetic analysis with equal stoichiometry system cured at various temperatures (amine: square, epoxide: diamond, PN: triangle)

It was also found from table 5.2 that the kinetic constant for the catalytic PN formation

(k_2) is much larger than the kinetic constant for the non-catalytic constant (k_1), which

indicated that the non-catalytic reaction is only significant at the initial stage of cure and

the overall reaction rate was determined by catalytic reaction.

Table 5.2 Summary of kinetic parameters obtained from different set of experiments.

Temp	k_{PN}	$k_{\_PN}$	k_1	k_{PPN}	$k_{\_PPN}$	k_2
	[l/mol*sec]	[1/sec]	[l/mol*sec]	[l/mol*sec]	[1/sec]	[l/mol*sec]
50°C	0.0012	0.00008	0.0018	0.0052	0.0017	4.733
70°C	0.0011	0.00003	0.0169	0.0182	0.0220	10.928
90°C	0.0048	0.00002	0.1905	0.0794	0.1051	48.246
110°C	0.0033	0.00004	1.1231	0.3607	0.4651	101.731

The activation energies of PN formation could be obtained from Arrhenius plot of ln(k)

vs.1/T as shown in figure 5.5. From the logarithmic form of Arrhenius equation, $\ln(k) =$

$\ln(A) - E_a/RT$, where, A is pre-exponetial factor and R is gas constant, activation

energy (E_a) of the kinetic constant (k) could be obtained by taking slope of the equation.

The values of k_1 and k_2 were 112.189 and 54.946 KJ/mol respectively. Xu et al.

calculated kinetic constants of PN formation from PGE-NmA system via Near Infrared

analysis [9]. The authors reported the activation energies from non catalytic and catalytic

reactions were 69.30 and 55.03 KJ/mol respectively. The activation energy from catalytic

reaction (k_2) had a reasonable agreement with the reported value but that from k_1 showed

slight deviation from the reported value.
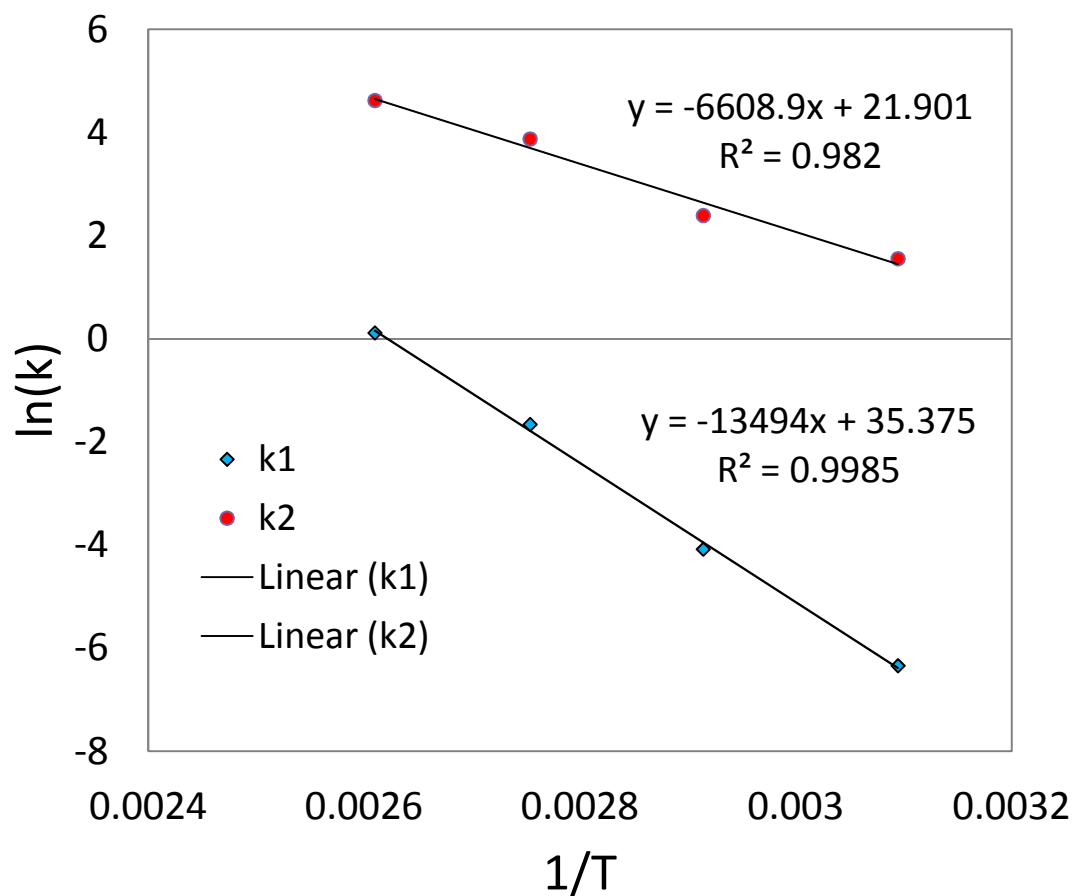
Figure 5.5 Activation energy calculation of PN formation

5.1.2 Phenylglycidylether and Aniline System Analysis

Extinction coefficients of the reactant as well as products were obtained experimentally by putting a single reactant in a mobile phase. For the starting material, Aniline, samples with different concentrations were analyzed via HPLC. Based on the extinction coefficients of the starting materials, the concentration profiles were made and from the mass balance equation, extinction coefficients of Secondary and Tertiary Amine species were estimated.

For Secondary Amine, Concentration data of Aniline was chosen at the time span when Secondary Amine species had their maximum absorbance under the assumption that majority of Aniline was converted to Secondary Amine.

For Tertiary Amine, concentration profiles of Secondary Amine and PGE were both utilized at relatively lower temperature of $80^{o}C$, where the side reactions such as etherification and homopolymerization were negligible. Obtained values from different experimental sets were averaged. Figure 5.6 showed the extinction coefficient determination plots of reaction participants and all the extinction coefficients showed over 99% of R square values.
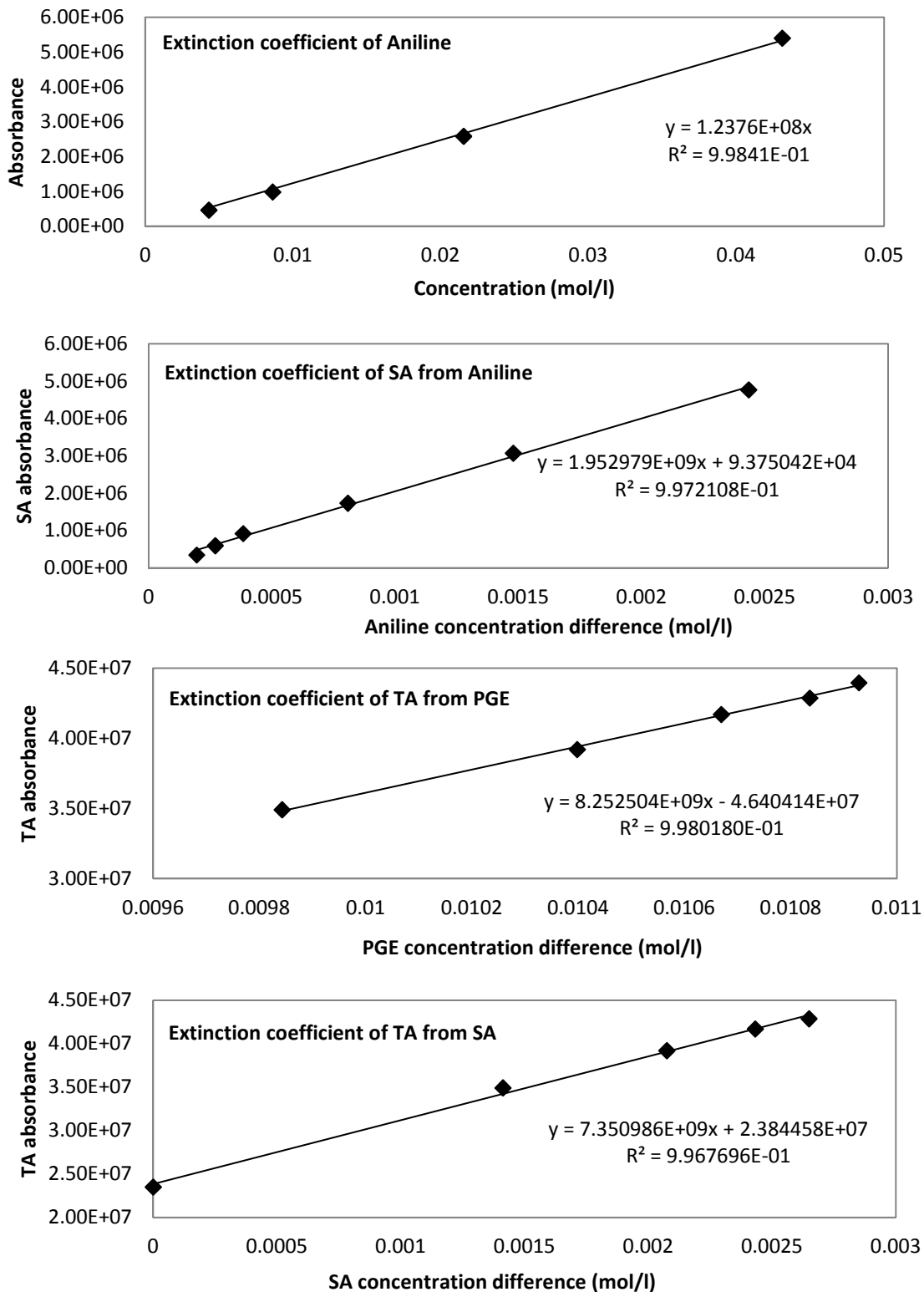
Figure 5.6 Extinction coefficient determinations for Aniline, Secondary Amine and Tertiary Amine

Termolecular model was also employed for PGE-Aniline system. This model contains to

complex, C_{PA} and C_{SAP} which show the autocatalytic behavior. In this model, there are

two pathways to form secondary amine and tertiary amine species each, one from C_{PA}

complex and the other from C_{SAP}

$$A + P \overset{K_{PA}}{\Longleftrightarrow} C_{PA} \,, K_{PA} = {k_{PA}}/{k_{-PA}} \tag{5.10}$$

$$C_{PA} + A \overset{k_1}{\rightarrow} SA + A \tag{5.11}$$

$$C_{PA} + SA \overset{k_2}{\rightarrow} TA + A \tag{5.12}$$

$$SA + P \overset{K_{SAP}}{\Longleftrightarrow} C_{SAP} \,, K_{SAP} = {k_{SAP}}/{k_{-SAP}} \tag{5.13}$$

$$C_{SAP} + A \overset{k_3}{\rightarrow} SA + SA \tag{5.14}$$

$$C_{SAP} + A \overset{k_4}{\rightarrow} TA + SA \tag{5.15}$$

Termolecular model could successfully fit the cure data of PGE-Aniline system. Xu et al.

also proposed a model for PGE-Aniline system [4]. They also proposed that termolecular

complexes were introduced to produce secondary amines and tertiary amines in the

model. The major difference of the model in this research from Xu's model was that the

hydroxyl groups were separated into secondary and tertiary amines in this analysis.

Another difference was that the equilibrium state of non-reactive complexes were not

considered here. However, the model could successfully fit the cure data of PGE-Aniline

system. Figure 5.7 showed the model fitting result of the proposed termolecular

mechanism. Comparing with the fitting result of Xu's model, this model showed a better

estimation on the secondary amine evolution, but both models showed poor estimation of product concentrations at the later stage of cure.

The rate constant k_1 and k_3 were related with Secondary Amine formation and k_2, and k_4 were related with Tertiary Amine formation. The activation energies were 67.4, 50.9, 45.4, and 46.4 KJ/mol respectively. Among them, k_2 indicated that Tertiary Amine was formed from the complex composed of Amine and Epoxide. However, at the later stage of cure, when Tertiary Amine was formed, Complex of SA and Aniline is more prominent than the complex of PGE and Aniline. Therefore, the reaction was minor comparing with another Tertiary Amine reaction (k_4).

From the literature, the activation energy of the Secondary Amine formation catalyzed by Primary Amine was 72.3 KJ/mol and the activation energy values of Secondary Amine formation catalyzed by Hydroxyl group and Tertiary Amine formation by Hydroxyl group were 50.4 and 52.2 KJ/mol, which proved that the kinetic analysis was reasonable [4].

The substitution effect (ρ), which is defined as a ratio of Tertiary amine formation to Secondary Amine formation ($\rho = k_4/k_3$) was 0.36 at $90^{o}C$, which was close to the value reported for the same system at the same temperature, 0.38 [5].
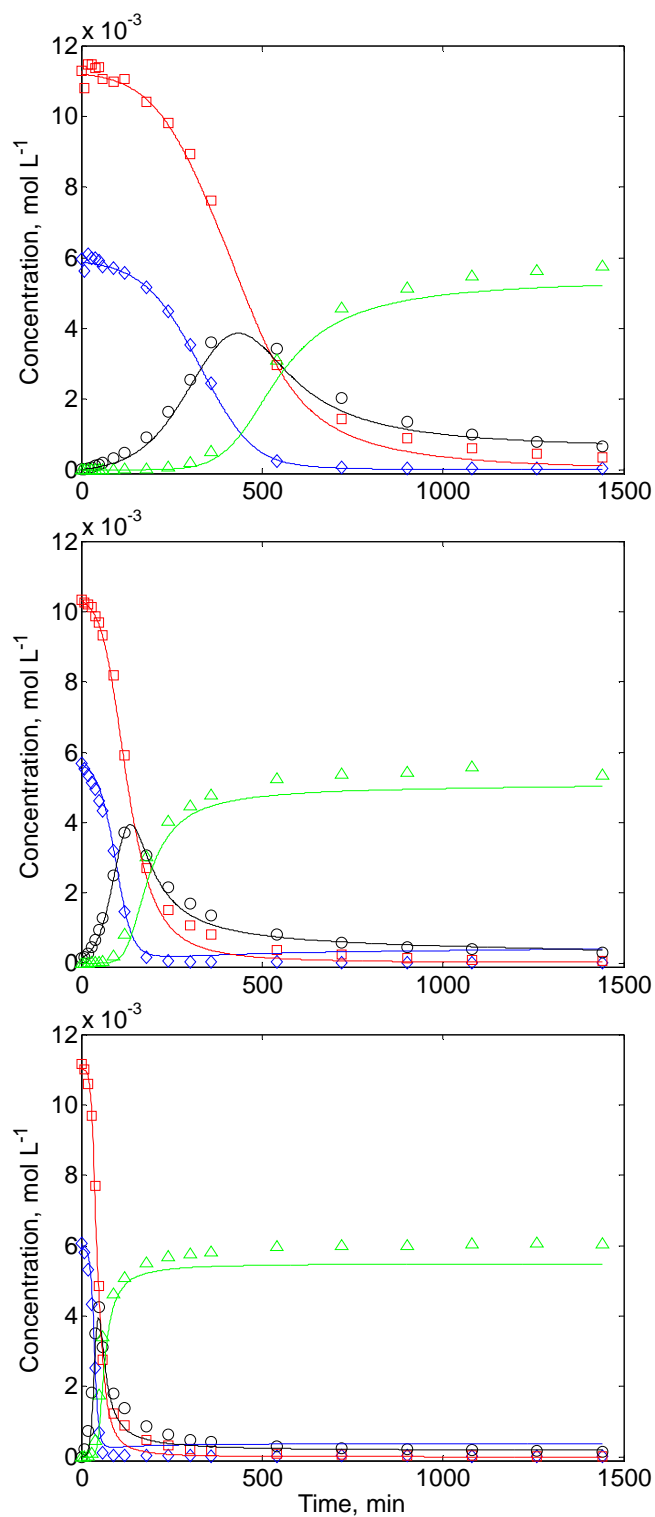
Figure 5.7 Model fitting of PGE-Aniline system at 70°C (upper), 90°C (middle) and 110°C (lower), (PGE: square, aniline: diamond, SA: circle, and TA: triangle)
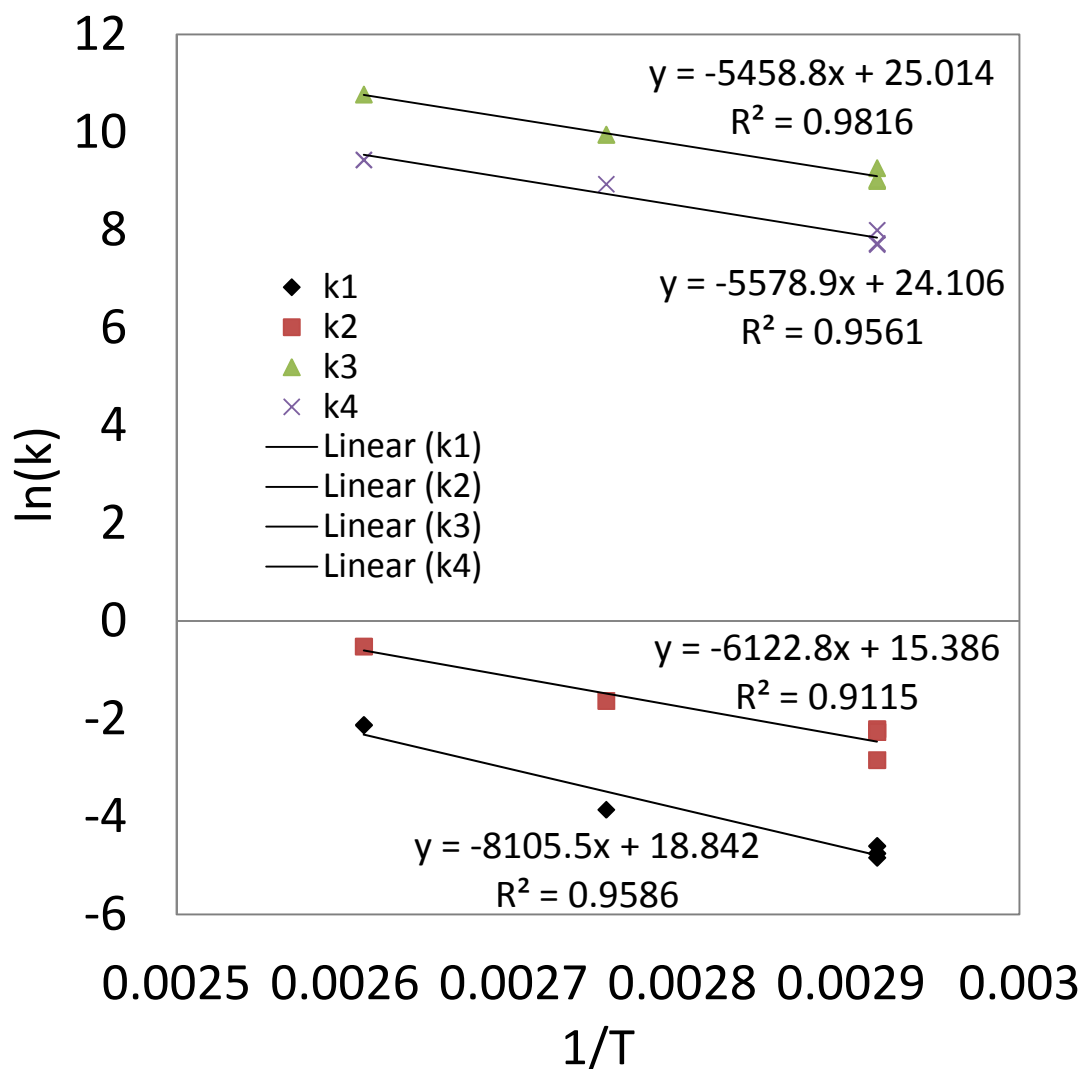
Figure 5.8 Activation energy calculation for Secondary Amine and Tertiary Amine formation

5.2   FT-IR Analysis of Phenylglycidylether and N-methylaniline system

In section 5.1, HPLC analysis of phenylglycidylehther with N-methylaniline and aniline system was conducted and their kinetic analyses were successfully done. The kinetic information obtained from HPLC analysis would be used as a validation standard for the

kinetic information from quantitative FT-IR methodology. The overall FT-IR spectra for the cure of PGE with NmA at 80°C were shown in figure 5.9. In order to quantitatively analyze the spectra, the analysis will be processed via three different regions, i.e. 3245 to 3670 cm^{-1}, 770 to 900 cm^{-1}, and 1250 to 1450 cm^{-1} respectively in the following sections.
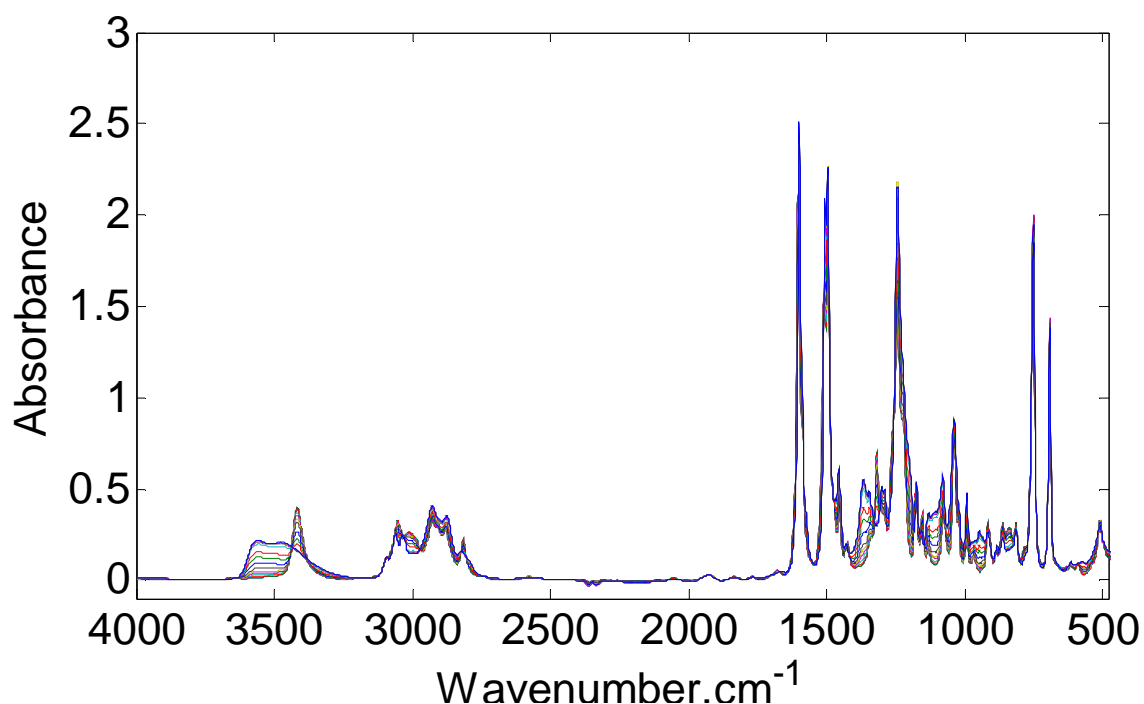
Figure 5.9 FT-IR spectra of PGE-NmA isothermal cure at 80°C with baseline correction via the detrending method. Lines are at the following times: 0, 30, 60, 90, 120, 150, 180, 240, 300, 360, 450, 540, 720, 900, 1080, 1260, and 1440 mins

To determine the extinction coefficients of the peaks of interest, FT-IR spectra of single materials were taken with path lengths of 3, and 5 microns at temperature condition of 80°C, which was the reaction temperature of amine-epoxy system. Elevated temperature condition was required since the FT-IR spectral line shape was significantly affected by

temperature. Aniline and NmA were selected to obtain the extinction coefficients of Amine group and PGE was chosen to obtain the extinction coefficient of epoxide. Subsequently, the results from the individual spectral regions will be unified in Section 5.2.2 and the FT-IR analysis of the PGE with NmA reaction will be compared to the HPLC results given in Section 5.1.

5.2.1 Amine and Hydroxyl Group Analysis

The evolution of FT-IR spectral area of 3200-3700 cm^{-1} during the reaction of PEG with NmA at $80^{o}C$ is shown in figure 5.10. During the reaction there is the decrease of a well defined peak centered at 3417 cm^{-1} and the growth of broad peak between 3300 and 3600 cm^{-1}. Based upon the DFT analysis, it was confirmed that both amine and hydroxyl groups evolve in the 3245 to 3670 cm^{-1} region of the FT-IR spectra and by examining the spectral line evolution, the peak at 3414 cm^{-1} was assigned to the amine N-H stretch because the peak showed continuous decrease during the reaction.

Based upon the FT-IR analysis of N-methylaniline self association presented in Chapter 3, the 3414 cm^{-1} peak was composed of multiple inter hydrogen bonding peaks. For ease of peak fitting, the multiple hydrogen bonding peaks were tied with one asymmetric peak with an asymmetric factor of 0.0124, where the parameter 'a' was constrained in range between 0.012 to 0.013 in fitting of the neat N-methylaniline peak. Using neat NmA specimens with 3μm and 5 μm path lengths, the extinction coefficient of the 3414 cm^{-1} amine peak was determined to be $1.09711x10^{5}cm^{2}/g$.
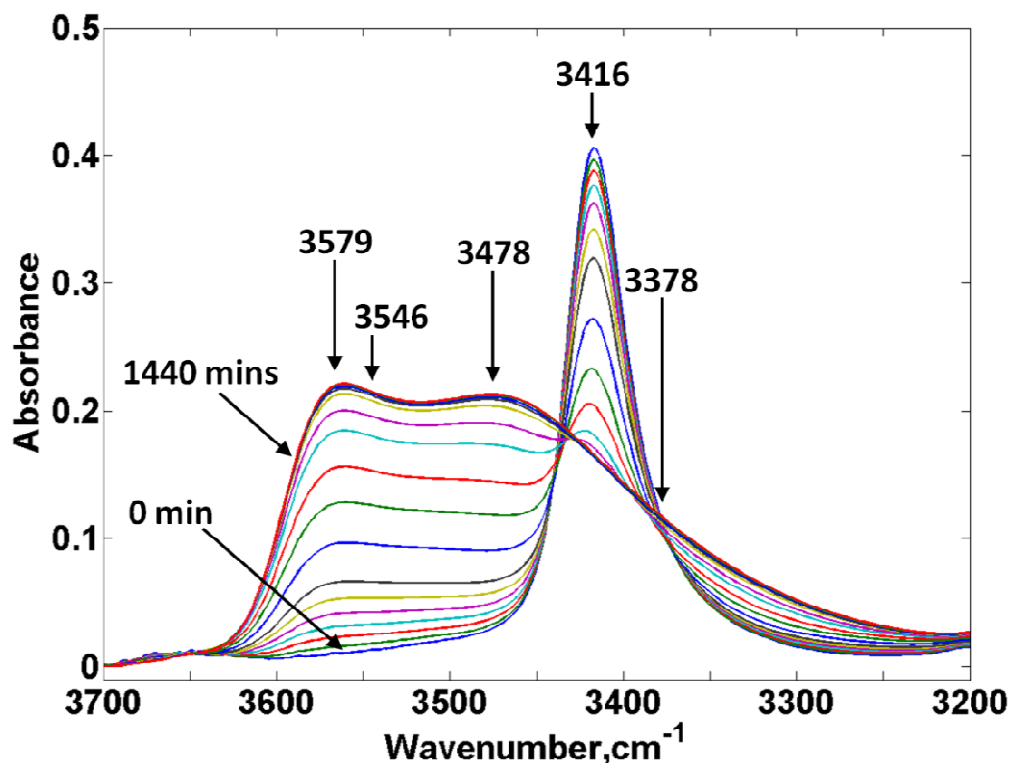
Figure 5.10 FT-IR spectra of 1:1 PGE-NmA curing reaction at $80^{o}C$ where the spectrums are for cure times from 0 to 24 hours every 30 mins

Although DFT calculations indicate only one hydroxyl peak in this spectral region, the growing broad peak clearly indicated that multiple peaks were required to fit the data. Deconvolution of the experimental FT-IR data was performed by assuming the presence of 4 hydroxyl peaks in this region, where optimization determined the location of the 4 hydroxyl peaks at 3579, 3546, 3478, and 3378 cm^{-1} in addition to the amine peak that was fixed at 3416 cm^{-1}. The quantitative deconvolution of the FT-IR spectra in the 3245 to 3670 cm^{-1} spectral region is shown in figure 5.11 for the selected reaction time, where the individual line shape parameters (as well as the bounds on these parameters used in the fitting algorithm) are given in Table 5.3. If less than 4 hydroxyl peaks were used a poor fit of the FT-IR data resulted, and using 5 or more hydroxyl peaks did not provide

significant improvement in fitting the FT-IR data. The existence of multiple hydroxyl group peaks was suspected as associations of hydroxyl groups with various hydrogen bonding acceptors in the system as investigated in isopropanol association study in Chapter 3. However, unlike amine peak in NmA, it was not possible to express multiple associated peaks in one asymmetric factor because the vibrational bands of associated hydroxyl group were much broader and stronger than that of amine group.
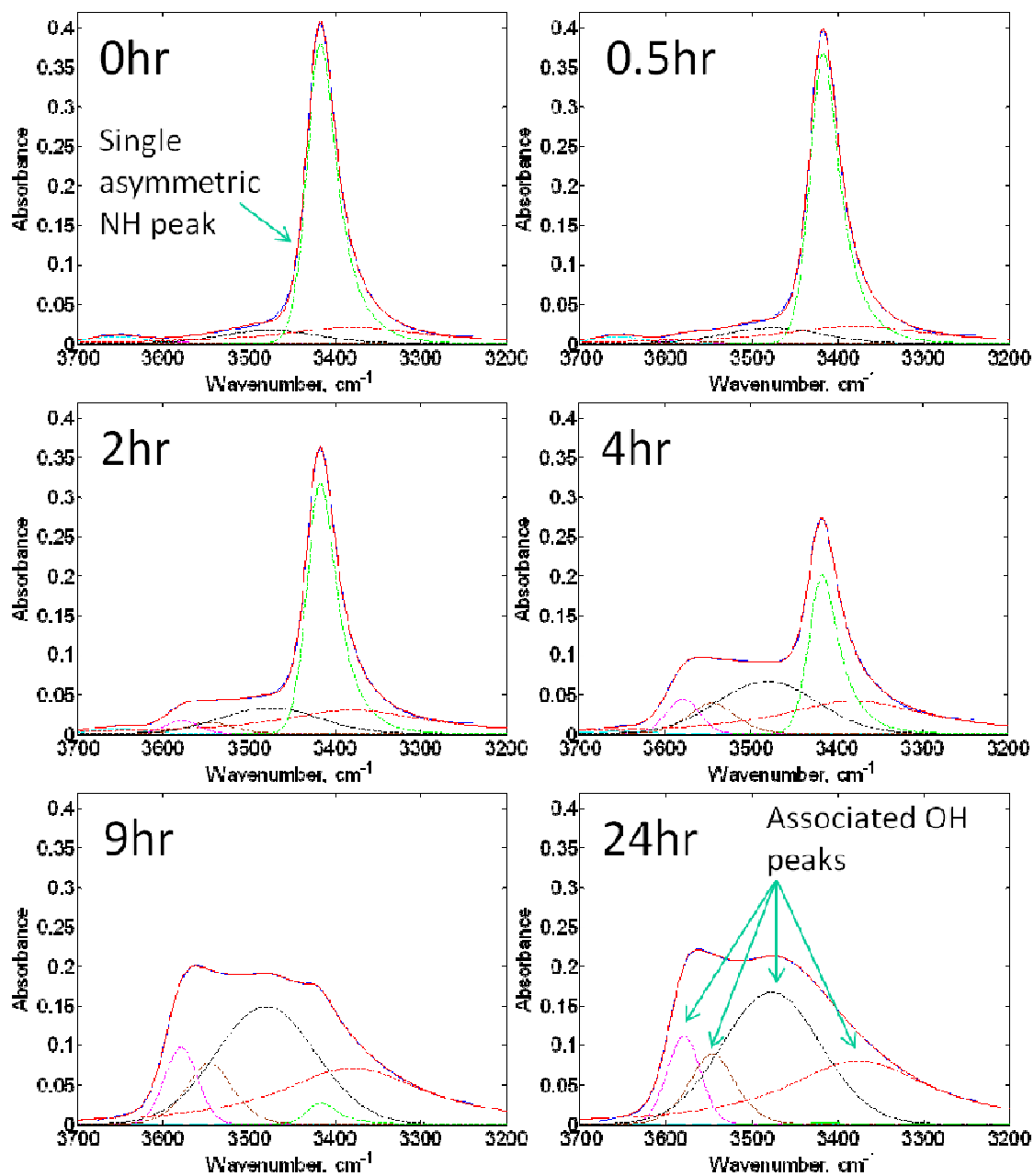
Figure 5.11 Spectral deconvolution of 3100-3700 cm^{-1} area during cure of PGE with NmA

Table 5.3 Constraints on amines and hydroxyl groups

	OH at 3579cm^{-1} Value(LB-UB) [†]	OH at 3546cm^{-1} Value(LB-UB)	OH at 3478cm^{-1} Value(LB-UB)	OH at 3378cm^{-1} Value(LB-UB)	NH at 3416cm^{-1} Value(LB-UB)
H	0.14(0-2.5)	0.16(0-2.5)	0.16(0-2.5)	0.1(0-1)	0.4(0-1)
m	0.012(0-0.1)	0.49(0-0.5)	0.01(0-0.1)	0.9(0.7-1)	0.84(0.7-0.9)
x_0	3579(3575-3582)	3547(3540-3550)	3478(3470-3490)	3378(3370-3380)	3414(3414-3420)
w	45(44-60)	65(60-70)	138(130-140)	210(200-220)	42(40-44)
A	N/A	N/A	N/A	N/A	0.0124(0.012-0.013)

†LB: lower bounds, UB:upper bounds

Figure 5.12 shows normalized line shapes of the deconvoluted peaks divided by each peak area at 3100 -3700 cm^{-1}. All the deconvoluted peaks generally showed a good line shape consistency through the reaction. However, there were slight line shape changes during the reaction for the peaks at 3478 and 3378 cm^{-1}, and their shape changes seem to have influence on their neighboring peaks. Therefore, it was necessary to narrow parameter set that governs the entire cure spectra. Obtained parameters for each spectrum were averaged with weighted mean method shown in equation (5.16), and used as initial guesses for the line fitting of the entire spectra set.

$$\bar{x}_w = \frac{\sum_{i=1}^{N} w_i x_i}{\sum_{i=1}^{N} w_i} \qquad (5.16)$$

Narrowing the constraints could be performed using weighted standard deviation method shown in equation (5.17),

$$SD_w = \sqrt{\frac{\sum_{i=1}^{N} w_i(x_i - \bar{x}_w)^2}{\frac{(N'-1)\sum_{i=1}^{N} w_i}{N'}}} \qquad (5.17)$$

Where, N' and $\bar{x}_w$ were number of non-zero weight and weighted mean of the observations respectively.

Figure 5.13 showed fitting results of the series of spectra with the finalized parameter sets and its error evaluation.
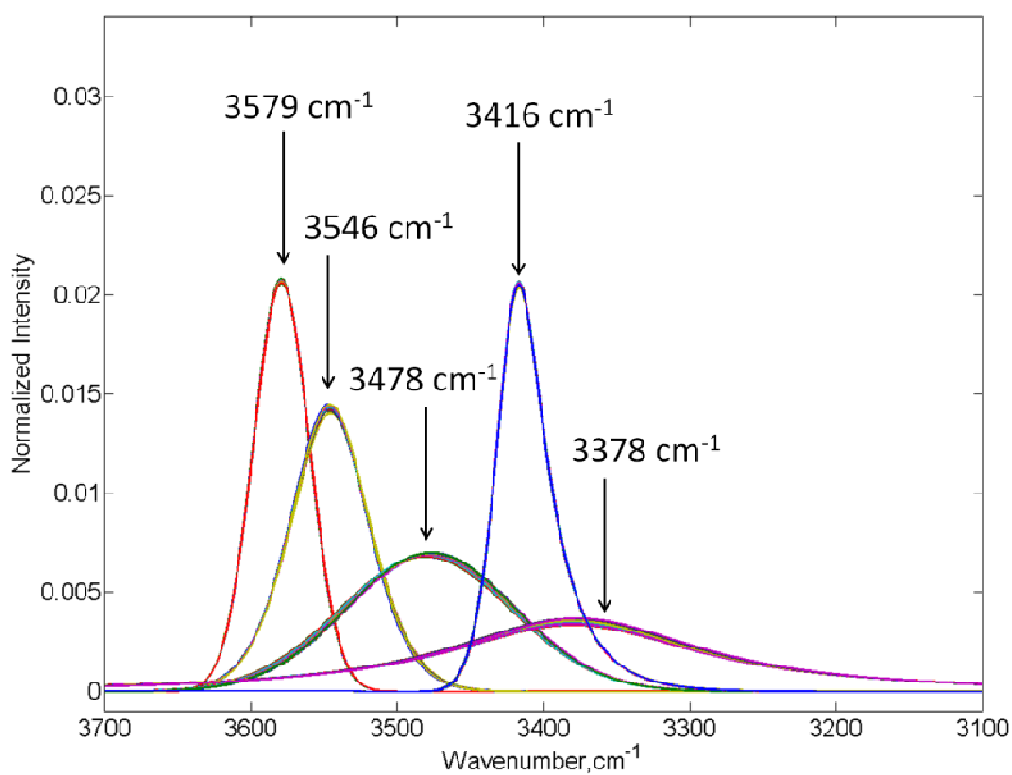
Figure 5.12 Peak line shapes for Hydroxyl groups and Amine group; (a) deconvoluted peak line shape evolution, and (b) normalized peak line shapes divided by peak area of each peak line shape
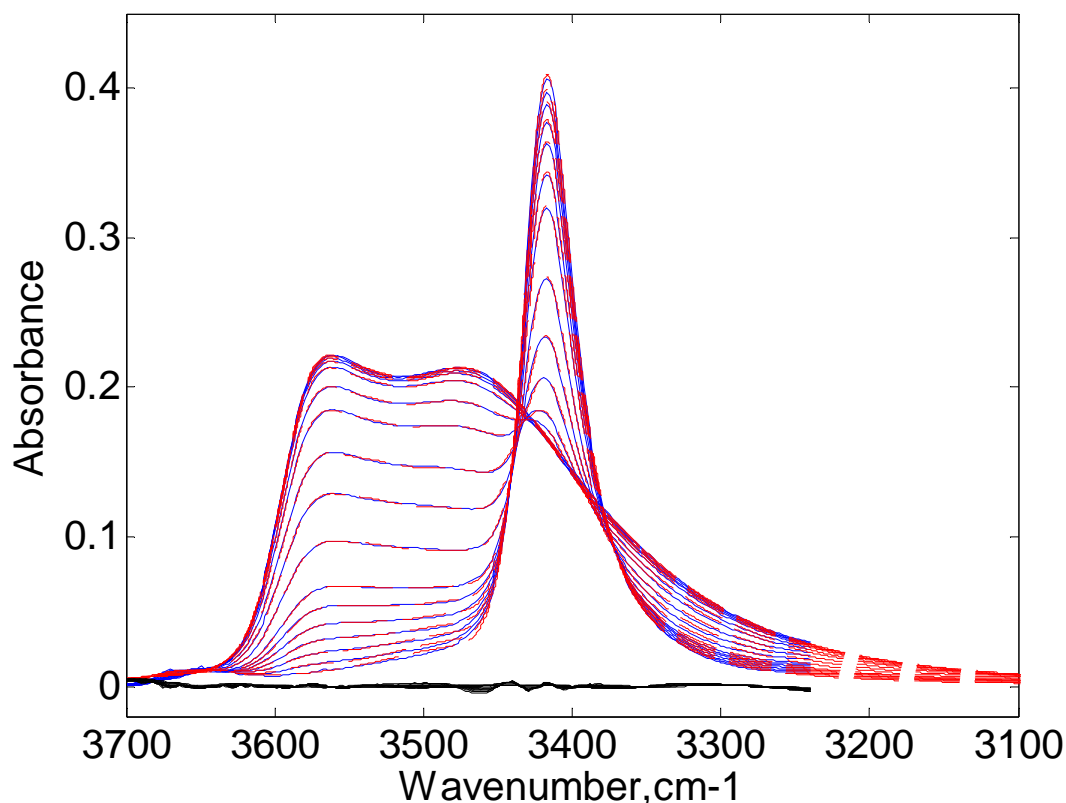
Figure 5.13 Comparison of real IR spectra (solid blue) with synthesized peak line shapes from deconvoluted peaks (red dot) and their deviation (at the bottom)

To assess the viability of the hydrogen bonding as the mechanistic origin of the broad peak between 3100 to 3600 cm^{-1}, 1.9 wt% to 7.6 wt% of the fully cured PGE with NmA reaction mixture (i.e. cured for 24 hours at 80°C sample) was diluted in CCl$_4$, placed in a KBr cell for liquid purchased form New Era Enterprise Inc., and the FT-IR spectra was measured. A comparison of IR spectra obtained from diluted samples with neat resin product is shown in Figure 5.14, where the spectral line at 3600 cm^{-1} significantly sharpened with addition of solvent. Peaks at 3600 cm^{-1} were proportional to the solution concentration at high dilution range, indicating that the peaks were α and β peaks of free OH vibrations [24, 47, 59]. α and β denoted a vibrational peak of OH group in a free

monomer and a free OH end group whose oxygen molecule was bound by another proton in an association. In contrast, the relative contribution of the broad band decreased significantly with increasing dilution, which indicated that those peaks were the hydrogen bonding associated hydroxyl groups.
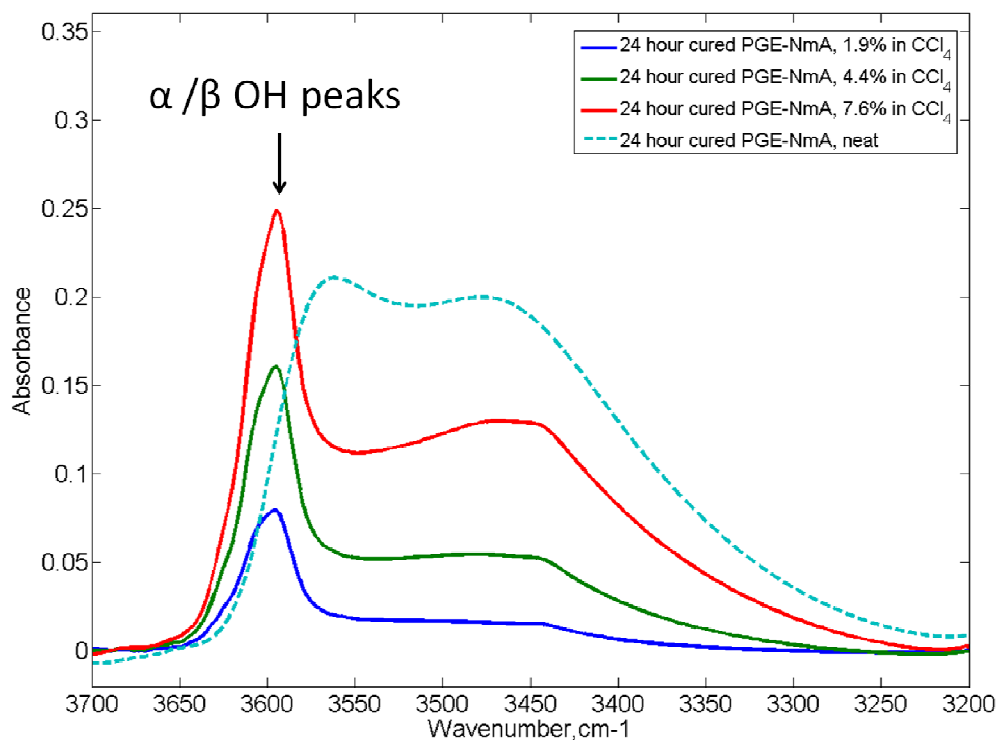
Figure 5.14 Comparison of spectral line shape of neat resin spectrum with diluted resin spectra

To clarify the existence of hydrogen bonding associations, association of hydroxyl group with various hydrogen bonding acceptors were tested via isopropanol (IPA) dilution experiment in Chapter 3. Toluene, Dipropylether (DPE), and Triethylamine (TEA) were chosen to represent ether, phenyl group and amine hydrogen bonding acceptors, which were potential hydrogen bonding acceptors in PGE-NmA system respectively. The

positions of associated peak in isopropanol-H-bond acceptor-CCl_4 ternary system as well as that of self association verified in IPA-CCl_4 system were listed and compared with the deconvolution result of cured PGE-NmA sample spectrum in table 5.4. It was found from iPA-CCl_4 binary system that IPA had a self association and the hydrogen bonding vibration peak for the hydroxyl group of which both oxygen and hydrogen were bound by other hydroxyl groups (δ bond) was shown at 3345 cm^{-1}. It was also noted from ternary system analysis that O-H···N associated band showed longer Δν than O-H···O. Based on the empirical relationship that the stretching vibration red shift is inversely proportional to the hydrogen bond length of H···B in A-H···B structure [38], the strength of hydrogen bonding association of OH group was in an order of tertiary amine>hydroxyl group>ether>phenyl group (π-bond) and 4 deconvoluted peaks in PGE-NmA system could be assigned with same order.

Table 5.4 Associated peak positions of isopropanol ternary system and comparison with deconvoluted peak positions of cured PGE-NmA spectrum

Systems	IPA-Toluene-CCl_4 ,cm^{-1}	IPA-DPE-CCl_4 ,cm^{-1}	IPA-CCl_4 ,cm^{-1}	IPA-TEA-CCl_4 ,cm^{-1}
Associated peak positions (deconvoluted peak positions in PGE-NmA)	3595 (3576)	3494 (3546)	3345 (3478)	3229 (3378)

Once amine concentration profile during the reaction was established using the extinction coefficient for the peak at 3416 cm^{-1}, the extinction coefficient value for the hydroxyl group peak at 3572 cm^{-1} was determined using a mass balance, where one hydroxyl

group is formed for each amine group that is consumed, as shown in figure 5.15. Both the

amine and hydroxyl group concentration profiles based on the defined extinction

coefficients were shown in figure 5.15 along with the sum of the amine and hydroxyl

concentration which was constant within $\pm0.46\%$.
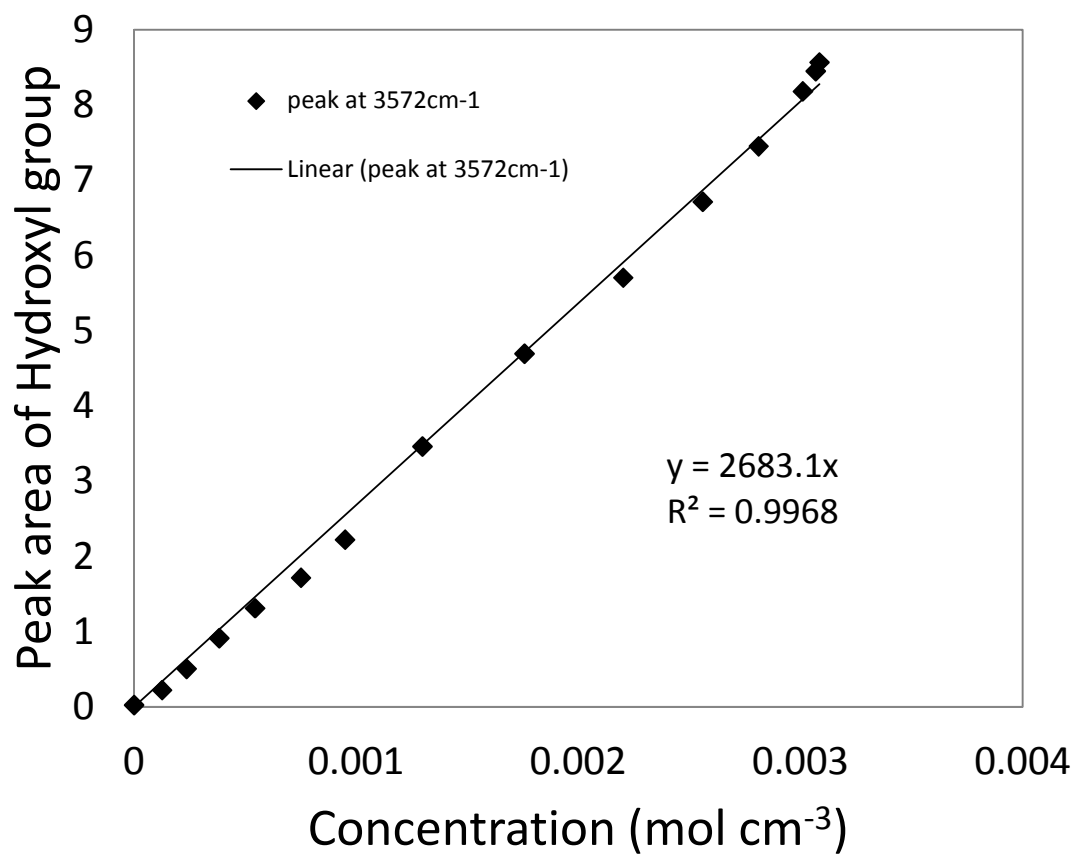
Figure 5.15 Hydroxyl group extinction coefficient determined form a mass balance of amine decrease
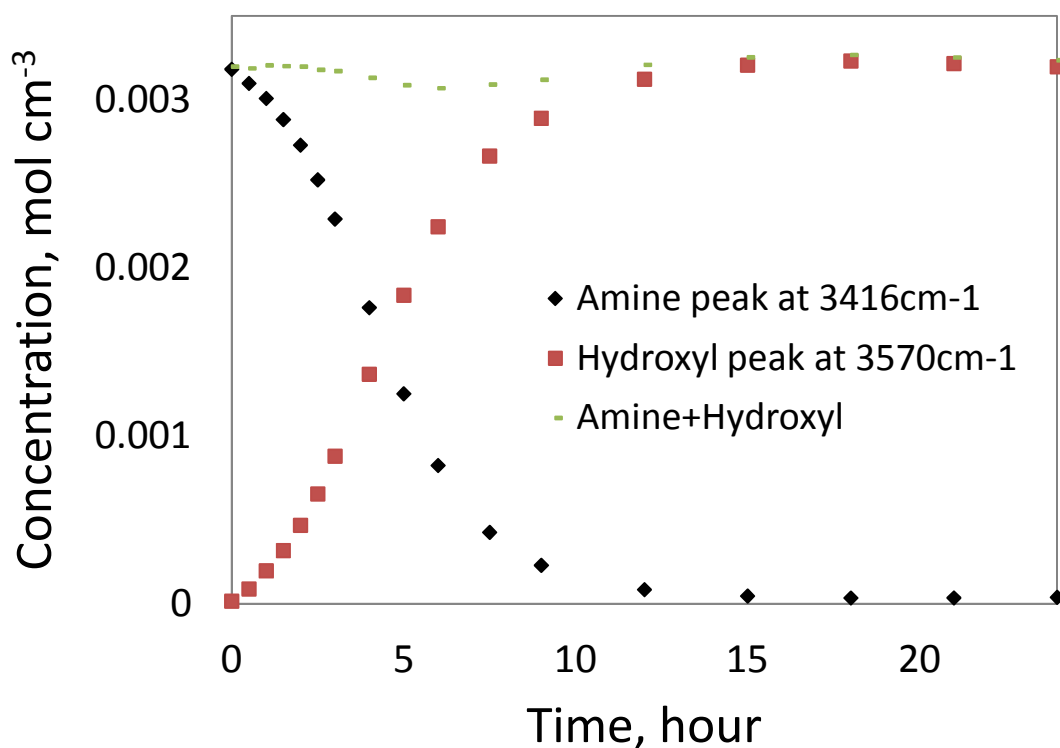
Figure 5.16 Concentration profiling of amine and hydroxyl groups

5.2.2 Epoxide Group Analysis

Frequency area of 800-1002 cm^{-1} was chosen for monitoring epoxide peak evolution.

Figure 5.16 shows simple comparison of single NmA, PGE, and a mixture of PGE-NmA

spectra in that wavenumber area as well as the error analysis in between a mixture

spectrum and a spectral summation of single PGE and NmA spectra. These spectra were

compared with DFT frequency calculation data for the peak deconvolution. NmA peaks

were easy to be assigned due to their simplicity and accuracy in peak intensity and

frequency order. On the other hand, PGE peaks showed complex and disorder in

frequency when comparing a real spectrum with theoretical spectrum. Therefore, only

number of peaks, not the detailed peak information, could be estimated from the DFT

calculation result and applied for the peak deconvolution in the given wavenumber area.
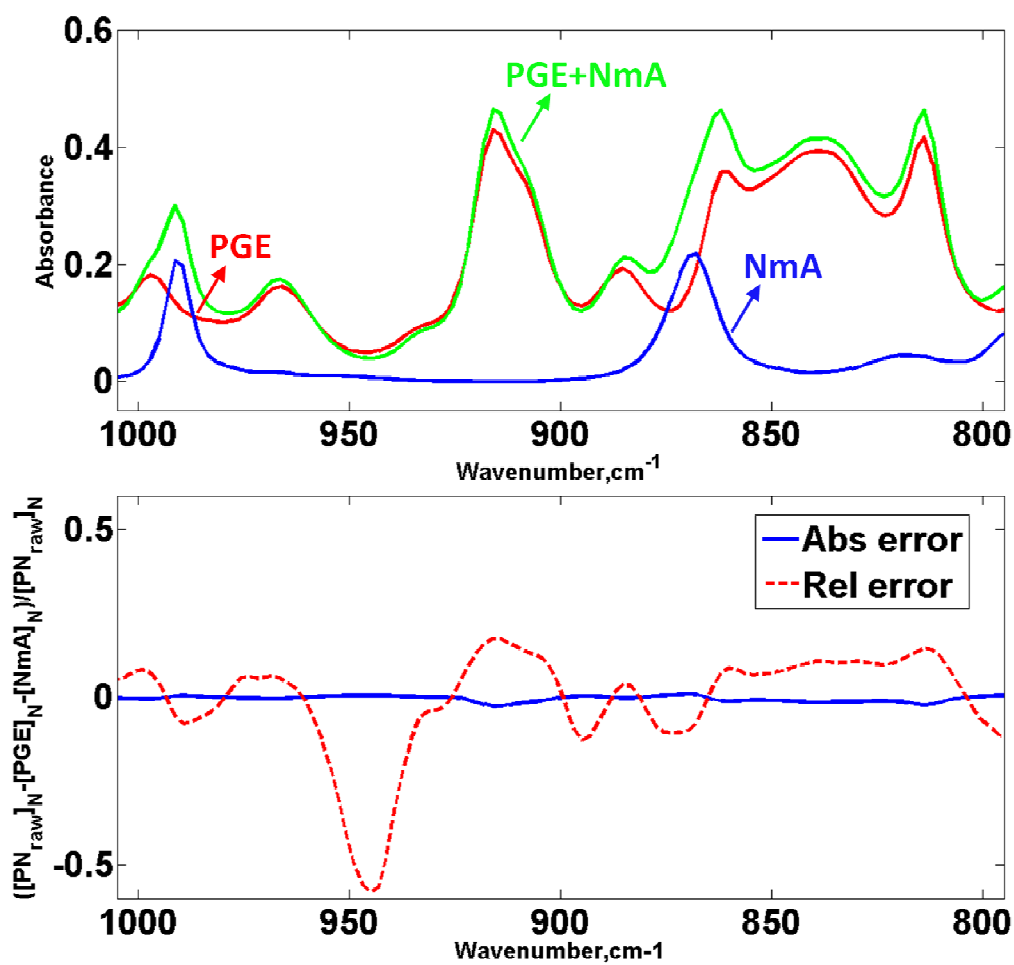
Figure 5.17 Comparison of neat PGE, NmA and a stoichiometric mixture of PGE and NmA spectra (upper) and their spectral error evaluations

First, number of peaks existing in the spectrum obtained at 0hr was investigated from

DFT frequency calculations of single materials, PGE and NmA. Single PGE had 10

theoretical peaks and single NmA had 4 peaks in the area. 14 peaks showed a good fit of the given area with an error value of 0.0057.

Three spectral region showed decreasing trends in peak intensity as a result of epoxide reaction with Amine, in the wavenumber areas of 780-790 cm^{-1}, 830-850 cm^{-1}, and 900-920 cm^{-1} respectively. DFT calculation also supported that there were three epoxide-related vibrations at the given spectral region, C-O-C asymmetric stretching, C-O-C symmetric stretching, and epoxide C-H symmetric stretching. Among them, two spectral regions were chosen and utilized to obtain the concentration profiles of epoxide, 780-790 cm^{-1} and 830-850 cm^{-1} here. The spectral region of 890-930 cm^{-1} was abandoned even though an observation of clear decreasing trend because of difficulty in peak deconvolution. Mijovic et al also reported that using a peak at 915 cm^{-1} for epoxide evolution was in controversial due to overlapping peaks [5].

Figure 5.18 showed three spectral regions that were potential resources of epoxide evolution. It was found that the wavenumber region at around 945 cm^{-1} had series of increasing peaks during cure and the tails of increasing peaks had an influence on the peak at 915 cm^{-1}, which was epoxide trace. From DFT frequency calculation, it was also confirmed that, in this spectral region, three new peaks were formed as a result of epoxide ring opening by the reaction with Amine group as shown in peak assignment of table 2.1 in Chapter 2.
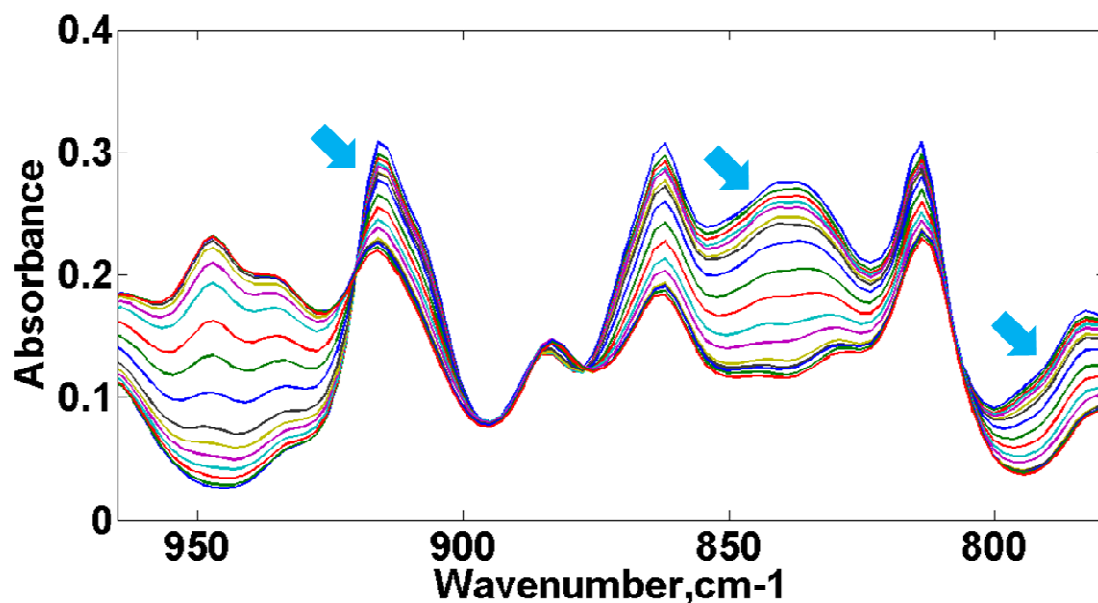
Figure 5.18 Three potential wavenumber regions of epoxide evolution

Spectral region of 780-790 cm^{-1} was also difficult to deconvolute due to significant influence of the large peak at 754cm^{-1}, which was from a vibration of Benzene C-H wagging, on the peak of interest. Data should have been re-treated to eliminate the effect of large neighboring peak.

Spectral area of 830-860 cm^{-1} was determined to be deconvoluted first because there was no interference of neighboring peaks and then, region of 780-790 cm^{-1} was considered next, after post-data-treatment. These two deconvolution results were compared with each other for the consistency check.

To determine the exact peak position for epoxide peak in the wavenumber area of 830-860 cm^{-1}, wider area of 800-895 cm^{-1} was selected and deconvolted with 7 peaks totally, 2 from NmA and 5 from PGE. Based on the DFT frequency calculation at the target wavenumber area, it was found that all the peaks except for the epoxide peaks were from

non-reactive species. Therefore, peak height as well as position and G-L ratio were tightly regulated. Constraints applied to the peaks were shown in table 5.5.

Table 5.5 Constraints details on the peaks at 800-900 cm^{-1}

	Peak at 813.2cm^{-1} Value (LB-UB)	Peak at 813.2cm^{-1} Value (LB-UB)	Peak at 813.2cm^{-1} Value (LB-UB)	Peak at 813.2cm^{-1} Value (LB-UB)	Peak at 813.2cm^{-1} Value (LB-UB)	Peak at 813.2cm^{-1} Value (LB-UB)	Peak at 813.2cm^{-1} Value (LB-UB)
H	0.26 (0.2145-0.27)	0.5185 (0.5185-0.06)	0.11 (0.1-0.115)	0.1 (0-0.15)	0.14 (0.11-0.15)	0.078 (0.07-0.08)	0.105 (0.09-0.11)
m	0.92 (0.85-1)	0.05 (0-0.1)	0.8 (0.8-0.85)	0.67 (0.64-0.7)	0.88 (0.86-0.9)	0.97 (0.95-1)	0.9 (0.7-1.0)
x_0	813.17 (813-814)	829.5 (829-830)	841.5 (841-842.5)	844.8 (844.6-845.6)	862.3 (862-863)	869.5 (868-869)	885 (884-886)
W	24.07 (24-25)	14 (12-15)	29 (28-29.4)	32 (30-33)	14 (13.7-14.3)	21.8 (21-22)	14.7 (13-15.7)
a	0	0	0	0	0	0	0

†LB: lower bounds, UB:upper bounds

Initial (0 hour) and final stages (24 hour) of cure sample spectra were compared with each other to estimate peak positions at a given wavenumber area, and then six peaks were used to fit the 24 hour cured sample spectrum under the assumption that epoxide group were completely consumed after 24 hours of cure with NmA at the setting temperature of 96°C. Then, the constraints on those six peaks were kept through all the

cure data and one epoxide peak was added at around 845 cm^{-1} for the completion of the fitting.

Spectral region of 780-790 cm^{-1} was also deconvoluted to obtain epoxide concentration profile. However, for that Spectral region, additional treatment was required to eliminate the effect of the neighboring peak at 754 cm^{-1} on the target epoxide peak. The intensity of neighboring peak was so high that even small peak line shape change in the peat at 754 cm^{-1} significantly changed the peak line shape of the target peak at 789 cm^{-1}.

First, peak fitting was performed on the peak at 754 cm^{-1}. It was found from DFT frequency calculation that the peak was originated from C-H wagging vibration of the benzene group in PGE and NmA, whose intensity should be constant throughout the cure process. Therefore, peak fitting for the peak at 754 cm^{-1} was performed through the whole series of cure spectra. Then, the optimized peak parameters such as peak position, peak width, G-L ratio and peak height were averaged through the spectra to produce a single synthetic peak. Finally the synthetic peak was subtracted from the whole series of spectra. By subtracting the synthetic peak line shape at 754 cm^{-1} from series of spectra, interference of the neighboring peak resulted from a slight change of peak line shape of the peak at 754 cm^{-1} to the target peak could be reduced.

Figure 5.19 showed subtracting result of PGE-NmA cure data set from a reference peak at 754 cm^{-1}. It was shown from (a) of figure 9 that the line shape of the peak at 754 cm^{-1} could be significantly changed by a small change of the peak height but that effect could be removed by subtracting the averaged peak at 754 cm^{-1}.

After eliminating a neighboring peak, a part of spectral data was taken from 763 to 1002 cm^{-1} for the peak deconvolution. However, peak of interest at around 790 cm^{-1} could still

be interfered by remaining peaks at around 760 cm^{-1}. Therefore, weight factor was applied at the edge of the spectra to completely remove the interference of neighboring peak.
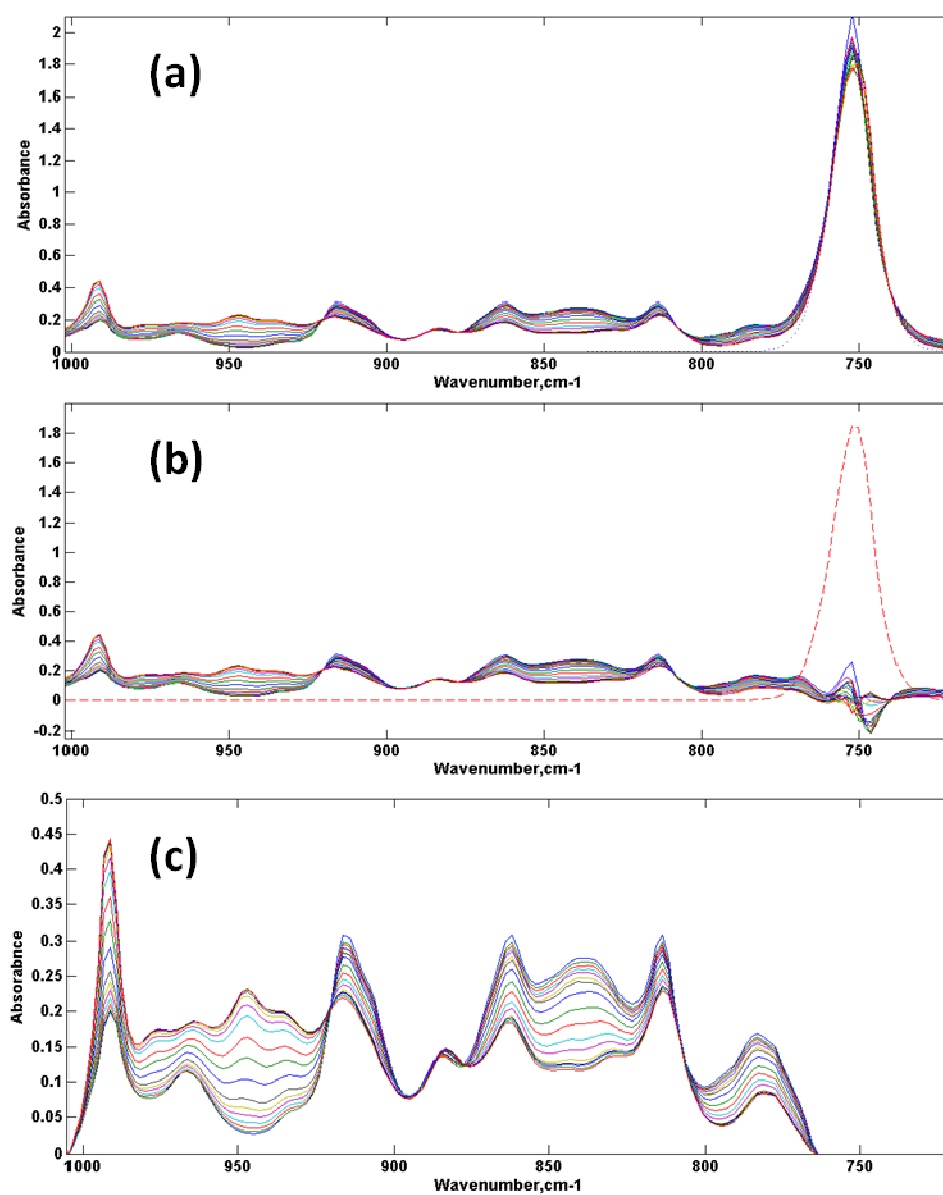

Figure 5.19 Peak subtraction and applying weighing factor: (a) before subtraction, (b) after subtraction and (c) after applying weighing factor

Figure 5.20 showed the deconvolution result at the spectral area of 763-898 cm^{-1}. Thicker pink and green deconvoluted lines indicated two epoxide assigned peaks. It was noted that two peak areas of epoxide at 845 and 785 cm^{-1} were systematically reduced as cure time increased while those of remaining peaks were consistently maintained during cure. Extinction coefficient of the epoxide peak at 845 cm^{-1} was determined from neat PGE with 3 and 5micron path length samples. Peaks at 869.9 cm^{-1} which was originated from NmA was eliminated and the same peak constraints used for fitting PGE-NmA cure sample spectra were applied to neat PGE sample spectra. Peak area vs. path length showed good correlation coefficiency (R^2) value of 99%. Figure 5.21 shows the concentration profile obtained from PGE-NmA cured at 80°C.

From figure 5.20, it was found that Amine species consumption was faster at the initial stage of cure up to 9 hours than the epoxide species consumption, which was not feasible in the Amine-epoxide reaction system. Epoxide has various paths for consumption by ring opening reaction during thermal cure but Amine group has the only way to be consumed, reaction with epoxide ring. Therefore, the deviation of Amine concentration from epoxide concentration should have been an error. Nevertheless, this FT-IR methodology provided accurate cure data when compared with the HPLC results. Termolecular complex reaction mechanism proposed by Mijovic et al was used to fit the kinetic data of PGE-NmA system obtained from FT-IR as well as HPLC [5]. Stoichiometric PGE and NmA reactions were conducted at 4 different temperatures to obtain the activation energy (i.e. 50, 70, 90 and 110°C) and in-situ IR analysis was conducted at 80°C. The kinetic constants obtained from FT-IR and HPLC results were listed in table 5.6. The activation energies for the formation of resultant species from the

first complex and the second complex were 112.39 and 54.91 KJ mol^{-1} respectively. The

second activation energy value was well agreed with the literature value reported by Xu

et al, 55 KJ mol^{-1} [4]. However, the obtained first activation energy was 60% higher than
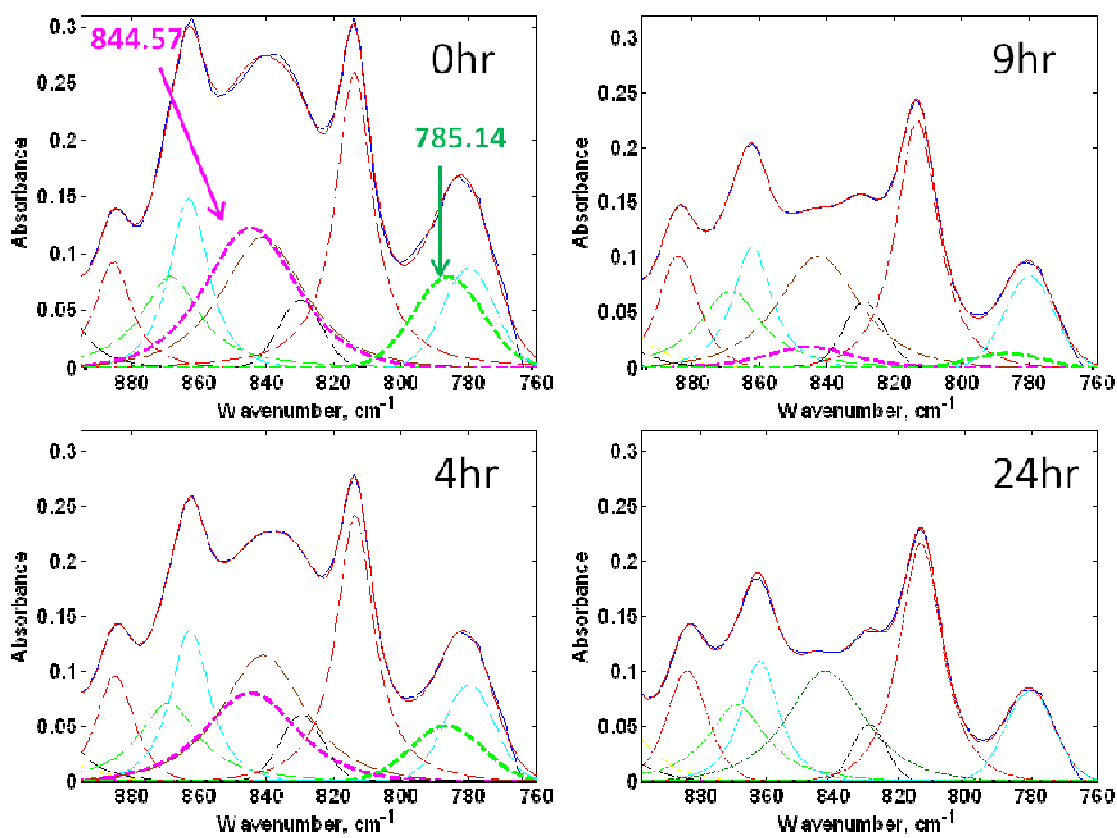
the reported value, 69.3 KJ mol^{-1}.

Figure 5.20 Peak deconvolution results at 845 cm^{-1} and 785 cm^{-1} during PGE-NmA reaction at 80°C
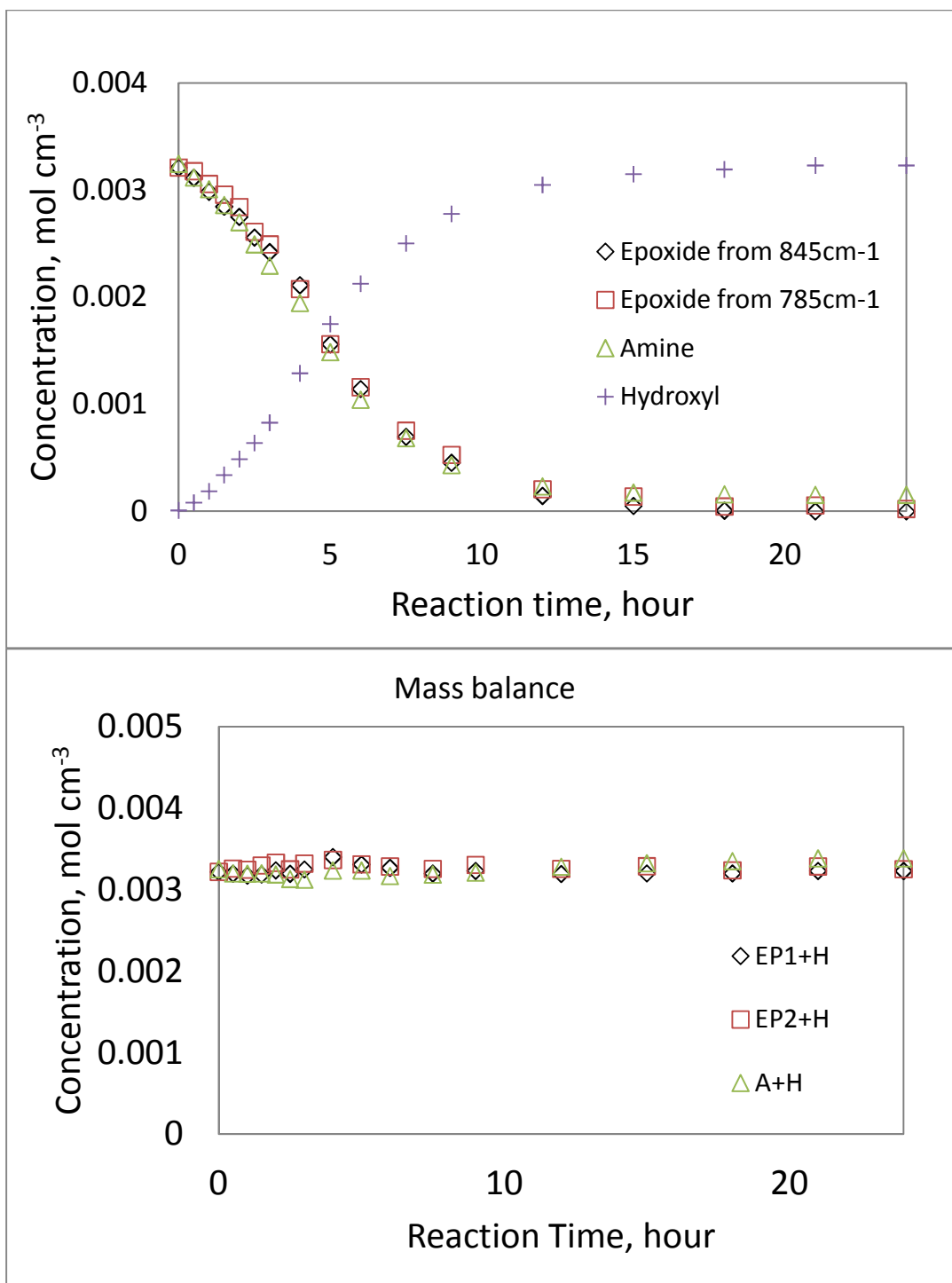
Figure 5.21 Concentration profiles of PGE, NmA, PN (upper) and their mass balance (lower)

Table 5.6 Summary of kinetic constants

Analysis	Temperature (^{o}C)	$k_1 \times 10^3$, cm^3 mol^{-1} min^{-1}	k_2, cm^3 mol^{-1} min^{-1}
HPLC	50	3.095	-2.244
HPLC	70	2.914	0.014
HPLC	90	2.754	2.436
HPLC	110	2.610	4.210
FT-IR	80	2.832	1.599

5.3   FT-IR Analysis of Phenylglycidylether and Aniline System

In the previous section, Phenylglycidylether and N-methylaniline reaction could be successfully monitored via quantitative FT-IR method. It could provide concentration profiles of exoxide, secondary amine and tertiary amine groups. Now reaction species of interest would be expanded to the real applications of amine epoxy system, i.e. primary amine (PA)-secondary amine (SA)-tertiary amine (TA) development. Phenylglycidylether-Aniline system was employed to investigate PA-SA-TA evolution. Same experimental conditions that were applied to PGE-NmA reaction were used for PGE-Aniline reaction, equal stoichiometry at 80°C reaction for up to 24 hours. Obtained spectra were baseline corrected with a quadratic lines passing through some wavenumber points that were not supposed to be assigned to any chemical species. Three main wavenumber areas were deconvoluted to obtain absorbance information on epoxide, PA, SA and OH groups, 3200-3650 cm^{-1} where PA, SA, and OH are convoluted, 1550-1650 cm^{-1}, where PA was developing, and 750-950 cm^{-1} where multiple epoxide peaks were present.
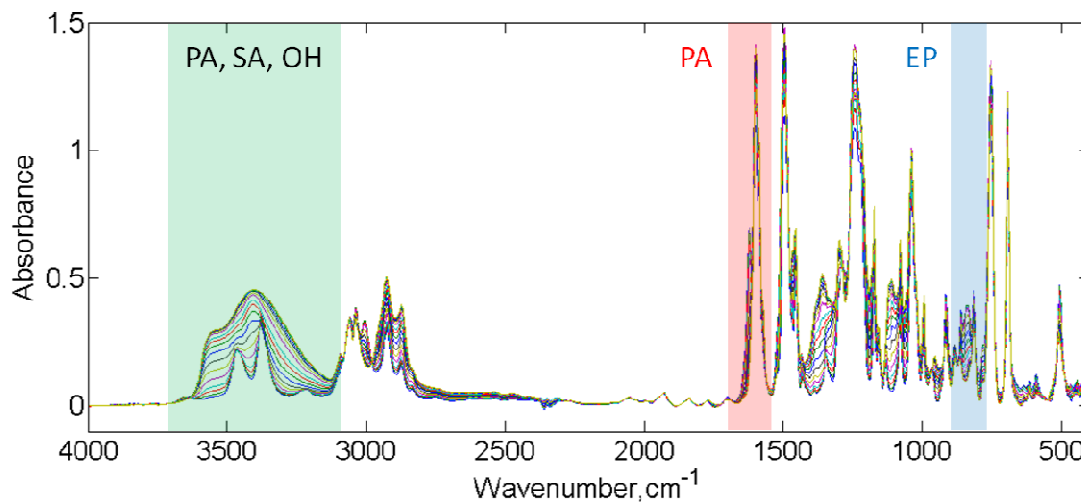
Figure 5.22 Series of spectra obtained for PGE-Aniline system, after baseline correction

5.3.1   Amine and Hydroxyl Group Analysis

The first spectral region, 3200-3650 cm^{-1} was investigated. It was found from previous sections that amine group and hydroxyl group form self and intermolecular hydrogen bonding with the existence of hydrogen bonding acceptor species. Here, three peaks were assigned for each primary amine peak based on the number of peak that was set to best describe a convoluted wavenumber area. At 0 hour spectrum, a peak at 3377 cm^{-1} which was the highest peak became a reference peak and the relative heights of the other 5 peaks were fixed throughout the series of spectra. Secondary amine peak was developed at 3404 cm^{-1} and an asymmetric peak whose asymmetric parameter ranging from 0.013 to 0.015 was set to describe multiple association of SA. The strategy to tie the secondary amine peaks as one asymmetric peak was successfully applied to NmA as well as SA species in PGE-aniline system. Peak deconvolution parameters of Amine peaks were

fixed throughout the spectra. For hydroxyl group fitting, four peaks were set at 3574, 3538, 3434 and 3320 cm^{-1} respectively. Four peaks deconvolution had a satisfactory deconvoluiton result for PGE-NmA system. Detailed constraints applied to fit the wavenumber area of 3200 to 3650 were summarized in table 5.7 through 5.9, and figure 5.24 showed a selected deconvolution result of the first area of interest.

Table 5.7 Parameters for primary amine peaks in PGE-aniline system

	Peak at 3468.2cm^{-1}	Peak at 3441.9cm^{-1}	Peak at 3408.3cm^{-1}	Peak at 3378.2cm^{-1}	Peak at 3361.3cm^{-1}	Peak at 3321.7cm^{-1}
Relative peak height	0.7321	0.4145	0.1479	1	0.6440	0.1299
m	0.9942	0.0332	0.0376	0.2813	0.526	0.1519
W	44.41	46.91	26.86	31.42	46.58	51.86
a	0	0	0	0	0	0

Table 5.8 Constraints for SA in PGE-aniline system

	Parameter value (LB-UB)
m	0.1 (0-0.1)
x_0	3404.55 (3404-3404.5)
W	52 (50-55)
a	0.014 (0.013-0.015)

Table 5.9 Constraints for OH groups in PGE-anline system

	OH1	OH2	OH3	OH4
m	0.004 (0-0.1)	0.48 (0.45-0.55)	0.1 (0-0.1)	0.8 (0.75-0.85)
x_0	3574 (3573-3576)	3538 (3530-3541)	3434 (3430-3440)	3320 (3318-3321)
W	49.7 (47-52)	80 (76-82)	169 (165-175)	240.8 (235-245)
a	0	0	0	0
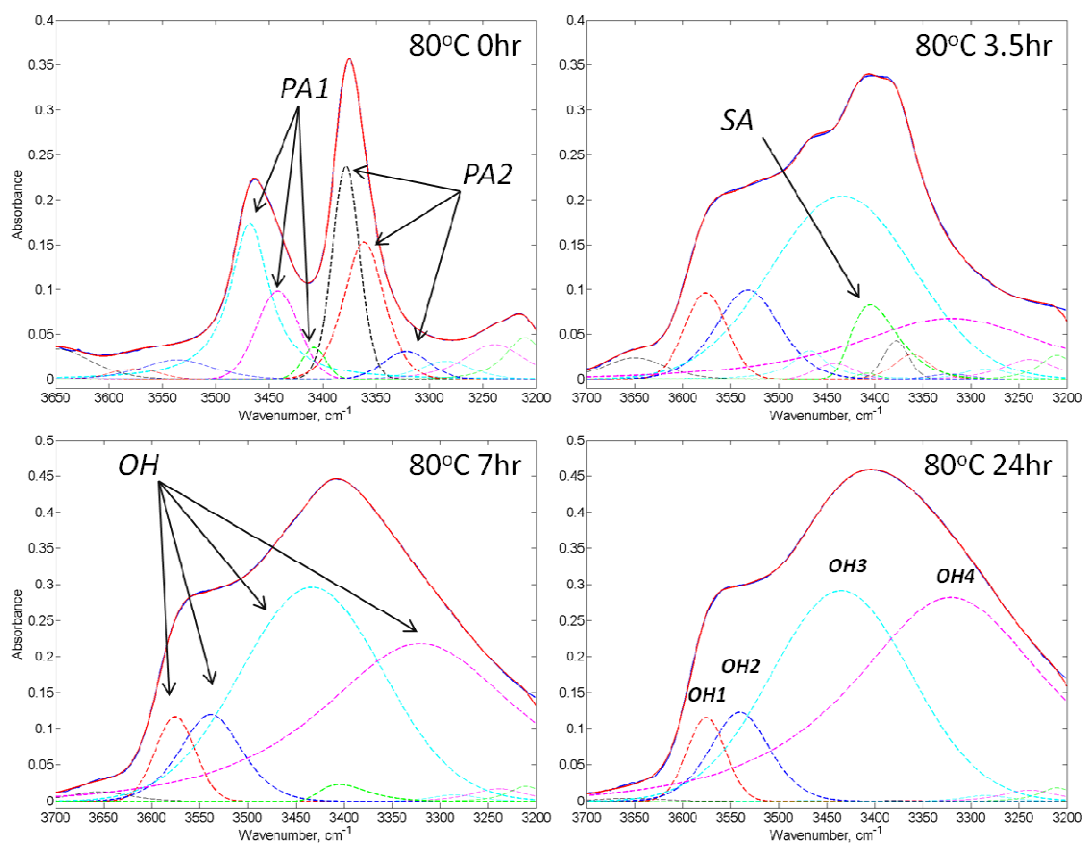
Figure 5.23 Selected deconvolution results for primary amine, secondary amine, and hydroxyl groups

The absorbance profiles of two PAs, SA and four OHs were shown in figure 5.25. The absorbance profiles for 4 different kinds of OHs showed little different evolutions here but generally showed smooth evolution lines. Unlike other peaks, peak absorbance for OH4 showed a gradual increase in its absorbance and this was because the spectral line at around 3200 cm^{-1} also had some overlapping of the neighboring bands.
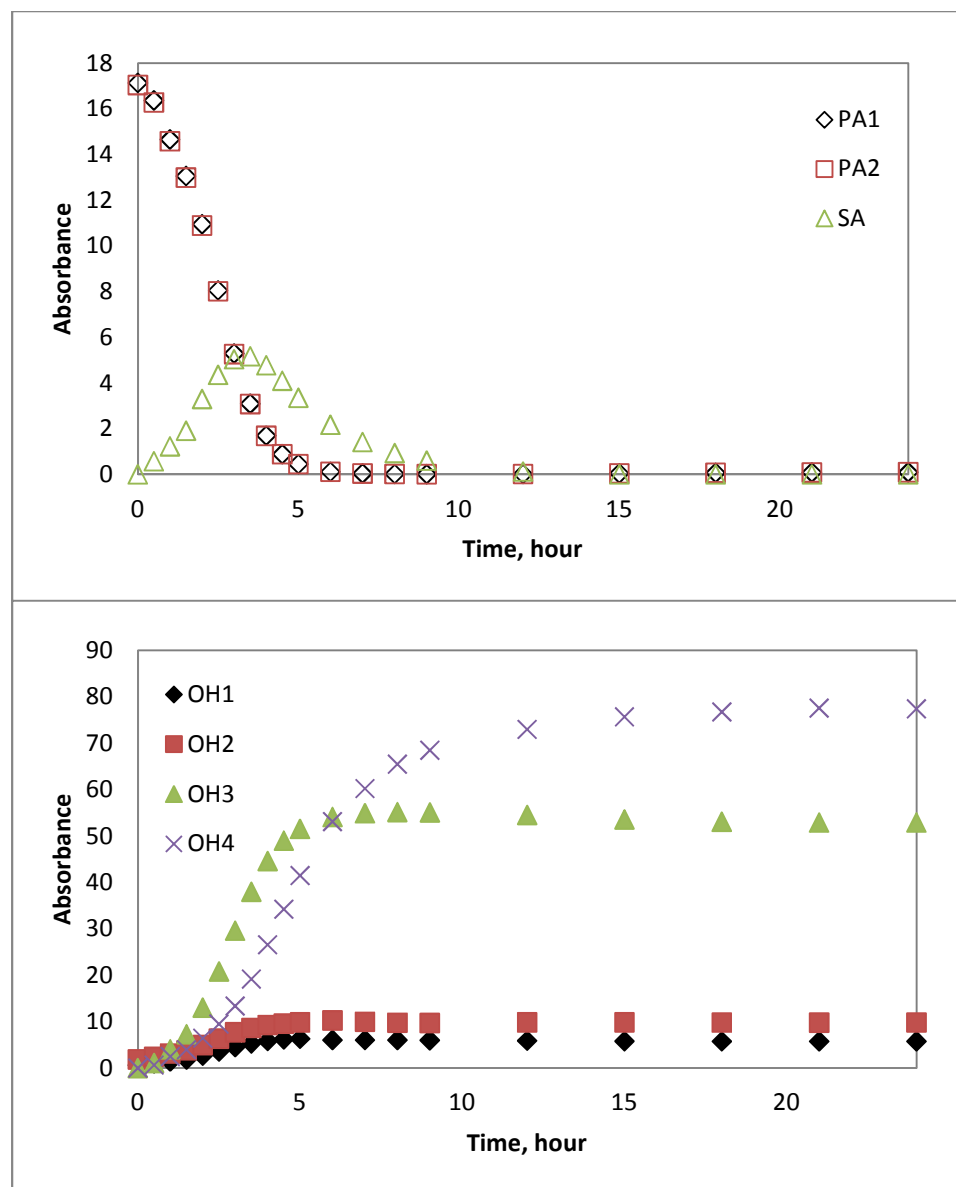
Figure 5.24 Primary amine, secondary amine and hydroxyl group peak evolutions during reaction at 80°C

5.3.2 Primary Amine Group Analysis

Second part of interest was 1550-1650 cm^{-1}, where PA was developing. In this spectral

area, PA peak was positioned at 1622 cm^{-1} with values of FWHM and

Gaussian/Lorentzian ratio of 22.9 and 0.82 respectively. Even though PA peak was on the

shoulder of a big peak assigned to phenyl group C-C vibration at 1602 cm^{-1}, extraction of

PA peak from the convoluted spectrum required less effort due to the peak's large

intensity. After applying tight constraints on the peak line shape parameters for the PA

peak at 1622 cm^{-1}, the absorbance evolution profile could be obtained and compared with

that obtained from the first spectral area as shown in figure 5.26. The normalized

intensities of both PA peaks showed a good consistency.
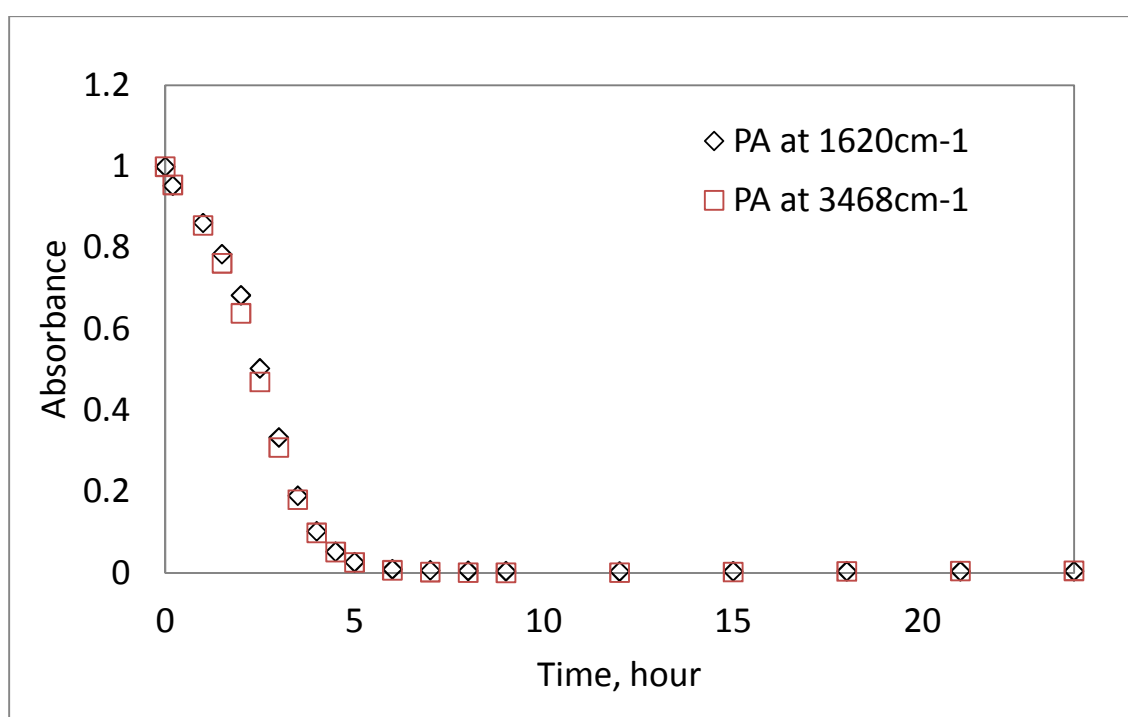
Figure 5.25 Comparison of primary amine evolutions obtained at different wavenumber areas

5.3.3   Epoxide Group Analysis

The third spectral area of 750-950 cm^{-1} was deconvoluted to evolutions of multiple

epoxide peaks shown at 840 and 783 cm^{-1}. Similar to the spectral area analysis of PGE-

NmA system, originally, three peaks of epoxide traces existed in this spectral region, 915, 840 and 783 cm^{-1}, however, using epoxide peak at 915 cm^{-1}, which was assigned to the epoxide C-O-C asymmetric stretching was difficult due to a intensity increase at a neighboring peak at 945 cm^{-1}. Figure 5.27 showed spectral evolutions of two epoxide peaks at 840 (blue thick line) and 783 cm^{-1} (black thick line). 11 peaks were used to fit the spectral areas and epoxide peak evolutions were compared with each other in figure 5.28.
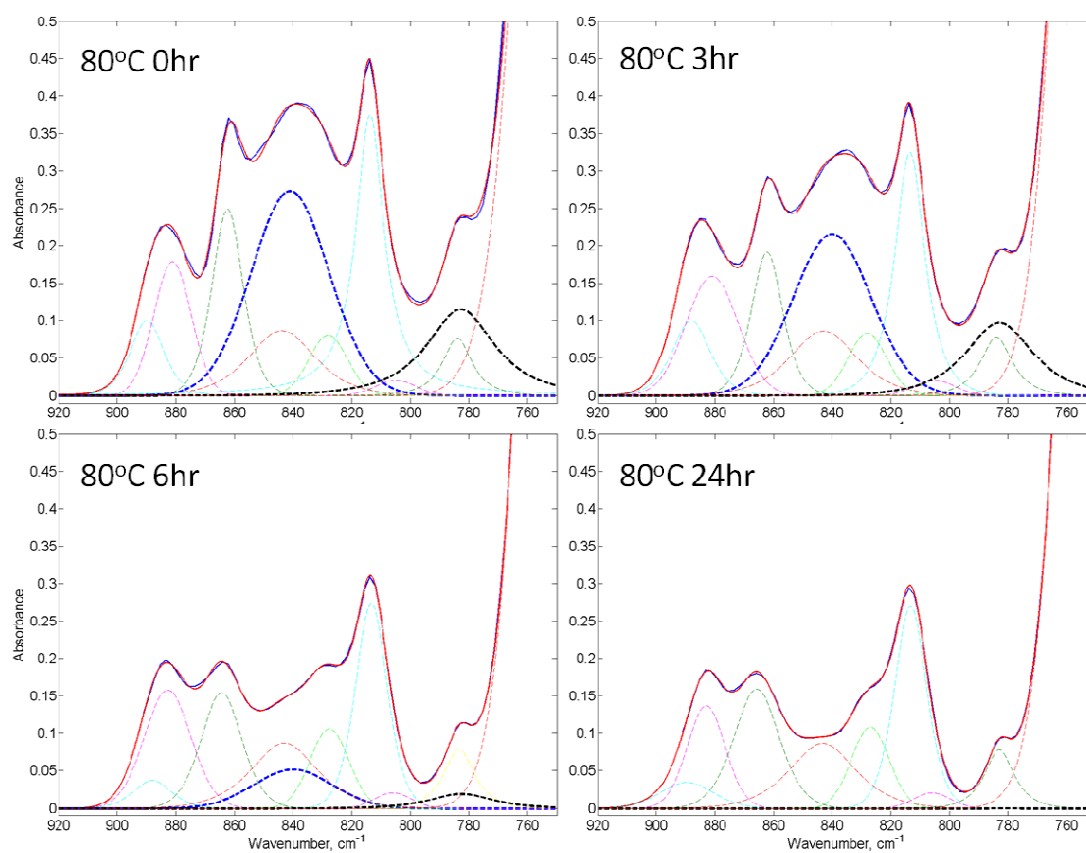
Figure 5.26 Selected deconvolution results of the third spectral area for epoxide peak evolutions
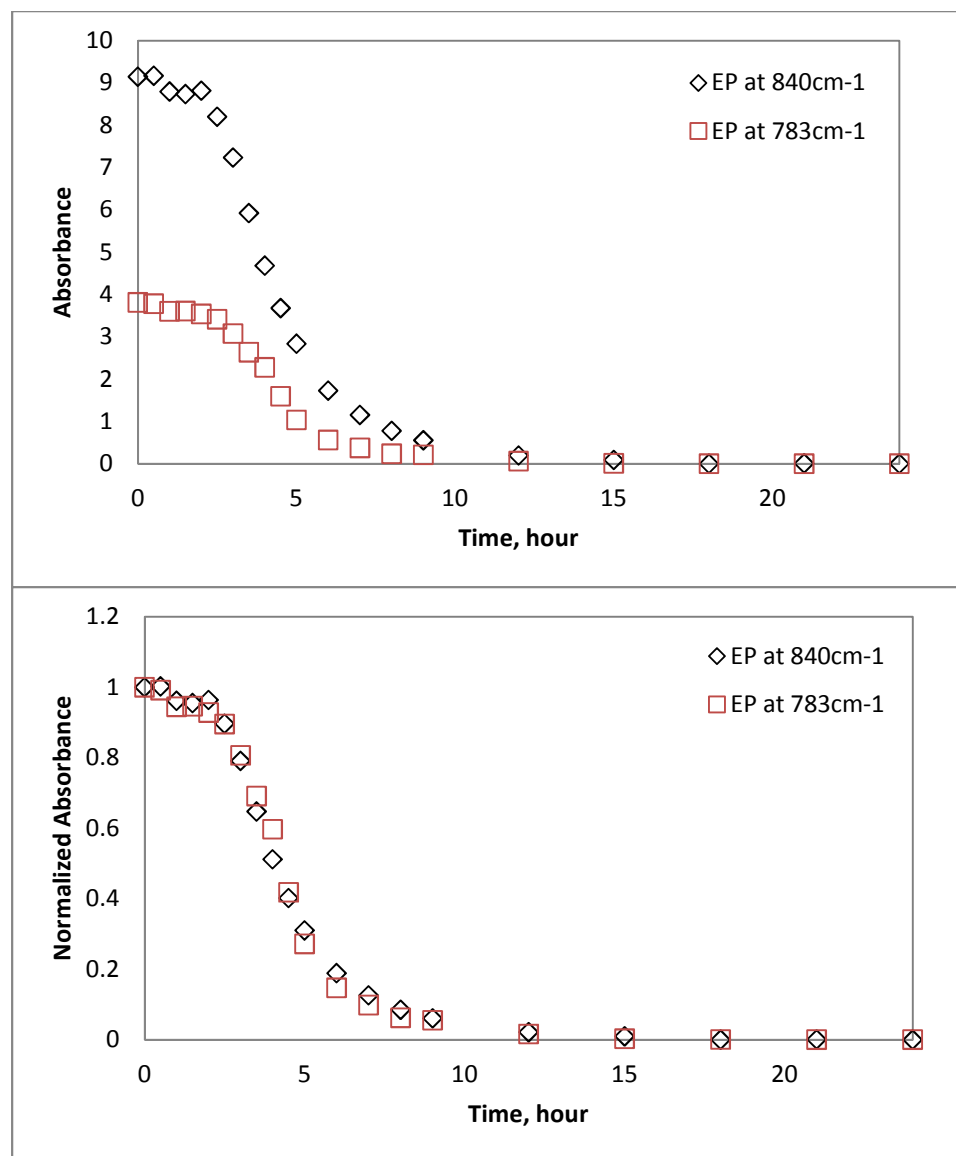
Figure 5.27 Epoxide peak evolutions

Among epoxide peaks, peak at 840 cm^{-1} was chosen to be compared with PA peak at 3468 cm^{-1} due to its larger intensity. From normalized absorbance evolutions of PA and epoxide peaks shown in figure 5.29, it was found that PA consumption rate was faster than epoxide species consumption and the difference would contribute to the formation of secondary amine. Therefore, the normalized peak difference obtained from the

comparison of normalized absorbance intensity of PA peak with that of epoxide peak was compared with normalized absorbance intensity of SA peak obtained at 3402 cm^{-1}. This comparison revealed that the quantitative analysis methodology applied to PGE-Aniline system could successfully provide the reaction information of all the chemical species, PA, SA, OH and epoxide groups.
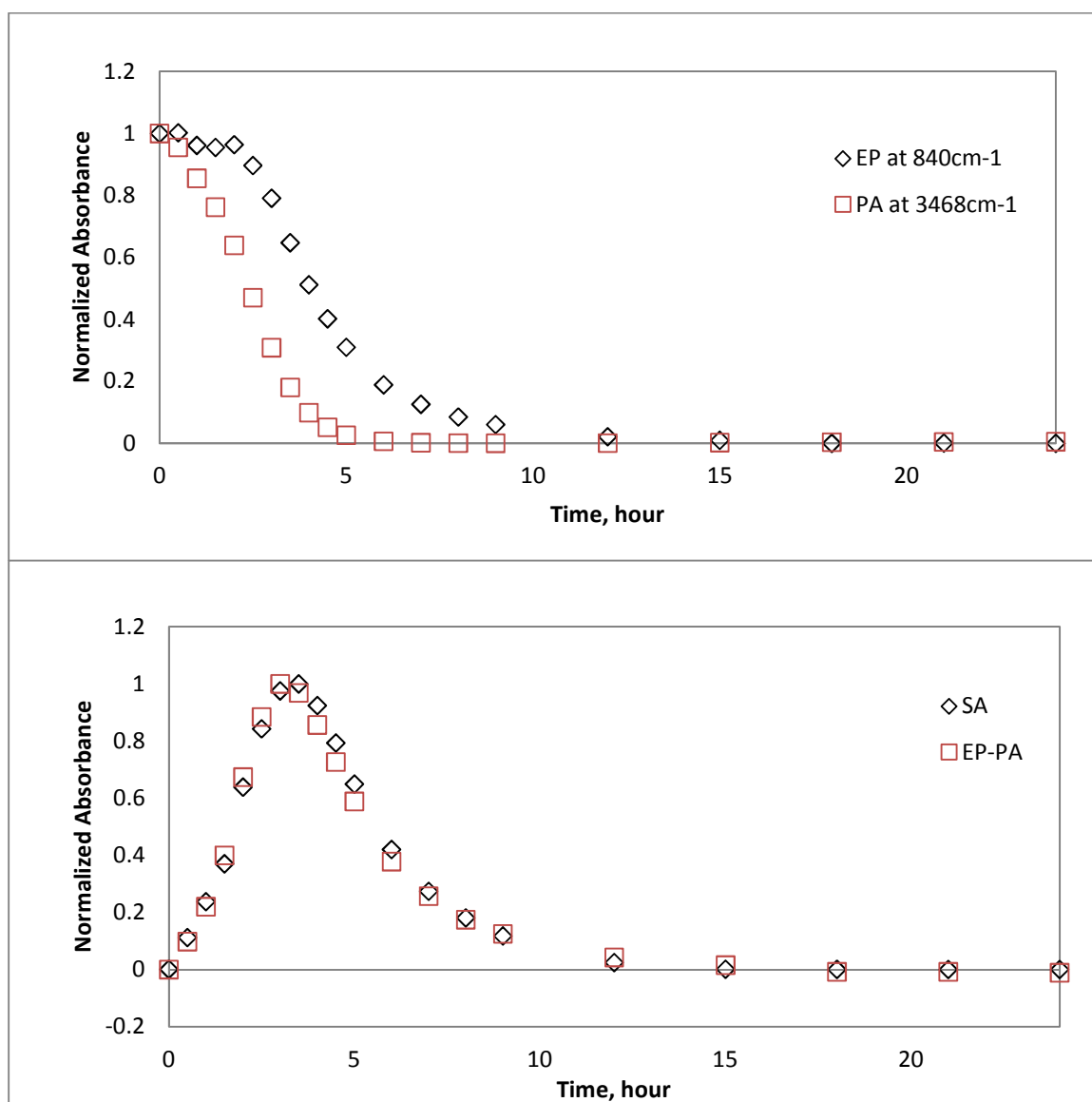
Figure 5.28 Comparison of SA evolution with qualitative [EP-PA]

In the next chapter, the same technique will be applied to the polymeric system to evaluate if the quantitative technique developed for the non-polymeric system would be also efficacious to the polymeric system.

CHAPTER 6. POLYMERIC SYSTEM ANALYSIS

Quantitative FT-IR technique has been utilized to obtain Absorbance evolution information and concentration profiles of non-polymeric epoxy-amine system successfully. The quantitative method for the concentration profiling also could be verified by the external method, HPLC analysis as well as the internally by comparing peaks of different vibrational modes of the same chemical species of interest. In this chapter, quantitative FT-IR analysis technique was applied to the polymeric material.

6.1   Epon825 and Aniline System Analysis

Epon825, which is the simplest form of diglycidylether of bisphenol A (DGEBA) type resin and Aniline were selected as epoxy amine system. Two reactant species form a linear polymer. Glass transition temperature of the fully cured material was known to be 95°C [62]. Epon825 was first melt on a hot plate with temperature of 60°C since the melting point of Epon825 is 45-50°C. Then stoichiometric amount of aniline was added to the liquid Epon825. After stirring at the room temperature, the sample mixture was put in between KBr window assembly with 5 micron thick copper spacer. The cure schedule was 80°C for 12 hours followed by 120°C for 3 hours. A series of spectra could be obtained for both cure and post-cure process. Figure 6.1 showed a series of spectra

obtained during an isothermal cure of Epon825 with Aniline at 80°C for 12 hours. Initial

guesses on the peak assignment could be obtained from literature [3].
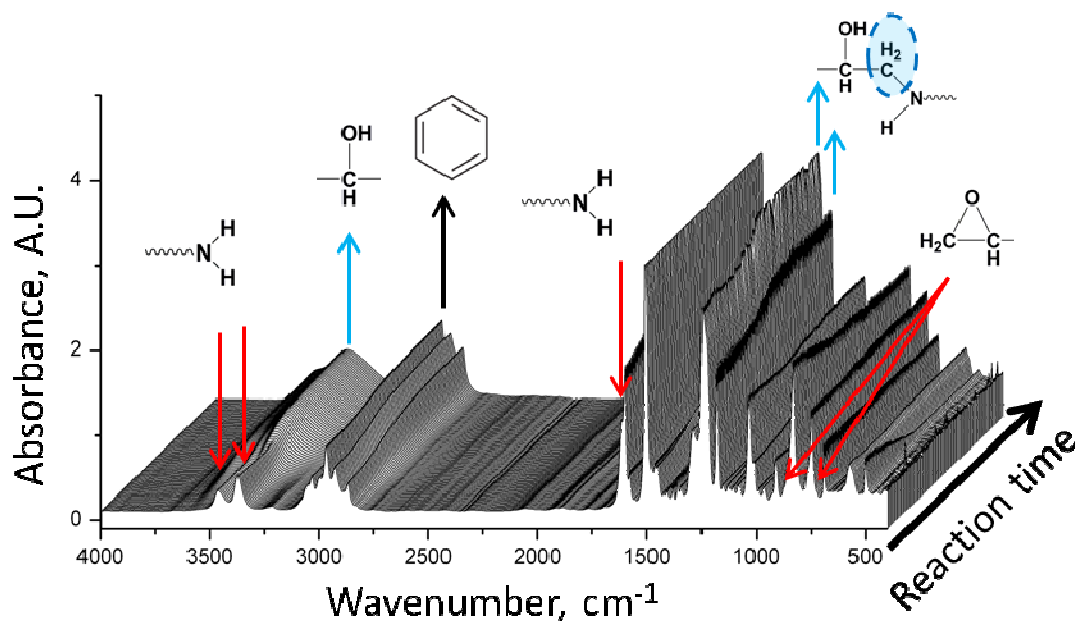
Figure 6.1 Series of spectra obtained from Epon825 and aniline isothermal cure at 80°C
for 12hours

Figure 6.2 showed baseline correction procedure. Baseline correction was performed on

the raw spectra by subtraction of quadratic line (green line) passing through no chemical

species assigned data points (red data points). Three wavenumber areas were chosen and

analyzed as chosen in the previous section of PGE-aniline analysis to obtain absorbance

information of PA, SA, OH and epoxide groups. The deconvolution process was

performed for 80°C procure sample spectra first followed by 120°C post-cure sample

spectra to see the effect of post-cure on the extent of the reaction. The validation of

baseline correction method utilized for Epon825-Aniline system was examined by a

simple peak curve line shape fitting of the isolated peak at 695 cm^{-1}. The quadratic line

subtracted from the original spectrum showed an inclined feature at the lower wavenumber area. However, curve fitting of the isolated peak at 695 cm^{-1} with a symmetric peak line shape showed a good fitting result, which confirmed that the baseline correction method was reasonable.
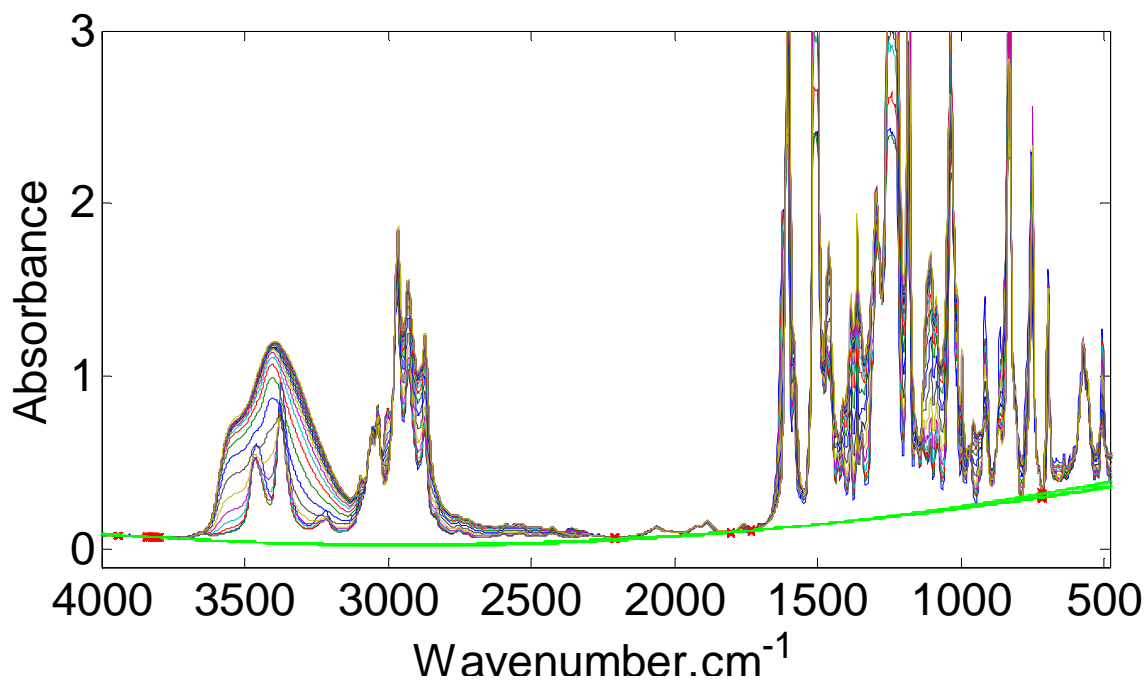
Figure 6.2 Baseline corrections of the series of spectra

6.2 Chemical Species Analysis-Isothermal Cure at 80˚C

6.2.1 Amine and Hydroxyl Group Analysis

PA had multiple peaks of self associations as shown in section 3.3.2 and 5.3.1. Three bands of 3481, 3467, and 3436 cm^{-1} were assigned to the first PA peaks of self association and three bands of 3395, 3385, and 3356 cm^{-1} peaks were assigned to the

second PA peak. Total 6 peaks were tied by relative peak height throughout the reaction
spectra and dealt as two asymmetric peaks. Five peaks were added to fit the overtone
peak areas at 3200-3300 cm^{-1}. For SA peak, asymmetric peak line shape was applied at
3411 cm^{-1} with constraints of Gassian/Lorentzian ratio and asymmetric factor, 0.79-0.89
and 0.012-0.013 respectively. The peak position of SA showed about 10 cm^{-1} blue shift
(decreased in wave length or moved to higher wavenumber) when compared with SA
peak position in PGE-Aniline system. Four peaks were assigned to OH association peaks
at 3576, 3540, 3438, and 3319 cm^{-1}, of which peak positions were very similar to OH
association peaks assigned for PGE-Aniline system (3574, 3538, 3434 and 3320 cm^{-1})
since hydrogen bonding acceptor species of Epon825-Aniline were basically same as
PGE-Aniline system. Three selected deconvolution of the spectra of 0 hour, 3.5 hour and
12 hour cured samples were shown in figure 6.3.

Table 6.1 Parameters for primary amine peaks in Epon825-aniline system

	Peak at 3467.1cm^{-1}	Peak at 3440.0cm^{-1}	Peak at 3407.4cm^{-1}	Peak at 3377.3cm^{-1}	Peak at 3361.3cm^{-1}	Peak at 3319.9cm^{-1}
Relative peak height	0.74693	0.41161	0.13834	1	0.67591	0.11631
m	0.8933	0.0122	0.0141	0.3283	0.5824	0.0258
W	41.83	44.68	25.55	30.54	45.84	50.67
a	0	0	0	0	0	0

Table 6.2 Constraints for SA in Epon825-aniline system

	Parameter value (LB-UB)
m	0.1 (0-0.1)
x_0	3404 (34004-3404.5)
W	52 (50-55)
a	0.016 (0.015-0.017)

Table 6.3 Constraints for OH groups in Epon825-anline system

	OH1	OH2	OH3	OH4
m	0.004 (0-0.1)	0.49 (0.45-0.55)	0.1 (0-0.15)	0.7 (0.65-0.75)
x_0	3574 (3573-3576)	3538 (3536-3540)	3427 (3425-3430)	3318.5 (3316-3320)
W	49.7 (47-52)	80 (78-82)	161 (160-165)	265 (260-270)
a	0	0	0	0
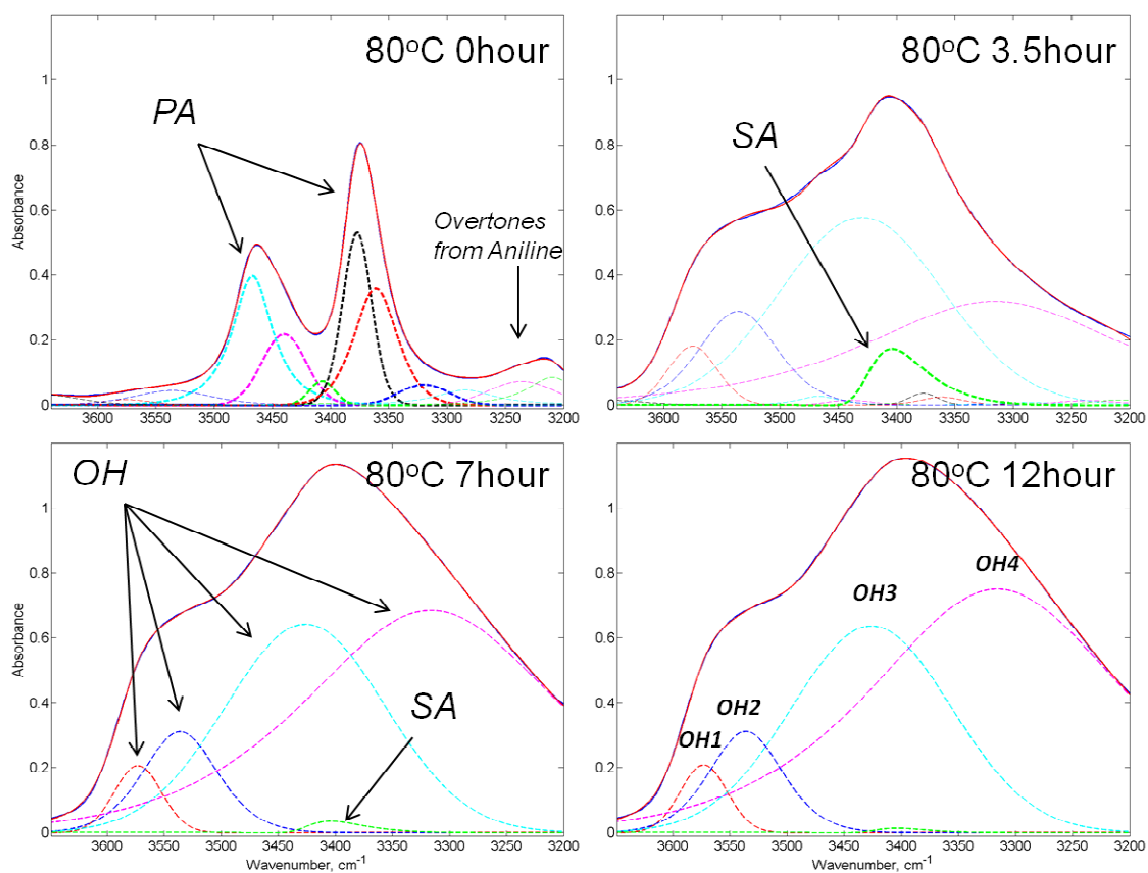
Figure 6.3 Amine and hydroxyl peaks evolutions at 3200-3700 cm^{-1} during an isothermal cure at 80°C

It was noted from the deconvoluted spectra that the SA species were remaining at the end of procure at 80°C, where as PA peaks were consumed completely. Absorbance evolutions of PA and SA shown in figure 6.4 also support that 6.6% of SA were

remaining after 8 hours of procure at 80$^{\text{o}}$C, where as 0.3% of PA was remaining after

procure. The maximum SA was formed at 3 hours cure.
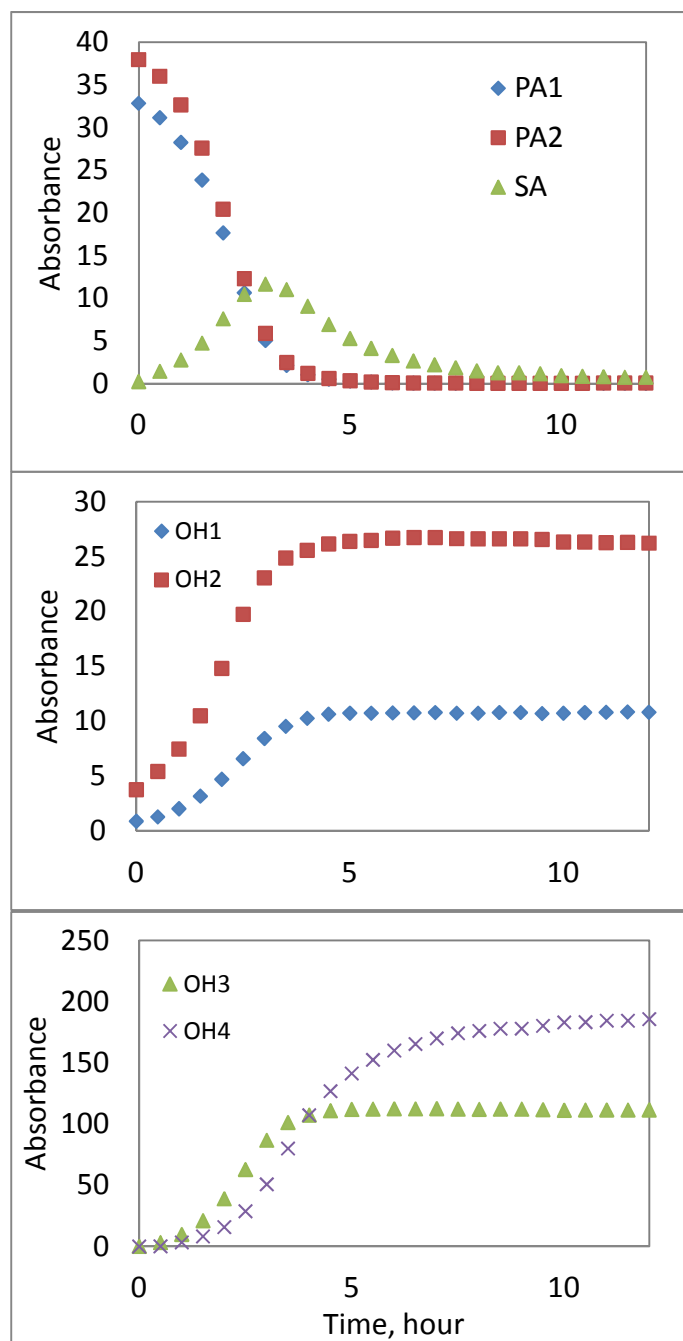
Figure 6.4 Absorbance evolutions of the PA, SA, and OH groups at 3200-3700 cm^{-1} during an isothermal cure at 80$^{\text{o}}$C

6.2.2   Primary Amine Group Analysis

PA peak at 1622 cm^{-1} in the second wavenumber area was well distinguished due to its intense peak absorbance, although the peak was on the shoulder of the peak at 1605 cm^{-1}, which was assigned to phenyl group C-C vibration. Peak at 1600 cm^{-1} was developed as a result of epoxide ring opening. Comparison of DFT frequency calculation result of PGE-Aniline reaction product with that of PGE revealed that CH2 scissoring vibration of the epoxide peak originally shown at 1523 cm^{-1}(in theoretical frequency) had a blue shift by Δv of 20 cm^{-1} after the linking reaction. Scissoring vibration of CH$_2$ of PGE attached to N molecule was shown at 1543 cm^{-1}. However, deconvoluted peak area of the peak at 1600 cm^{-1} had a minor effect on PA peak evolution.
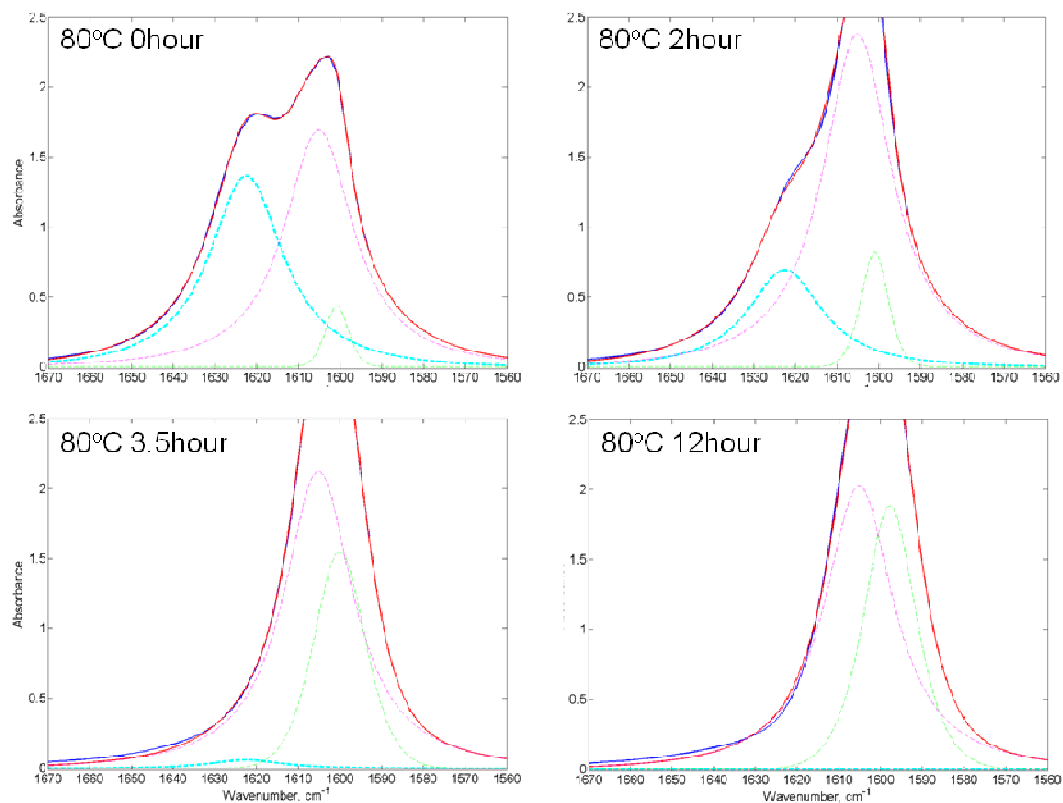
Figure 6.5 PA peak evolution at 1500-1700 cm^{-1} during an isothermal cure at 80°C

Figure 6.6 showed a comparison of normalized absorbance of PA peak obtained at 1622 cm^{-1} with that obtained at higher wavenumber area and they showed a good consistency in their absorbance evolutions. Both PA evolutions revealed that after 4.5 hour of epoxy amine reaction, all PA species was consumed.
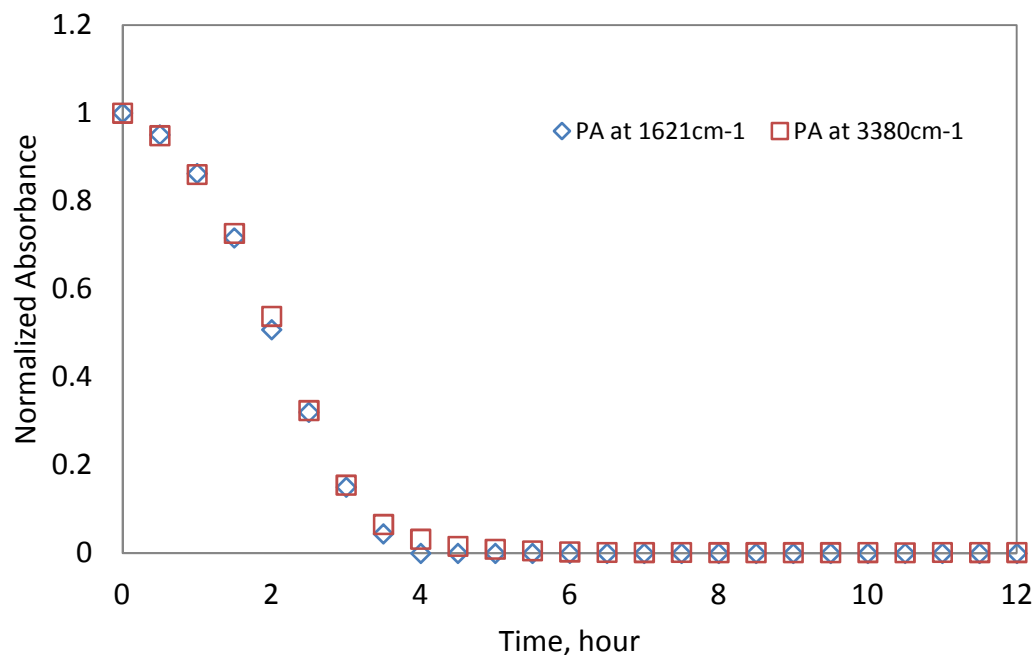
Figure 6.6 Comparison of normalized primary amine absorbance at 1622 cm^{-1} with that measured at 3380 cm^{-1}.

6.2.3 Epoxide Group Analysis

The last wavenumber area of interest contained epoxide peak. Here only one epoxide peak at 771 cm^{-1} was analyzed. Two peaks assigned to other epoxide vibrations were not examined in this analysis due to the spectral complexity. Seven peaks were used to fit the wavenumber area with assignments based on the DFT frequency calculation of PGE-Aniline system. It was noted that the epoxide peak was overlapped by the neighboring peak at 767 cm^{-1} which was assigned to phenyl group C-C stretching vibration mode. Therefore, peak parameters of at 767cm^{-1} was fixed throughout the spectra to eliminate the absorbance interference of the peak to the target epoxide peak. Figure 6.7 showed selected deconvlution results with peak assignment. It was also noted that the peak at 748

cm^{-1} was developing as cure reaction went on. DFT calculation result supported that the

absorbance increase was due to a formation of C-N-C structure.
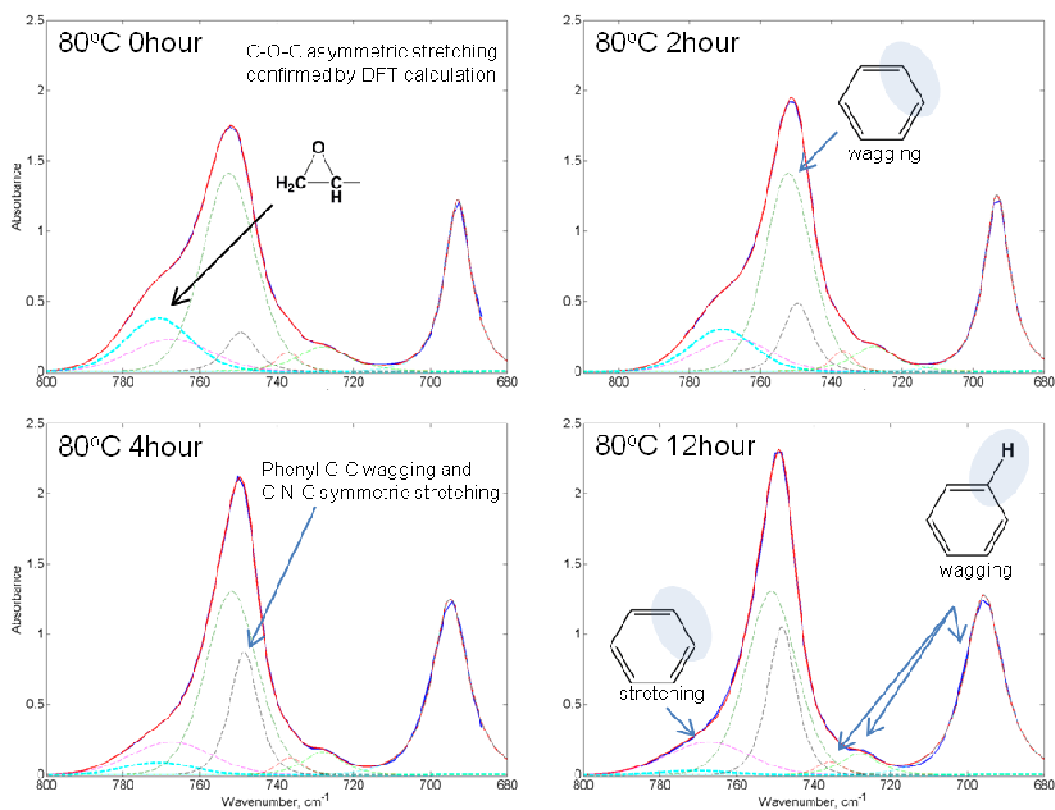
Figure 6.7 Epoxide peak evolution at 600-800 cm^{-1} during an isothermal cure of Epon825
with Aniline at 80°C

The same SA absorbance comparison analysis as performed in PGE-Aniline system was

also applied to Epon825-Aniline system. The absorbance difference of normalized

epoxide from normalized PA would directly proportional to the SA absorbance with the

assumption of no side reaction. Comparison of normalized SA absorbance with

[Epoxide]-[PA] showed good consistency.
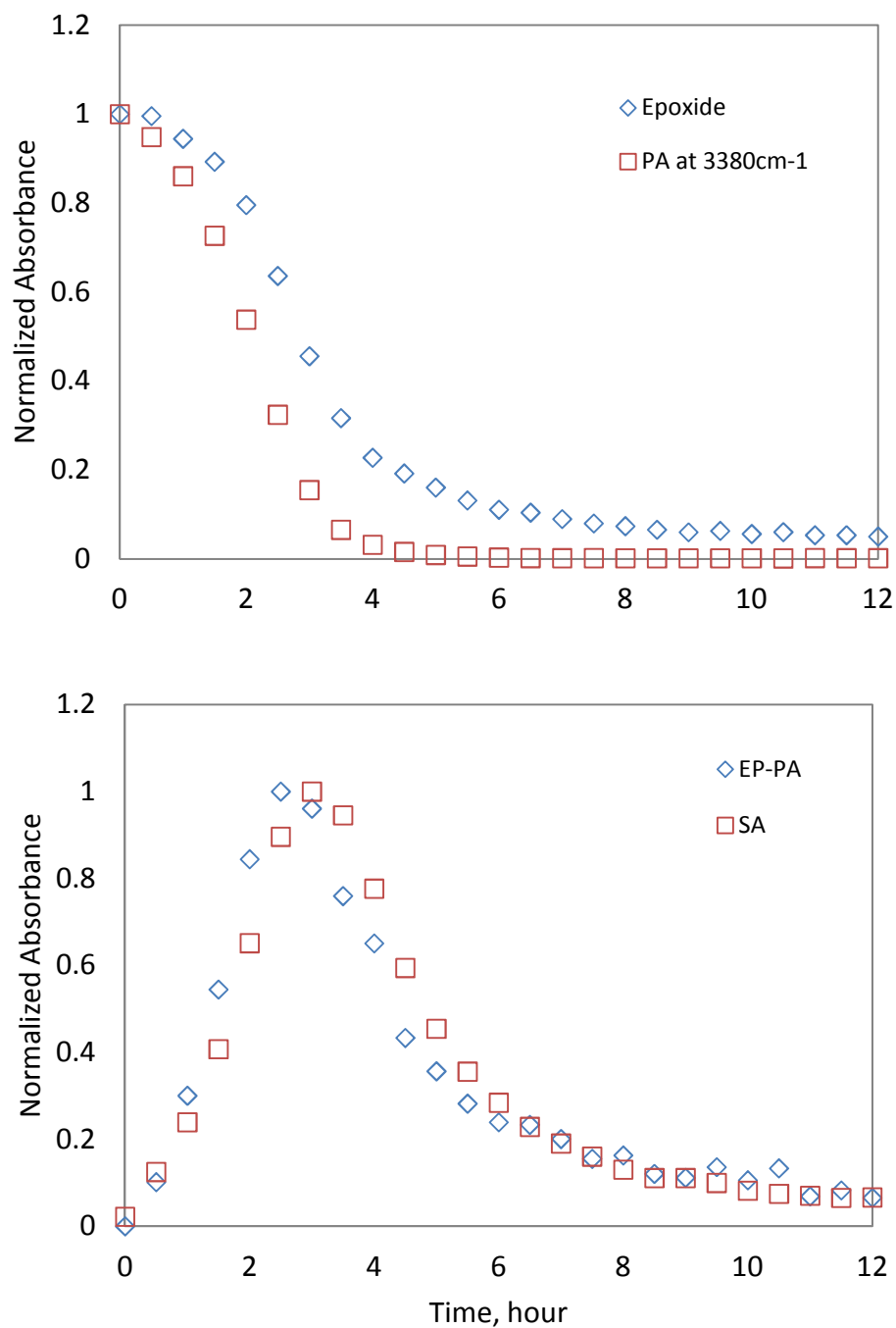
Figure 6.8 Comparison of normalized epoxide evolution with primary amine evolution (upper) and a comparison of normalized secondary amine evolution with difference of normalized [Epoxide] from [PA] (lower)

6.3   Comparison of Cure and Post-cure Process

The absorbance evolution of post-cured sample spectrum was compared with that of procured spectra to investigate the extent of cure development due to the post-cure process. Since the spectral line shape is critically dependent upon temperature, a simple comparison of peak areas before post-cure (80^oC) and after post-cure (120^oC) was meaningless. Therefore, Infrared spectrum of the post-cured sample was taken at 80^oC to eliminate temperature effect. It was found in the first wavenumber area, 3200-3650 cm^{-1}, PA was depleted as a result of 8 hours of pre-cure at 80^oC and the only species able to react with epoxide was SA species. Figure 6.9 showed a comparison of pre-cured sample spectrum with post-cured sample spectrum and it was found from the absorbance comparison of SA species that 6.6% of remaining SA has been consumed during the post-cure reaction. It was also noted that absorbance of all the OH peaks had increased as a result of the post-cure and their increments in the peak intensities were 6.5, 3.2, 1.2, and 3.4% respectively for OH1 through OH4 peak.

Since it was confirmed from the spectral evidence that all the reactant species, PA, SA, and epoxide groups have been depleted after the post-cure, it was concluded that the sample was fully cured after going through pre and post-cure process. Fully cured sample was still trapped in KBr assembly and the edge of the assembly was sealed with silicon rubber so that water could not penetrate into the cured sample. Thermal analysis was then performed using fully cured epoxy material in a temperature range of room temperature to 120^oC to examine the temperature dependency of IR spectrum as well as chemical and structural behavior of cured sample along with temperature change.
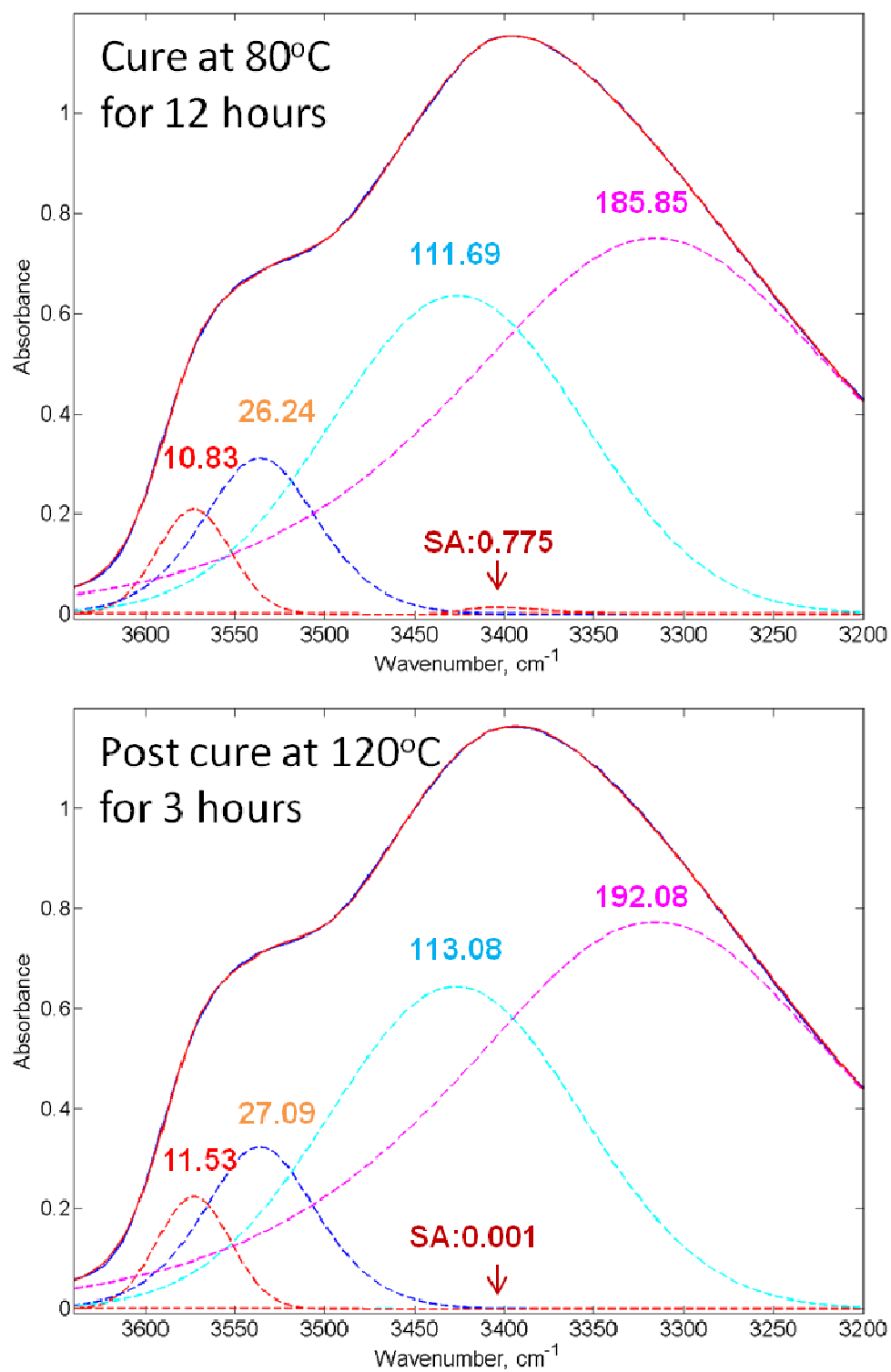
Figure 6.9 Comparison of spectral change after cure with that after post-cure

6.4   Thermal Cycle Analysis

In the previous sections, quantitative information regarding association and cure chemistry have been obtained through an isothermal condition since spectral line shape of FT-IR is significantly affected by temperature. However, it is valuable to investigate spectral line shape behavior as a function of temperature, because it could also provide the chemical aspects of the system at a certain temperature condition. Moreover, polymeric materials possesses multiple phases as a function of temperature and IR study at different temperature could be used to elucidate chemical and physical properties of polymeric materials by temperature study.

In this section, temperature effects on the spectral line shape as well as chemical and structural behaviors inside of the cured material were investigated using in-situ FT-IR technique. Cured Epon825 with stoichiometric amount of aniline that was used to obtain kinetic information in a previous section was used as a system of interest. To set up the experimental condition of thermal cycle analysis, the glass transition temperature of fully cured Epon825-Aniline system was found from the literature [62]. Based on T_g of full cured material, 95^oC, upper limit of the thermal cycle analysis was set to T_g+25^oC, where thermal decomposition was not occurring in a short exposure time. Figure 6.10 showed a series of spectra obtained during 3 thermal cycles of temperature change from the room temperature to 120^oC. One thermal cycle was composed of three steps, increase of 10^oC every 20 minutes up to 120^oC, 2 hour of annealing at 120^oC and decrease of 10^oC every 20 minute to the room temperature. Temperature was controlled by Omega temperature controller (CNi32) with K-type thermocouples, and temperature change was occurring in

a short time (less than 1 minute). It was noted that the OH association peaks had relatively large amount of spectral line shape change compared with the peaks for the chemical species that had no associations. In figure 6.10, peaks at around 3040 and 3060 cm^{-1} were assigned to C-H vibrations of phenyl groups on the main structure and these peaks had relatively little movement during the temperature change. Thermal cycle analysis also revealed that the spectral line shapes at the same temperature had great reproducibility regardless of number of thermal cycle and, as shown in the lower image of figure 6.10, the spectra obtained during increasing temperature schedule were perfectly overlapped with those obtained during decrease schedule at the same temperature More detailed thermal analysis on the association peaks were done by deconvolution technique. The constraints applied to fit the spectra were summarized in table 6.4.

Table 6.4 Constraints applied to fit OH bands

Parameters	OH1 (LB-UB)	OH2 (LB-UB)	OH3 (LB-UB)	OH4 (LB-UB)
m	0.004 (0-0.1)	0.49 (0.45-0.55)	0.1 (0.05-0.15)	0.7 (0.64-0.7)
x_0	3574 (3573-3576)	3538 (3536-3540)	3427 (3425-3430)	3312.84 (3310-3315)
W	49.7 (47-52)	80 (78-82)	171 (168-173)	266.48 (260-270)
a	0	0	0	0
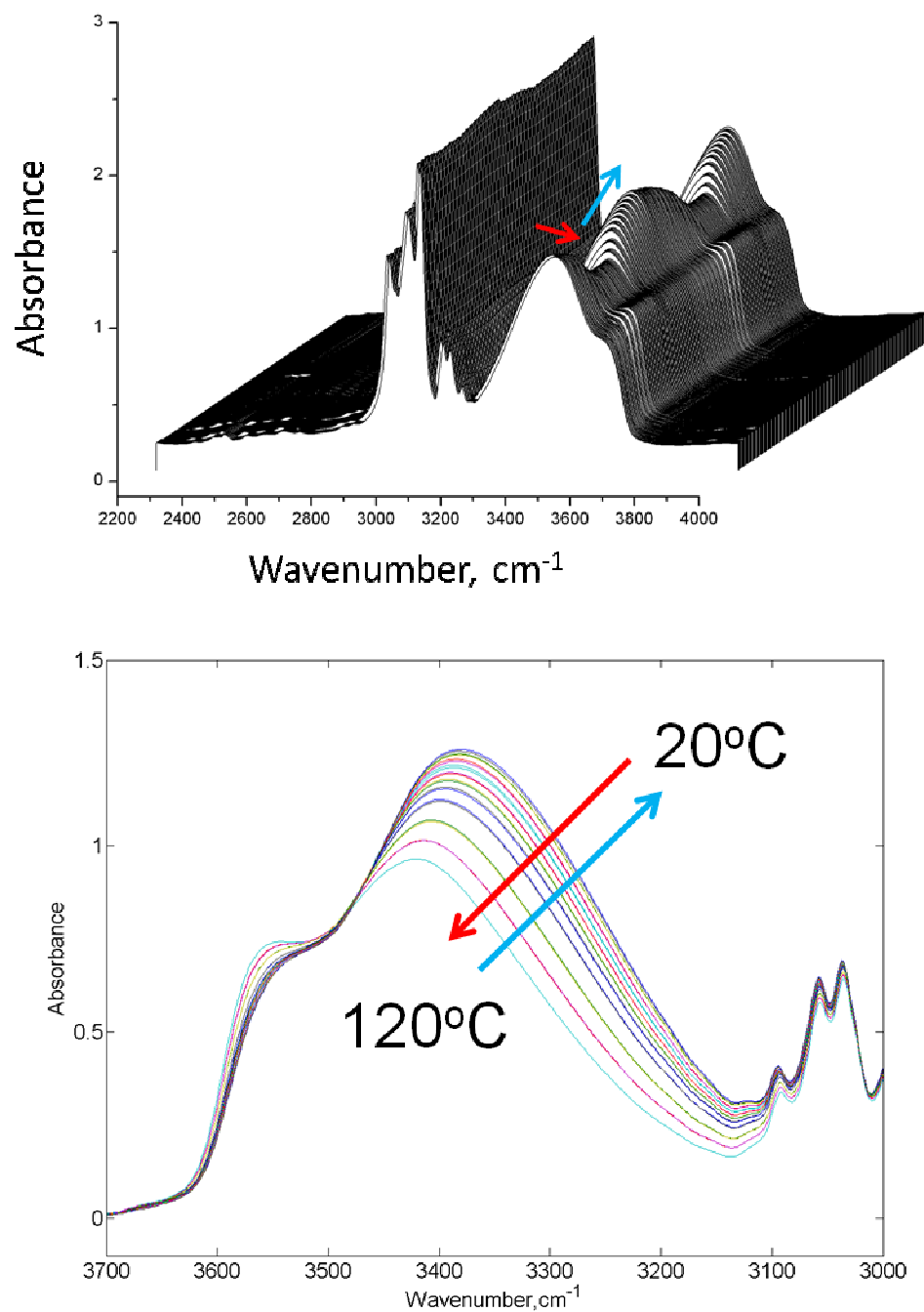
Figure 6.10 Spectral line shape change of fully cured Epon825 with Aniline during thermal cycles of 20 to 120°C (upper) and baseline corrected spectra during the second thermal cycle (lower)

Figure 6.11 was absorbance evolutions of OH1 through OH4 which were positioned at 3574, 3538, 3427, and 3313 cm^{-1} respectively. Each peak showed a different behavior when it comes to the temperature change in the cured system. However, they had an abrupt absorbance changing point in common, 95°C, which was T$_g$ of fully cured sample.
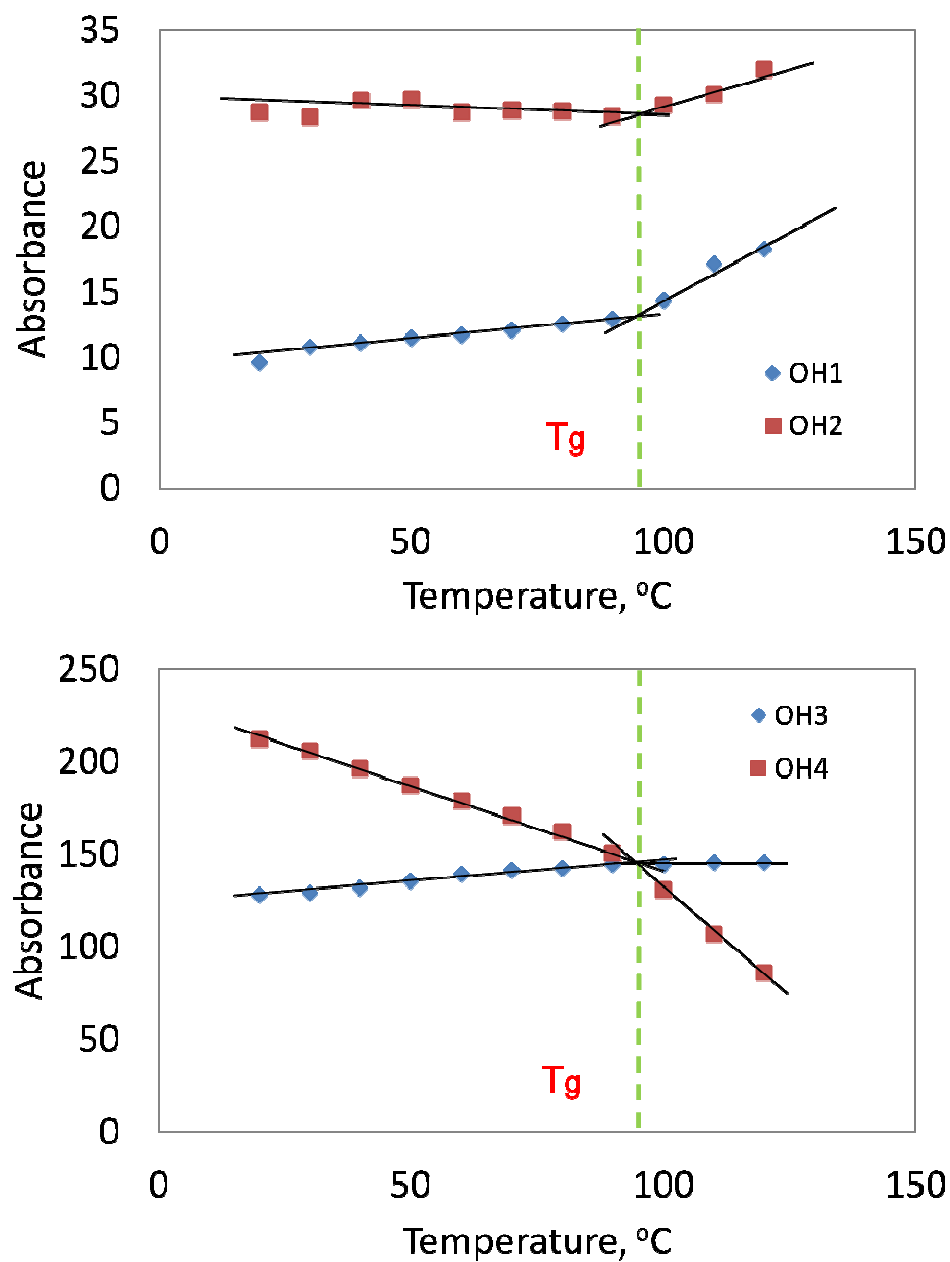
Figure 6.11 OH peak area evolutions during a thermal cycle of 20 to 120°C

Absorbance analysis was also performed on the isolated peak at 696 cm^{-1}, which was assigned to C-C vibration of phenyl group. It was noted that the absorbance had a systematic increase as the temperature of the system decreased.
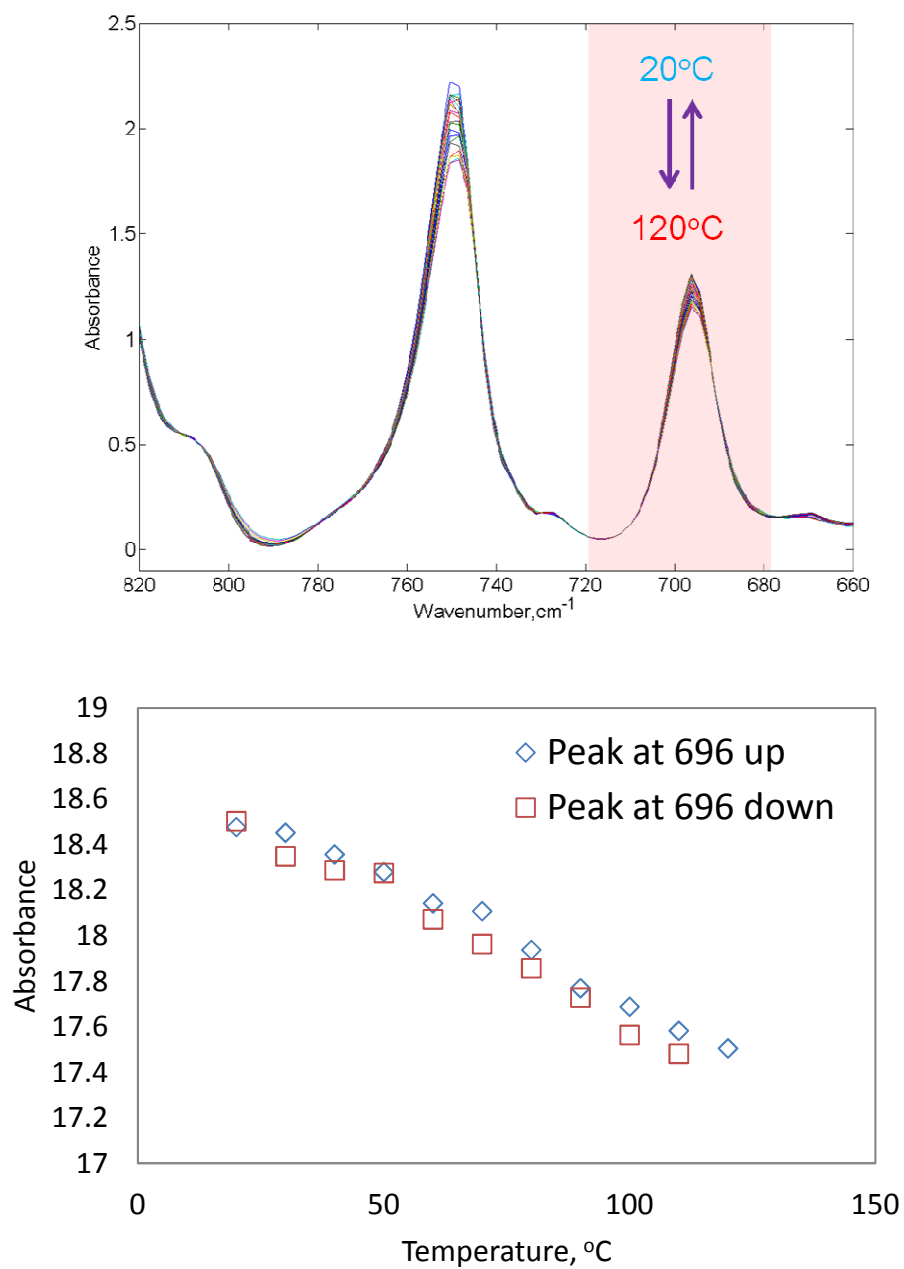
Figure 6.12 Evolution of peak area at 696 cm^{-1} during a thermal cycle

6.5   Preliminary Observation of Relaxation

Amorphous polymer has three states as a function of the system temperature, liquid,

rubbery and glassy state. The glass transition temperature (T_g) could be a standard point

that categorizes physical state of the amorphous polymer. At high temperature above T_g,

polymer behaves like liquid. Then as the temperature approaches to its T_g, the polymer

becomes rubbery state and if the system cools down below T_g, it becomes glassy state

which is non-equilibrium state. The physical state of polymer could be also described by

its free volume inside of the crosslinking structure and the temperature of the system. At

above T_g, polymer backbone becomes free to move by thermal energy and conducts a

continuous rearrangement of the crosslinking structure. In this state, the free volume of

the system is in equilibrium. However, as the temperature moves down below T_g,

polymer backbone gets confined in its thermal movement and the free volume becomes

quenching rate dependent. This volume relaxation is important because it can alter the

physical properties such as yield stress or material brittleness by changing mechanical

response of the polymeric material at a glassy state, which was known as physical aging

[63-65].

The relaxation phenomenon has been mainly measured by Thermomechanical Analysis

(TMA) or Dilatometer. Here, the relaxation of amorphous polymer was evaluated by

quantitative FT-IR analysis since peak intensity (absorbance) reflects the density of the

material by Beer-Lambert's law. Fully cured Epon825 with stoichiometric amount of

aniline that was previously manufactured and analyzed via thermal cycle analysis was

used as a sample specimen. Sample was installed in an IR chamber and temperature

down-jump and up-jump were performed on the sample with a temperature range from 85°C to 110°C. Before temperature down- and up-jump experiments were started, sample specimen has been put at 110°C (T$_g$+15°C) to erase previous thermal history. Then, for temperature down-jump, rapid temperature down was performed and a series of IR spectra has been obtained for three hours at 80°C (T$_g$−10°C). For temperature up-jump experiment, the sample has been annealed at 80°C for 3 hours after thermal history erasing and then rapid temperature up was performed for another 3 hours. A whole series of IR spectra was obtained every 1 minute during the entire analysis time, total 205 minutes (25 minutes before jump and 180 minutes after jump). Temperature was controlled by Omega CNi32 PID controller with K-type thermocouple and the temperature information has been obtained every 1 second during the analysis. Wavenumber area of 3150-3650 cm^{-1} was chosen to investigate the relaxation of Epon825 cured with aniline sample since the hydroxyl groups had showed the most dramatic changes in their absorbance in a previous thermal cycle analysis. Baseline correction of the raw spectra and deconvolution parameters were the same as those used in thermal cycle analysis. Figures 6.13 and 6.14 showed temperature jump experiment protocol and the spectral line shape changes of OH bands during the temperature jump experiment schedule. As shown in the previous thermal cycle analysis, 4 peak areas of OH bands at 3574, 3538, 3427, and 3313 cm^{-1} had their own absorbance change behaviors. Figure 6.15 and 6.16 showed the temperature profile and the absorbance changes of 4 hydroxyl groups during the temperature down-jump and up-jump respectively. In both temperature jump experiments, temperature jump was not conducted instantly and had 15 minutes of lagging. Therefore, 15 minutes absorbance profile after

the jump was not recorded here to prevent the temperature effect on the spectral line shape. Figure 6.15 showed the absorbance profiles of 4 OH bands after the temperature down-jump. Since the temperature applied for the down-jump was 10°C below T_g, the physical state of the sample material is glassy, which is non-equilibrium state. All OH bands showed gradual evolution in their absorbance and this indicated that the OH bands relaxed towards equilibrium. In figure 6.16, absorbance evolution during temperature up-jump was evaluated. The red line in the figure is absorbance quantity of each OH bands in equilibrium, which was measured at 110°C after three hours of annealing. OH2 and OH4 bands showed absorbance profiles that approached to the equilibrium but OH1 and OH3 was not sensitive to follow the relaxation towards equilibrium. Conventional relaxation monitoring has been performed using dilatometer and it directly measured specific volume change with given temperature schedule. FT-IR measured absorbance of OH band which showed the most dramatic change during temperature change. The specific relationship in between the absorbance and the density is not clear However, this relaxation measurement through FT-IR is meaningful in that it provided a possibility of monitoring relaxation property of glass forming material with widely used spectroscopic analysis than traditional relaxation measurement using TMA or Dilatometer.
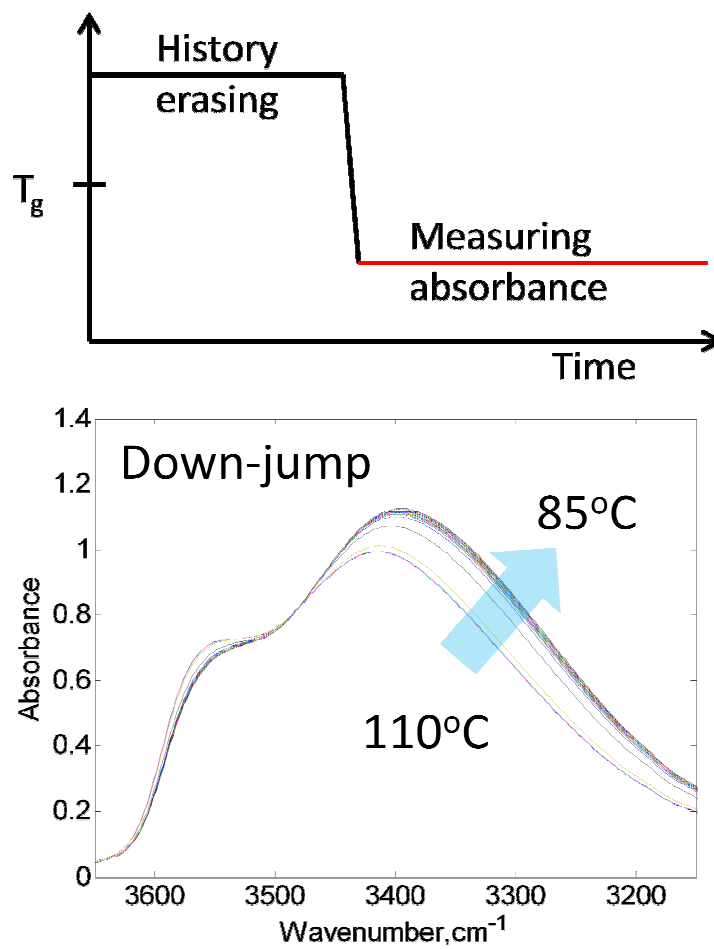
Figure 6.13 Temperature down-jump protocol and its spectral line shape change
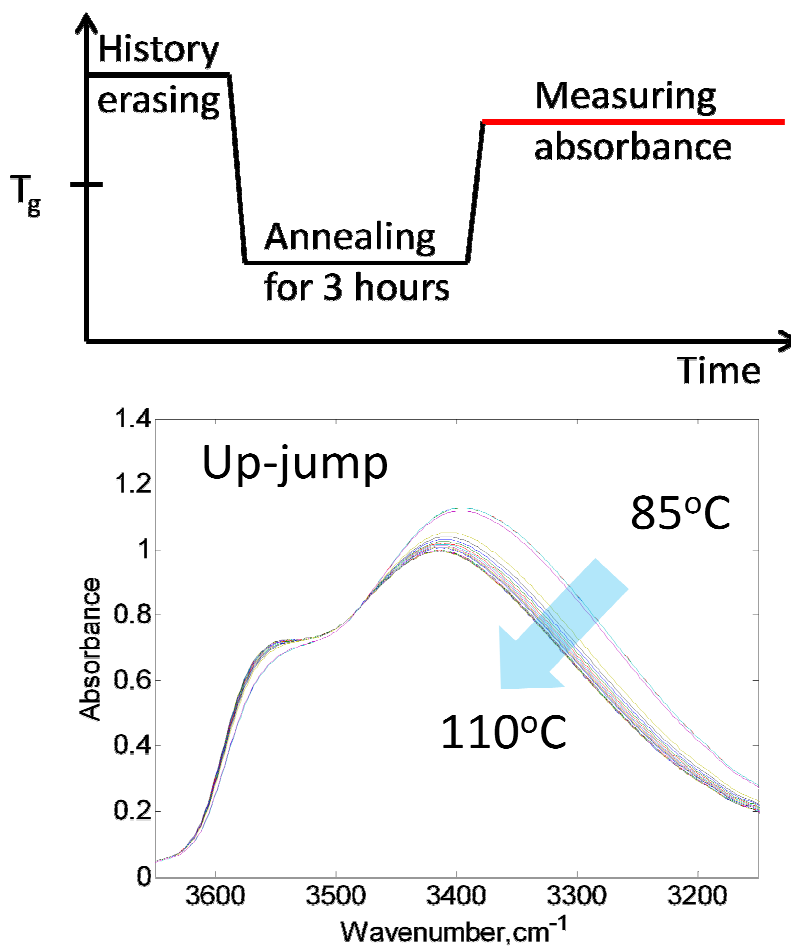
Figure 6.14 Temperature up-jump protocol and its spectral line shape change
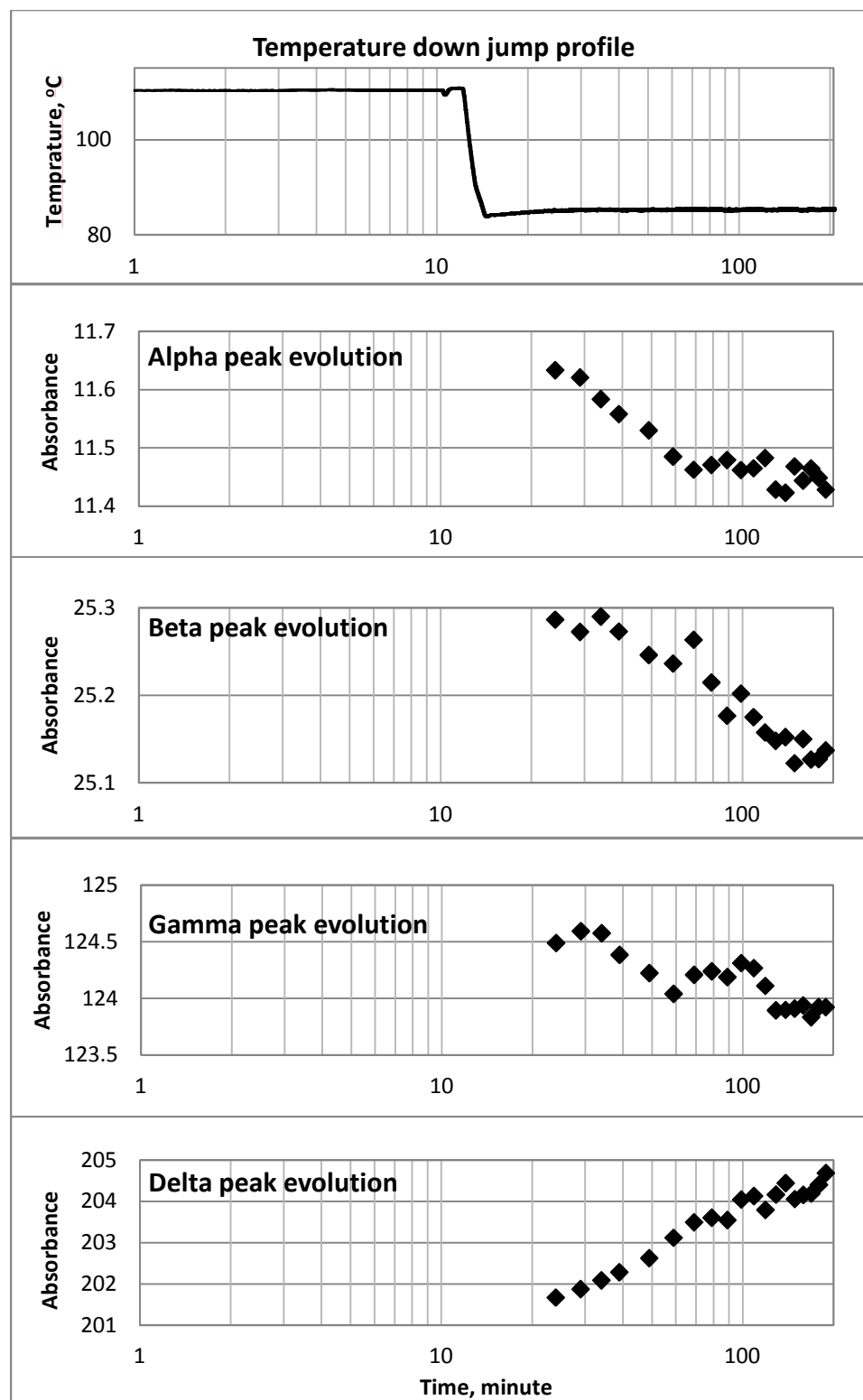
Figure 6.15 OH peak absorbance evolutions during temperature down-jump
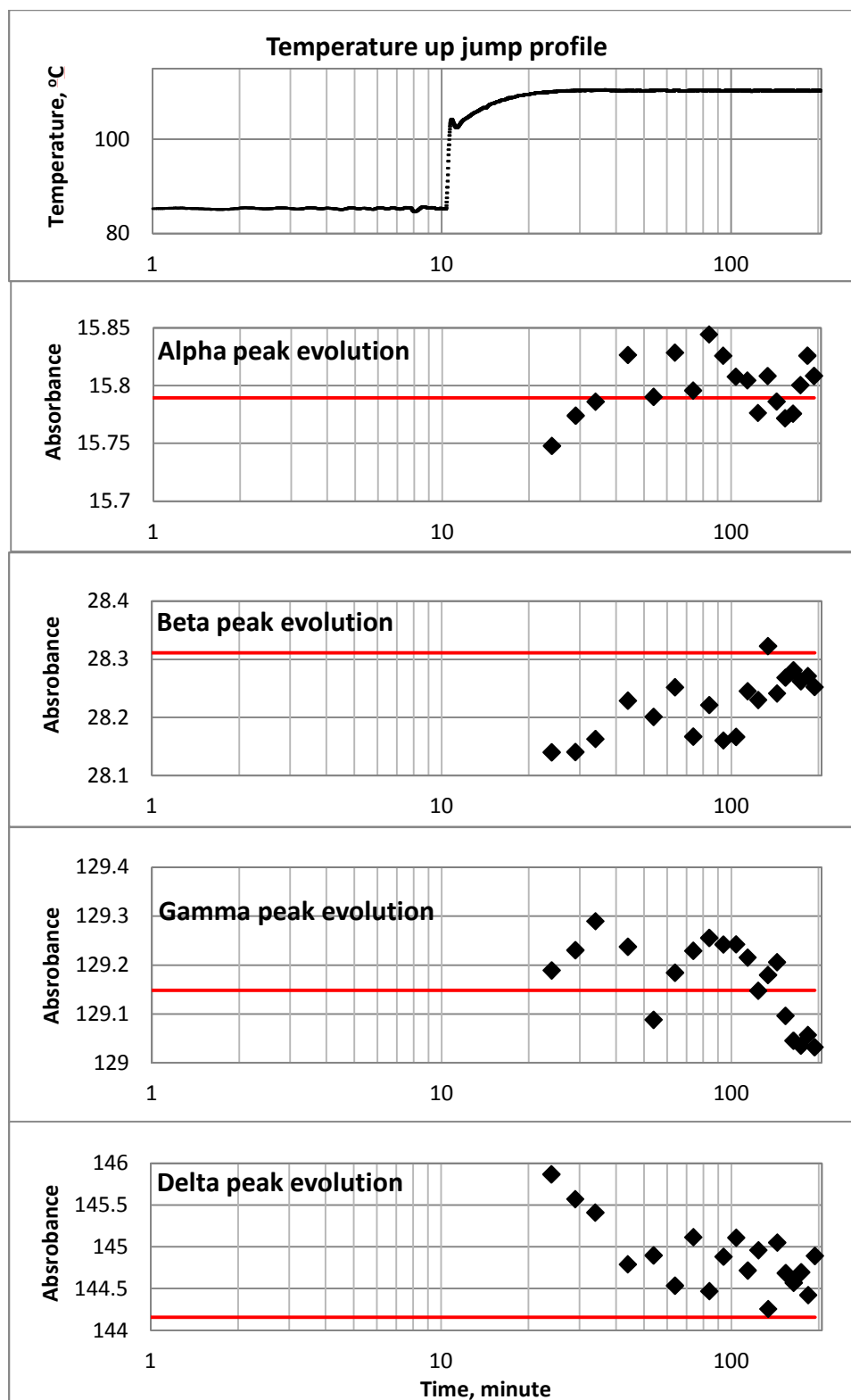
Figure 6.16 OH peak absorbance evolutions during temperature up-jump

CHAPTER 7. CONCLUSIONS

Quantitative FT-IR analysis methodology was developed and successfully applied to various systems such as hydrogen bonding equilibrium of amine and hydroxyl groups as well as amine-epoxy reaction system.

Baseline correction was first applied to the obtained spectra to offset the curvilinearly shifted baseline. Then, peak deconvolution was conducted on the spectra of specific wavenumber of interest. For the peak deconvolution, a product form of Gaussian and Lorentzian was used as a peak line shape equation with multiple parameters of width, position, and a ratio of Gaussian and Lorentzian shape. The chemical origins of the peaks were identified using density functional theory (DFT) calculation. The ground state of the molecules of interest were determined with Gaussian03 with B3LYP functional and Lanl2dz basis set and the molecular motion associated with a particular vibratioanl line was determined visually using GaussView.

Hydrogen bonding equilibria of amine and hydroxyl groups were investigated first because these chemical species were the main participants in amine-epoxy reaction system and their hydrogen bonding associations resulted in formation of various types of hydrogen bonding peaks in amine-epoxy reaction system. Self and inter-association of N-methylaniline and isopropanol were investigated. As hydrogen bonding acceptors, toluene and triethylamine, which were model π-bond and an amine electron pair

respectively, were mixed with N-methylaniline and isopropanol in CCl_4. DFT calculation at B3LYP/Lanl2DZ level also provided vibrational frequency shift by two different types of H-bonding in ternary systems as well as hydrogen bonding distance. Spectral deconvolution has been conducted for various dilution concentration samples and finally, concentration profile of free monomer could be obtained. It was shown that the hydrogen bond equilibrium models were only valid at the diluted concentration range and monomer concentration decreased when liquid-liquid phase transition occurred at a constant temperature. Moreover, decrease of monomer concentration had a curvature rather than a linear line, which would have been expected from the simple lever rule along the tie line inside of coexistence curve at isothermal and isobaric conditions. For N-methylaniline, association equilibrium model with dimerization and multimerization equilibrium constants was adapted to fit the absorbance data. The equilibrium constants were evaluated and further utilized to describe equilibria in N-methylaniline with multiple proton acceptors mixtures. For isopropanol, the association was more complex since various types of association species were present. Association model based on Flory-Schultz distribution was adapted to fit the absorbance data and it was compared with two equilibrium constant model (Coggeshall-Saier model, which was used for N-methylaniline system). Comparison indicated that the single equilibrium constant model (Flory-Schultz model) showed similar chain length and molecular weight distribution of two equilibrium model (Coggeshall-Saier model). Based on the single equilibrium constant model, self and inter-association of isopropanol was investigated and their equilibrium constants were evaluated.

Quantitative analysis was then applied to the reaction system of amine-epoxy. Model system of non-crosslinking materials, Phenylglycidylether (PGE) and N-methylaniline (NmA) were selected first to validate the quantitative FT-IR method by HPLC analysis. In order to find the activation energy of Amine and Epoxy reaction, reactions with 4 different temperatures from 50 to 110°C were conducted for PGE and NmA system. Termolecular complex theory was applied to obtain kinetics of autocatalytic reaction and the calculated activation energy by Arrhenius equations were 112.2 and 54.9 KJ/mol from the first and second complex respectively. Then, in-situ FT-IR cure was conducted at 80°C for 24 hours and the concentration profiles of reactants and a resultant could be obtained.

Two mid-IR regions of interest were deconvoluted to obtain kinetic information, 3000-3650 cm^{-1} and 750-900 cm^{-1}. From the spectral analysis of the first wavenumber region, it was noted that amine and hydroxyl groups had multiple peaks, which were originated from hydrogen bonding associations of amine and hydroxyl groups with various proton acceptors such as π-bond on phenyl group and electron pairs of amine, ether, or hydroxyl groups. In the second region of interest, it was also noted with an aid of DFT that epoxide peaks for symmetric and asymmetric stretching vibrations were found at 875 cm^{-1} and 845 cm^{-1}. All peaks were chemically assigned based on the DFT frequency calculation and deconvoluted. Obtained absorbance evolution of amine and epoxide showed a good overlap with each other and the mass balance of the concentration profiles of reaction participants also showed a good consistency. The kinetic constant value was well fitted into Arrhenius plot of HPLC result.

Finally, quantitative analysis was applied to crosslinking system. Epon825 and Aniline were employed as model epoxide and amine. Cure process was conducted at 80^oC for 12 hours followed by post cure at 120^oC for another 3 hours in-situ. Three wavenumber areas were investigated for chemical species of primary amine, secondary amine, hydroxyl group and epoxide peaks. In the first section, 3100-3700 cm^{-1}, multiple peaks were assigned to the associated primary amine, secondary amine and hydroxyl peaks based on the former investigation of hydrogen bonding association. It was noted from the deconvolution result that the primary amine was completely consumed in the first 12 hours cure at 80^oC and the remaining secondary amine at the end of cure was all consumed after the post cure. In the second region, 1560-1670 cm^{-1}, primary amine peak evolution was observed and the absorbance evolution showed a good consistency with that obtained in the upper wavenumber region. Epoxide peak was deconvoluted at 680-800 cm^{-1} with a support from DFT peak assignment and its evolution was compared with primary amine and secondary amine evolutions.

Thermal cycle analysis was conducted for the fully cured Epon825-Aniline system. Three cycles of heating up to 120^oC-Annealing-cooling down to 20^oC were applied and it was shown that the hydrogen bonding associated peaks had big spectral line shape changes at around the ultimate glass transition temperature, 95^oC. Absorbance evolution of the peak at 698 cm^{-1} which was assigned to phenyl C-H stretching vibration was monitored as a comparison and it did not show an abrupt change throughout the entire thermal cycle. Relaxation properties were also monitored by temperature jump experiment. It was difficult to see the relaxation effect by current FT-IR analysis due to absence of sophisticated temperature control. However, it brought the insight that FT-IR could be

used to monitor not only chemistry inside of the system but also bulk physical property such as relaxation and glass transition temperature.

In summary, Quantitative FT-IR method could provide detailed chemical information of polymer regarding cure and post cure reactions and it can also be applied to the degradation of polymer. Therefore, chemically based life time performance monitoring of polymeric material could be achieved by quantitative FT-IR analysis technique.

CHAPTER 8. FUTURE WORK

FT-IR technique is used in various fields of application spanning the diluted systems as well as the polymeric systems. This experimental method can be an effective and straightforward way to monitor the chemical processes occurring inside a system of interest. The advantages are that i) it uses conventional FT-IR analyzer, ii) allows for re-using of previously obtained IR data.

In this study, quantitative FT-IR method was used to examine not only chemical equilibrium of hydrogen bonding association but also to obtain kinetic information of amine-epoxy reaction. This methodology also provided the possibility of physical property measurement of polymeric material such as glass transition temperature or relaxation properties. One of the most interesting findings in this study was that in addition to the cure reaction, the post-cure reaction could be quantitatively analyzed. This is also true with regard to the cure reaction proper as occurring at the later stages of cure. The later stages of cure are important in both chemical and physical aspects because the crosslinking that determines physical properties of polymeric material is formed at these stages. At the same time, it is noted that chemical reaction hardly proceeds further because of the crosslinking. FT-IR analysis would be effectively utilized in these stages of cure since the cure observation by monitoring peak line shape change could be more

sensitive than the observation by conventional DSC method. Therefore, in the future, FT-IR could be used to monitor cure of polymeric material at later stages of cure.

It was also observed from the deconvoluted peak absorbance profile in the temperature jump experiment that FT-IR method can also demonstrate relaxation of vibrating molecules in the cured system. However, in this study, the exact reason of relaxation of molecular vibration has not been verified yet. Identification of associated hydroxyl groups in amine-epoxy cure system that were involved in the relaxation monitoring can elucidate the relationship in between temperature and molecular vibration and it will aid to verify the origins of relaxation shown in the quantitative IR analysis. Elaborated DFT calculation as well as cure reaction with different stoichiometry will be performed to resolve peak identification issue in the future.

The relaxation at high temperature around T_g is strongly related with α transition in a structure-property relationship. Once the origin of relaxation in a molecular level observed via FT-IR has been verified, the same relaxation monitoring experiment will be performed at lower temperature, where β transition occurs, to see if the quantitative FT-IR technique can also observe the relaxation in this temperature range.

REFERENCES

REFERENCES

1. K. E. Chike, M. L. Myrick, R. E. Lyon, and S. M. Angel, "Raman and Near-Infrared Studies of an Epoxy Resin, Applied Spectroscopy", 47, 1631-1635, 1993

2. Qian Wang, Girgit K. Storm, Lars P. Houmøller, "Study of the isothermal curing of an epoxy prepreg by near-infrared spectroscopy", Journal of Applied Polymer Science, 87(14),2295-2305, 2003

3. Liang Li, Qili Wu, shanjun Li, Peiyi Wu, "Study of the Infrared Spectral Features of an Epoxy Curing Mechanism", Applied Spectroscopy, 62(10), 1129-1136, 2008

4. L. Xu, J. H. Fu, J. R. Schlup, "In Situ Near-Infrared Spectroscopic Investigation of Epoxy Resin-Aromatic Amine Cure Mechanisms", Journal of American Chemical Society, 116(7), 2821-2826, 1994

5. Jovan Mijovic, Sasa Andjelic, "A Study of Reaction Kinetics by Near-Infrared Spectroscopy. 1. Comprehensive Analysis of a Model Epoxy/Amine system", Macromolecules, 28(8), 2787-2796, 1995

6. Pellegrino Musto, Giuseppe Ragosta, Pietro Russo, Leno, Mascia, "Thermal-Oxidative Degradation of Epoxy and Epoxy-Bismaleimide Networks: Kinetics and Mechanism", Macromolecular chemistry and physics, 202(18), 3445-3458, 2001

7. John. R. Dyer, "Applications of Absorption Spectroscopy of Organic Compounds", Prentice Hall, 1965

8. Gaussian 03, Revision C.02, M. J. Frisch, G. W. Trucks, H. B. Schlegel, G. E. Scuseria, M. A. Robb, J. R. Cheeseman, J. A. Montgomery, Jr., T. Vreven, K. N. Kudin, J. C. Burant, J. M. Millam, S. S. Iyengar, J. Tomasi, V. Barone, B. Mennucci, M. Cossi, G. Scalmani, N. Rega, G. A. Petersson, H. Nakatsuji, M. Hada, M. Ehara, K. Toyota, R. Fukuda, J. Hasegawa, M. Ishida, T. Nakajima, Y. Honda, O. Kitao, H. Nakai, M. Klene, X. Li, J. E. Knox, H. P. Hratchian, J. B. Cross, V. Bakken, C. Adamo, J. Jaramillo, R. Gomperts, R. E. Stratmann, O. Yazyev, A. J. Austin, R. Cammi, C. Pomelli, J. W. Ochterski, P. Y. Ayala, K. Morokuma, G. A. Voth, P. Salvador, J. J. Dannenberg, V. G. Zakrzewski, S. Dapprich, A. D. Daniels, M. C. Strain, O. Farkas, D. K. Malick, A. D. Rabuck, K. Raghavachari, J. B. Foresman, J. V. Ortiz, Q. Cui, A. G. Baboul, S. Clifford, J. Cioslowski, B. B. Stefanov, G. Liu, A. Liashenko, P. Piskorz, I. Komaromi, R. L. Martin, D. J. Fox, T. Keith, M. A. Al-Laham, C. Y. Peng, A. Nanayakkara, M. Challacombe, P. M. W. Gill, B. Johnson, W. Chen, M. W. Wong, C. Gonzalez, and J. A. Pople, Gaussian, Inc., Wallingford CT, 2004.

9. G. Jeffrey, "An Introduction to Hydrogen Bonding", Oxford University Press, New York, Oxford, 1997
10. Guatam R, Desiraju and Thomas Steiner, "The Weak Hydrogen Bond", Oxford Science Publications, 1999
11. Irving. M. Klotz and James. S. Franzen, "Hydrogen Bonds between Model Peptide Groups in Solution", Journal of American Chemical Society, 84(18), 3461-3466, 1962
12. H. Kempter and R. Mecke, "Spectroscopic determination of association equilibrium", *Z. Phys. Chem.*, 46, 229-241, 1941
13. N. D. Coggeshall and E. L. Saier, "Infrared Absorption Study of Hydrogen Bonding Equilibria", Journal of American Chemical Society, 73(11), 5414-5418, 1951
14. Aaron N. Fletcher, "Molecular structure of ethanol-d1 solutions. Near-infrared study of hydrogen bonding", The Journal of Physical Chemistry, 76(18), 2562-2571, 1972
15. Kazuko Shinomiya, Toshiomi Shinomiya," An Equilibrium Model of the Self-Association of 1- and 3-Pentanols in Heptane", Bulletin of the Chemical Society of Japan, 63(4), 1093-1097, 1990
16. Mansel Davies and D. K. Thomas, "Energies And Entropies Of Association For Amides In Benzene Solutions. Part I", The Journal of Physical Chemistry,60(6), 763-766, 1956
17. Kermit B. Whetsel and J. H. Lady, "Infrared Studies of Amine Complexes. II. Formation Constants and Thermodynamic Properties of Amine-Chloroform Complexes1", The journal of physical chemistry, 68(5), 1010-1016,1964
18. J. Harold Lady and Kermit B. Whetsel, "Infrared studies of amine complexes. IV. The N-H-O hydrogen bond in aromatic amine complexes of ethers ketones, esters, and amides", The journal of physical chemistry, 71(5), 1421-1429, 1967
19. A.D. Nikolić, M. Tarjani, N. Perišić-Janjić, S.D. Petrović, "N–H···O hydrogen bonding: FT IR, NIR and 1H NMR study of N-methylpropionamide – Cyclic ether systems", Journal of molecular structure, 174, 129-134, 1988
20. Herbert R. Ellison and Barbara W. Meyer, The journal of physical chemistry, 74, 3861-3867, 1970
21. G.C. Pimentel, A.L. McClellan, The Hydrogen Bond, W.H. Freeman and Co., San Francisco and London, 1960
22. P. Schuster, G. Zundel, C. Sandorfy, The Hydrogen Bond. Recent Developments in Theory and Experiments, vol. I–III, North Holland Publishing Co., 1976
23. S.N. Vinogradov, R.H. Linnel, Hydrogen Bonding, Van Nostrand Reinhold Co., New York, 1971
24. Andrea Choperena, Paul Painter, Vibrational Spectroscopy, 51, 110-118, 2009
25. Jean-Joseph Max and Camille Chapados, J. Chem. Phys. 128, 224512, 2008
26. Fanny Schwager, Eva Marand, and Richey M. Davis, J. Phys. Chem. 1996, 100, 19268-19272
27. Georgios M. Kontogeorgis, Ioannis Tsivintzelis, Nicolas von Solms, Andreas Grenner, David Bøgh, Michael Frost, Anders Knage-Rasmussen, Ioannis G. Economou, Fluid Phase Equilibria, 296, 219-229, 2010

28. Krzysztof Pralat, Jan Jadzyn, Stefania Balanicka, J. Phys. Chem. 87, 1385-1390, 1983
29. Urner Liddel and Edwin D. Becker, Spectrochimica Acta 10, 70-84, 1957
30. N. Asprion, H. Hasse, G. Maurer, Fluid Phase Equilibria 186, 1–25, 2001
31. Olof Kristiansson, Journal of Molecular Structure, 477, 105-111, 1999
32. Ram B. Gupta and Ray L. Brinkley, AIChE Journal. 44, 207-213, 1998
33. Igor A. Sedov, Boris N. Solomonov, Journal of molecular liquids, 167, 47-51, 2012
34. Xiaoming Yang, Pau C. Painter, and Michael M. Coleman, Macromolecules, 25, 2156-2165. 1992
35. Egil Nodland, Applied Spectroscopy, 54, 1339-1349, 2000
36. Jenn-Shing Chen, Cheng-Chang Wu, Dah-Yu Kao, Spectrochimica Acta Part A, 60, 2287-2293, 2004
37. A.V. Iogansen, Spectrochimica Acta Part A, 55, 1585–1612, 1999
38. Mark Rozenberg, Aharon Loewenschuss and Yizhak Marcus, Phys. Chem. Chem. Phys., 2, 2699-2702, 2000
39. Marie-Claude Bernard-Houplain, C. Sandorfy, Can. J. Chem. 51, 1075-1082, 1973
40. R. Laenen and C. Rauscher, J. Chem. Phys. 107, 9759, 1997
41. A Nikolic, B. Jovic S. Csanady, S Petrovic, Journal of Molecular Structure 834-836, 249-252, 2007
42. H. Graener, T. Q. Ye, and A. Laubereau, Journal of chemical Physics, 90, 3413-3416, 1989
43. Whetsel, K. B. and Lady, J. H. Spectrometry of Fuels; Friedel, H., Ed.; Plenum Press: London, 1970; Chapter 20
44. Michael M. Coleman, Xiaoming Tang, Paul C. Painter, John F. Graf, Macromolecules, 25, 4414-4424, 1992
45. Michael M. Coleman, Paul C. Painter, Progress in Polymer Science, 20, 1-59, 1995
46. Neil A. Dotson, Rafael Galvan, Robert L. Laurence, Matthew Tirrell, Polymerization process modeling, chapter2, VSH publishers, Inc.
47. Nancy E. Levinger, Paul H. Davis and M. D. Fayer, Journal of Chemical Physics, 115, 9352-9360, 2001
48. Coleman, M. M.; Graf, J. F.; Painter, P. C. Specific interactions and the miscibility of polymer blends, Technomic Publishing Inc: USA, 1991
49. Coleman, M. M.; Graf, J. F.; Painter, P. C. Miscible Polymer Blends, DEStech Publications Inc: USA, 2006
50. H. Dannenberg, Polymer Engineering and Science, 3, 78-88, 1963
51. Nigel A. St John, Graeme A. George, Polymer, 33, 2679-2688, 1992
52. B. G. Min, Z. H. Stachurski, J. H. Hodgkin, G. R. Heath, Polymer, 34, 3620-3627, 1993
53. Lisheng Xu, John R. Schlup, Journal of Applied Polymer Science, 70, 895-901, 1998
54. Soo-Jin Park, Gun-Ho Kwak, Masao Sumita, Jae-Rock Lee, Polymer Engineering and Science, 40, 2569-2576, 2000

55. C. Billaud, M. Vandeuren, R. Legras, V. Carlier, Applied Spectroscopy, 56, 1413-1421, 2002

56. C. J. Bakker, N. A. St John, G. A. Geroge, Polymer, 34, 716-725, 1993

57. H. Kun Hseih, Chean C. Su, Eamor M. Woo, Polymer, 39, 2175-2183, 1998

58. Courtney L. Sherman, Robert C. Zeigler, Nikhil E. Verghese, Maurice J. Marks, Polymer, 49, 1164-1172, 2008

59. Marco Paolantoni, Paola Sassi, Assunta Morresi, Rosario Sergio Cataliotti, Chemical Physics, 310, 169-178, 2005

60. Nicolas Von Solms, Lars Jensen, Jonas L. Kofod, Michael L. Michelson, Georgios M. Kontogeorgis, Fluid Phase Equilibria, 261, 272-280, 2007

61. R. F. Blanks and J.M. Prausnitz, The Journal of Chemical Physics, 38, 1500-1504, 1963

62. Steven Swier, Guy Van Assche, Wendy Vuchelen, Bruno Van Mele, Macromolecules, 38, 2281-2288, 2005

63. G. B. MacKenna, S. L. Simon, , "Time Dependent Volume and Enthalpy Responses in Polymers," "Time Dependent and Nonlinear Effects in Polymer and Composites", ASTMSTP 1357, R.A. Schapery and C. T. Sun Eds., American Society for Testing and Materials, West Conshohocken, PA, 2000, pp. 18-46

64. Srinvas Kolla, Volume Recovery of an Epoxy Material: Resolution of the Tau Effective Paradox, Thesis, Texax Tech University, 2003

65. A.J. Kovacs, "Glass Transition in Amorphous Polymers: A Phenomenological Study," Advances in Polymer Science, Vol3, 394-507, 1963

VITA

VITA

SANG HA SON
Graduate School, Purdue University

<u>Education</u>

B.S., Chemical Engineering, 2005, Yonsei University, Seoul, South Korea
Thesis: Effect of NaOH on the Decomposition of Halogenated Hydrocarbon by Supercritical Water Oxidation.
Advisor: Professor Chang-Ha Lee

M.S., Chemical Engineering, 2007, Yonsei University, Seoul, South Korea
Thesis: Catalytic Effect of Corroded Metal Alloys on Subcritical and Supercritical Water Oxidations of 2-Chlorophenol.
Advisor: Professor Chang-Ha Lee

Ph.D., Chemical Engineering, 2013, Purdue University, West Lafayette, Indiana
Dissertation: Development of Quantitative FTIR Methods for Analyzing the Cure Kinetics of Epoxy Resins
Advisor: Dr. James M. Caruthers

<u>Research Interests</u>

Graduate Research Assistant, Purdue University, West Lafayette, IN
Synthesis epoxy and phenoxy film.
In-situ cure monitoring via FT-IR.
Concentration profiling using peak deconvolution and baseline correction of FT-IR spectra.
Peak identification and characterization using Density Functional Theory (DFT) calculation of frequency data.
Inter and intra-molecular hydrogen bonding analysis of hydroxyl and amine groups via FT-IR.
Epoxy film weathering via thermal oxidative and UV oxidative degradation.
Developing and testing e-lab notebook, SciAether.

Graduate Research Assistant, Yonsei University, Seoul, South Korea
Development of anti-corrosive Supercritical Water Oxidation Reactor.
Metal corrosion study under supercritical water oxidation process.
Synthesis of nano phosphors using supercritical water.

Teaching Experience
Graduate Teaching Assistant, Purdue University, West Lafayette IN
Chemical Reaction Engineering (CHE348), spring 2011
Senior Design Lab (CHE430), spring 2010
Summer Undergraduate Research Fellowships mentor
Rubber vulcanization with XDR viscometer, Sunmmer 2008
Graduate Teaching Assistant, Yonsei University, Seoul, South Korea
Chemical Engineering Thermodynamics (2), Fall 2005

Selected Leadership Experience
Purdue University, West Lafayette IN
President of Purdue Korean Tennis Club, Aug 2011-Dec 2012
President of Purdue Korean Association, Aug 2010-Jul 2011
Representative of Korean Chemical Engineers at Purdue, Aug 2009- Jul 2010
Military Service, South Korea
Headquarters, Reconnoitering battalion, The Key division, Korean Army
Jan 1999- Mar 2001
Yonsei University, Seoul, South Korea
Association leader, 'Uwoorukee', Korean traditional music performance group
Mar 1998-Dec 1998

Affiliation
American Chemical Society, Polymer division, *Spring 2013*